Proceedings of

RAGtime 10–13: Workshops on black holes and neutron stars

15–17/20–22/15–17/14–16
September '08/'09/'10/'11
Opava, Czech Republic

Editors:
Z. Stuchlík, G. Török,
T. Pecháček

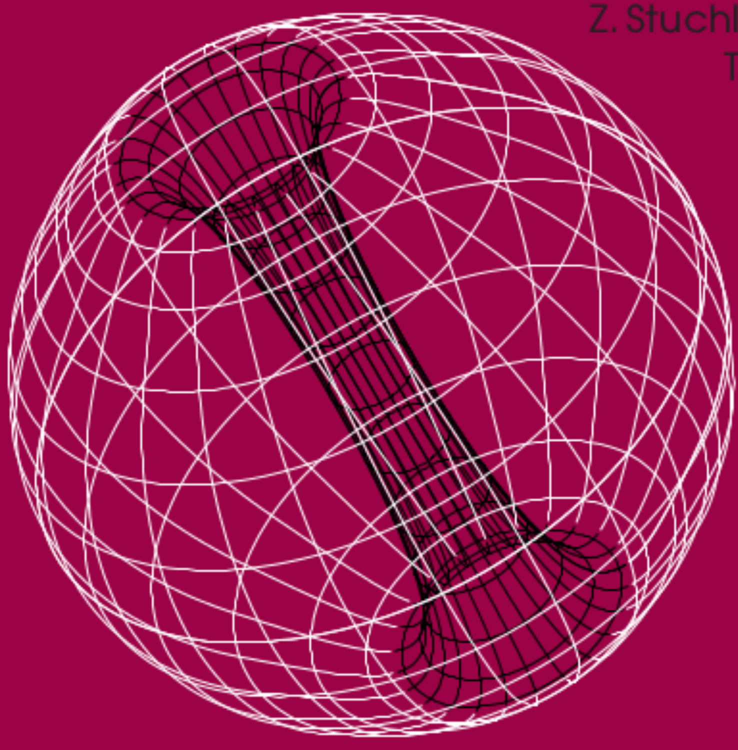

SILESIAN UNIVERSITY IN OPAVA

Publications of the Institute of Physics No. 6

Proceedings of RAGtime 10–13:
Workshops on black holes and neutron stars
15–17/20–22/15–17/14–16 September
2008/2009/2010/2011
Opava, Czech Republic

Z. Stuchlík, G. Török and T. Pecháček, editors

Opava 2014

Annotation: In this Proceedings, the talks presented during workshops *RAGtime 10–13: Workshops on black holes and neutron stars, Opava, 15–17/20–22/15–17/14–16 September 2008/2009/2010/2011* are collected.

ISBN 978-80-7510-125-9

PREFACE

Since 1999, the RAGtime meetings have been organized by the Relativistic Astrophysics Group (RAG) at the Institute of Physics, the Faculty of Philosophy and Science of the Silesian University in Opava in order to provide opportunities for discussing the recent advances and developments in the field of relativistic astrophysics. During the past sixteen years, RAGtime has grown from a small workshop to become a regular international conference that brings together collaborators of the Opava's reseach group who are coming from EU, USA, China and Japan. It has also provided a starting point for many new collaborations. Among the involved institutions are the Astronomical Institute of the Academy of Sciences of the Czech Republic, the Faculty of Mathematics and Physics of the Charles University in Prague, the International School for Advanced Studies and the Abdus Salam International Centre for Theoretical Physics in Trieste, the Institute of Astrophysics at the University of Oxford, the Department of Astrophysics of the University in Gothenburg, the Institute of Astronomy of the Polish Academy of Sciences, the Massachusetts Institute of Technology, the Harvard University, the Cornell University, the Hiroshima University, the Fudan University, and the Xiamen University.

Concordantly, the scope of the topics discussed at the meetings has widened considerably in recent years. New results have been presented at the conference from different areas, such as the alternative theories of gravitation and their astrophysical implications, physics of plasma and magnetic fields in the presence of a strong gravity and X-ray variability modelling connected, but not limited, to the proposed ESA X-ray missions ATHENA and LOFT. However, the main focus of the meeting remains on the general physical phenomena connected to accretion processes onto black holes and neutron stars and the internal structure of neutron stars and quark stars.

The RAGtime workshops and conferences have always provided an important and unique opportunity for undergraduate and graduate students of the Silesian University to meet and discuss problems with the world's leading astrophysicists. Among the regular guests are Marek Abramowicz, John Miller, Włodzimierz Kluźniak, and Vladimír Karas, Jeff McClintock, Shoji Kato, Ron Remillard, Didier Barret, Luciano Rezzolla, Yasufumi Kojima, Wen Fei Yu.

We would like to thank all the authors for a careful preparation of their contributions. This publication has been made possible through the support provided in the framework of the project "Supporting Integration with the International Theoretical and Observational Research Network in Relativistic Astrophysics of Compact Objects", CZ.1.07/2.3.00/20.0071. The project is co-financed by the European Social fund and state budget of the Czech Republic.

Opava, December 2014

Z. Stuchlík, G. Török and T. Pecháček
editors

CONTENTS

Proceedings of *RAGtime 10–13, 15–17/20–22/15–17/14–16 September, 2008/2009/2010/2011, Opava, Czech Republic*
Z. Stuchlík, G. Török and T. Pecháček, editors, Silesian University in Opava, 2014, pp. 1–14

Magnetized tori around Kerr superspinars

Karel Adámek[a] and Zdeněk Stuchlík

Institute of Physics, Faculty of Philosophy & Science, Silesian University in Opava,
Bezručovo nám. 13, CZ-746 01 Opava, Czech Republic
[a]karel.adamek@fpf.slu.cz

ABSTRACT
We study properties of the magnetized toroidal structures orbiting the Kerr superspinars predicted by the string theory. We demonstrate specific features of the unmagnetized perfect fluid tori created in the deep potential well near the surface of the superspinars, enabling clear distinction between Kerr superspinars and black holes. Then we consider the effect of the magnetization of the perfect fluid tori and shift of their properties induced by the presence of the magnetic field.

Keywords: Kerr spacetime – naked singularity – superspinars – magnetized tori

1 INTRODUCTION

Kerr superspinars are considered as primordial, large remnants of very early evolution period of the Universe giving thus signature of the string theory effects (Gimon and Hořava, 2009). However it cannot be excluded that Kerr superspinars were created by the collapse of superspinning differentially rotating compact stars (Giacomazzo et al., 2011). The superspinars are not contradicting the Penrose cosmic censorship hypothesis (Penrose, 1969) since their extension is expected to be limited to $r < R < M$ covering thus the region of causality violations by a correctly behaving stringy solution. Outside a Kerr superspinar, the standard Kerr naked singularity geometry is assumed.

Unstable gravitational perturbation modes has been found for Kerr superspinars with small values of the spin (Pani et al., 2010), however, it does not prove a general instability of Kerr superspinars, since mixing of modes, accretion phenomena or change of boundary conditions related to the Universe expansion could alter the conclusion on the instability. Although there is no uniqueness theorem for Kerr naked singularities (superspinars) similar to the one holding for Kerr black holes, studies of astrophysical phenomena in Kerr naked singularity (superspinars) backgrounds could be quite relevant and useful at least as a test bed model for more complex objects (D. and Manko, 1991). It is convenient (and standardly applied in the literature) to assume the surface radius of Kerr superspinars at $r(\theta) = R = 0.1\,M$, here we shall use the minimal restriction of $R = 0$.

Kerr superspinars (or Kerr naked singularities) were extensively studied for a variety of astrophysical (de Felice, 1974; Calvani and Nobili, 1979; Stuchlík, 1980; Gibbons and Hawking, 1977) and optical (Stuchlík, 1981; Stuchlík and Hledík, 2000; Stuchlík and

978-80-7510-125-9

Schee, 2010, 2011) phenomena. Considering evolution of primordial Kerr superspinars due to Keplerian accretion discs, it has been demonstrated that they could well survive to the era of high-redshift quasars or even longer, if the amount of accreting matter is limited (Stuchlík et al., 2011). Of course it is of high relevance to consider the properties of thick accretion discs represented by toroidal structures of perfect fluid that are complementary to Keplerian thin discs. Here we shall discuss such tori including even the effect of a magnetic field on their structure assuming for simplicity tori with uniform distribution of the specific angular momentum.

2 KERR SUPERSPINARS

In the Boyer–Lindquist coordinates and the geometrical units, the exterior of Kerr superspinars is governed by the line element (Kerr, 1963; Misner et al., 1973)

$$\mathrm{d}s^2 = -\left(1-\frac{2Mr}{\Sigma}\right)\mathrm{d}t^2 + \frac{\Sigma}{\Delta}\,\mathrm{d}r^2 + \Sigma\,\mathrm{d}\theta^2 + \frac{A}{\Sigma}\sin^2\theta\,\mathrm{d}\varphi^2 - \frac{4M^2ar\sin^2\theta}{\Sigma}\,\mathrm{d}t\,\mathrm{d}\varphi\,, \quad (1)$$

where

$$\Delta = r^2 - 2Mr + \left(aM\right)^2, \quad \Sigma = r^2 + \left(aM\right)^2\cos^2\theta\,, \quad (2)$$

and

$$A = \left(r^2 + \left(aM\right)^2\right)^2 - \Delta\left(aM\right)^2\sin^2\theta\,, \quad (3)$$

M is mass and $a > 1$ is dimensionless spin of the superspinar.

The physical ring singularity of the spacetime is located at $r = 0, \theta = \pi/2$. The causality violation region is determined by Carter (1973)

$$g_{\phi\phi} = \left[r^2 + (aM)^2 + \frac{2M^3a^2r\sin^2\theta}{\Sigma}\right]\sin^2\theta < 0\,; \quad (4)$$

it can occur only at $r < 0$ (Calvani et al., 1978). Realistic models of Kerr superspinars have to remove the causality violating region and the ring singularity. Therefore, the minimal condition for the boundary surface of Kerr superspinars reads $r(\theta) = R = 0$. In recent papers concerning the Kerr superspinars, the boundary at $r(\theta) = R = 0.1\,M$ is assumed (Gimon and Hořava, 2009; Takahashi and Takahashi, 2010; Pani et al., 2010; Stuchlík and Schee, 2010). We keep this assumption, guaranteeing that all the interesting physical phenomena could be relevant (Stuchlík, 1980; Stuchlík et al., 2011).

The geodesic motion in the Kerr spacetimes is given in a separated and integrated form by the Carter (1973):

$$\Sigma\dot{r} = \pm\sqrt{R(r)}\,, \quad (5)$$

$$\Sigma\dot{\theta} = \pm\sqrt{W(\theta)}\,, \quad (6)$$

$$\Sigma\dot{\phi} = -\left(aE - \frac{\Phi}{\sin^2\theta}\right) + \frac{a}{\Delta}P(r)\,, \quad (7)$$

$$\Sigma\dot{t} = -a\left(aE\sin^2\theta - \Phi\right) + \frac{r^2+a^2}{\Delta}P(r)\,, \quad (8)$$

where $\dot{} \equiv \mathrm{d}/\mathrm{d}w$ with w being the affine parameter and

$$P(r) = E\big(r^2 + a^2\big) - \Phi a\,, \tag{9}$$
$$R(r) = P^2 - \Delta\big[m^2 r^2 + (\Phi - aE)^2 + Q\big]\,, \tag{10}$$
$$W(\theta) = Q - \cos^2\theta \left[a^2\big(m^2 - E^2\big) + \frac{\Phi^2}{\sin^2\theta}\right]. \tag{11}$$

The motion constants are energy relative to infinity E, angular momentum about the symmetry axis Φ, rest mass m and Q related to the total angular momentum (Carter, 1973). For equatorial motion $Q = 0$. The radial profiles of the specific energy E_K/m and specific axial angular momentum Φ_K/m of the equatorial circular geodesics are given by Bardeen et al. (1972) and Stuchlík (1980):

$$\frac{E_\mathrm{K}}{m} = \frac{r^{3/2} - 2r^{1/2} \pm a}{r^{3/4}\sqrt{r^{3/2} - 3r^{1/2} \pm 2a}}\,, \tag{12}$$
$$\frac{\Phi_\mathrm{K}}{mM} = \pm\frac{r^2 + a^2 \mp 2ar^{1/2}}{r^{3/4}\sqrt{r^{3/2} - 3r^{1/2} \pm 2a}}\,, \tag{13}$$

where we introduced dimensionless radial coordinate $r/M \to r$.

The Keplerian velocity with respect to static observers at infinity $\Omega = \mathrm{d}\phi/\mathrm{d}t$ is given by the relation

$$\Omega_\mathrm{K} = \pm\frac{1}{M\big(r^{3/2} \pm a\big)} \tag{14}$$

and the profile of the specific angular momentum related to the covariant energy is given by

$$l_\mathrm{K} = \frac{\Phi_\mathrm{K}}{E_\mathrm{K}} = \pm\frac{r^2 \mp 2ar^{1/2} + a^2}{r^{3/2} - 2r^{1/2} \pm a}\,. \tag{15}$$

Behaviour of $l_\mathrm{K}(r;a)$ is crucial for determining of the equilibrium tori since it determines the centre and cusps of the tori. The upper (lower) sign in these and the following relations corresponds to the circular geodesics of the 1st (2nd) family. All the 2nd family orbits are counterrotating with $\Phi/mM < 0$. The 1st family orbits are co-rotating ($\Phi/mM > 0$) everywhere in the field of superspinars with spin $a > a_\mathrm{c} = 3^{3/2}/4 \sim 1.3$, but they are counter-rotating, with $\Phi/mM < 0$, if appropriately located in the vicinity of superspinars with spin $a < a_\mathrm{c}$. Clearly, the 1st family orbits can extend down to the superspinar, they are allowed at all $r > 0$. On the other hand, the 2nd family orbits are allowed at $r > r_\mathrm{ph}$; the retrograde photon circular orbit has radius given by

$$r_\mathrm{ph} = 2 + \left[a + \sqrt{a^2 - 1}\right]^{2/3} + \left[a + \sqrt{a^2 - 1}\right]^{-2/3}. \tag{16}$$

The limit value for extreme black holes is $r_\mathrm{ph}(a = 1) = 4$. The bound orbits (with $E/m < 1$) that could be relevant in toroidal discs (Kozlowski et al., 1978; Stuchlík et al., 2000; Slaný and Stuchlík, 2005) are limited by the radii of marginally bound orbits with $E/m = 1$ given by

$$r_{\mathrm{mb}} = 2 + a \pm 2(1+a)^{1/2}\,, \tag{17}$$

There is $r_{\mathrm{mb}}(a=1) = 5.38$ for the 2nd family orbits and $r_{\mathrm{mb}}(a=1) = 0.172$ for the 1st family orbits. The stable circular orbits determining the inner edge of the Keplerian discs are allowed at radii $r > r_{\mathrm{ms}}$; the innermost (marginally) stable circular orbit (ISCO) is determined by

$$r_{\mathrm{ms}} = 3 + Z_2 \mp \sqrt{(3-Z_2)(3+Z_1+2Z_2)}\,, \tag{18}$$

where

$$Z_1 = 1 + \left(1-a^2\right)^{1/3}\left[(1+a)^{1/3}(1-a)^{1/3}\right], \quad Z_2 = \sqrt{3a^2 + Z_1^2}\,. \tag{19}$$

The minimal value of $r_{\mathrm{ms}} = 2M/3$ is obtained for superspinars with $a = a_{\mathrm{e}} = (4/3)(2/3)^{1/2} \sim 1.089$ (Stuchlík, 1980). On the other hand, $r_{\mathrm{ms}} \to M$ from below when $a \to 1$ from above. Notice that the Kerr superspinar surface radius $r(\theta) = R = 0.1\,M$ is really chosen in such a way that the inner edge of both thin ($r_{\mathrm{in}} = r_{\mathrm{ms}}$) and thick ($r_{\mathrm{ms}} > r_{\mathrm{in}} > r_{\mathrm{mb}}$) accretion discs is located above the surface.

The 1st family orbits are co-rotating relative to distant observers ($\Omega_{\mathrm{K}} > 0$) – such orbits are locally co-rotating ($\Phi_{\mathrm{K}} > 0$) in regions distant from superspinars, but could be locally counter-rotating ($\Phi_{\mathrm{K}} < 0$) in vicinity of superspinars with the spin parameter $a < a_{\mathrm{c}} = (3/4)\,3^{1/2} \sim 1.3$. For superspinars with spin $a < a_{\mathrm{e}} = (3/4)\,(3/2)^{1/2} \sim 1.089$ the 1st family orbits with $\Phi_{\mathrm{K}} < 0$ could have negative energy ($E < 0$), while located close enough to the superspinar boundary. The marginally stable circular orbit of 1st family is located under $x = 1$ for $a < 5/3$ (Stuchlík, 1980).

The 1st family orbits reveal a strong jump in their properties when transition from a naked singularity spacetime to a black hole spacetime occurs. The jump is most profoundly demonstrated for the profiles of near-extreme Kerr superspinar and Kerr black hole states with spin $a = 1 \pm \delta, \delta \ll 1$ – in the Kerr superspinar spacetimes, stable circular orbits exist at $x = 1$ for all $\delta > 0$, while in the Kerr black hole spacetimes, the stable circular orbits exist at $x > 1$ for $\delta > 0$ and there is an enormous jump between the energy level of the ISCO orbits in the superspinar and black hole spacetimes. On the other hand, the 2nd family orbits are counter-rotating relative to distant observers ($\Omega_{\mathrm{K}} < 0$) and locally counter-rotating ($\Phi_{\mathrm{K}} < 0$) at all $r > r_{\mathrm{ph}}$ for all Kerr superspinars. The Keplerian energy E_{K} and angular momentum Φ_{K} radial profiles of 2nd family orbits change smoothly when the conversion from the superspinar to the black hole state with $a = 1$ occurs (Stuchlík et al., 2011).

3 MAGNETIZED PERFECT FLUID TORI

Properties of the radial profiles of Keplerian specific angular momentum $l_{\mathrm{K}}(r;a)$ are crucial for governing accretion toroidal structures of perfect fluid since the centre of the tori and its cusp, i.e. the edge of accretion tori, are given by condition $l(r) = l_{\mathrm{K}}(r)$, where $l(r)$

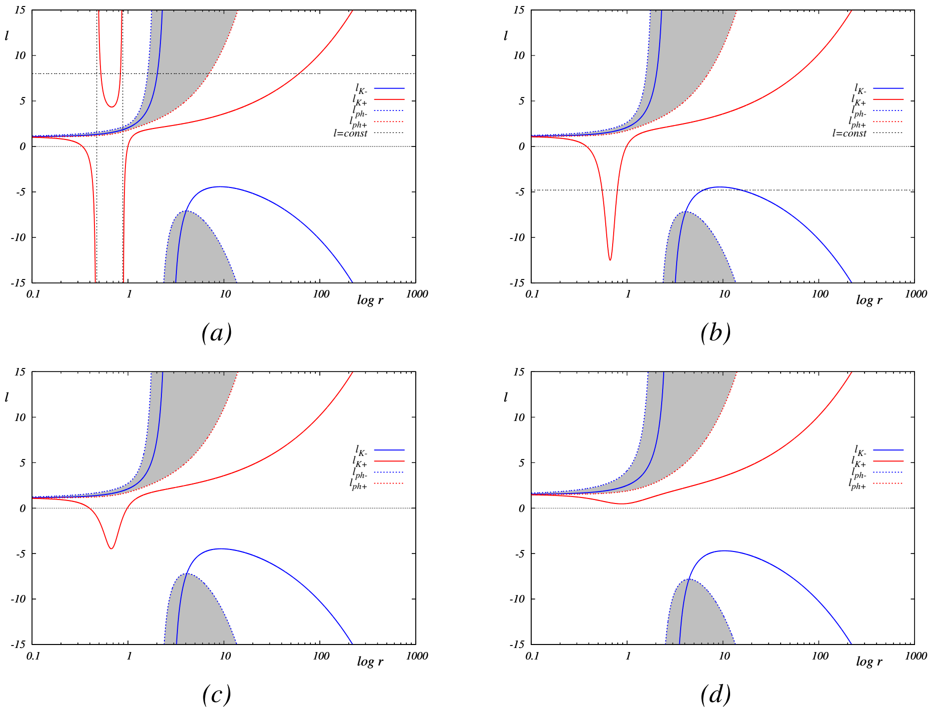

Figure 1. Behaviour of Keplerian angular momentum $l_{\mathrm{K}+}$ and $l_{\mathrm{K}-}$ for *(a)* $a = 1.05$, *(b)* $a = 1.1$, *(c)* $a = 1.118$ and *(d)* $a = 1.5$. The inner disc configurations are possible in the cases *(a)* and *(b)*, for the case *(c)* and *(d)* the inner disc configuration are not possible. For specific angular momentum $l > l_{\mathrm{min}}$ in the case *(a)* and for $l_{\mathrm{min}+} < l < l_{\mathrm{max}-}$ in the case *(b)* it is possible to have both inner and outer discs for the same $l = \mathrm{const}$. As examples we have used two values of the specific angular momentum l, in the case *(a)* it is $l = 8.0$ and in the case *(b)* it is $l = -4.8$. Both $l = \mathrm{const}$ are show as dotted horizontal lines. Regions without circular orbits are greyed out.

is the profile of the angular momentum distribution in the equatorial plane of the tori. Profiles of $l_{\mathrm{K}}(r; a)$ are fundamentally different for Kerr black holes and naked singularities (superspinars), implying fundamental differences of the orbital equilibrium configurations. Here we give overview for superspinars with boundary surface at minimal surface radius $R = 0$ guaranteeing covering of the physical singularity and causality violating region by some regular, say stringy, solution.

We can separate three basic cases of behaviour of the 1st family orbits due to behaviour of $\Phi_{\mathrm{K}}(r; a)$ and $E_{\mathrm{K}}(r; a)$, which can be seen in the Fig. 1. In the field of Kerr superspinars there is no 1st family Keplerian photon circular orbit and the related divergence of l_{K}. However for superspinars with $a < a_{\mathrm{e}} = 1.089$, there is a discontinuity of $l_{\mathrm{K}}(r; a)$ at two radii where $E_{\mathrm{K}}(r; a) = 0$. For $a < a_{\mathrm{c}} \sim 1.3$, $l_{\mathrm{K}}(r; a)$ of 1st family orbits reaches the region of $L < 0$. Then we can obtain possibility to have two distinct tori with the same $l = \mathrm{const} < 0$, if $l_{\mathrm{K}+(\mathrm{min})} < l_{\mathrm{K}-(\mathrm{max})}$. We can demonstrate that this condition can be fulfilled for $a = 1.1 < a_{\mathrm{c}}$.

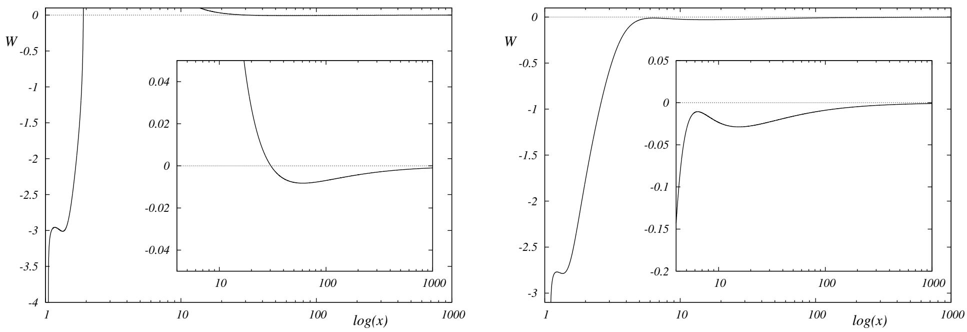

(a) *(b)*

Figure 2. Profiles of the potential W in Kerr–Schild coordinates for $a = 1.05, l = 8.0$ in the case *(a)* and for $a = 1.1, l = -4.8$ in the case *(b)*.

Rotating perfect fluid is governed by the Boyer's conditions, which implies that boundary of any stationary, barotropic, perfect fluid equilibrium configuration has to be an closed equipotential surface (Boyer, 1965). Equations of the ideal relativistic magnetohydrodynamics (RMHD) of the perfect fluid are for fluid described by stress-energy tensor $T^{\mu\nu}$ and electromagnetic tensor $F^{\mu\nu}$ given by relations (Komissarov, 2006):

$$\nabla_\mu T^{\mu\nu} = 0\,, \tag{20}$$
$$\nabla_\mu {}^*F^{\mu\nu} = 0\,, \tag{21}$$
$$\nabla_\mu F^{\mu\nu} = J^\nu\,, \tag{22}$$
$$\nabla_\mu \rho u^\mu = 0\,. \tag{23}$$

The 4-current J^ν from Maxwell Eq. (22) can be expressed as

$$J^\nu = \sigma e^\nu + q_0 u^\nu\,, \tag{24}$$

where σ is an scalar electric conductivity, q_0 is a electric proper charge and e^ν is 4-vector of the electric field, which in comoving frame reads $e^\nu = (0, \mathbf{E})$, where $\mathbf{E}$ is the 3-vector of the electric field. In the comoving frame and in the kinetic theory approach (Blackman and Field, 1993)

$$J^\nu = \sigma E^j\,. \tag{25}$$

Taking into account the limit of ideal RMHD, $\sigma \to \infty$, and the condition that 4-current must be finite, we get

$$F_{\mu\nu} u^\nu = 0\,. \tag{26}$$

Since $F_{\mu\nu}$ can be fully expressed by the means of b_ν, the Eq. (22) just defines 4-current and it is redundant.

The energy-momentum tensor for ideal perfectly conducting fluid reads

$$T^{\mu\nu} = \left(\omega + b^2\right)u^\mu u^\nu + \left(p + \frac{1}{2}b^2\right) g^{\mu\nu} - b^\mu b^\nu \tag{27}$$

while the Faraday tensor

$$^*F^{\mu\nu} = b^\mu u^\nu - b^\nu u^\mu \,, \tag{28}$$

where ω, p and u^μ are fluid enthalpy, pressure and 4-velocity respectively, $g_{\mu\nu}$ is the metric tensor and b^μ is the 4-vector of the magnetic field. In the comoving frame $b^\mu = (0, \mathbf{B})$, where $\mathbf{B}$ is 3-vector of the magnetic field measured in comoving frame, thus

$$u^\mu b_\mu = 0 \,. \tag{29}$$

We assume that

- the flow is stationary and axisymmetric; therefore

  $$\partial_t f = \partial_\phi f = 0 \tag{30}$$

  holds for any physical parameter f,
- the flow rotates only

  $$u^r = u^\theta = 0 \,, \tag{31}$$

- the magnetic field is purely azimuthal:

  $$b^r = b^\theta = 0 \,. \tag{32}$$

Under these assumptions the Faraday Eq. (21) and the continuity Eq. (23) are automatically fulfilled and the only non-trivial result follows from projection of the conservation law of the energy-momentum tensor (20) on the hyperplane orthogonal to 4-velocity by the projection tensor $h^\alpha_\beta = \gamma^\alpha_\beta + u^\alpha u_\beta$. From (20) we obtain

$$\left(\omega + b^2\right)u^\nu u_{\nu,i} + \left(p + b^2\right)_{,i} - b_\nu b^\nu_{,i} = 0 \,, \tag{33}$$

where $i = r, \theta$. The angular velocity and specific angular momentum of the rotating fluid are defined by

$$\Omega = \frac{u^\phi}{u^t} \,, \quad l = -\frac{u_\phi}{u_t} \,, \tag{34}$$

implying the relation

$$\Omega = -\frac{l g_{tt} + g_{t\phi}}{l g_{t\phi} + g_{\phi\phi}} \,. \tag{35}$$

Using Eq. (34) we can rewrite Eq. (33) to a form

$$\left(\ln |u_t|\right)_{,i} - \frac{\Omega}{1 - l\Omega} l_{,i} + \frac{p_{,i}}{\omega} + \frac{\left(\mathcal{L} b^2\right)_{,i}}{2\mathcal{L}\omega} = 0 \,, \tag{36}$$

where

$$\left(u_t\right)^2 = \frac{g_{t\phi}^2 - g_{tt}g_{\phi\phi}}{g_{tt}l^2 + 2g_{t\phi}l + g_{\phi\phi}}. \tag{37}$$

Assuming relationship (35), we obtain

$$\mathrm{d}\left(\ln|u_t| + \int_0^p \frac{\mathrm{d}p}{\omega} - \int_0^l \frac{\Omega\,\mathrm{d}l}{1 - l\Omega}\right) = -\frac{\mathrm{d}\left(\mathcal{L}b^2\right)}{2\mathcal{L}\omega}\,, \tag{38}$$

where the term in parenthesis is just what we would get for perfect barotropic fluid without magnetic field in it. Following Komissarov (2006) we assume the relationship

$$\tilde{\omega} = \tilde{\omega}(\tilde{p}_{\mathrm{m}})\,, \tag{39}$$

where $\tilde{\omega} = \mathcal{L}\omega$, $\tilde{p}_{\mathrm{m}} = \mathcal{L}p_{\mathrm{m}}$ and $p_{\mathrm{m}} = b^2/2$. Implementing (39) into (38) gives

$$\ln|u_t| + \int_0^p \frac{\mathrm{d}p}{\omega} - \int_0^l \frac{\Omega\,\mathrm{d}l}{1 - l\Omega} + \int_0^{p_{\mathrm{m}}} \frac{\mathrm{d}\tilde{p}_{\mathrm{m}}}{\tilde{\omega}} = \mathrm{const}\,. \tag{40}$$

Introducing the total potential W by

$$W = \ln|u_t| + \int_l^{l_\infty} \frac{\Omega\,\mathrm{d}l}{1 - l\Omega}\,, \tag{41}$$

where l_∞ is the angular momentum at infinity; assuming that l_∞ is finite, we obtain $u_t(r \to \infty) = -1$ and $W = 0$. Using total potential we arrive at the relation

$$W - W_{\mathrm{in}} + \int_0^p \frac{\mathrm{d}p}{\omega} + \int_0^{p_{\mathrm{m}}} \frac{\mathrm{d}\tilde{p}_{\mathrm{m}}}{\tilde{\omega}} = 0, \tag{42}$$

where W_{in} is the value of the total potential at the inner edge of the disc.

4 CONSTRUCTION OF MAGNETIZED TORI

The simplest configuration occurs if the ideal barotropic fluid has uniform distribution of the specific angular momentum

$$l = l_0 = \mathrm{const}\,. \tag{43}$$

Then the potential governing the equilibrium tori is given by

$$W = \ln|u_t| \tag{44}$$

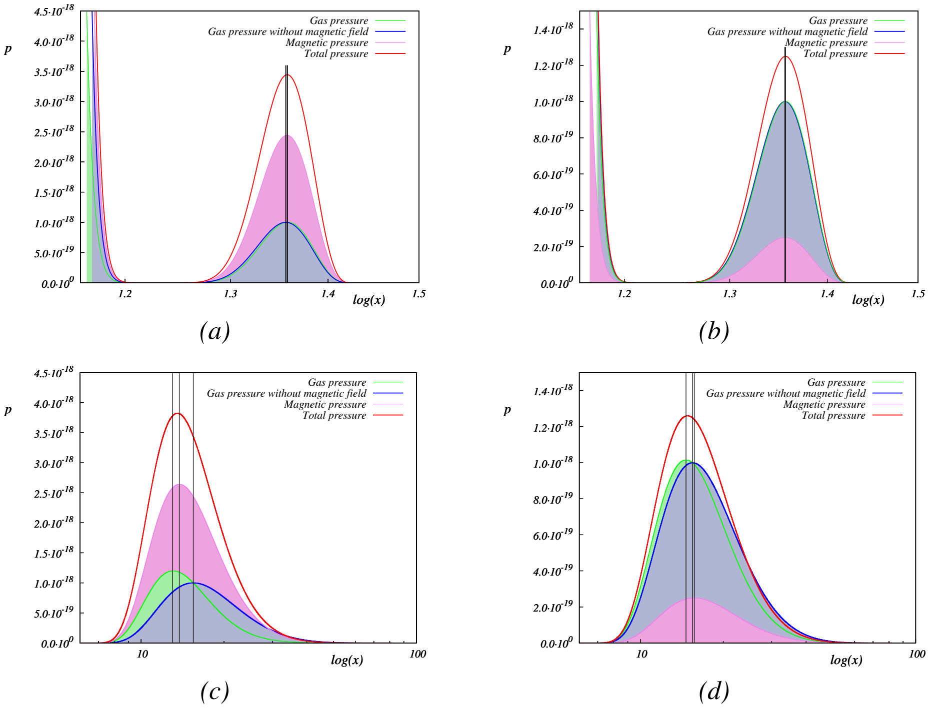

Figure 3. Pressure profiles in Kerr–Schild coordinates for inner discs *(a)*, *(b)* and outer disc *(c)*, *(d)*. with initial magnetization *(a)*, *(c)* $\beta_{\rm c} = 2.5$ and *(b)*, *(d)* $\beta_{\rm c} = 0.25$ for parameters $a = 1.1$, $l_{\rm ms-} > l = -4.8 > l_{\rm mb-}$. The pressure of the gas at the center of the disc is set to $p = 10^{-18}$.

and for $l =$ const it is given by geometry of the spacetime only. The shape of the equipotential toroidal configurations is illustrated in the Figs. 4 or 5. Following Komissarov (2006) we adopt the these relationships for pressure p and magnetic pressure $p_{\rm m}$

$$p = K\omega^{\kappa}\,, \tag{45}$$

$$p_{\rm m} = K_{\rm m}\mathcal{L}^{\eta-1}\omega^{\eta}\,. \tag{46}$$

Then we can rewrite Eq. (42) into the form

$$W - W_{\rm in} + \frac{\kappa}{\kappa-1}\frac{p}{\omega} + \frac{\eta}{\eta-1}\frac{p_{\rm m}}{\omega} = 0\,. \tag{47}$$

The geometry of the disc is defined by the potential W and the disc center and cusp are defined as points where specific angular momentum of the disc coincides with the specific angular momentum of a particle on the geodetical circular orbit, i.e. where

$$l_0 = l_{\rm K\pm} = \frac{\pm\left(r^2 \mp 2ar^{1/2} + a^2\right)}{r^{3/2} - 2r^{1/2} \pm a}\,; \tag{48}$$

the upper sign holds for co-rotating 1st family orbits while the lower sign holds for counter-rotating 2nd family orbits. Parameters of the model are κ, η, l_0 and $W_{\rm in}$, further parameters are enthalpy at the center of the disc $\omega_{\rm c}$ and initial magnetization

$$\beta_{\rm c} = p_{\rm mc}/p_{\rm c}. \tag{49}$$

From Equation (47) we can separate pressure at the center

$$p_{\rm c} = \omega_{\rm c}\,(W_{\rm in} - W)\left(\frac{\kappa}{\kappa-1} + \frac{\eta\beta_{\rm c}}{\eta-1}\right)^{-1}. \tag{50}$$

Using these we can calculate K and $K_{\rm m}$, then separating enthalpy ω from (47) we can get the solution anywhere inside the toroidal disc configuration. We shall focus our attention to the most interesting case when two toroidal configurations with $l = l_0 = \text{const}$ can exist.

4.1 Equilibrium configurations of perfect barotropic fluid

Behaviour of the Keplerian angular momentum $l_{\rm K+}$ and $l_{\rm K-}$ is shown in the Fig. 1. The profiles of the potential W (44) are shown in the Fig. 2. Behaviour of the function $l_{\rm K+}$ strongly depends on the spin parameter a. For $a < a_{\rm e} < 1.089$, a discontinuity occurs due to the fact that circular geodesics with $E_{\rm K} = 0$ exist in such spacetimes. Then the inner configurations with $l = l_0 > 0$ correspond to tori with $\phi = \text{const} < 0$ that are co-rotating relativity to distant observers.

For Kerr naked-singularity metric with rotational parameter $a > 1$, there are two possible disc structures with $l = l_0 = \text{const}$, inner and outer disc. For the 1st family of orbits both inner and outer disc structures are admitted. The inner disc configuration is possible for both $l > 0, a < a_{\rm c}$ and $l < 0, a > a_{\rm c}$ while outer disc configurations can be found only for $l > 0$. Also the inner discs with $l = l_0 < 0$ around naked singularities with $a > a_{\rm c}$ are co-rotating relative to distant observers. The 2nd family admit the outer toroidal configurations only centred around counter-rotating geodesics. We shall concentrate our attention on the case when two equilibrium tori with $l_0 = \text{const}$ are given. We shall study both the inner and outer tori and we are using Kerr–Schild coordinates

$$x = \sqrt{r^2 + a^2}\,\sin\theta\,\cos\varphi\,, \tag{51}$$
$$y = \sqrt{r^2 + a^2}\,\sin\theta\,\sin\varphi\,, \tag{52}$$
$$z = r\cos\theta\,, \tag{53}$$

where $y = 0$ due to axial-symmetry.

4.2 Behaviour of the pressure extremes

We are interested in behaviour of gas pressure p, magnetic pressure $p_{\rm m}$ and total pressure $p_{\rm t} = p + p_{\rm m}$ radial profiles and particularly in possible shift of the extreme positions with comparison to the case of a perfect barotropic fluid without magnetic field. We study the difference

$$\varDelta x = x^{(a)}_{\rm i(o)} - x_{\rm c}\,, \tag{54}$$

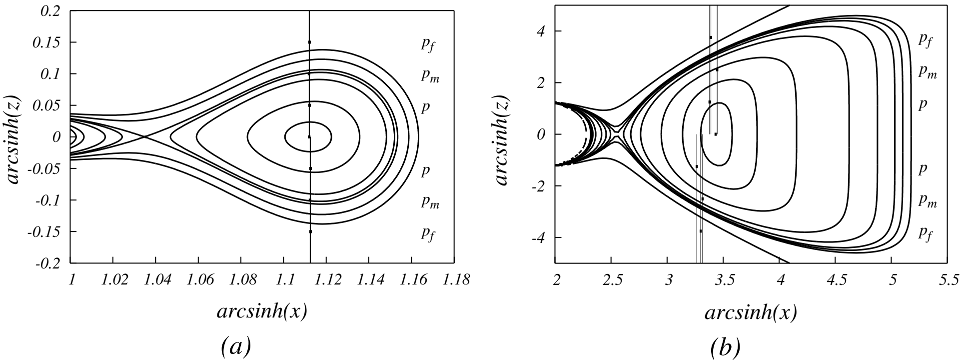

Figure 4. Equipotential surfaces for inner *(a)* and outer *(b)* disc configuration with parameters $a = 1.1$ and $l = -4.8$. Each graph shows two sets of vertical lines, which represent the positions of respective maximums of p, p_{m} and p_f. The upper lines are for initial magnetization $\beta_{\mathrm{c}} = 0.25$ while the lower ones are for $\beta_{\mathrm{c}} = 2.5$.

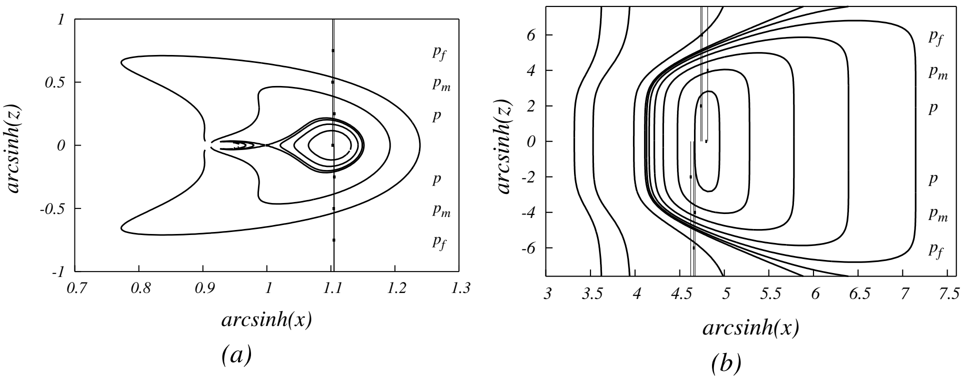

Figure 5. Equipotential surfaces for inner *(a)* and outer *(b)* disc configuration with parameters $a = 1.05$ and $l = 8.0$. Each graph shows two sets of vertical lines, which represent the positions of respective maximums of p, p_{m} and p_f. The upper lines are for initial magnetization $\beta_{\mathrm{c}} = 0.25$ while the lower ones are for $\beta_{\mathrm{c}} = 2.5$.

where $a = f, m$; $x_{i(o)}^{(a)}$ denotes position of the pressure maximum of fluid (f) and magnetic field (m) for inner (i) and outer (o) discs. Pressure profiles for inner disc configurations and outer disc configurations are shown in the Fig. 3. For outer disc configurations we can see that maximum of the total pressure is shifted closer to a compact object. For inner discs the maximum of the total pressure is receding from the compact object. This behaviour is consistent for all investigated inner and outer disc configurations. Numerical calculations of extremes of the total pressure are shown in the Figs. 6 and 7.

If the initial magnetization goes to zero ($\beta_{\mathrm{c}} \to 0$) the configuration is reduced to the case without magnetic field. If $\beta_{\mathrm{c}} \to \infty$ the disc is dominated by the magnetic pressure, while gas pressure vanishes. In this case the maximum of magnetic pressure reaches its maximal deviation, this is in the Figs. 6 and 7 depicted as a vertical line.

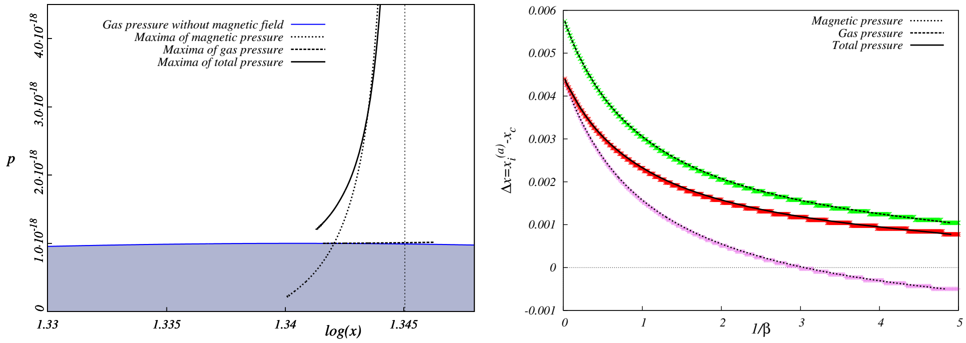

(a) (b)

Figure 6. Behaviour of the maximum's position $x_{\mathrm{i}}^{(a)}$ and it's distance $\Delta x = x_{\mathrm{i}}^{(a)} - x_{\mathrm{e}}$ from the disc center x_{c} as a function of the initial magnetization β_{c} for inner toroidal disc configurations with parameters set to $a = 1.05$, $l = 8.0$. On the upper graph we can see the positions of the maximum of the pressure for p, p_{m} and p_f compared with the behaviour of the gas pressure without magnetic field (filled area). On the lower graph we can see the distance Δx of the maximum from the disc center x_{c}.

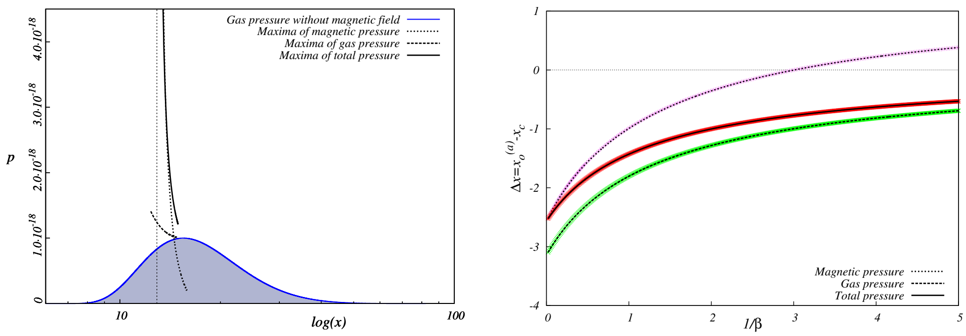

(a) (b)

Figure 7. Behaviour of the maximum's position $x_{\mathrm{i}}^{(a)}$ and it's distance $\Delta x = x_{\mathrm{i}}^{(a)} - x_{\mathrm{e}}$ from the disc center x_{c} as a function of the initial magnetization β_{c} for outer toroidal disc configurations with parameters set to $a = 1.1$, $l = -4.8$. On the upper graph we can see the positions of the maximum of the pressure for p, p_{m} and p_f compared with the behaviour of the gas pressure without magnetic field (filled area). On the lower graph we can see the distance Δx of the maximum from the disc center x_{c}.

5 CONCLUSIONS

We have studied magnetized tori around Kerr superspinars, focusing attention to the study of cases when doubled tori exist with the same $l = \mathrm{const}$, and different potential depth. We have demonstrated that the magnetization of the inner tori shifts their pressure maximum away from the Kerr superspinar, while in the outer tori the shift in maximum is toward the Kerr superspinar. We expect this effect could influence the character of optical appearance of oscillating tori around resonant points and we plan to study related phenomena in a future work.

REFERENCES

Bardeen, J. M., Press, W. H. and Teukolsky, S. A. (1972), Rotating black holes: locally nonrotating frames, energy extraction, and scalar synchrotron radiation, *Astrophys. J.*, **178**, pp. 347–369.

Blackman, E. G. and Field, G. B. (1993), Ohm's law for a relativistic pair plasma, *Phys. Rev. Lett.*, **71**, pp. 3481–3484, arXiv: `arXiv:astro-ph/9402068`.

Boyer, R. H. (1965), *Proc. Cambridge Phil. Soc.*, **61**, p. 527.

Calvani, M., de Felice, F., Salmistraro, F. and Muchotrzeb, B. (1978), Time machine and geodesic motion in Kerr metric, *General Relativity and Gravitation*, **9**, pp. 155–163.

Calvani, M. and Nobili, L. (1979), Dressing up a Kerr naked singularity, *Nuovo Cimento B*, **51B**, pp. 247–261.

Carter, B. (1973), Black hole equilibrium states, in C. D. Witt and B. S. D. Witt, editors, *Black Holes*, pp. 57–214, Gordon and Breach, New York–London–Paris.

D., N. I. and Manko, V. S. (1991), On the gravitational field of an arbitrary axisymmetric mass with a magnetic dipole moment, in A. Zichichi, V. de Sabbata and . N. Sanchez, editors, *Gravitation and Modern Cosmology. The Cosmological Constant Problem*, p. 121.

de Felice, F. (1974), Repulsive phenomena and energy emission in the field of a naked singularity, *Astronomy and Astrophysics*, **34**, pp. 15–19, URL `http://adsabs.harvard.edu/article_service.html`.

Giacomazzo, B., Rezzolla, L. and Stergioulas, N. (2011), Collapse of differentially rotating neutron stars and cosmic censorship, *Phys. Rev. D*, **84**, p. 024022 (16 pages), URL `http://link.aps.org/doi/10.1103/PhysRevD.84.024022`.

Gibbons, G. W. and Hawking, S. W. (1977), Cosmological event horizons, thermodynamics, and particle creation, *Phys. Rev. D*, **15**, pp. 2738–2751.

Gimon, E. G. and Hořava, P. (2009), Astrophysical violations of the Kerr bound as a possible signature of string theory, *Phys. Rev. B*, **672**, pp. 299–302, arXiv: `0706.2873`.

Kerr, R. P. (1963), Gravitational Field of a Spinning Mass as an Example of Algebraically Special Metrics, *Phys. Rev. Lett.*, **11**, p. 237.

Komissarov, S. S. (2006), Magnetized tori around Kerr black holes: analytic solutions with a toroidal magnetic field, *Monthly Notices Roy. Astronom. Soc.*, **368**, pp. 993–1000, arXiv: `arXiv:astro-ph/0601678`.

Kozlowski, M., Jaroszyński, M. and Abramowicz, M. A. (1978), The analytic theory of fluid disks orbiting the Kerr black hole, *Astronomy and Astrophysics*, **63**(1–2), pp. 209–220, URL `http://adsabs.harvard.edu/abs/1978A%26A....63..209K`.

Misner, C. W., Thorne, K. S. and Wheeler, J. A. (1973), *Gravitation*, W. H. Freeman and Co, New York, San Francisco.

Pani, P., Barausse, E., Berti, E. and Cardoso, V. (2010), Gravitational instabilities of superspinars, *Phys. Rev. D*, **82**(4), 044009, arXiv: `1006.1863`.

Penrose, R. (1969), Gravitational collapse: The role of general relativity, *Nuovo Cimento B*, **1**(special number), pp. 252–276.

Slaný, P. and Stuchlík, Z. (2005), Relativistic thick discs in the Kerr–de Sitter backgrounds, *Classical Quantum Gravity*, **22**(17), pp. 3623–3651, URL `http://www.iop.org/EJ/abstract/-search=44947255.2/0264-9381/22/17/019`.

Stuchlík, Z. (1980), Equatorial circular orbits and the motion of the shell of dust in the field of a rotating naked singularity, *Bull. Astronom. Inst. Czechoslovakia*, **31**(3), pp. 129–144.

Stuchlík, Z. (1981), Evolution of Kerr naked singularities, *Bull. Astronom. Inst. Czechoslovakia*, **32**(2), pp. 68–72.

Stuchlík, Z. and Hledík, S. (2000), Equatorial photon motion in the Kerr–Newman spacetimes with a non-zero cosmological constant, *Classical Quantum Gravity*, **17**(21), pp. 4541–4576, ISSN 0264-9381/00, arXiv: `0803.2539`, URL `http://www.iop.org/EJ/abstract/0264-9381/17/21/312`.

Stuchlík, Z., Hledík, S. and Truparová, K. (2011), Evolution of Kerr superspinars due to accretion counterrotating thin discs, *Classical Quantum Gravity*, **28**(15), p. 155017.

Stuchlík, Z. and Schee, J. (2010), Appearance of Keplerian discs orbiting Kerr superspinars, *Classical and Quantum Gravity*, **27**(21), p. 215017, arXiv: `1101.3569`.

Stuchlík, Z. and Schee, J. (2011), Influence of the cosmological constant on the motion of Magellanic Clouds in the gravitational field of Milky Way, *Journal of Cosmology and Astroparticle Physics*, **9**, p. 18.

Stuchlík, Z., Slaný, P. and Hledík, S. (2000), Equilibrium configurations of perfect fluid orbiting Schwarzschild–de Sitter black holes, *Astronomy and Astrophysics*, **363**(2), pp. 425–439, ISSN 0004-6361 (printed version), 1432-0746 (parallel-to-print version), URL `http://adsabs.harvard.edu/abs/2000A%26A...363..425S`.

Takahashi, R. and Takahashi, M. (2010), Anisotropic radiation field and trapped photons around the Kerr black hole, *Astronomy and Astrophysics*, **513**, A77, arXiv: `1002.4245`.

Proceedings of *RAGtime 10–13, 15–17/20–22/15–17/14–16 September, 2008/2009/2010/2011, Opava, Czech Republic*
Z. Stuchlík, G. Török and T. Pecháček, editors, Silesian University in Opava, 2014, pp. 15–26

Stationary particles in the field of magnetized slowly rotating neutron stars

Pavel Bakala[a], Martin Urbanec, Eva Šrámková, Zdeněk Stuchlík and Gabriel Török

Institute of Physics, Faculty of Philosophy & Science, Silesian University in Opava, Bezručovo nám. 13, CZ-746 01 Opava, Czech Republic
[a]`pavel.bakala@fpf.slu.cz`

ABSTRACT
We study circular motion of charged test particles in the field of magnetized slowly rotating neutron stars. The gravitational field is approximated by the Lense–Thirring geometry, the magnetic field is of the standard dipole character. Using a fully-relativistic approach we determine influence of the electromagnetic interaction (both attractive and repulsive) on the circular motion. We focus on the behaviour of the orbital frequency of the motion. Components of the four-velocity of the orbiting charged test particles are obtained by numerical solution of equations of motion. The role of the combined effect of the neutron star magnetic field and its rotation in the character of the orbital frequency is discussed. It is demonstrated that even in the Lense–Thirring spacetime particles being static relative to distant observers can exist due to the combined gravo-electromagnetic interaction.

Keywords: Lense–Thirring – neutron star – magnetic and electric fields – accretion

1 INTRODUCTION

Charged particle motion in strong gravitational and electromagnetic fields of black holes and neutron stars enables us to understand the nature of combined effects of these fields and their role in astrophysical phenomena. The motion has been investigated both for Kerr–Newman black holes having intrinsically coupled gravitational and electromagnetic fields and for strong gravitating objects (black holes and neutron stars) with a test electromagnetic field influenced by gravity (see, e.g. Johnston and Ruffini, 1974; Prasanna and Vishveshwara, 1978; Prasanna, 1980; Calvani et al., 1982; Bálek et al., 1989; Bičák et al., 1989; Stuchlík and Hledík, 1998; Stuchlík et al., 1999; Abdujabbarov and Ahmedov, 2009; Frolov and Shoom, 2010). Motion of charged particles in the magnetic field generated by accretion discs orbiting black holes was discussed in (Znajek, 1976; Mobarry and Lovelace, 1986). The magnetic field tied to a neutron star could substantially influence the structure of an equatorial accretion disc orbiting the neutron star and has been studied in (Kluźniak and Rappaport, 2007).

In the case of motion in test fields on strong gravity backgrounds, the equations of motion are complex and have to be integrated numerically (Prasanna and Vishveshwara, 1978; Prasanna and Sengupta, 1994; Preti, 2004). Numerical integration of the motion equations

978-80-7510-125-9

gives a number of interesting results, but is not sufficient for a complete classification and understanding of the motion in the equatorial plane. In order to extend the understanding of the charged particle motion, the quasi-circular equatorial epicyclic motion corresponding to oscillations of particles around stable circular orbits has been studied (Bakala et al., 2010). Such epicyclic motion can be excited in the innermost parts of the accretion discs orbiting a neutron star by inhomogeneities (mountains) on its surface (Stuchlík et al., 2008). Recently, off-equatorial circular orbits were discussed in astrophysically relevant situations (Kovář et al., 2008, 2010; Kopáček et al., 2010). Of high interest is the equatorial motion, especially the circular and quasi-circular orbits of charged test particles that seem to be crucial from the point of view of accretion processes. Moreover, quite recently, fluid charged tori were discussed in the approximation of zero conductivity (Kovář et al., 2011); such dielectric tori could be also relevant in some astrophysically interesting situations.

Here we focus attention on the equatorial orbital motion in the combined gravitational and dipole magnetic fields related to a slowly rotating neutron star. We generalize our previous results obtained under much simpler case of neutron star represented by the Schwarzschild geometry and the related magnetic field (Bakala et al., 2010). We assume a dipole field whose axis of symmetry coincides with the axis of neutron star's rotation. The spacetime outside the neutron star is described by the Lense–Thirring geometry that reflects the slow rotation of the neutron star and influences the structure of the magnetic field – the effects of frame-dragging are thus considered in the linear approximation. Such approximation is suitable for describing the charged particles motion around slowly rotating neutron stars with a relatively weak magnetic field which does not affect the spacetime curvature in the vicinity of the neutron star, but its structure is governed by the neutron star spacetime structure.[1]

In our study we focus our attention on the possibility of existence of charged particles that appear stationary to distant observers. Existence of such particles was demonstrated for ultrarelativistic charged particles located near the black hole horizon of charged and rotating (Kerr–Newman) black hole (Bálek et al., 1989). Here we test such possibility in different physical conditions when the interplay of gravitational dragging and electromagnetic force can imply interesting and unexpected results. The problem of the epicyclic motion and the related frequencies (see e.g. Aliev and Galtsov, 1981; Abramowicz and Kluźniak, 2005; Török and Stuchlík, 2005) is postponed for future studies.

2 LENSE–THIRRING GEOMETRY AND DIPOLE MAGNETIC FIELD OF SLOWLY ROTATING NEUTRON STARS

The external gravitational field of slowly rotating neutron or strange stars is sometimes approximated by the Lense–Thirring metric[2] (Lense and Thirring, 1918; Hartle and Sharp,

[1] The neutron star magnetic field is however fully dominant over the magnetic field generated by the currents in the disc.

[2] The term "Lense–Thirring metric" is substituted frequently by the term "slow-rotation approximation" (see Konno and Kojima (2000)).

1967; Hartle, 1967), with line element given by

$$\mathrm{d}s^2 = -\eta(r)^2\,\mathrm{d}t^2 + \frac{\mathrm{d}r^2}{\eta(r)^2} + r^2\left[\mathrm{d}\theta^2 + \sin^2\theta\,\left(\mathrm{d}\phi^2 - 2\omega\,(r)\,\mathrm{d}t\,\mathrm{d}\phi\right)\right], \tag{1}$$

where the function $\eta(r)$ reads

$$\eta(r) \equiv \left(1 - \frac{2M}{r}\right)^{1/2} . \tag{2}$$

The Lense–Thirring angular velocity $\omega(r)$ can be interpreted as angular velocity of freely falling observers relative to static observers at infinity and outside the neutron star is given by

$$\omega(r) = \frac{2J}{r^3} , \tag{3}$$

where J is the total angular momentum of the neutron star with mass M and radius R. Using the moment of inertia $I(M, R)$ and angular velocity of the (rigidly) rotating star $\Omega_{\rm star}$ measured by a static observer at infinity, we can write $J = I(M, R)\Omega_{\rm star}$. The rotational parameter of the neutron star (called spin) is given by $a = J/M^2$. We have adopted here geometric units, $c = G = 1$, that we will use throughout the paper.

In Rezzolla et al. (2001), an analytical solution of the Maxwell equations is presented for a general orientation of the dipole magnetic field in the Lense–Thirring metric (1) to first order in J, including the conditions for matching the internal spacetime of the star under assumption of both infinite and finite conductivity of the star interior. We assume for simplicity the symmetry axis of the magnetic dipole identical with rotation axis (zero declination) and infinitely conductive star interior implying force lines frozen into the star and dragged by its rotation. Under such assumptions, the relatively complex general dipole solution is reduced to much simpler form (Konno and Kojima, 2000), with the azimuthal component of the electromagnetic 4-potential A_ϕ being identical with the Schwarzschildian case (e.g. Wasserman and Shapiro, 1983; Braje and Romani, 2001)

$$A_\phi = -\,f(r)\frac{\mu\sin^2\theta}{r} , \tag{4}$$

i.e. to the magnetic dipole solution of the Maxwell equations in the flat spacetime corrected by the general relativistic factor $f(r, M)$ that is given by

$$f(r) = \frac{3r^3}{8M^3}\left[\ln\eta(r)^2 + \frac{2M}{r}\left(1 + \frac{M}{r}\right)\right]. \tag{5}$$

In contrast to the dipole solution in the static spherically symmetric spacetime, the 4-potential contains also non-zero electrical (time) component that can be expressed in the form

$$A_t(r,\theta) = a_{t0}(r) + a_{t2}(r)\mathrm{P}_2\left(\cos\theta\right) ; \tag{6}$$

P_2 is the Legendre polynome of the 2nd kind (Konno and Kojima, 2000). The terms a_{t0} a a_{t2} are given by the Maxwell equations and take the form

$$
\begin{aligned}
a_{t0} &= \frac{c_0}{r} + \frac{J\mu}{2M^3r^2}(3r - M) + \frac{J\mu}{4M^4r}(3r - 4M)\ln\eta^2(r)\,, && (7)\\
a_{t2} &= \frac{c_1}{M^2}(r - M)(r - 2M)\\
&\quad + c_2\left[\frac{2}{Mr}\left(3r^2 - 6Mr + M^2\right) + \frac{3}{M^2}\left(r^2 - 3Mr + 2M^2\right)\ln\eta^2(r)\right]\\
&\quad - \frac{J\mu}{2M^6r^2}\left[\left(9r^4 - 3Mr^3 - 30M^2r^2 + 8M^3r + 2M^4\right)\right.\\
&\quad \left. + \left(12r^4 - 36Mr^3 + 24M^2r^2 + M^3r\right)\ln\eta^2(r)\right], && (8)
\end{aligned}
$$

where c_0, c_1 a c_2 are integration constants (Konno and Kojima, 2000). The first constant c_0 corresponds to the electric charge of the star and it is astrophysically natural to put ($c_0 = 0$). Requirement of regularity of the solution at infinity implies (Konno and Kojima, 2000)

$$
c_1 = \frac{9J\mu}{2M^4}\,; \tag{9}
$$

c_2 can be fixed by the matching conditions on the star surface. Assuming perfectly conducting interior of a star rotating with angular momentum Ω_{star} and frozen-in magnetic field ($u^\mu F_{\mu\nu} = 0$, $u^\mu = (u^t, 0, 0, \Omega_{\mathrm{star}}u^t)$), we arrive at (Konno and Kojima, 2000)

$$
\begin{aligned}
c_2 &= \left\{\frac{\mu J}{M^5R^2}\left(12R^3 - 24MR^2 + 4M^2R + M^3\right)\right.\\
&\quad + \frac{\mu J}{2M^6R}\left(12R^3 - 36MR^2 + 24M^2R + M^3\right)\ln\eta^2(r)\\
&\quad \left. - \frac{\mu\Omega_{\mathrm{star}}}{4M^3}\left[2MR + 2M^2 + R^2\ln\eta^2(r)\right]\right\}\\
&\quad \Big/ \left[\frac{2}{MR}\left(3R^2 - 6MR + M^2\right) + \frac{3}{M^2}\left(R^2 - 3MR + 2M^2\right)\ln\eta^2(r)\right]. && (10)
\end{aligned}
$$

The Maxwell tensor $F_{\mu\nu}$ related to the four-potential A_μ by

$$
F_{\mu\nu} = \frac{\partial A_\nu}{\partial x^\mu} - \frac{\partial A_\mu}{\partial x^\nu}\,, \tag{11}
$$

has four independent non-vanishing components

$$
F_{r\phi} = \frac{\mu\sin^2\theta\left(f(r) - rf'(r)\right)}{r^2}\,, \tag{12}
$$

$$
F_{\theta\phi} = -\frac{\mu f(r)\sin 2\theta}{r}\,, \tag{13}
$$

$$F_{tr} = -a'_{t0}(r) - \frac{a'_{t2}(r)}{4}(1 + 3\cos 2\theta)\,, \tag{14}$$

and

$$F_{t\theta} = a_{t2}(r)\, 3\cos\theta \sin\theta\,. \tag{15}$$

corresponding to appropriate parts of electric and magnetic field three-vectors in the frames of local observers. Note that "coma" in Eqs. (12, 14) denotes partial derivative with respect to the radial coordinate r.

Notice that the electric component of the 4-potential is in astrophysically relevant case of electrically uncharged star induced only by the star rotation and the effect of dragging of inertial frames is indicated by its dependence on the angular velocity of the star $\Omega_{\rm star}$ and its internal angular momentum J.

2.1 Relation between spin and angular frequency

The internal angular momentum J and the angular velocity of the star $\Omega_{\rm star}$ are linearly connected by the moment of inertia through the relation $J = I\Omega_{\rm star}$. To find the value of angular velocity necessary for matching the condition given by Eq. (10) in terms of a dimensionless spin $a = J/M^2$, we can use the findings of Lo and Lin (2011) that the maximal value of spin, $a_{\max} = 0.7$, is almost the same for all masses and equations of state. Using a model of neutron star with mass $M = 1.5\,M_\odot$ we can find (see, e.g. Haensel et al., 2009) that maximal frequency $\nu_{\rm star}^{\max} = \Omega_{\rm star}^{\max}/2\pi$ for neutron star is roughly 750–1200 Hz. The exact value of the maximal frequency depends very significantly on the assumed equation of state of the neutron star matter (Lattimer and Prakash, 2001; Říkovská Stone et al., 2003; Urbanec et al., 2010). Since we are dealing here with a neutron star test model, in further analysis we use the value of $\nu_{\rm star}^{\max} = 1000$ Hz. Therefore, the linear relation between the spin a and the rotational frequency $\Omega_{\rm star}$ can be written in the form

$$\Omega_{\rm star} = \alpha a\,, \tag{16}$$

where parameter α is given as the ratio of maximal values of neutron star's spin and the angular velocity;

$$\alpha = \Omega_{\rm star}^{\max}/a_{\max}\,. \tag{17}$$

2.2 Intrinsic magnetic dipole moment

Intrinsic magnetic dipole moment of a neutron star μ can be obtained from the presumed magnetic field strength at the neutron star surface. Locally measured magnetic field strength is given by the projection of the Maxwell tensor into the orthonormal basis of a observer connected with the surface of the star, $F_{\hat\alpha\hat\beta}=e_{\hat\alpha}{}^{\mu} e_{\hat\beta}{}^{\nu} F_{\mu\nu}$. The tetrad related to the observers at the surface of the neutron star is given by the relations

$$e_{\hat t} = \left\{u^t, 0, 0, \Omega_{\rm star}\, u^t\right\}, \qquad e_{\hat r} = \left\{0, \eta(r), 0, 0\right\}, \tag{18}$$

$$e_{\hat{\theta}} = \left\{0, 0, \frac{1}{r}, 0\right\}, \qquad e_{\hat{\phi}} = \left\{0, 0, 0, \frac{1}{r\ \sin\theta}\right\},$$

The magnetic components of the Maxwell tensor of the electromagnetic field in the Lense–Thirring metric correspond to the static (Schwarzschild) solution – therefore, the relation of the magnetic dipole moment of the neutron star and the magnetic induction on its surface takes precisely the same form as in (Bakala et al., 2010)

$$\mu = \frac{4M^3 R^{3/2}\sqrt{R-2M}}{6M(R-M) + 3R(R-2M)\log\eta\,(R)^2} B^{\hat{\theta}}\,. \tag{19}$$

We use here as the test model for our analysis a neutron star with a rather weak magnetic field strength, $B = 10^7$ Gauss $\simeq 2.875 \times 10^{-16}\,\mathrm{m}^{-1}$,[3] mass $M = 1.5 M_{\odot} \simeq 2216.85$ m and radius $R = 4M \simeq 8867.4$ m, as in our previous analysis of the static geometry (Bakala et al., 2010). Then we have $\mu = 1.06 \times 10^{-4}\,\mathrm{m}^2 = 2.157 \times 10^{-11} M^2$.

3 EQUATORIAL CIRCULAR MOTION

In a curved spacetime with presence of an electromagnetic field, the Lorentz equation of motion for a charged test particle of mass m and charge q reads

$$\frac{\mathrm{d}U^{\mu}}{\mathrm{d}\tau} + \Gamma^{\mu}_{\alpha\beta} U^{\alpha} U^{\beta} = \tilde{\mathrm{q}}\, F^{\mu}_{\nu} U^{\nu}\,, \tag{20}$$

where U^{μ} is the four-velocity and $\tilde{\mathrm{q}} \equiv q/m$ is the specific charge of the particle.

Symmetry properties of the spacetime geometry (1) and electromagnetic field (4) allow for charged test particles circular motion restricted to the equatorial plane $\theta = \pi/2$. The four-velocity then has only two non-vanishing components, $U^{\mu} = (U^t, 0, 0, U^{\phi})$. Solving the radial component of Eq. (20) together with the normalization condition $U^{\mu} U_{\mu} = -1$ for metric (1) and potential (4) we obtain two pair of implicit equations for nonzero components of U^{μ} in the form

$$U^t_{\pm} = \left(\pm\sqrt{4a^2M^4(U^{\phi})^2 + (r-2M)r\left(1 + (U^{\phi})^2 r^2\right)} - 2aM^2 U^{\phi}\right) \Big/ \left(r - 2M\right), \tag{21}$$

$$U^{\phi}_{\pm} = \left(\frac{1}{2} r^{-3}\right)\Bigg[-2aM^2U^t - \tilde{\mathrm{q}}\mu\Phi(r) \pm \sqrt{\left(2aM^2U^t + \tilde{\mathrm{q}}\mu\Phi(r)\right)^2 + 2r^3U^t\left(2MU^t + \tilde{\mathrm{q}}r^2\Sigma(r)\right)}\Bigg]. \tag{22}$$

Here and hereafter $\Phi(r)$ and $\Sigma(r)$ are given by

$$\Phi(r) \equiv f(r) - r f'(r)\,, \tag{23}$$

and

$$\Sigma(r) \equiv a'_{t0}(r) - 2a'_{t2}(r)\,. \tag{24}$$

[3] $B\,[\mathrm{cm}^{-1}] = (\mathrm{G}^{1/2}/c^2)\, B\,[\mathrm{Gauss}] \simeq 2,875 \times 10^{-25}\, B\,[\mathrm{Gauss}]$

For uncharged particles we arrive at the equations governing circular geodesic in the Lense–Thirring spacetime, where non-zero components of 4-velocity and orbital angular velocity read

$$U^{\phi}_{0\pm} = \pm\left[\frac{r^2}{M}(r-3M) + 2aM\left(aM \pm \sqrt{a^2M^2 + r^3/M}\right)\right]^{-1/2}, \tag{25}$$

$$U^{t}_{0\pm} = \left(aM \pm \sqrt{a^2M^2 + r^3/M}\right)U^{\phi}_{0\pm}, \tag{26}$$

$$\Omega_{0\pm} = \left(aM \pm \sqrt{a^2M^2 + r^3/M}\right)^{-1}. \tag{27}$$

In order to obtain appropriate angular velocities in the presence of the Lorentz force, the pair of Eqs. (21, 22) has to be solved numerically, taking into account only the physically relevant forward-directed time component of the 4-velocity U^t_+. The solution $\Omega_+ = U^{\phi}_+/U^t_+$ then corresponds in the geodesic limit to the corotating orbits and will be referred as corotating in the following, while the solution $\Omega_- = U^{\phi}_-/U^t_+$ will be referred as counterrotating (retrograde). Nevertheless, due to the electromagnetic interaction, in the case of the retrograde solution the real orientation of the orbital velocity depends on the values of the neutron star spin and the specific charge of the test particle.

For circular motion in the equatorial plane, the Lorentz force on the Rhs of the equations of motion (20) has the only non-zero, radial component that is given by the expression $K^r = \tilde{q}(F^r_{\ t}U^t + F^r_{\ \phi}U^{\phi})$, where the first term corresponds to the electric (coulombic) part of the interaction of the test charged particle with with electric field of the star induced by its spin, while the second term corresponds to the magnetic part of the interaction induced by the orbital motion of the charged particle. While orientation of the magnetic component depends both on the sign of the specific charge of the particle $\tilde{q}$ and the orientation of the orbital angular velocity $\Omega_{\pm}$, the electric component is for a fixed neutron star spin $a > 0$ always repulsive for $\tilde{q} > 0$, but attractive for $\tilde{q} < 0$. Nevertheless, both parts depend on the product of μ and $\tilde{q}$ determining magnitude of the whole electromagnetic interaction. Therefore, instead of changing magnitude and orientation of μ we can, without any loss of generality, study only influence of changes of the specific charge $\tilde{q}$ similarly as in analysis of the static Schwarzschild case (Bakala et al., 2010). However, we have to analyse separately the corotating and retrograde orbits due to the rotation of the neutron star. We analyse behaviour of orbiting test particles with value of specific charge $\tilde{q} \in (-1.0 \times 10^{13}, 1.0 \times 10^{13})$. Absolute values of such used specific charge values are very low in comparison with $\tilde{q} = 1.111 \times 10^{18}$ corresponding to matter consisting purely of ions of hydrogen.

4 ORBITAL MOTION AND STATIONARY PARTICLES

For corotating orbits with $\Omega_+ = U^{\phi}_+/U^t_+$ the magnetic part of the Lorentz force is attractive for $\tilde{q} > 0$, while for $\tilde{q} < 0$ we observe magnetic repulsion. Inversely oriented electric part of the Lorentz force partially compensates influence of the magnetic component, but for the family of corotating orbits the magnetic component is decisive for the final orientation

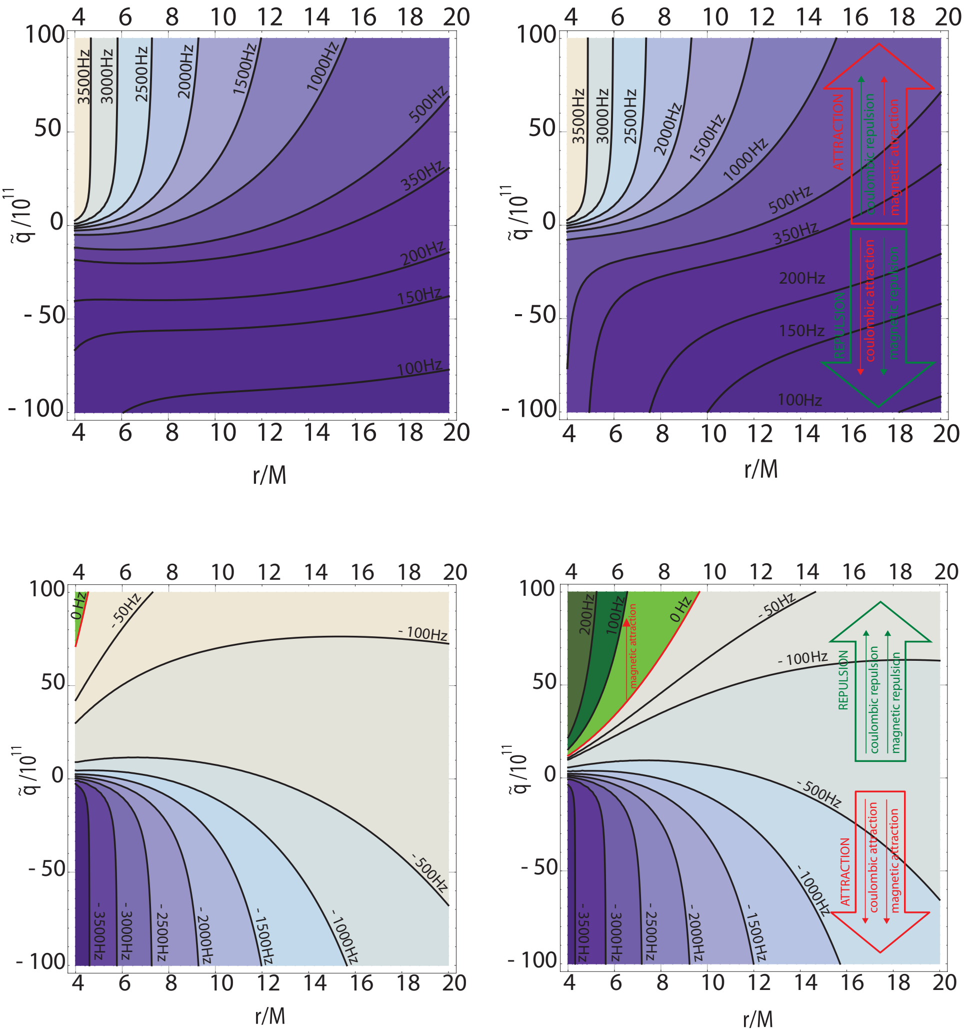

Figure 1. Contour plot of the orbital frequency $\nu = \Omega/2\pi$ as a function of the specific charge $\tilde{q}$ and the radial coordinate constructed for the test neutron star with $M = 1.5\,M_{\odot}$ and $\mu = 1.06 \times 10^{-4}\,\mathrm{m}^2$. *Top left*: Corotating solution for spin $a = 0.05$. *Top right*: Corotating solution for spin $a = 0.3$. *Bottom left*: Counterrotating solution for spin $a = 0.05$. *Bottom right*: Counterrotating solution for spin $a = 0.3$. The electrostatic radii at which the stationary particles are located are given by the red contour line ($\nu = 0\,\mathrm{Hz}$).

of the Lorentz force. Ω_+ increases monotonically with increasing specific charge $\tilde{q}$; in the region of $\tilde{q} < 0$ the repulsive electromagnetic interaction causes decreasing of Ω_+ in comparison with the geodesic orbital frequency Ω_{0+}, while in the attractive region of $\tilde{q} > 0$ there is $\Omega_+ > \Omega_{0+}$. In top panels of Fig. 1 we illustrate behaviour of the orbital angular velocity Ω (related frequency $\nu = \Omega/2\pi$) of orbits described by the corotating solution in dependency on the specific charge $\tilde{q}$ using the test model neutron star with small and extremal values of the spin, $a = 0.05$ and $a = 0.3$.

4.1 Orbital angular velocity of counterrotating solution and stationary particles at electrostatic radius

In the case of the retrograde solution $\Omega_- = U^\phi_-/U^t_+$ the resulting orientation of the Lorentz force is inverse in comparison to the corotating solution. Therefore, $|\Omega_-|$ decreases monotonically with increasing value of the specific charge $\tilde{q}$. For $\tilde{q} < 0$ the attractive Lorentz interaction increases $|\Omega_-|$ in comparison with the geodesic orbital frequency $|\Omega_{0-}|$, while in the repulsive region of $\tilde{q} > 0$ there is $|\Omega_-| < |\Omega_{0-}|$. Nevertheless the relations of both components of the Lorentz force are qualitatively different as compared to the case of the corotating solution.

In the case of the retrograde orbits, both parts of the Lorentz force are oriented identically and the magnetic repulsion and attraction are supported by the electric part of the interaction. Starting from a critical specific charge $\tilde{q}_{\mathrm{es}}$, character of the electromagnetic interaction at the repulsive region enables existence of electrostatic radius $r_{\mathrm{es}}(\tilde{q})$, where the limiting case of the circular orbit with $\Omega_- = 0$ appears. Such particles are static relative to static observers at infinity, with gravitational attraction of the neutron star being compensated by the electric repulsion due to the particle charge. (However, the static particles at the electrostatic radii are rotating relative to the Lense–Thirring spacetime. An analogical situation has been discovered for motion of charged particles in the equatorial plane of the Kerr–Newman geometry (Bálek et al., 1989). In both cases the effect is caused by the combined influence of the frame dragging and the electromagnetic interaction.)

The electric repulsion increases strongly with decreasing radial coordinate. The existence of retrograde solutions for particles with large specific charges orbiting at low radii ($r < r_{\mathrm{es}}(\tilde{q})$, $\tilde{q} \geq \tilde{q}_{\mathrm{es}}$) requires presence of compensating magnetic attraction implying change of the orbital velocity orientation. Then even the retrograde solution determines a special family of corotating (relative to observers at infinity) orbits with relatively low orbital frequency $\Omega_- > 0$ existing paralelly at the same radial coordinate as the orbits of corotating solution demonstrating high $\Omega_+ > 0$.

In bottom panels of Fig. 1 we illustrate behaviour of the orbital angular velocity Ω (related frequency $\nu = \Omega/2\pi$) of orbits described by counterrotating solution in dependency on the specific charge $\tilde{q}$ using test model neutron star with with small and extremal values of the spin, $a = 0.05$ and $a = 0.3$.

5 CONCLUSIONS

The aim of the present paper is to study the influence of the Lorentz force generated by a dipole magnetic field of a slowly rotating neutron star on the equatorial circular motion. We focus on the combined effects of the frame dragging and electromagnetic interaction, representing the frame dragging in the linear approximation of the Lense–Thirring metric. In general, the Lorentz force may be of attractive or repulsive character depending on the sign of orbiting particle's specific charge, the magnetic dipole moment and orbital velocity orientations and the sense of rotation of the neutron star. Surprisingly enough, the combined effect of frame dragging and electro-magnetic interaction implies even in the case of the slow rotation, and in intermediate radii, i.e. radii not close to the gravitational radius, the existence of charged particles being in states appearing static relative to distant static observers. Such particles are located at the so called electrostatic radii. The phenomenon of stationary particles in strong gravity was discovered for the first time in the case of charged particles orbiting the Kerr–Newman black hole, but for ultrarelativistic particles located at close vicinity of the black hole horizon (Bálek et al., 1989). Here we have demonstrated its existence in slightly less exotic conditions around slowly rotating magnetized neutron stars. We shall discuss stability of this kind of motion in a future paper.

ACKNOWLEDGEMENTS

This work has been supported by the Czech grants MSM 4781305903, LC 06014 and GAČR 202/09/0772. The authors further acknowledge the internal student grants of the Silesian University in Opava, SGS/1/2010 and SGS/2/2010. The authors also would like to thank Lenka Čápová and Jaroslav Hýbner for technical help with improving the figures.

REFERENCES

Abdujabbarov, A. A. and Ahmedov, B. J. (2009), Electromagnetic fields and charged particle motion around magnetized wormholes, *Astrophys. and Space Sci.*, **321**, pp. 225–232, arXiv: `0903.0446`.

Abramowicz, M. A. and Kluźniak, W. (2005), Epicyclic Frequencies Derived From The Effective Potential: Simple And Practical Formulae, *Astrophys. and Space Sci.*, **300**, pp. 127–136, arXiv: `astro-ph/0411709`.

Aliev, A. N. and Galtsov, D. V. (1981), Radiation from relativistic particles in nongeodesic motion in a strong gravitational field, *General Relativity and Gravitation*, **13**, pp. 899–912.

Bakala, P., Šrámková, E., Stuchlík, Z. and Török, G. (2010), On magnetic-field-induced non-geodesic corrections to relativistic orbital and epicyclic frequencies, *Classical and Quantum Gravity*, **27**(4), 045001.

Bálek, V., Bičák, J. and Stuchlík, Z. (1989), The motion of the charged particles in the field of rotating charged black holes and naked singularities. II - The motion in the equatorial plane, *Bulletin of the Astronomical Institutes of Czechoslovakia*, **40**, pp. 133–165.

Bičák, J., Stuchlík, Z. and Bálek, V. (1989), The motion of charged particles in the field of rotating charged black holes and naked singularities, *Bulletin of the Astronomical Institutes of Czechoslovakia*, **40**, pp. 65–92.

Braje, T. M. and Romani, R. W. (2001), Magnetospheric Scattering and Emission in Millisecond Pulsars, *Astrophys. J.*, **550**, pp. 392–396, arXiv: `astro-ph/0004407`.

Calvani, M., de Felice, F., Fabbri, R. and Turolla, R. (1982), Off-equatorial circular orbits in the Kerr-Newman space-time, *Nuovo Cimento B Serie*, **67**, pp. 1–10.

Frolov, V. P. and Shoom, A. A. (2010), Motion of charged particles near a weakly magnetized Schwarzschild black hole, *Phys. Rev. D*, **82**(8), 084034, arXiv: `1008.2985`.

Haensel, P., Zdunik, J. L., Bejger, M. and Lattimer, J. M. (2009), Keplerian frequency of uniformly rotating neutron stars and strange stars, *Astronomy and Astrophysics*, **502**, pp. 605–610, arXiv: `0901.1268`.

Hartle, J. B. (1967), Slowly Rotating Relativistic Stars. I. Equations of Structure, *Astrophys. J.*, **150**, p. 1005.

Hartle, J. B. and Sharp, D. H. (1967), Variational Principle for the Equilibrium of a Relativistic, Rotating Star, *Astrophys. J.*, **147**, p. 317.

Johnston, M. and Ruffini, R. (1974), Generalized Wilkins effect and selected orbits in a Kerr-Newman geometry, *Phys. Rev. D*, **10**, pp. 2324–2329.

Kluźniak, W. and Rappaport, S. (2007), Magnetically Torqued Thin Accretion Disks, *Astrophys. J.*, **671**, pp. 1990–2005, arXiv: `0709.2361`.

Konno, K. and Kojima, Y. (2000), General Relativistic Modification of a Pulsar Electromagnetic Field, *Progress of Theoretical Physics*, **104**, pp. 1117–1127, arXiv: `astro-ph/0011240`.

Kopáček, O., Karas, V., Kovář, J. and Stuchlík, Z. (2010), Transition from Regular to Chaotic Circulation in Magnetized Coronae near Compact Objects, *Astrophys. J.*, **722**, pp. 1240–1259, arXiv: `1008.4650`.

Kovář, J., Kopáček, O., Karas, V. and Stuchlík, Z. (2010), Off-equatorial orbits in strong gravitational fields near compact objects – II: halo motion around magnetic compact stars and magnetized black holes, *Classical and Quantum Gravity*, **27**(13), 135006, arXiv: `1005.3270`.

Kovář, J., Slaný, P., Stuchlík, Z., Karas, V., Cremaschini, C. and Miller, J. C. (2011), Role of electric charge in shaping equilibrium configurations of fluid tori encircling black holes, *Phys. Rev. D*, **84**(8), 084002, arXiv: `1110.4843`.

Kovář, J., Stuchlík, Z. and Karas, V. (2008), Off-equatorial orbits in strong gravitational fields near compact objects, *Classical and Quantum Gravity*, **25**(9), 095011, arXiv: `0803.3155`.

Lattimer, J. M. and Prakash, M. (2001), Neutron Star Structure and the Equation of State, *Astrophys. J.*, **550**, pp. 426–442, arXiv: `astro-ph/0002232`.

Lense, J. and Thirring, H. (1918), Über den Einfluß der Eigenrotation der Zentralkörper auf die Bewegung der Planeten und Monde nach der Einsteinschen Gravitationstheorie, *Physikalische Zeitschrift*, **19**, p. 156.

Lo, K.-W. and Lin, L.-M. (2011), The Spin Parameter of Uniformly Rotating Compact Stars, *Astrophys. J.*, **728**, 12, arXiv: `1011.3563`.

Mobarry, C. M. and Lovelace, R. V. E. (1986), Magnetohydrodynamic flows in Schwarzschild geometry, *Astrophys. J.*, **309**, pp. 455–466.

Prasanna, A. R. (1980), General-relativistic analysis of charged-particle motion in electromagnetic fields surrounding black holes, *Nuovo Cimento Rivista Serie*, **3**, pp. 1–53.

Prasanna, A. R. and Sengupta, S. (1994), Charged particle trajectories in the presence of a toroidal magnetic field on a Schwarzschild background, *Phys. Rev. A*, **193**, pp. 25–30.

Prasanna, A. R. and Vishveshwara, V. (1978), Charged particle motion in an electromagnetic field on Kerr background geometry, *Pramana*, **11**, pp. 359–377.

Preti, G. (2004), On charged particle orbits in dipole magnetic fields around Schwarzschild black holes, *Classical and Quantum Gravity*, **21**, pp. 3433–3445.

Rezzolla, L., Ahmedov, B. J. and Miller, J. C. (2001), General relativistic electromagnetic fields of a slowly rotating magnetized neutron star - I. Formulation of the equations, *Monthly Notices Roy. Astronom. Soc.*, **322**, pp. 723–740, arXiv: `astro-ph/0011316`.

Říkovská Stone, J., Miller, J. C., Koncewicz, R., Stevenson, P. D. and Strayer, M. R. (2003), Nuclear matter and neutron-star properties calculated with the Skyrme interaction, *Phys. Rev. C*, **68**(3), 034324.

Stuchlík, Z., Bičák, J. and Bálek, V. (1999), The Shell of Incoherent Charged Matter Falling onto a Charged Rotating Black Hole, *General Relativity and Gravitation*, **31**, pp. 53–71.

Stuchlík, Z. and Hledík, S. (1998), Stationary spherical shells around Kerr-Newman naked singularities., *Acta Physica Slovaca*, **48**, pp. 549–562.

Stuchlík, Z., Konar, S., Miller, J. C. and Hledík, S. (2008), Gravitational excitation of high frequency QPOs, *Astronomy and Astrophysics*, **489**, pp. 963–966, arXiv: `0808.3641`.

Török, G. and Stuchlík, Z. (2005), Radial and vertical epicyclic frequencies of Keplerian motion in the field of Kerr naked singularities. Comparison with the black hole case and possible instability of naked-singularity accretion discs, *Astronomy and Astrophysics*, **437**, pp. 775–788, arXiv: `astro-ph/0502127`.

Urbanec, M., Běták, E. and Stuchlík, Z. (2010), Observational Tests of Neutron Star Relativistic Mean Field Equations of State, *Acta Astronomica*, **60**, pp. 149–163, arXiv: `1007.3446`.

Wasserman, I. and Shapiro, S. L. (1983), Masses, radii, and magnetic fields of pulsating X-ray sources – Is the 'standard' model self-consistent, *Astrophys. J.*, **265**, pp. 1036–1046.

Znajek, R. (1976), On being close to a black hole without falling in, *Nature*, **262**, p. 270.

Proceedings of *RAGtime 10–13, 15–17/20–22/15–17/14–16 September, 2008/2009/2010/2011, Opava, Czech Republic*
Z. Stuchlík, G. Török and T. Pecháček, editors, Silesian University in Opava, 2014, pp. 27–35

Stress-energy tensor of magnetized plasmas in spatially non-symmetric kinetic equilibria

Claudio Cremaschini[1], Zdeněk Stuchlík[1], and Massimo Tessarotto[2]

[1] Institute of Physics, Faculty of Philosophy & Science, Silesian University in Opava, Bezručovo nám. 13, CZ-746 01 Opava, Czech Republic
[2] Department of Mathematics and Geosciences, University of Trieste, Via Valerio 12, 34127 Trieste, Italy

ABSTRACT

Collisionless astrophysical plasmas at kinetic equilibrium can exhibit geometrical structures characterized by the absence of well-defined global spatial symmetries. Plasmas of this type can arise in the surrounding of compact objects and are likely to give rise to relativistic regimes, being subject to intense gravitational and electromagnetic fields. This paper deals with the investigation of the physical mechanisms related to the occurrence of a non-vanishing equilibrium fluid stress-energy tensor associated with each collisionless species of plasma charged particles belonging to these systems. This permits one to obtain information about the thermal properties of the plasma and to display the related contributions generated by phase-space anisotropies. The issue is addressed from a theoretical perspective in the framework of a covariant Vlasov statistical description, based on the adoption of a relativistic gyrokinetic theory for the single-particle dynamics.

Keywords: collisionless magnetized plasmas – gyrokinetic theory – kinetic equilibria – Vlasov equation – stress-energy tensor

1 INTRODUCTION

The description of the complex phenomenology of plasmas arising in the surrounding of compact objects represents a challenging problem in theoretical astrophysics. In these systems, both single-particle and macroscopic fluid velocities of the plasma can become relativistic, at least in particular subsets of the configuration domains, while space-time curvature effects associated with strong gravitational fields can be relevant. When these circumstances occur, relativistic covariant approaches need to be adopted.

In the following we consider strongly-magnetized collisionless plasmas that can be treated in the framework of a covariant Vlasov–Maxwell formulation and in which single-particle dynamics is relativistic. This allows for both phase-space single-particle as well as electromagnetic (EM) and gravitational collective system dynamics to be consistently taken into account. Within such a description, the fundamental quantity is represented by the species

978-80-7510-125-9

kinetic distribution function (KDF) f_s, where s is the species index, whose dynamical evolution is determined by the Vlasov equation.

Astrophysical magnetized plasmas can generate kinetic plasma regimes which persist for long times (with respect to the observer and/or plasma characteristic times), despite the presence of macroscopic time-varying phenomena of various origin, such as flows, non-uniform gravitational/EM fields and EM radiation, possibly including that arising from single-particle radiation-reaction processes (Hazeltine and Mahajan, 2004; Cremaschini and Tessarotto, 2011). For collisionless plasmas, these states might actually correspond to some kind of kinetic equilibrium which characterizes the species KDFs. This is realized when the latter distributions are all assumed to be functions only of the single-particle adiabatic invariants. Therefore, in this sense kinetic equilibria may arise also in physical scenarios in which macroscopic fluid fields (e.g. fluid stress-energy tensor) and/or the EM field might be time dependent when observed from an observer reference frame.

For non-relativistic axisymmetric systems, the subject was treated in Cremaschini et al. (2010, 2011); Cremaschini and Stuchlík (2013); Cremaschini et al. (2013b), where kinetic equilibria were investigated for collisionless magnetized plasmas subject to stationary or quasi-stationary EM and gravitational fields. A number of peculiar physical properties have been pointed out in this reference, which range from quasi-neutrality, the self-generation of equilibrium EM fields and the production of macroscopic azimuthal and poloidal flow velocities, together with the occurrence of temperature and pressure anisotropies. Further interesting developments concern, however, a more general physical setting in which some of the relevant symmetry properties characteristic of the equilibria indicated above, may be in part lost. These include both spatially non-symmetric kinetic equilibria in which energy is conserved (Cremaschini and Tessarotto, 2013) as well as energy-independent kinetic equilibria (Cremaschini et al., 2013a) in which a continuous spatial symmetry of some kind still survives.

Extension of these results to relativistic plasmas of the type indicated above has been established in recent contributions (Cremaschini et al., 2014b,a). In particular, in Cremaschini et al. (2014b) kinetic equilibria of relativistic collisionless plasmas in the presence of non-stationary EM fields have been addressed, while Cremaschini et al. (2014a) dealt with the covariant formulation of spatially non-symmetric kinetic equilibria in magnetized plasmas and the determination of the physical mechanisms responsible for the occurrence of a non-vanishing 4-flow. This concerns systems characterized by non-axisymmetric morphologies as far as the behaviour of both the EM and fluid fields is concerned, while the background gravitational field can still be allowed to exhibit space-time symmetries of some kind (e.g. to be defined with respect to the distant observer coordinate system).

In both these cases, the theory has required the development of a systematic non-perturbative formulation of covariant gyrokinetic theory (Beklemishev and Tessarotto, 1999, 2004) for the appropriate Lagrangian variational description of single-particle dynamics in relativistic plasma regimes. The GK theory in fact provides the appropriate framework for the determination of exact and adiabatic phase-space particle conservation laws. In particular, the novel GK theory presented in Cremaschini et al. (2014b,a) permits one to identify a non-perturbative representation of the particle magnetic moment, which is shown to be conserved even when global space-time symmetries may be absent. In addition, in Cremaschini et al. (2014a) a perturbative representation of the exact GK theory has been developed based on the so-called Larmor-radius expansion, allowing the magnetic moment to be evaluated asymptotically as an adiabatic invariant with prescribed accuracy and the higher-order Larmor-radius corrections to its expression to be consistently determined.

The adiabatic conservation of the single-particle magnetic moment is a distinctive feature of collisionless magnetized plasmas. Indeed, for both relativistic and non-relativistic systems, the magnetic moment is the primary source of temperature anisotropy, while for spatially non-symmetric configurations it is essential in order to generate macroscopic plasma flows along both the parallel and perpendicular directions with respect to the local magnetic field.

Based on these premises and extending the research pursued in Cremaschini et al. (2014a), the purpose of the present work is to investigate the physical mechanisms which determine the properties of the equilibrium fluid stress-energy tensor $T^{\mu\nu}$ associated with relativistic collisionless plasmas in spatially non-symmetric configurations. This provides the correct equilibrium fluid closure condition for these systems, which carries information about the thermal properties of the plasma and the different contributions generated by phase-space anisotropies. The issue is addressed from a theoretical perspective in the framework of a covariant Vlasov statistical description of magnetized plasmas, based on the adoption of the covariant GK theory for the single-particle dynamics earlier developed. In particular, the main goals of the study are as follows:

(1) To summarize the main features of the GK theory and provide the perturbative representation of the relativistic magnetic moment.

(2) To outline the method for the construction of kinetic equilibria, providing an explicit representation of the species KDF in the form of a generalized Gaussian distribution.

(3) To calculate the expression of the stress-energy tensor and to show that this is generally non-isotropic. It is pointed out that this feature arises primarily from the conservation of the magnetic moment carried by the equilibrium KDF. The asymptotic expression of the magnetic moment correct up to first order in the Larmor-radius expansion is adopted for this task, which permits an analytical estimate of the corresponding distinctive contributions to the stress-energy tensor.

2 NON-PERTURBATIVE GK THEORY

In this section we summarize the main results concerning the non-perturbative formulation of the covariant GK theory, treating particles as point-like having specific charge $q \equiv Ze/M_0c^2$, with M_0 being the mass of the species component particles, and moving in a prescribed background metric tensor $g_{\mu\nu}(r)$ and EM 4-potential A_μ. The GK theory is obtained by introducing an extended phase-state transformation of the form

$$\mathbf{x} \equiv \left(r^\mu, u^\mu\right) \leftrightarrow \mathbf{z}' \equiv \left(\mathbf{y}', \phi'\right) , \tag{1}$$

where ϕ' is the gyrophase angle, $\mathbf{z}'$ is the GK state and $\mathbf{y}'$ is a suitable 7-component vector. The GK state $\mathbf{z}'$ is constructed in such a way that its equations of motion are gyrophase independent, namely $\mathrm{d}\mathbf{z}'/\mathrm{d}s \equiv \mathbf{F}(\mathbf{y}', s)$, where $\mathbf{F}$ is a suitable vector field. A non-perturbative covariant GK theory is established by introducing the extended local transformation of the type

$$r^{\mu} = r'^{\mu} + \rho_1'^{\mu}, \tag{2}$$

$$u^{\mu} = u'^{\mu} \oplus \nu_1'^{\mu}, \tag{3}$$

denoted as extended guiding-center transformation, where $\rho_1'^{\mu} = \rho_1'^{\mu}\left(r'^{\mu}, u'^{\mu}\right)$ and $\nu_1'^{\mu} = \nu_1'^{\mu}\left(r'^{\mu}, u'^{\mu}\right)$ are suitably prescribed in terms of $\left(r'^{\mu}, u'^{\mu}\right)$. Here r'^{μ} is the guiding-center position 4-vector, with primed quantities denoting dynamical variables which are evaluated at r'^{μ}. Thus, $\rho_1'^{\mu}$ is referred to as the relativistic Larmor 4-vector, while both u^{μ} and u'^{μ} are by construction 4-velocities, so that $u^{\mu}u_{\mu} = u'^{\mu}u'_{\mu} = 1$, with $\oplus$ denoting the relativistic 4-velocity composition law. Notice that by construction $u_1'^{\mu} \equiv u'^{\mu} \oplus \nu_1'^{\mu}$ is necessarily a 4-velocity, although $\nu_1'^{\mu}$ is not necessarily so.

The guiding-center transformation (2) and (3) are required to fulfil the equation

$$\frac{\mathrm{d}}{\mathrm{d}s}\left(r'^{\mu} + \rho_1'^{\mu}\right) = u'^{\mu} \oplus \nu_1'^{\mu}, \tag{4}$$

which relates the transformed physical velocity to the rate of change of the displacement vector $r'^{\mu} + \rho_1'^{\mu}$.

The 4-velocity u'^{μ} is projected along the EM-tetrad of unit 4-vectors $\left(a'^{\mu}, b'^{\mu}, c'^{\mu}, d'^{\mu}\right)$ evaluated at the guiding-center position (guiding-center EM-tetrad, see Cremaschini et al. (2014a)), yielding the representation

$$u'^{\mu} \equiv u_0' a'^{\mu} + u_{\parallel}' b'^{\mu} + w'\left[c'^{\mu}\cos\phi' + d'^{\mu}\sin\phi'\right], \tag{5}$$

where $u_0' = \sqrt{1 + u_{\parallel}'^2 + w'^2}$. The derivation of the GK equations of motion and of the related conservation laws follow standard procedures in the framework of variational Lagrangian approach. In particular, provided the two transformations (1), (2) and (3) actually exist, i.e. are invertible, one obtains the following expression for the non-perturbative representation of the particle magnetic moment m':

$$m' = \left\langle \frac{\partial \rho_1'^{\mu}}{\partial \phi'}\left[\left(u_{\mu}' \oplus \nu_{1\mu}'\right) + qA_{\mu}\right]\right\rangle_{\phi'}, \tag{6}$$

which is by construction a 4-scalar.

3 PERTURBATIVE GK THEORY

The perturbative GK theory is obtained by introducing a perturbative method based on the introduction of the dimensionless Larmor-radius parameter, namely the frame-invariant ratio $\varepsilon \equiv r_L/L \ll 1$, to be considered as an infinitesimal. Here r_L is the Larmor-radius 4-vector, while L is a suitable characteristic invariant length of the system. Then we introduce the assumption that both $\rho_1'^{\mu}$ and $\nu_1'^{\mu}$ are considered as infinitesimals and are represented in terms of the power series

$$\varepsilon\rho_1'^{\mu} = \varepsilon r_1'^{\mu} + \varepsilon^2 r_2'^{\mu} + \cdots, \tag{7}$$

$$\varepsilon v_1'^{\mu} = \varepsilon v_1'^{\mu} + \varepsilon^2 v_2'^{\mu} + \cdots \tag{8}$$

Similarly, the 4-vector potential is Taylor-expanded in ε around the guiding-center position r'^{μ}. Then, introducing these expressions in the GK Lagrangian differential form and evaluating its gyrophase average yields the following perturbative representation for the particle magnetic moment m':

$$m' = \mu' + \varepsilon\mu_1' + O\left(\varepsilon^2\right). \tag{9}$$

In detail, here μ' is the leading-order contribution given by

$$\mu' = \frac{w'^2}{2qH'}, \tag{10}$$

where H' is the magnetic field strength in the EM-tetrad reference frame. Furthermore, μ_1' is the first-order contribution, which can be written in compact form as

$$\mu_1' = \mu'\left(u_0'\Delta'_{u_0'}\left(r'\right) + u_\parallel'\Delta'_{u_\parallel'}\left(r'\right)\right) + \mu' w'\Delta'_{w'}\left(r'\right), \tag{11}$$

where the 4-scalar coefficients $\Delta'_{u_0'}(r')$, $\Delta'_{u_\parallel'}(r')$ and $\Delta'_{w'}(r')$ are only position-dependent. We omit to calculate here their precise expression as this is not needed for the subsequent developments.

Some important features must be pointed out regarding the asymptotic representation of the magnetic moment given above:

(1) The contribution μ_1' is linearly proportional to the leading-order magnetic moment μ'.

(2) Provided $\Delta'_{u_0'}\left(r'\right)$ and $\Delta'_{u_\parallel'}\left(r'\right)$ are non-zero, the first-order magnetic moment μ_1' contains linear velocity dependences in terms of u_0' and $u_\parallel'$.

(3) The contribution proportional to u_0' is an intrinsically-relativistic effect since u_0' is related to the other components of the 4-velocity by means of a square-root dependence. Concerning the dependences in terms of $u_\parallel'$, we notice that besides the linear one, there is an additional intrinsically relativistic one appearing through u_0'.

4 RELATIVISTIC KINETIC EQUILIBRIA

In this section the construction of relativistic spatially non-symmetric kinetic equilibria for collisionless plasmas in curved space-time is considered. To reach the target, the method of invariants is implemented, which consists in expressing the species KDF in terms of exact or adiabatic single-particle invariants. In the present case the latter is identified with the set (P_0, m'), where P_0 is the conserved momentum conjugate to the ignorable time coordinate, as it follows from the stationarity condition. Therefore one can always represent the species equilibrium KDF in the form $f_s = f_{*s}$, with

$$f_{*s} = f_{*s}\left(\left(P_0, m'\right), \Lambda_*\right) \tag{12}$$

being a smooth strictly-positive function of the particle invariants only which is sum-able in velocity-space. Concerning the notation, in Eq. (12) $\left(P_0, m'\right)$ denote explicit functional dependences, while Λ_* denotes the so-called structure functions (Cremaschini et al., 2011), namely functions suitably related to the observable velocity moments of the KDF. In the following for simplicity the particular choice $\Lambda_* = \text{const}$ is adopted. Notice that in the following, for simplicity of notation but without possible misunderstandings, we omit to indicate the index s in the set of structure functions entering each species KDF.

For the sake of illustration, we consider here a specific realization of each species KDF f_{*s} in terms of a generalized Gaussian distribution. To this aim, we denote with $P_\mu = (u_\mu + qA_\mu)$ the particle generalized 4-momentum in the observer (laboratory) frame which is characterized by the co-moving 4-velocity U^μ, so that in this frame one has simply $U^\mu = (1, 0, 0, 0)$. As a consequence, in the observer frame $P_\mu U^\mu = P_0$ (rest energy), which is a conserved 4-scalar by assumption. Therefore, it follows that f_{*s} can be identified with the 4-scalar

$$f_{M*s} = \beta_* e^{-P_\mu U^\mu \gamma_* - m'\alpha_*}, \tag{13}$$

where the structure functions are represented by the set of 4-scalars fields $\{\Lambda_*\} \equiv \{\beta_*, \gamma_*, \alpha_*\}$. From the physical point of view, here β_* is related to the plasma 4-flow, or equivalently the plasma number density when measured in the fluid co-moving frame, while γ_* and α_* are related to the temperature anisotropy. We stress that the representation of the KDF in Eq. (13) is still exact, in the sense that no asymptotic approximations have been introduced there, so that the magnetic moment m' in the exponential factor must be given by its non-perturbative representation by Eq. (6).

In order to determine explicitly the 4-velocity moments of f_{M*s}, the magnetic moment m' must be preliminarily evaluated at the actual particle position by means of an inverse guiding-center transformation. When the latter is applied to the perturbative representation of m' given by Eq. (9), this leads, with the same accuracy, the following expression for the magnetic moment m:

$$m = \mu + \varepsilon\mu_1 + \varepsilon\delta_{(\mu)}. \tag{14}$$

Here $\mu \equiv w^2/2qH$ is the leading-order contribution, μ_1 is the first-order term which coincides with that in Eq. (11) when evaluated at the particle position, while the $O(\varepsilon)$ correction $\delta_{(\mu)} = \delta_{(\mu)}\left(r, u_\parallel, \mu, \phi\right)$ contains explicit gyrophase dependences and originates from the inverse guiding-center transformation applied to μ'. Finally, in terms of Eq. (14) and neglecting second-order corrections in ε, the equilibrium species KDF (13) becomes

$$f_{M*s} = \beta_* e^{-P_{\mu R} U_R^\mu(r)\gamma_* - \mu\alpha_*}\left[1 - \left(\varepsilon\mu_1 + \varepsilon\delta_{(\mu)}\right)\alpha_*\right], \tag{15}$$

where all quantities are represented in the EM-tetrad with origin at the actual particle position. Thus, $P_{\mu R}$ is the canonical momentum and $U_R^\mu(r)$ the 4-velocity corresponding to U^μ, both expressed in the same EM-reference frame.

5 THE STRESS-ENERGY TENSOR

As shown in Cremaschini et al. (2014a), the phase-space functional dependences contained in the KDF f_{M*s} given by Eq. (15) give rise to corresponding fluid equilibria characterized by non-uniform 4-flows $N^{\mu}(r)$. In this section we consider another velocity-moment of the KDF. In particular we investigate the form of the fluid stress-energy tensor $T^{\mu\nu}(r)$, in order to prove that this is generally non-isotropic and to identify the different phase-space contributions that determine its form.

In detail, the plasma stress-energy tensor $T^{\mu\nu}(r)$ is defined as

$$T^{\mu\nu}(r) = \sum_s T_s^{\mu\nu} , \tag{16}$$

where $T_s^{\mu\nu}$ denotes the generic species stress-energy tensor given by the 4-velocity integral

$$T_s^{\mu\nu}(r) = 2M_o c^2 \int \sqrt{-g}\, \mathrm{d}^4 u\, \Theta\left(u^0\right) \delta\left(u^{\mu} u_{\mu} - 1\right) u^{\mu} u^{\nu} f_{M*s} . \tag{17}$$

In the previous expression the Dirac-delta takes into account the kinematic constraint for the 4-velocity when performing the integration, while $\sqrt{-g}$ is the square-root of the determinant of the background metric tensor. Invoking the EM-tetrad representation for the 4-velocity, the integral can be reduced to

$$T_s^{\mu\nu}(r) = M_o c^2 \int \frac{\sqrt{-g}\, \mathrm{d}^3 u}{\sqrt{1 + u_{\parallel}^2 + w^2}} u^{\mu} u^{\nu} f_{M*s} . \tag{18}$$

When the previous integral is evaluated with respect to the EM-tetrad reference frame, then locally $\sqrt{-g} = 1$, thanks to the principle of equivalence. In such a framework, one can introduce the cylindrical coordinates in the velocity space:

$$\int \mathrm{d}^3 u \to \int_0^{2\pi} \mathrm{d}\phi \int_0^{+\infty} w\, \mathrm{d}w \int_{-\infty}^{+\infty} \mathrm{d}u_{\parallel} , \tag{19}$$

where $u_{\parallel}$ and w coincide with the scalar components of the 4-velocity analogous to those entering Eq. (5) when expressed at the actual particle position and in terms of which the KDF is represented. Hence, in the EM-tetrad frame the integral becomes finally

$$T_s^{\mu\nu}(r) = M_o c^2 \int_0^{2\pi} \mathrm{d}\phi \int_0^{+\infty} w\, \mathrm{d}w \int_{-\infty}^{+\infty} \mathrm{d}u_{\parallel} \frac{u^{\mu} u^{\nu} f_{M*s}}{\sqrt{1 + u_{\parallel}^2 + w^2}} . \tag{20}$$

Although its explicit evaluation can be in principle carried out numerically, in this study we are interested in evaluating its qualitative features in terms of an analytical analysis.

First we notice that, once u^{μ} is represented in the EM-tetrad in terms of the basis formed by $(a^{\mu}, b^{\mu}, c^{\mu}, d^{\mu})$, the same 4-vectors also identify the tensorial components of $T_s^{\mu\nu}(r)$, which are generally position-dependent. Once the expression of $T_s^{\mu\nu}(r)$ is known in such a frame in terms of the EM-tetrad, its representation can then be determined in arbitrary reference frames (i.e. coordinate-systems). A second feature to mention is that, by construction, the tensor $T_s^{\mu\nu}(r)$ is symmetric, with non-vanishing diagonal components. Additional properties can be inferred when the representation (15) is adopted. In particular:

(1) The leading-order contribution to $T_s^{\mu\nu}(r)$ is generated by the velocity dependences contained in the exponential factor, carried respectively by the 4-scalars $P_{\mu R} U_R^{\mu}(r)$ and μ. This determines the leading-order fluid closure condition of the system and the tensorial equation of state of the plasma, to be generally of non-polytropic type for these systems, providing information about the thermal state of the kinetic equilibrium. Since the magnetic moment μ depends only on the component w of the 4-velocity, the separate contributions of the leading-order tensor are different. In the EM-tetrad frame the tensor acquires its simplest representation and becomes diagonal at this order, so that an anisotropy clearly arises in analogy with the non-relativistic solution. This realizes the so-called temperature anisotropy.

(2) The first-order term generated by μ_1 contains three separate contributions, according to the expression (11). In particular, the terms proportional to μu_0 and μw yield corrections to the leading-order solution, thus affecting only the diagonal terms and exhibiting the same kind of anisotropy when the tensor is expressed in the EM-tetrad frame. Instead, more interesting, the term proportional to $\mu u_{\parallel}$ is odd in the parallel component $u_{\parallel}$, and therefore it generates non-vanishing contributions in the tensorial directions (hyperplane) $a^{\mu} b^{\nu}$, so that in the EM-tetrad frame this provides non-diagonal contributions. It is important to stress that the latter feature is a unique consequence of the first-order correction to the magnetic moment, which is missing in the leading-order solution, implying that, for consistency, the first-order perturbations cannot generally be neglected.

(3) Similar considerations apply also to the first-order term associated with the correction $\delta_{(\mu)}$ to the magnetic moment. In view of the general form of its functional dependence and its explicit gyrophase dependence, this term is expected to possibly contribute to all components of the stress-energy tensor, thus extending the number of possible non-vanishing off-diagonal terms (in the EM-tetrad frame).

Finally, a comment is in order concerning the spatial dependences in terms of r^{μ} arising in $T_s^{\mu\nu}(r)$. In the present case in which the structure functions are constant, non-trivial configuration-space dependences still arise due to the following physical effects: 1) the explicit dependence in terms of the 4-scalar $A_{\mu} U_R^{\mu}(r)$ associated with P_{μ}; 2) the functional form of the 4-vector $U_R^{\mu}(r)$, which is determined by the boost transformation; and finally 3) the spatial dependences appearing in the 4-scalars μ, μ_1 and $\delta_{(\mu)}$ occurring due to the inhomogeneities of the background EM field.

6 CONCLUSIONS

In this study the physical properties of the stress-energy tensor associated with relativistic magnetized collisionless plasmas belonging to spatially non-symmetric configurations have been investigated. An analytical approach has been adopted to address the problem. The theory has been developed in the framework of a covariant Vlasov statistical description, based on the adoption of a relativistic gyrokinetic theory for the single-particle dynamics.

A fundamental element is the calculation of the relativistic single-particle magnetic moment, which represents an adiabatic invariant of prescribed accuracy. A perturbative solution correct through first-order in the Larmor-radius expansion has been determined in this context. The expression of the magnetic moment is fundamental for the consistent realization of kinetic equilibria, obtained here in terms of generalized Gaussian-like distributions. In addition, it has been shown that the same adiabatic invariant represents the main source of phase-space anisotropies which ultimately give rise to a non-isotropic stress-energy tensor. When the latter is evaluated in the EM-tetrad frame, the occurrence of a leading-order temperature anisotropy is manifest, while non-vanishing off-diagonal first-order corrections are characteristic of these systems.

The results obtained here are useful in order to display the thermal properties of spatially non-symmetric plasmas and provide the appropriate theoretical framework for a better understanding of the statistical features of astrophysical collisionless plasmas arising in relativistic regimes and subject to the simultaneous action of intense gravitational and electromagnetic fields.

ACKNOWLEDGEMENTS

The present work was supported by the project CZ.1.07/2.3.00/20.0071 Synergy.

REFERENCES

Beklemishev, A. and Tessarotto, M. (1999), Covariant descriptions of the relativistic guiding-center dynamics, *Phys. Plasmas*, **6**, pp. 4487–4496.

Beklemishev, A. and Tessarotto, M. (2004), Covariant gyrokinetic description of relativistic plasmas, *Astronomy and Astrophysics*, **428**, pp. 1–19.

Cremaschini, C., Miller, J. C. and Tessarotto, M. (2010), Kinetic axisymmetric gravitational equilibria in collisionless accretion disk plasmas, *Phys. Plasmas*, **17**(7), p. 072902.

Cremaschini, C., Miller, J. C. and Tessarotto, M. (2011), Kinetic description of quasi-stationary axisymmetric collisionless accretion disk plasmas with arbitrary magnetic field configurations, *Phys. Plasmas*, **18**(6), p. 062901.

Cremaschini, C. and Stuchlík, Z. (2013), Magnetic loop generation by collisionless gravitationally bound plasmas in axisymmetric tori, *Phys. Rev. E*, **87**(4), p. 043113.

Cremaschini, C., Stuchlík, Z. and Tessarotto, M. (2013a), Collisionless energy-independent kinetic equilibria in axisymmetric magnetized plasmas, *Phys. Rev. E*, **88**(3), p. 033105.

Cremaschini, C., Stuchlík, Z. and Tessarotto, M. (2013b), Kinetic theory of quasi-stationary collisionless axisymmetric plasmas in the presence of strong rotation phenomena, *Physics of Plasmas*, **20**(5), p. 052905.

Cremaschini, C. and Tessarotto, M. (2011), Exact solution of the EM radiation-reaction problem for classical finite-size and Lorentzian charged particles, *European Physical Journal Plus*, **126**, p. 42.

Cremaschini, C. and Tessarotto, M. (2013), Theory of spatially non-symmetric kinetic equilibria for collisionless plasmas, *Phys. Plasmas*, **20**(1), pp. 133–165.

Cremaschini, C., Tessarotto, M. and Stuchlík, Z. (2014a), Covariant formulation of spatially non-symmetric kinetic equilibria in magnetized astrophysical plasmas, *Phys. Plasmas*, **21**(5), p. 052901.

Cremaschini, C., Tessarotto, M. and Stuchlík, Z. (2014b), Kinetic equilibria of relativistic collisionless plasmas in the presence of non-stationary electromagnetic fields, *Phys. Plasmas*, **21**(3), p. 032902.

Hazeltine, R. D. and Mahajan, S. M. (2004), Closed fluid description of relativistic, magnetized plasma interacting with radiation field, *Phys. Rev. E*, **70**(3), p. 036404.

Proceedings of *RAGtime 10–13, 15–17/20–22/15–17/14–16 September, 2008/2009/2010/2011, Opava, Czech Republic*
Z. Stuchlík, G. Török and T. Pecháček, editors, Silesian University in Opava, 2014, pp. 37–44

Critical curves of triple gravitational microlenses

Kamil Daněk and David Heyrovský

Institute of Theoretical Physics, Faculty of Mathematics and Physics,
Charles University, Prague, Czech Republic

ABSTRACT
In the theory of gravitational lensing the lens caustic and its primary image, the critical curve, have fundamental importance. Knowledge of these curves greatly facilitates the interpretation and analysis of time-dependent gravitational microlensing events. A binary lens modelled by two point masses can form caustics of three different topologies, which correspond to three topologies of the critical curve. Here we analyse critical curve topologies of the triple lens. While the binary lens is characterized by two parameters, five parameters are needed to describe the triple lens. We present an example illustrating the analysis of special triple-lens models described by two parameters. We find analytical conditions for the change of critical-curve topology, which define boundaries of regions in parameter space with different critical-curve topology. For each region we present corresponding critical curves and caustics. We also include sample results for a three-parameter model describing a triple lens with equal masses in a general spatial configuration.

1 INTRODUCTION

Gravitational microlensing is a special regime of gravitational lensing in which the lensing body is of stellar or sub-stellar mass, so that the deflection angle is too small for resolving individual images of a background star (the "source" in lensing terminology). The main measurable quantity is the time-dependent amplification of flux from the source, i.e. the light curve of a microlensing event. The amplification peaks sharply when the source crosses the caustic of the lens, which – if we could resolve individual images – corresponds to the formation or destruction of a pair of images on the critical curve of the lens.

The single-point-mass lens was discussed in detail by Refsdal (1964). The first theoretical study of two-point-mass lenses was carried out by Schneider and Weiss (1986) who described the properties of the critical curve and caustic of an equal-mass binary lens. A complete analysis of caustic and critical-curve topologies of the general binary lens was performed by Erdl and Schneider (1993).

The first convincing triple-lens microlensing event, OGLE-2006-BLG-109, was found in 2006 (Gaudi et al. 2008). The lens system consisted of a star with two planets forming a Sun + Jupiter + Saturn analogue. The possibility of detecting triple lenses was discussed in several papers (e.g. star with an exoplanet with a moon by Liebig and Wambsganss 2010, Han 2008; planet in a binary-star system by Lee et al. 2008, Chung and Park 2010).

978-80-7510-125-9

At the same time, gravitational microlensing by a system of three bodies has not been satisfactorily analysed theoretically yet. Inspired by the Erdl and Schneider (1993) analysis of the parameter dependence of binary lensing, we extend their approach to special cases of the triple lens, focusing here on the classification of critical-curve topologies.

For binary lenses, there are only three different topologies of the critical curve, corresponding to three different topologies of the caustic. These are usually labelled according to the binary separation as "close" (critical curve formed by three loops), "resonant" (one loop), and "wide" (two loops), with boundaries between the regimes depending on the binary mass ratio. Apart from the merger of loops at these boundaries, the loops of a binary lens caustic never self-intersect, never intersect mutually, and are never nested. The more complex triple-lens caustics often exhibit self-intersections, loop intersections and loop nesting without a change in critical-curve topology. However, the number of loops of the caustic is always the same as the number of loops of the critical curve. In the following we classify the critical-curve topologies by studying the conditions for the merger of critical-curve loops. Such a classification may then serve as a basis for classifying the topologies of the triple-lens caustic.

2 CRITICAL CURVES IN GRAVITATIONAL MICROLENSING

For an n-point-mass lens system, the equation tying the position of the source and its images may be expressed in complex form as

$$\zeta = z - \sum_{i=1}^{n} \frac{\mu_i}{\bar{z} - \bar{z}_i}\,, \tag{1}$$

where ζ is the source position, z is the image position in the lens plane, z_i are the point-mass positions (barred variables $\bar{z}$, $\bar{z}_i$ are complex conjugates of z, z_i), and μ_i are their relative masses with unit total mass ($\sum_{i=1}^{n} \mu_i = 1$). This complex notation was introduced by Witt (1990). All angular positions are normalized to the total-mass Einstein radius, i.e. the radius of a ring-shaped image of a source positioned directly behind a single lens. The amplification of a given image is obtained as the reciprocal value of the determinant of the Jacobi matrix of lens Eq. (1), $J = (\partial\zeta/\partial z)$. The equation of the critical curve is obtained by setting $\det J = 0$, which leads to

$$\sum_{i=1}^{n} \frac{\mu_i}{(z - z_i)^2} = e^{-2\mathrm{i}\phi}\,, \tag{2}$$

where the real phase ϕ varies along the curve from 0 to 2π.

The critical curve in fact is the $\det J = 0$ contour of the Jacobian in the lens plane. Hence, it forms the boundary between regions of positive and negative $\det J$. As a consequence, the point on a critical curve at which loops of the critical curve merge must also be a saddle point of $\det J$. The additional saddle-point condition for such a merging point can be computed from the Hessian, which yields

$$\sum_{i=1}^{n} \frac{\mu_i}{(z - z_i)^3} = 0\,. \tag{3}$$

By solving (2) and (3) simultaneously we get analytic conditions for merging points. These define the boundaries separating regions in parameter space with different critical-curve topologies.

3 TRIPLE LENS: TWO-PARAMETER MODEL

The triple lens is described by five parameters: two relative masses and three position parameters. Finding the merger conditions as equations combining all five parameters is prohibitive because of algebraic complexity and thus demands on computational time. Therefore, we used special triple-lens models with fewer free parameters for an initial exploration of the parameter space.

To give a two-parameter example, we present here the results for a triple-lens system in an equilateral triangle configuration with two masses set equal. Our variable parameters are the mass μ of the third lens, and the length d of a side of the triangle. Using the Sylvester matrix method of Erdl and Schneider (1993), we get four independent conditions for critical-curve merger. Two of them have a similar form, both being polynomials of sixth degree in d^2:

$$a_{12}d^{12} + a_{10}d^{10} + a_8 d^8 + a_6 d^6 + a_4 d^4 + a_2 d^2 + a_0 = 0\,, \tag{4}$$

$$a_{12}d^{12} - a_{10}d^{10} + a_8 d^8 - a_6 d^6 + a_4 d^4 - a_2 d^2 + a_0 = 0\,, \tag{5}$$

where

$$\begin{aligned}
a_{12} &= 32\,,\\
a_{10} &= 48(3\mu - 1)\,,\\
a_8 &= -48(3\mu - 1)(3\mu - 5)\,,\\
a_6 &= 8\big(81\mu^3 + 27\mu^2 - 45\mu + 35\big)\,,\\
a_4 &= 6(3\mu - 1)\big(621\mu^3 - 981\mu^2 + 351\mu + 25\big)\,,\\
a_2 &= -3(3\mu - 1)\big(243\mu^4 - 972\mu^3 + 1098\mu^2 - 372\mu - 13\big)\,,\\
a_0 &= -108\mu^3 + 324\mu^2 - 180\mu - 4\,.
\end{aligned} \tag{6}$$

The third has the form of a polynomial of third degree in d^4,

$$\begin{aligned}
&16d^{12} - 24\big(9\mu^2 - 6\mu - 1\big)d^8 - \big(243\mu^4 + 972\mu^3 + 1134\mu^2 - 468\mu + 15\big)d^4 +\\
&+54\mu^3 - 162\mu^2 + 90\mu + 2 = 0\,,
\end{aligned} \tag{7}$$

and the fourth is a polynomial of twelfth degree in d^4,

$$\sum_{l=0}^{12} b_{4l}\, d^{4l} = 0\,, \tag{8}$$

where b_{4l} are functions of μ that we don't specify here due to their complexity.

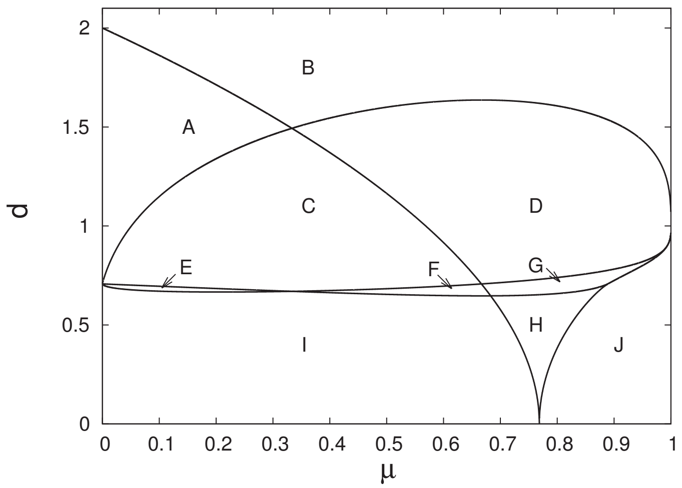

Figure 1. Parameter space regions according to critical-curve topology for a triple lens in an equilateral triangle configuration. Parameters: mass of vertex μ; length of side d.

The curves in the $[\mu, d]$ plane given implicitly by Eqs. (4), (5), (7), and (8) form boundaries that divide the parameter space into several regions. To make sure that regions on either side of each curve correspond to different topologies, it is necessary to check whether each solution of (4), (5), (7), and (8) also fulfils the original conditions (2) and (3).

In Figure 1 we plotted the parameter space of the equilateral-triangle lens with curves given by (4), (5), (7), and (8). These curves divide the parameter space into ten regions, labelled in the Figure A through J. Examples of critical curves and caustics from all ten regions are shown in Fig. 2. There are altogether seven different topologies of the critical curve. The topologies in E and G are the same, so are those in F and H, and in I and J. The critical curve in B consists of three loops that separate in the limit $d \to \infty$ into Einstein rings of three single lenses. The critical curve in I and J consists of an outer loop and four inner loops. In the limiting case $d \to 0$ the inner loops disappear at the lens position and the outer loop turns into the Einstein ring of a single lens with total mass $\sum_{i=1}^{3} \mu_i = 1$.

The analysis of two other two-parameter models can be found in Daněk (2010).

4 TRIPLE LENS: THREE-PARAMETER MODEL

Using the Sylvester matrix method for three-parameter triple-lens configurations usually leads to multi-page expressions for merging conditions. Factorizing the final result into separate surfaces dividing the parameter space presents a further hurdle to this method. It is necessary, therefore, to find an alternative approach.

We noticed a nice property of (2) and (3) that can be used to obtain the parameters of critical-curve mergers. If we multiply both sides of (2) by a real positive number α and perform the transformation $z' = \alpha^{-1/2} z$, $z'_i = \alpha^{-1/2} z_i$, we obtain the equation of

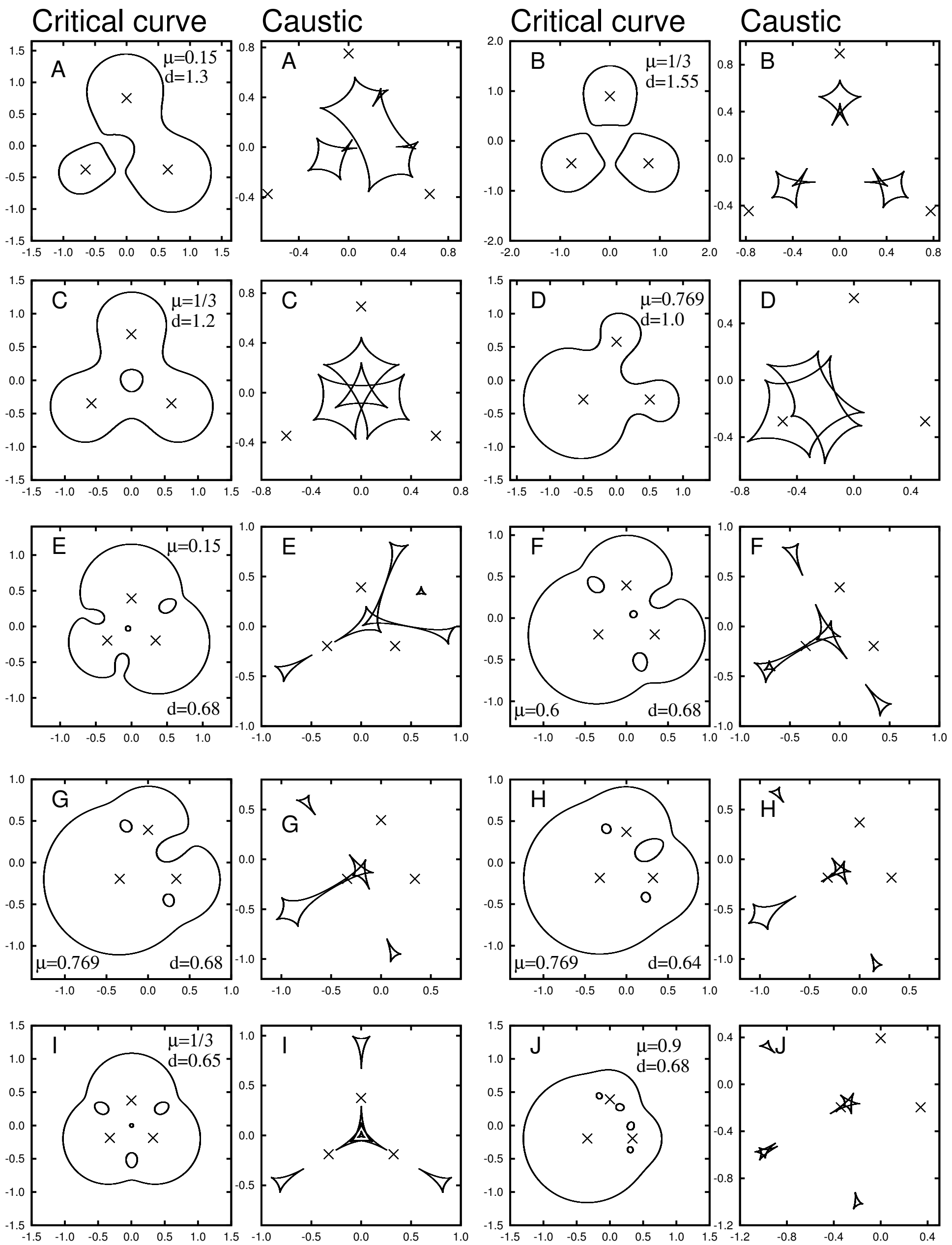

Figure 2. Critical curves and caustics of a triple lens in an equilateral triangle configuration. First and third column: critical curves; second and fourth column: caustics; crosses: lens positions. Letters labelling the panels correspond to regions in Fig. 1.

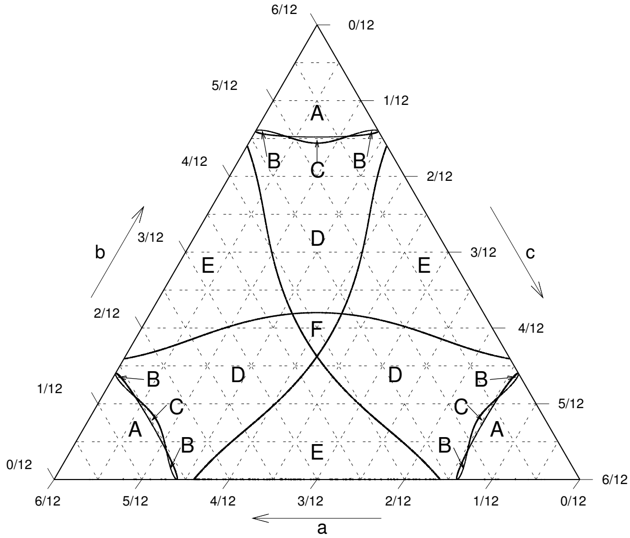

Figure 3. Parameter space regions according to critical-curve topology for a triple lens with equal masses and circumference $o = 4.8$. Lengths of sides a, b, c are in units of o.

a Jacobian contour line with $\det J' = 1 - \alpha^2$ in z'. The saddle-point condition (3) holds for both transformed and untransformed values. This enables us to find the value of $\det J'$ in a saddle point z' for some chosen lens positions z'_i and a contour line going through the saddle point. By inverting the transformation we can find lens parameters z_i with a critical curve equal, up to a scaling factor, to the found contour line. For any configuration of the triple lens there are six saddle points of the Jacobian. Hence, we obtain six values of $\det J'$ that tell us how to re-scale the lens positions to obtain parameters of critical-curve mergers.

As an example we present a triple lens with equal masses and arbitrary lens positions. The system is parametrized by the triangle circumference o and three lengths of sides as fractions of the circumference a, b, c, constrained by $a+b+c = 1$. Taking advantage of the symmetry of this problem we draw $o = \text{const}$ slices of the parameter space as ternary plots. The $o = 4.8$ slice is shown for illustration in Fig. 3. Here the parameter space is divided into nineteen regions, due to symmetry representing only six distinct types of regions, labelled in the Figures A through F.

Examples of critical curves and caustics corresponding to the six regions are presented in Fig. 4. There are altogether five different critical-curve topologies in this slice of the parameter space, with regions B and C having the same topology. The topologies in A and B / C do not occur in the two-parameter equilateral-triangle model described earlier. D has the same critical-curve topology as A in Fig. 2, their caustics have the same total number of cusps but the latter has four more intersections. The critical-curve topology and number of caustic cusps are the same for the following pairs of examples: E from Fig. 4 and D from Fig. 2; F from Fig. 4 and B from Fig. 2. Note that the example F in Fig. 4 has the parameters of an equilateral triangle; its parameters lie in B of Fig. 1.

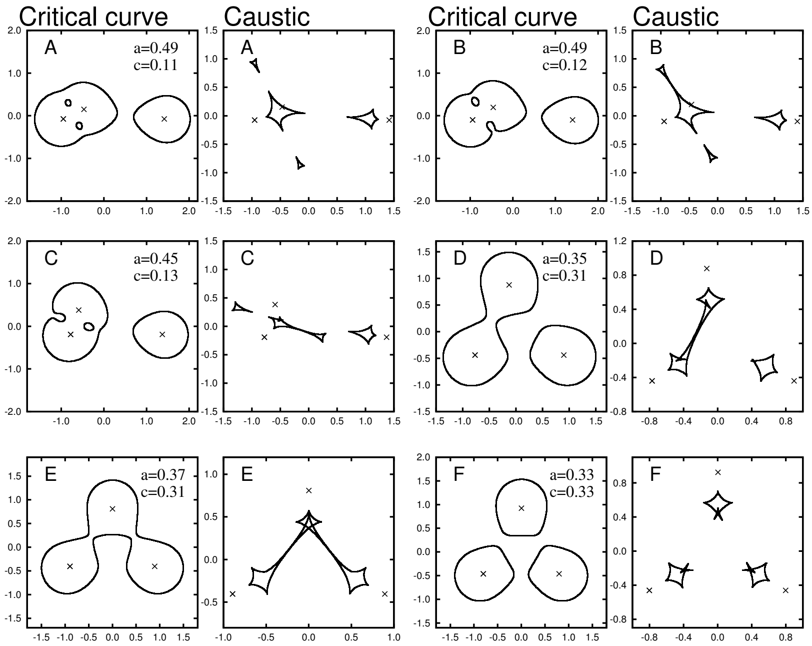

Figure 4. Critical curves and caustics of a triple lens with equal masses and circumference $o = 4.8$. First and third column: critical curves; second and fourth column: caustics; crosses: lens positions. Letters labelling the panels correspond to regions in Fig. 3.

5 CONCLUSION

The topological analysis of critical curves and caustics of binary lenses provides a priceless theoretical background for analysing observed microlensing light curves. We have shown that it is possible to find algebraic conditions for critical-curve merger for special two-parameter models of triple lenses. We have found a numerical method for obtaining merger parameters for a general multiple lens, by identifying the contour lines of the Jacobian passing through its saddle points with the critical curves of re-scaled lens configurations.

The number of possible critical-curve topologies in the full parameter space of a triple lens still remains unclear. For a more instructive insight into all possible light curves of triple-lens microlensing we also need to refine the analysis to cover other caustic transformations. In particular, the number of caustic cusps can change even without mergers. For a complete caustic-topology analysis, also caustic intersections should be taken into account.

ACKNOWLEDGEMENTS

This research project was supported by the Czech Ministry of Education project MSM0021620860, by Czech Science Foundation grant GACR P209/10/1318 and by the projects SVV 263301 and GAUK 428011 of the Charles University in Prague.

REFERENCES

Chung, S.-J. and Park, B.-G. (2010), Properties of microlensing central perturbations by planets in binary stellar systems under the strong finite-source effect, *The Astrophys. J.*, **713**, p. 865.

Daněk, K. (2010), *Gravitational microlensing by a few-body system*, Charles University in Prague, Prague, master's thesis.

Erdl, H. and Schneider, P. (1993), Classification of the multiple deflection two point-mass gravitational lens models and application of catastrophe theory in lensing, *Astronomy and Astrophysics*, **268**, p. 453.

Gaudi, B. S. et al. (2008), Discovery of a Jupiter/Saturn analog with gravitational microlensing, *Science*, **319**, p. 927.

Han, C. (2008), Microlensing Detections of Moons of Exoplanets, *The Astrophys. J.*, **684**, p. 684.

Lee, D.-W. et al. (2008), Microlensing detection of planets in binary stellar systems, *The Astrophys. J.*, **672**, p. 623.

Liebig, C. and Wambsganss, J. (2010), Detectability of extrasolar moons as gravitational microlenses, *Astronomy and Astrophysics*, **520**, p. A68.

Refsdal, S. (1964), The gravitational lens effect, *Monthly Notices Roy. Astronom. Soc.*, **128**, p. 295.

Schneider, P. and Weiss, A. (1986), The two-point-mass lens: detailed investigation of a special asymmetric gravitational lens, *Astronomy and Astrophysics*, **164**, p. 237.

Witt, H. J. (1990), Investigation of high amplification events in light curves of gravitationally lensed quasars, *Astronomy and Astrophysics*, **236**, p. 311.

Proceedings of *RAGtime 10–13, 15–17/20–22/15–17/14–16 September, 2008/2009/2010/2011, Opava, Czech Republic*
Z. Stuchlík, G. Török and T. Pecháček, editors, Silesian University in Opava, 2014, pp. 45–52

Secular evolution of the young stellar disc in the Galactic Centre

Jaroslav Haas[a] and Ladislav Šubr

Astronomical Institute, Faculty of Mathematics and Physics, Charles University,
V Holešovičkách 2, CZ-180 00 Praha, Czech Republic
[a]haas@sirrah.troja.mff.cuni.cz

ABSTRACT
A significant number of early-type stars have been discovered in the innermost parsec of the Milky Way. Roughly one half of those which are orbiting the central supermassive black hole at projected distances $\gtrsim$0.03 pc appear to form a coherently rotating disc-like structure. A massive molecular torus and an extended cusp of late-type stars have also been detected in this region. Assuming that the stellar disc is initially thin and geometrically circular, we investigate its secular orbital evolution by means of numerical N-body integration. We include the gravitational influence of both the torus and cusp, as well as the self-gravity of the disc. Our calculations show that for a variety of initial configurations, the system evolves to a state compatible with the current observational data within the life-time of the early-type stars. In particular, the core of the disc naturally reaches a perpendicular orientation with respect to the torus. We thus suggest that all the early-type stars may have been born within a single gaseous disc.

Keywords: numerical methods – stellar dynamics – Galactic Centre

1 INTRODUCTION

The centre of the Milky Way harbours, according to recent observations, nearly 200 early-type stars moving on Keplerian orbits around a highly concentrated mass (Allen et al., 1990; Genzel et al., 2003; Ghez et al., 2003, 2005; Paumard et al., 2006; Bartko et al., 2009, 2010), presumably a supermassive black hole (SMBH) of mass $\approx 4 \times 10^6\,M_\odot$ (Ghez et al., 2003; Eisenhauer et al., 2005; Gillessen et al., 2009; Gillessen et al., 2009; Yelda et al., 2011). Most of them are located at projected distance 0.03 pc $\lesssim r \lesssim$ 0.5 pc from the SMBH (Bartko et al., 2009, 2010). Out of these stars, roughly one half form a disc-like structure, the so-called clockwise system (CWS; discovered by Levin and Beloborodov, 2003), while the other half reside on randomly oriented orbits. Observations indicate that all of these stars are coeval and 6 ± 2 Myr old (Paumard et al., 2006). Their origin is, however, rather puzzling. Due to strong tidal field of the SMBH, it is not possible for a star to be formed by any standard star formation mechanism. On the other hand, no transport mechanism is efficient enough to bring them from farther regions, where their formation would be easier, to the observed location within their estimated lifetime. Various hypotheses have, therefore, been suggested in order to explain the origin of these stars.

978-80-7510-125-9

In situ fragmentation of a self-gravitating disc is probably the currently most widely accepted formation scenario for the stars of the CWS (Levin and Beloborodov, 2003; Paumard et al., 2006) as this process naturally forms stars in a disc-like structure. It does not, however, explain the origin of the stars observed outside the CWS. Hence, in order to justify the in-disc formation scenario, another mechanism that would force some of the stars to leave the parent disc plane is needed. Šubr et al. (2009) suggested that this might have happened due to gravity of a massive ($\sim 10^6\,M_\odot$) molecular torus, the circumnuclear disc (CND), which is observed between 1.6 pc and 2.0 pc from the SMBH (Christopher et al., 2005). They argue that the CND would cause differential precession of the individual orbits within the parent stellar disc. Consequently, the stars from the outer parts of the disc would be dragged out of the disc plane while the inner parts of the disc would remain undisturbed. This core can be identified as the CWS today.

In this work, we further analyse the mechanism suggested by Šubr et al. (2009). In particular, we focus on the impact of the self-gravity of the parent stellar disc on its orbital evolution in a predefined external potential of the SMBH, CND and a cusp of late-type stars which is also observed in the Galactic Centre (Genzel et al., 2003; Schödel et al., 2007; Do et al., 2009). As the first approximation, we consider the cusp to be spherically symmetric and centred on the SMBH.

2 NUMERICAL MODEL

The gravitational potential induced by the SMBH in the vicinity of the stellar disc can be, to a very high accuracy, considered Keplerian. It is thus natural to describe the stellar orbits in the disc by means of the Keplerian elements: semi-major axis a, eccentricity e, inclination i, longitude of the ascending node Ω and argument of pericentre ω. For sake of definiteness, let us define the z-axis of our reference system as the symmetry axis of the CND, i.e. orbital inclination i is the angle between the symmetry axis of the CND and angular momentum of the star. If the only component of the overall gravitational potential were the gravity of the SMBH, the Keplerian elements of all the individual orbits would be constant in time. On the other hand, inclusion of any additional gravitational potentials may lead to an intricate secular evolution of some of the elements.

Šubr et al. (2009) have investigated the influence of the CND and spherical cusp on the stellar disc with the stars treated as test particles. They found that the CND causes differential precession of the individual stellar orbits in the disc. Furthermore, provided the spherical cusp is massive enough, the first time derivative of Ω, the precession rate, is constant and can be written as

$$\frac{\mathrm{d}\Omega}{\mathrm{d}t} = -\frac{3}{4}\frac{\cos i}{T_{\mathrm{K}}}\frac{1+\frac{3}{2}e^2}{\sqrt{1-e^2}} \tag{1}$$

with

$$T_{\mathrm{K}} \equiv \frac{M_\bullet}{M_{\mathrm{CND}}}\frac{R_{\mathrm{CND}}^3}{a\sqrt{GM_\bullet a}}\,, \tag{2}$$

where $M_\bullet$ represents the mass of the SMBH, $M_{\rm CND}$ and $R_{\rm CND}$ stand for the mass and radius of the CND, respectively, and G denotes the gravitational constant. It thus appears that the precession rate strongly depends upon the semi-major axis of the orbit. Hence, the outer parts of the disc are more affected by the precession than the inner parts, which results in warping of the disc and, eventually, in its complete dissolution.

Including the gravity of the stars in the disc leads to random variations of the individual orbital elements due to two-body relaxation of the disc. Although these changes are not large enough to have an impact on the overall shape of the disc by themselves (Cuadra et al., 2008), they can, according to formula (1), affect the precession rate of the individual orbits. Let us, therefore, further focus on the combined effects of differential precession and two-body relaxation of the disc.

For this purpose, we model the individual components of the Galactic Centre as follows: (i) the SMBH of mass $M_\bullet = 4 \times 10^6\,M_\odot$ is considered to be a source of the Keplerian potential, (ii) the CND is modelled as a single massive particle of mass $M_{\rm CND}$ orbiting the SMBH on a geometrically circular orbit of radius $R_{\rm CND} = 1.8$ pc, (iii) the spherical cusp is represented by a smooth power-law density profile, $\rho\,(r) \propto r^{-\beta}$, and mass $M_{\rm c}$ within the radius $R_{\rm CND}$, (iv) the stars in the disc are treated as a group of N gravitating particles orbiting the SMBH on orbits that are initially geometrically circular. Their radii are generated randomly between 0.04 pc and 0.4 pc in compliance with relation $\mathrm{d}N \propto a^{-1}\,\mathrm{d}a$. Distribution of masses of the individual stars in the disc follows a power-law mass function $\mathrm{d}N \propto m^{-\alpha}\,\mathrm{d}m$, $m \in [m_{\rm min}, m_{\rm max}]$. Evolution of this system is investigated numerically by means of the N-body integration code NBODY6 (Aarseth, 2003).

3 DISCUSSION OF THE RESULTS

The course of the orbital evolution of the stellar disc depends upon many parameters that describe the overall gravitational potential in the system: $M_{\rm CND}$, $M_{\rm c}$, β, N, $m_{\rm min}$, $m_{\rm max}$, α, initial inclination of the disc with respect to the CND, $i^0_{\rm CWS}$, and its initial half-opening angle, $\varDelta_0$. Our calculations show that, for a wide set of these parameters, the system reaches a configuration compatible with the current observational data after ≈ 6 Myr of its orbital evolution (for a detailed discussion, see Haas et al., 2011a).

In particular, it appears that the orbits in the outer parts of the disc are indeed affected by the precession of the ascending node more strongly than those in the inner parts. This leads, in accord with formula (1), to gradual deformation of the disc and, eventually, to disruption of its entire outskirts. Moreover, it turns out that the precession is, on longer time-scales, globally accelerated in the outer parts of the disc, which we attribute to the two-body relaxation of the disc. This acceleration was not observed by Šubr et al. (2009) as they had not considered the self-gravity of the disc.

Furthermore, our results show that the mean inclination of the orbits in the outer parts of the disc is decreasing. On the other hand, it grows up and saturates at $\approx 90°$ in the inner parts. We further find that the evolution of the mean values of both the inclination and longitude of the ascending node is similar for all the orbits in the inner parts of the disc. The core of the disc thus remains undisturbed and coherently changes its orientation towards perpendicular with respect to the CND. This effect can be seen in the left panel

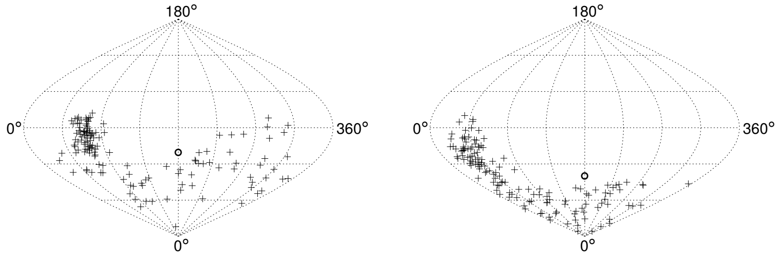

Figure 1. Angular momenta of individual stars in the disc in sinusoidal projection after 6 Myr of orbital evolution. The initial state is denoted by an empty circle. Latitude on the plots corresponds to i while longitude is related to Ω. *Left*: One realization of a model with $i^0_{\rm CWS} = 70°$. *Right*: $i^0_{\rm CWS} = 50°$. The other parameters are set to their canonical values for both panels. For a more convenient comparison with the currently available observational data which suggest that the early-type stars are massive, only stars with $m \geq 12\,M_\odot$ are displayed. The less massive stars with $m = 4$–$12\,M_\odot$ have been included in our calculations since it is likely that a number of them exist undetected in the Galactic Centre.

of Fig. 1 which shows the directions of the individual angular momenta of the stars in sinusoidal projection for one of the realizations of the 'canonical' model: $M_{\rm CND} = 0.3\,M_\bullet$, $M_{\rm c} = 0.03\,M_\bullet$, $m \in [4\,M_\odot, 120\,M_\odot]$, $N = 200$, $\alpha = 1$, $\beta = 7/4$, $i^0_{\rm CWS} = 70°$, $\Delta_0 = 2.5°$. Our results suggest that the compact group of stars at inclination $\approx 90°$ is formed by the stars from the inner parts of the disc, while the stars scattered all around the bottom half of the plot represent the disrupted outer parts. Hence, we see that it is possible to reconstruct the currently observed configuration of the studied early-type stars in the Galactic Centre from a single and initially thin stellar disc. In particular, its compact core can represent the CWS observed today while the stars from the dismembered outer parts can be identified with the stars observed off the CWS plane.

In order to compare our findings with the observations more thoroughly, let us define the CWS within our data as follows. As the zeroth step, the CWS is taken equivalent to a fixed number of the innermost stars from the initial disc. In the next step, we exclude all the stars whose angular momenta deviate from the mean angular momentum of the CWS by more than 20°. On the other hand, the stars initially from outside the CWS, which do not fulfil the latter condition, are included into the CWS. Then, we recalculate the mean angular momentum of the CWS and repeat the whole procedure iteratively until there are no changes of the CWS between two subsequent steps.

Observations indicate that the CWS harbours roughly one half of all the early-type stars between 0.03 pc and 0.5 pc from the SMBH (Paumard et al., 2006; Bartko et al., 2009, 2010). In order to confront this feature, we investigate the evolution of the relative number $N/N_{\rm CWS}$ of the stars belonging to the CWS within our calculations. As can be seen in the top left panel of Fig. 2, this number reaches for the canonical model ≈ 0.5 after 6 Myr of orbital evolution. Observations further suggest that the CWS is roughly perpendicular to the CND (Paumard et al., 2006). We thus follow in our calculations the inclination $i_{\rm CWS}$ of the CWS with respect to the CND. The top right panel of Fig. 2 shows that our results are in agreement even with this observational constraint as $i_{\rm CWS} \approx 90°$ at $t = 6$ Myr.

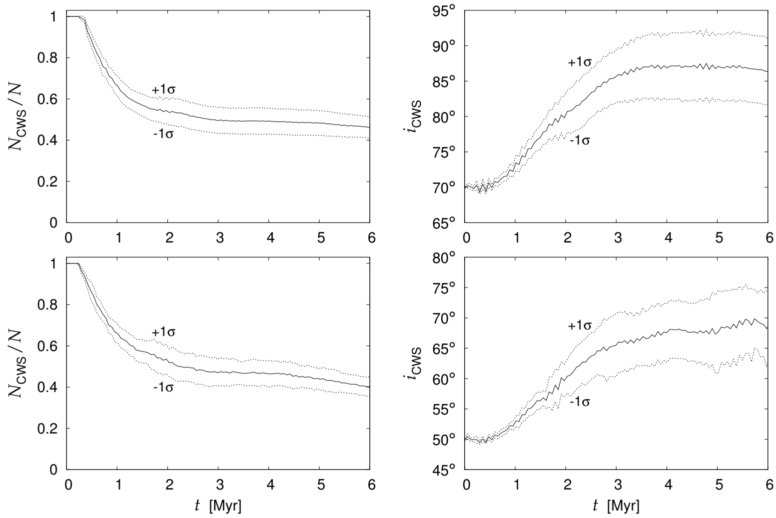

Figure 2. Evolution of the CWS for a model with $i^0_{CWS} = 70°$ (top panels) and $i^0_{CWS} = 50°$ (bottom panels). The other parameters are set to their canonical values in both cases. Only properties of the stars with $m \geq 12\,M_\odot$ are displayed. The dotted lines denote standard deviation for the set of 12 included realizations. *Left*: Number of stars within the CWS (i.e. with angular momentum deviating from the mean angular momentum of the CWS by less than 20°). *Right*: Inclination of the CWS with respect to the CND.

In order to illustrate the dependence of the discovered processes upon the initial parameters, we also show our results for a model with $i^0_{CWS} = 50°$. The other parameters remain set to their canonical values. As we can learn from the right panel of Fig. 1 and the bottom panels of Fig. 2, in this case, the CWS contains at $t = 6$ Myr only $\approx 40\,\%$ of the stars and its inclination reaches only $\approx 70°$. The evolution on longer time-scales proves that even though the inclination of the CWS continues to increase, the number of the stars within the CWS further decreases. Hence, the parent stellar disc is too severely damaged by the differential precession before its core can reach the perpendicular orientation, and, therefore, the observational criteria are not fulfilled for this model. Our results suggest that the studied system evolves after ≈ 6 Myr to a state which accommodates the observational constraints if $i^0_{CWS} \gtrsim 60°$. A more detailed discussion of the remaining parameters can be found in Haas et al. (2011a).

3.1 Physical background

As we have shown in Haas et al. (2011b) by means of standard perturbation methods of celestial mechanics, the dynamical processes described in previous paragraphs are a consequence of preservation of integrals of motion in the considered gravitational potential. In particular, beside the total energy and z-component of the total angular momentum of the stars in the disc, the potential energy which corresponds to their mutual interaction in the field of the CND is also preserved if averaged over one revolution of the stars around the

SMBH. Depending on the strengthens of this interaction, two modes of orbital evolution are possible. Either the stellar orbits interact strongly and, under such circumstances, they become dynamically coupled, precessing coherently in the potential of the CND. Or, if their mutual interaction is weaker, the orbits precess independently, interchanging periodically their angular momentum, which results in oscillations of inclinations. Hence, the dense core of the stellar disc, where the interaction of the orbits is strong enough, is not disrupted by the differential precession. On the other hand, the weakly interacting orbits from the outer parts can not overcome the disturbing influence of the CND and, therefore, the outskirts of the disc are entirely dismembered.

Moreover, the core of the disc inevitably changes its inclination towards higher values due to interaction with the outer parts of the disc as a whole, similarly to the case of two interacting orbits.

4 CONCLUSIONS

We have investigated the secular evolution of an initially thin and geometrically circular self-gravitating stellar disc around a dominating central mass. In accord with the observations of the Galactic Centre, we have included the perturbative gravitational potential of the CND and the cusp of late-type stars. Our results show that the CND causes differential precession of the stellar orbits in the disc which leads to gradual dissolution of its outer parts. On the other hand, the core of the disc remains, due to stronger mutual interaction of its stars, untouched forming the CWS. Simultaneously, the CWS changes coherently its orientation towards perpendicular with respect to the CND which is indeed the configuration observed in the Galactic Centre. We further find that these processes lead to a configuration compatible with the currently available observational data for a wide set of system parameters. Hence, we suggest that all the early-type stars observed at projected distances 0.03–0.5 pc from the SMBH may have been formed within a single gaseous disc and, subsequently, brought to their present location by the combined effects of differential precession and two-body relaxation.

ACKNOWLEDGEMENTS

This work was supported by the Czech Science Foundation via grants GACR-205/09/H033 and GACR-205/07/0052 and also from the project SVV 261301 of Charles University in Prague. The calculations were performed on the computational cluster Tiger at the Astronomical Institute of Charles University in Prague (`http://sirrah.troja.mff.cuni.cz/tiger`).

REFERENCES

Aarseth, S. J. (2003), *Gravitational N-Body Simulations*, Cambridge University Press, Cambridge.

Allen, D. A., Hyland, A. R. and Hillier, D. J. (1990), The source of luminosity at the Galactic Centre, *Monthly Notices Roy. Astronom. Soc.*, **244**, pp. 706–713.

Bartko, H., Martins, F., Fritz, T. K., Genzel, R., Levin, Y., Perets, H. B., Paumard, T., Nayakshin, S., Gerhard, O., Alexander, T., Dodds-Eden, K., Eisenhauer, F., Gillessen, S., Mascetti, L., Ott, T., Perrin, G., Pfuhl, O., Reid, M. J., Rouan, D., Sternberg, A. and Trippe, S. (2009), Evidence for Warped Disks of Young Stars in the Galactic Center, *Astrophys. J.*, **697**, pp. 1741–1763, arXiv: `0811.3903`.

Bartko, H., Martins, F., Trippe, S., Fritz, T. K., Genzel, R., Ott, T., Eisenhauer, F., Gillessen, S., Paumard, T., Alexander, T., Dodds-Eden, K., Gerhard, O., Levin, Y., Mascetti, L., Nayakshin, S., Perets, H. B., Perrin, G., Pfuhl, O., Reid, M. J., Rouan, D., Zilka, M. and Sternberg, A. (2010), An Extremely Top-Heavy Initial Mass Function in the Galactic Center Stellar Disks, *Astrophys. J.*, **708**, pp. 834–840, arXiv: `0908.2177`.

Christopher, M. H., Scoville, N. Z., Stolovy, S. R. and Yun, M. S. (2005), HCN and HCO^+ Observations of the Galactic Circumnuclear Disk, *Astrophys. J.*, **622**, pp. 346–365, arXiv: `astro-ph/0502532`.

Cuadra, J., Armitage, P. J. and Alexander, R. D. (2008), Stellar dynamical evidence against a cold disc origin for stars in the Galactic Centre, *Monthly Notices Roy. Astronom. Soc.*, **388**, pp. L64–L68, arXiv: `0804.3596`.

Do, T., Ghez, A. M., Morris, M. R., Lu, J. R., Matthews, K., Yelda, S. and Larkin, J. (2009), High Angular Resolution Integral-Field Spectroscopy of the Galaxy's Nuclear Cluster: A Missing Stellar Cusp?, *Astrophys. J.*, **703**, pp. 1323–1337, arXiv: `0908.0311`.

Eisenhauer, F., Genzel, R., Alexander, T., Abuter, R., Paumard, T., Ott, T., Gilbert, A., Gillessen, S., Horrobin, M., Trippe, S., Bonnet, H., Dumas, C., Hubin, N., Kaufer, A., Kissler-Patig, M., Monnet, G., Ströbele, S., Szeifert, T., Eckart, A., Schödel, R. and Zucker, S. (2005), SINFONI in the Galactic Center: Young Stars and Infrared Flares in the Central Light-Month, *Astrophys. J.*, **628**, pp. 246–259, arXiv: `astro-ph/0502129`.

Genzel, R., Schödel, R., Ott, T., Eisenhauer, F., Hofmann, R., Lehnert, M., Eckart, A., Alexander, T., Sternberg, A., Lenzen, R., Clénet, Y., Lacombe, F., Rouan, D., Renzini, A. and Tacconi-Garman, L. E. (2003), The Stellar Cusp around the Supermassive Black Hole in the Galactic Center, *Astrophys. J.*, **594**, pp. 812–832, arXiv: `astro-ph/0305423`.

Ghez, A. M., Duchêne, G., Matthews, K., Hornstein, S. D., Tanner, A., Larkin, J., Morris, M., Becklin, E. E., Salim, S., Kremenek, T., Thompson, D., Soifer, B. T., Neugebauer, G. and McLean, I. (2003), The First Measurement of Spectral Lines in a Short-Period Star Bound to the Galaxy's Central Black Hole: A Paradox of Youth, *Astrophys. J. Lett.*, **586**, pp. L127–L131, arXiv: `astro-ph/0302299`.

Ghez, A. M., Salim, S., Hornstein, S. D., Tanner, A., Lu, J. R., Morris, M., Becklin, E. E. and Duchêne, G. (2005), Stellar Orbits around the Galactic Center Black Hole, *Astrophys. J.*, **620**, pp. 744–757, arXiv: `astro-ph/0306130`.

Gillessen, S., Eisenhauer, F., Fritz, T. K., Bartko, H., Dodds-Eden, K., Pfuhl, O., Ott, T. and Genzel, R. (2009), The orbit of the star s2 around sgr a* from very large telescope and keck data, *Astrophys. J. Lett.*, **707**(2), pp. L114–L117.

Gillessen, S., Eisenhauer, F., Trippe, S., Alexander, T., Genzel, R., Martins, F. and Ott, T. (2009), Monitoring Stellar Orbits Around the Massive Black Hole in the Galactic Center, *Astrophys. J.*, **692**, pp. 1075–1109, arXiv: `0810.4674`.

Haas, J., Šubr, L. and Kroupa, P. (2011a), The coupling of a young stellar disc with the molecular torus in the Galactic Centre, *Monthly Notices Roy. Astronom. Soc.*, **412**, pp. 1905–1912, arXiv: `1011.3815`.

Haas, J., Šubr, L. and Vokrouhlický, D. (2011b), Secular theory of the orbital evolution of the young stellar disc in the Galactic Centre, *Monthly Notices Roy. Astronom. Soc.*, **416**, pp. 1023–1032, arXiv: `1105.4608`.

Levin, Y. and Beloborodov, A. M. (2003), Stellar Disk in the Galactic Center: A Remnant of a Dense Accretion Disk?, *Astrophys. J. Lett.*, **590**, pp. L33–L36, arXiv: `astro-ph/0303436`.

Paumard, T., Genzel, R., Martins, F., Nayakshin, S., Beloborodov, A. M., Levin, Y., Trippe, S., Eisenhauer, F., Ott, T., Gillessen, S., Abuter, R., Cuadra, J., Alexander, T. and Sternberg, A. (2006), The Two Young Star Disks in the Central Parsec of the Galaxy: Properties, Dynamics, and Formation, *Astrophys. J.*, **643**, pp. 1011–1035, arXiv: `astro-ph/0601268`.

Schödel, R., Eckart, A., Alexander, T., Merritt, D., Genzel, R., Sternberg, A., Meyer, L., Kul, F., Moultaka, J., Ott, T. and Straubmeier, C. (2007), The structure of the nuclear stellar cluster of the Milky Way, *Astronomy and Astrophysics*, **469**, pp. 125–146, arXiv: `astro-ph/0703178`.

Šubr, L. ., Schovancová, J. and Kroupa, P. (2009), The warped young stellar disc in the Galactic centre, *Astronomy and Astrophysics*, **496**, pp. 695–699.

Yelda, S., Ghez, A. M., Lu, J. R., Do, T., Clarkson, W. and Matthews, K. (2011), Increasing the Scientific Return of Stellar Orbits at the Galactic Center, in M. R. Morris, Q. D. Wang and F. Yuan, editors, *The Galactic Center: a Window to the Nuclear Environment of Disk Galaxies*, volume 439 of *Astronomical Society of the Pacific Conference Series*, p. 167, arXiv: `1002.1729`.

Proceedings of *RAGtime 10–13, 15–17/20–22/15–17/14–16 September, 2008/2009/2010/2011, Opava, Czech Republic*
Z. Stuchlík, G. Török and T. Pecháček, editors, Silesian University in Opava, 2014, pp. 53–60

On oscillations in turbulent accretion disks: I. A general approach

Jiří Horák

Astronomical Institute, Academy of Sciences, Boční II 141 31 Prague, Czech Republic

ABSTRACT
In this note, a general theory of a wave propagation in a turbulent media is reviewed. The main attention is paid to the case of the rotating flows with a weak magneto-hydrodynamic turbulence and vanishing mean magnetic flux. We derive the inhomogeneous wave equation and identify the excitation and damping terms. As a consequence of a weak turbulence, these terms can be treated as perturbations and the oscillations of the turbulent media can be decomposed into the normal modes of the laminar mean flow. Using the perturbation techniques we estimate the amplitudes of excited oscillations and show that their frequencies are shifted with respect to the case of the laminar flow.

Keywords: black hole physics – accretion disks – oscillations – turbulence

1 INTRODUCTION

According to a widely accepted scenario, the transport of angular momentum in accretion disks is accomplished by the magneto-hydrodynamic (MHD) turbulence driven by the magneto-rotational instability (MRI). On the other hand, in many studies of the accretion disk oscillations, the effects of turbulence are being neglected. It is not clear whether such idealized hydrodynamic perturbation of laminar background flow would survive also in highly turbulent magnetized media typical for real accretion disks.

Several attempts to resolve this issue using numerical simulations have lead to different conclusions. Brandenburg (2005) explored this problem in local shearing sheet simulations with negative result – his power spectra of time variability did not show any discrete frequencies. On the other hand, Arras et al. (2006) performed similar simulations and found an evidence for excitation of the radial epicyclic mode and various acoustic p-mode oscillations, but they did not find any evidence for inertial waves. Likely, differences between these results can be attributed to different strength of MHD turbulence – the zero net-magnetic-flux simulations by Arras et al. (2006) give rise to the weakest MRI-driven turbulence possible. There are also several global simulations partially devoted to this problem. For example, Kato (2004) studied radial and vertical oscillations in a thin MHD accretion flow. In his work, two pairs of oscillations are present in the region between 3.8 and 6.3 Schwarzschild radii. One of the oscillations could be identified as the radial $m = 1$ epicyclic mode excited in a resonance with the orbital motion. Contrary to this result, there is no evidence for such resonance in another global simulation of Reynolds and Miller (2009), but they agree with Arras et al. (2006) on the absence of inertial modes.

978-80-7510-125-9

Another way how to tackle this problem is to use the semi-analytical methods originally developed for solving similar problems in stars and Sun. The original idea by Lighthill (1952) was first used by Goldreich and Keeley (1977) in calculations of excitation/damping of solar p-modes by turbulent convection and it was later significantly developed by Goldreich and Kumar (1990); Samadi and Goupil (2001) and others (see Houdek, 2006, for a review). In this approach, the key role is plaid by so-called inhomogeneous wave equation (IWE) derived from the set of hydrodynamic equations by keeping also terms that are nonlinear in perturbations. While the homogeneous part that is linear in perturbations describes the oscillations of the laminar mean flow, the effects of the turbulence are included in the extra source terms on the right-hand side of the equation. From the mathematical point of view, IWE is a stochastic partial differential equation that can be translated to a set of stochastic ordinary differential equations if the oscillations can be decomposed into the normal modes.

In this paper we adopt this approach to the case of the differentially rotating unmagnetized flow with weak MHD turbulence. This setup is perhaps suitable for the accretion disks. In Section 2 we obtain IWE from the set of the nonlinear MHD equations. A decomposition into the normal modes is done in Section 3. We also derive the ordinary differential equations describing the instantaneous amplitudes of individual modes. Approximate solutions of these equations is found in Section 4. Finally, Section 5 is devoted to a discussion and conclusions.

2 INHOMOGENEOUS WAVE EQUATION

We generalize the approach of Goldreich and Keeley (1977) by considering MHD turbulence on a stationary (i.e. non-static) unmagnetized background flow. The evolution of the system is described by the continuity equation, induction equation and Euler equation,

$$\frac{\partial \rho}{\partial t} + \nabla_k\left(\rho v^k\right) = 0\,, \tag{1}$$

$$\frac{\partial B^i}{\partial t} + \nabla_k\left(B^i v^k - B^k v^i\right) = 0\,, \tag{2}$$

$$\frac{\partial}{\partial t}\left(\rho v^i\right) + \nabla_k\left(\rho v^i v^k\right) + \rho \nabla^i \Phi + \nabla^i\left(p + \frac{B^2}{8\pi}\right) - \frac{1}{4\pi}\nabla_k\left(B^k B^i\right) = 0\,, \tag{3}$$

together with the barotropic equation of state, $p = p(\rho)$, and the solenoidal condition $\nabla_k B^k = 0$. We assume that there exist a stationary and axisymmetric configuration with vanishing magnetic field, obtained from the above equations by setting $B^i = \partial_t = \partial_\phi = 0$, with a smooth velocity field describing a pure rotation $v^i = \Omega(r, z)\delta^i_\phi$ expressed in the cylindrical coordinates $\{r, \phi, z\}$. The *exact* equations describing perturbations of this equilibria are

$$\frac{\partial \delta\rho}{\partial t} + v^k \nabla_k \delta\rho + \nabla_k\left(\rho \delta v^k\right) = \mathcal{N}_\rho\,, \tag{4}$$

$$\frac{\partial \delta B^i}{\partial t} + v^k \nabla_k \delta B^i - \big(\nabla_k v^i\big)\delta B^k = \mathcal{N}_B^i \,, \tag{5}$$

$$\rho \left[\frac{\partial \delta v^i}{\partial t} + v^k \nabla_k \delta v^i + \big(\nabla_k v^i\big)\delta v^k + \nabla^i \left(c_{\mathrm{s}}^2 \frac{\delta\rho}{\rho} \right) \right] = \mathcal{N}_v^i \tag{6}$$

in which the nonlinear terms in perturbations on the right-hand sides are

$$\mathcal{N}_\rho = -\nabla_k \big(\delta\rho\,\delta v^k\big)\,, \tag{7}$$

$$\mathcal{N}_B^i = -\nabla_k \big(\delta v^k \delta B^i - \delta v^i \delta B^k\big)\,, \tag{8}$$

$$\begin{aligned}\mathcal{N}_v^i = &- \frac{\partial}{\partial t}\big(\delta\rho\,\delta v^i\big) - v^k \nabla_k \big(\delta\rho\,\delta v^i\big) - \big(\nabla_k v^i\big)\big(\delta\rho\,\delta v^k\big) - \nabla_k\big(\rho\,\delta v^i \delta v^k\big) \\ &- \nabla^i \left(\frac{1}{2}\frac{\mathrm{d}^2 p}{\mathrm{d}\rho^2}\delta\rho^2 \right) - \frac{1}{8\pi}\nabla^i \left(\delta B^k \delta B_k\right) - \frac{1}{4\pi}\nabla_k \left(\delta B^i \delta B^k\right) \\ &- \nabla_k \left(\delta\rho\,\delta v^i \delta v^k\right) + \mathcal{O}\big(\delta\rho^3\big)\end{aligned}$$

and $c_{\mathrm{s}} = (\mathrm{d}p/\mathrm{d}\rho)^{1/2}$ denotes the sound speed.

Using the continuity equation to eliminate the density perturbation from the left hand side of the Euler equation, we arrive at a single nonlinear equation governing the velocity perturbation

$$\hat{L}\,\delta\boldsymbol{v} = \boldsymbol{\mathcal{N}}\,. \tag{9}$$

The linear differential operator $\hat{L}$ is defined as

$$\hat{L}\,\delta v^i = \rho \left[\frac{\partial \delta v^i}{\partial t} + v^k \nabla_k \delta v^i + \big(\nabla_k v^i\big)\delta v^k \right] - \rho \nabla^i \left[\frac{c_{\mathrm{s}}^2}{\rho} \partial_\tau^{-1} \nabla_k \big(\rho\,\delta v^k\big) \right] \tag{10}$$

and the nonlinear part is given by

$$\mathcal{N}^i = \mathcal{N}_v^i - \rho \nabla^i \left[\frac{c_{\mathrm{s}}^2}{\rho} \partial_\tau^{-1} \mathcal{N}_\rho \right], \tag{11}$$

where ∂_τ^{-1} is the inverse operator to $\partial_\tau = \partial/\partial t + \Omega\,\partial/\partial\phi$ (note that in the space of the quadratically integrable functions this inversion makes sense).

If the nonlinearities are neglected, (i.e. when $\mathcal{N}^i = 0$), the Eq. (9) describes propagation of the acoustic or inertial waves on the stationary laminar background. If, in addition, a suitable boundary conditions are specified, this equation gives us the set of the normal modes of the system. In the presence of a *weak* turbulence we assume that both, the oscillations and turbulent fluctuations, can be treated as perturbation to the background stationary flow. Hence, we decompose the perturbation of any quantity $q = \{\rho, v^i, B^i\}$ into the part due to the oscillations and the one due to turbulence,

$$\delta q = \delta q_{\mathrm{osc}} + \delta q_{\mathrm{turb}}\,. \tag{12}$$

and assume a regime when

$$|\delta q_{\mathrm{osc}}| \ll |\delta q_{\mathrm{turb}}| \ll |q|\,. \tag{13}$$

Therefore, we safely neglect any influence of the oscillations on the turbulence, but we suppose that properties of both, the background flow and the turbulence, affect the oscillations.

If we now introduce the Lagrangian displacement ξ^i corresponding to the oscillations using the relations,

$$\delta v^i_{\rm osc} = \frac{\partial \xi^i}{\partial t} + v^k \nabla_k \xi^i - \xi^j \nabla_j v^i \,, \quad \delta\rho_{\rm osc} = -\nabla_k\big(\rho\xi^k\big)\,, \tag{14}$$

and substitute into the Eq. (9) keeping only terms linear in ξ^i, we arrive at the master equation

$$\left(\hat{\mathcal{L}}^i_j + \hat{\mathcal{D}}^i_j\right)\xi^j = \mathcal{S}^i \,. \tag{15}$$

The operator $\hat{\mathcal{L}}$ is defined by

$$\hat{\mathcal{L}}^i_j = \delta^i_j \left(\frac{\partial}{\partial t} + v^k \nabla_k\right)^2 - \frac{1}{\rho}\Big[(\gamma - 1)\nabla^i(p\nabla_j) + \nabla_j\big(p\nabla^i\big)\Big] + \nabla^i\nabla_j \Phi \,. \tag{16}$$

and is deterministic being given solely by the background flow quantities. On the other hand, $\hat{\mathcal{D}}^i_j$ and $\mathcal{S}^i$ are stochastic because they rely on both the background flow and the turbulent field. The operator $\hat{\mathcal{D}}^i_j$ is a contribution of nonlinearity $\mathcal{N}^i$; the part which is linear in $\delta v_{\rm osc}$ and $\delta\rho_{\rm osc}$, and therefore in ξ^i as well. It modify the operator $\hat{\mathcal{L}}^i_j$ and therefore slightly change the eigenfunctions and eigenfrequencies of the oscillation modes. The term $\mathcal{S}^i$ on the right-hand side depends only on the turbulent fluctuations and play the role of the stochastic source term. We do not show complicated expressions of these operator as the they are not needed in the rest of the paper. For a general discussion presented here their stochastic nature and the structure of Eq. (15) are sufficient.

3 DECOMPOSITION INTO NORMAL MODES

In absence of the turbulence, both $\hat{\mathcal{L}}$ and $\boldsymbol{\mathcal{S}}$ vanish and the Eq. (15) takes the form

$$\hat{\mathcal{L}}\boldsymbol{\xi} = \partial_t^2 \boldsymbol{\xi} + \hat{B}\,\partial_t \boldsymbol{\xi} + \hat{C}\boldsymbol{\xi} = 0\,, \tag{17}$$

where $\hat{B}$ and $\hat{C}$ are two linear differential operators. With appropriate boundary conditions, this equation describes linear modes of the system. Glampedakis and Andersson (2007) show that in absence of electromagnetic radiation on the surface of the body, the operator $\hat{C}$ is Hermitian and $\hat{B}$ is anti-Hermitian with respect to the standard scalar product weighted by mass density,

$$\langle \boldsymbol{\zeta}, \boldsymbol{\eta}\rangle = \int_V (\boldsymbol{\zeta}^* \cdot \boldsymbol{\eta})\,\rho\,\mathrm{d}V \,. \tag{18}$$

Assuming a harmonic time dependence for the perturbation, i.e. $\boldsymbol{\xi} = \boldsymbol{\zeta}(\boldsymbol{x})\exp[-\mathrm{i}wt]$, we obtain a set of linear modes $\{\omega_\alpha, \boldsymbol{\zeta}_\alpha\}$, each of them characterized by its eigenfrequency ω_α and eigenfunction $\boldsymbol{\zeta}_\alpha$. As shown by Schenk et al. (2002), the eigenfunctions (completed by the associated functions in the case of Jordan-chain modes) can be used as a basis of the corresponding phase space $\mathcal{H} \oplus \mathcal{H}$. The solution of the general equation

$$\hat{\mathcal{L}}\boldsymbol{\xi} = \boldsymbol{\mathcal{F}}(t, \boldsymbol{x}) \tag{19}$$

can be expressed as a linear combination of modal eigenfunctions

$$\begin{pmatrix} \boldsymbol{\xi} \\ \partial_t \boldsymbol{\xi} \end{pmatrix} = \sum_\alpha c_\alpha(t) \begin{pmatrix} \boldsymbol{\zeta}_\alpha \\ -\mathrm{i}\omega_\alpha \boldsymbol{\zeta}_\alpha \end{pmatrix}, \tag{20}$$

in which the coefficients $c_\alpha(t)$ satisfy the equations of forced oscillators

$$\frac{\mathrm{d}c_\alpha}{\mathrm{d}t} + \mathrm{i}\omega_\alpha c_\alpha = -\frac{\mathrm{i}}{b_\alpha}\left\langle \boldsymbol{\zeta}_\alpha, \boldsymbol{\mathcal{F}} \right\rangle \tag{21}$$

and $b_\alpha = \langle \boldsymbol{\zeta}_\alpha, \mathrm{i}\hat{B}\boldsymbol{\zeta}_\alpha \rangle + 2\omega_\alpha \langle \boldsymbol{\zeta}_\alpha, \boldsymbol{\zeta}_\alpha \rangle$.

Equation (15) represents a special case for which $\boldsymbol{\mathcal{F}} = -\hat{\mathcal{D}}\boldsymbol{\xi} + \boldsymbol{\mathcal{S}}$. With the aid of expansion (20), the Eq. (21) becomes

$$\frac{\mathrm{d}c_\alpha}{\mathrm{d}t} + \mathrm{i}\sum_\beta \left(\omega_\alpha \delta_{\alpha\beta} - \epsilon \mathcal{D}_{\alpha\beta} \right) c_\beta = \epsilon \mathcal{S}_\alpha \,, \tag{22}$$

where

$$\epsilon \mathcal{D}_{\alpha\beta} = \frac{1}{b_\alpha}\left\langle \boldsymbol{\zeta}_\alpha, \hat{\mathcal{D}}\boldsymbol{\zeta}_\beta \right\rangle, \quad \epsilon \mathcal{S}_\alpha = \frac{1}{b_\alpha}\left\langle \boldsymbol{\zeta}_\alpha, \boldsymbol{\mathcal{S}} \right\rangle . \tag{23}$$

For subsonic turbulence, these terms are small and can be treated as perturbations. That is why we formally introduced a small parameter $\epsilon \ll 1$ to the Eq. (22).

4 COHERENT AND RANDOM OSCILLATIONS

The stochastic functions $\mathcal{D}_{\alpha\beta}(t)$ and $S_\alpha(t)$ can be separated to the mean and fluctuating random components,

$$\mathcal{D}_{\alpha\beta}(t) = \bar{D}_{\alpha\beta} + D'_{\alpha\beta}(t) \,, \quad \mathcal{S}_\alpha(t) = \bar{S}_\alpha + S'_\alpha(t) \,. \tag{24}$$

The mean values and all statistical moments of the random components are assumed to be time-independent as a consequence of a stationary turbulence. Similarly, we suppose that also the resulting oscillations can be separated to coherent and random components as $c_\alpha(t) = \bar{c}_\alpha(t) + c'_\alpha(t)$. Ansamble average of Eq. (22) gives

$$\frac{\mathrm{d}\bar{c}_\alpha}{\mathrm{d}t} + \mathrm{i}\omega_\alpha \bar{c}_\alpha - \mathrm{i}\epsilon \sum_\beta \left[\bar{\mathcal{D}}_{\alpha\beta}\bar{c}_\beta + \left\langle \mathcal{D}'_{\alpha\beta} c'_\beta \right\rangle \right] = \epsilon \bar{S}_\alpha \,. \tag{25}$$

Subtracting it from the original Eq. (22) we obtain the equation governing the random component

$$\frac{\mathrm{d}c'_\alpha}{\mathrm{d}t} + \mathrm{i}w_\alpha c'_\alpha - \mathrm{i}\epsilon \sum_\beta \left[\bar{\mathcal{D}}_{\alpha\beta} c'_\beta + \mathcal{D}'_{\alpha\beta}\bar{c}_\beta + \mathcal{D}'_{\alpha\beta} c'_\beta - \left\langle \mathcal{D}'_{\alpha\beta} c'_\beta \right\rangle \right] = \epsilon \mathcal{S}'_\alpha \,. \tag{26}$$

We solve these equations using method of multiple time-scales. Instead of the physical time t, we introduce variables $T_n = \epsilon^n t$ with $n = 0, 1, 2, \ldots$ The time derivative is then replaced by the series

$$\frac{\mathrm{d}}{\mathrm{d}t} = \partial_0 + \epsilon\partial_1 + \epsilon^2\partial_2 + \ldots\,, \quad \partial_n = \frac{\partial}{\partial T_n} \tag{27}$$

and the solutions are looked for in the form

$$\bar{c}_\alpha(T_n) = \bar{c}_\alpha^{(0)}(T_n) + \epsilon\bar{c}_\alpha^{(1)}(T_n) + \epsilon^2\bar{c}_\alpha^{(2)}(T_n) + \ldots\,, \tag{28}$$

$$c'_\alpha(T_n) = c_\alpha^{\prime(0)}(T_n) + \epsilon c_\alpha^{\prime(1)}(T_n) + \epsilon^2 c_\alpha^{\prime(2)}(T_n) + \ldots \tag{29}$$

The zero-order equations,

$$(\partial_0 + \mathrm{i}\omega_\alpha)\,\bar{c}_\alpha^{(0)} = 0\,, \quad (\partial_0 + \mathrm{i}\omega_\alpha)\,c_\alpha^{\prime(0)} = 0\,, \tag{30}$$

give solutions

$$\bar{c}_\alpha^{(0)} = A_\alpha(T_1, T_2, \ldots)\,\mathrm{e}^{-\mathrm{i}\omega_\alpha T_0}\,, \quad c_\alpha^{\prime(0)} = 0\,. \tag{31}$$

The fluctuating component vanishes as a consequence of the assumption that $\langle c'_\alpha\rangle = 0$.

The first-order equations read

$$\begin{aligned}(\partial_0 + \mathrm{i}\omega_\alpha)\,\bar{c}_\alpha^{(1)} &= -\,\partial_1\bar{c}_\alpha^{(0)} + \mathrm{i}\sum_\beta \bar{\mathcal{D}}_{\alpha\beta}\bar{c}_\beta^{(0)} + \bar{\mathcal{S}}_\alpha = \\ &\qquad -\,(\partial_1 A_\alpha)\,\mathrm{e}^{-\mathrm{i}\omega_\alpha T_0} + \mathrm{i}\sum_\beta \bar{\mathcal{D}}_{\alpha\beta}A_\beta\mathrm{e}^{-\mathrm{i}\omega_\beta T_0} + \bar{\mathcal{S}}_\alpha\,, \\ (\partial_0 + \mathrm{i}\omega_\alpha)\,c_\alpha^{\prime(1)} &= \mathrm{i}\sum_\beta \mathcal{D}'_{\alpha\beta}\bar{c}_\beta^{(0)} + \mathcal{S}'_\alpha\,.\end{aligned} \tag{32}$$

For simplicity, we suppose that there is no degeneracy (i.e. if $\alpha \neq \beta$ then also $\omega_\alpha \neq \omega_\beta$). The secular terms on the right hand side of Eq. (4) are therefore eliminated when

$$-\partial_1 A_\alpha + \mathrm{i}\bar{\mathcal{D}}_{\alpha\alpha}A_\alpha = 0 \tag{33}$$

the solution of which is

$$A_\alpha(T_1, T_2, \ldots) = A_\alpha(T_2, \ldots)\exp\left[-\mathrm{i}\omega_\alpha^{(1)}T_1\right]\,, \quad \omega_\alpha^{(1)} = -\bar{\mathcal{D}}_{\alpha\alpha}. \tag{34}$$

Hence, $-\epsilon\bar{\mathcal{D}}_{\alpha\alpha}$ is a first-order correction to the eigenfrequency of the coherent oscillations. A particular solution for the coherent part is

$$\bar{c}_\alpha^{(1)} = -\frac{\mathrm{i}}{\omega_\alpha}\bar{\mathcal{S}}_\alpha + \sum_{\beta\neq\alpha}\frac{\bar{\mathcal{D}}_{\alpha\beta}}{\omega_\alpha - \omega_\beta}A_\beta\mathrm{e}^{-\mathrm{i}\omega_\beta T_0} \tag{35}$$

and for the random part

$$c_\alpha^{\prime(1)} = \mathrm{e}^{-\mathrm{i}\omega_\alpha T_0}\left(\sum_\beta I_{\alpha\beta}A_\beta + J_\alpha\right)\,, \tag{36}$$

where

$$I_{\alpha\beta} = \int_{-\infty}^{T_0} \mathcal{D}'_{\alpha\beta}(\tau) \mathrm{e}^{\mathrm{i}(\omega_\alpha - \omega_\beta)\tau}\, \mathrm{d}\tau\,, \quad J_\alpha = \int_{-\infty}^{T_0} \mathcal{S}'_\alpha(\tau) \mathrm{e}^{\mathrm{i}\omega_\alpha \tau}\, \mathrm{d}\tau. \tag{37}$$

A second-order approximation for the coherent part of oscillations is governed by

$$\begin{aligned}(\partial_0 + \mathrm{i}\omega_\alpha)\, \bar{c}^{(2)}_\alpha =& -\partial_2 \bar{c}^{(0)}_\alpha - \partial_1 \bar{c}^{(1)}_\alpha + \mathrm{i}\sum_\beta \left(\bar{\mathcal{D}}_{\alpha\beta} \bar{c}^{(1)}_\beta + \left\langle \mathcal{D}'_{\alpha\beta} c'^{(1)}_\beta \right\rangle \right) = \\ =& -(\partial_2 A_\alpha)\, \mathrm{e}^{-\mathrm{i}\omega_\alpha T_0} - \sum_{\beta\neq\alpha} \frac{\bar{\mathcal{D}}_{\alpha\beta} \bar{\mathcal{D}}_{\beta\beta}}{\omega_\alpha - \omega_\beta} A_\beta \mathrm{e}^{-\mathrm{i}\omega_\beta T_0} \\ &+ \sum_\beta \frac{1}{\omega_\beta} \bar{\mathcal{D}}_{\alpha\beta} \bar{\mathcal{S}}_\beta + \mathrm{i}\sum_\beta \sum_{\gamma\neq\beta} \frac{\bar{\mathcal{D}}_{\alpha\beta}\bar{\mathcal{D}}_{\beta\gamma}}{\omega_\beta - \omega_\gamma} A_\gamma \mathrm{e}^{\mathrm{i}\omega_\gamma T_0} \\ &+ \mathrm{i}\sum_\beta \left[\sum_\gamma \left\langle \mathcal{D}'_{\alpha\beta} I_{\beta\gamma} \right\rangle A_\gamma + \left\langle \mathcal{D}'_{\alpha\beta} J_\beta \right\rangle \right] \mathrm{e}^{-\mathrm{i}\omega_\beta T_0}\,. \end{aligned} \tag{38}$$

Due to the stationarity, the correlators on the right-hand side can be expressed as

$$\left\langle \mathcal{D}'_{\alpha\beta} I_{\beta\gamma} \right\rangle = C_{\alpha\beta\beta\gamma} \exp\left[\mathrm{i}(\omega_\beta - \omega_\gamma) T_0\right]\,, \tag{39}$$

$$\left\langle \mathcal{D}'_{\alpha\beta} J_\beta \right\rangle = C_{\alpha\beta\beta} \exp\left[\mathrm{i}\omega_\beta T_0\right]\,, \tag{40}$$

where

$$C_{\alpha\beta\beta\gamma} = \int_{-\infty}^0 \left\langle \mathcal{D}'_{\alpha\beta}(0) \mathcal{D}'_{\beta\gamma}(\tau) \right\rangle \mathrm{e}^{\mathrm{i}(\omega_\beta - \omega_\gamma)\tau} \mathrm{d}\tau\,, \tag{41}$$

$$C_{\alpha\beta\beta} = \int_{-\infty}^0 \left\langle \mathcal{D}'_{\alpha\beta}(0) \mathcal{S}'_\beta(\tau) \right\rangle \mathrm{e}^{\mathrm{i}\omega_\beta\tau} \mathrm{d}\tau \tag{42}$$

are constants. The secular terms on the right-hand side of Eq. (38) are eliminated when

$$-\partial_2 A_\alpha + \mathrm{i}\sum_{\beta\neq\alpha} \frac{\bar{\mathcal{D}}_{\alpha\beta}\bar{\mathcal{D}}_{\beta\alpha}}{\omega_\beta - \omega_\alpha} A_\alpha + \mathrm{i}\sum_\beta C_{\alpha\beta\beta\alpha} A_\alpha = 0\,, \tag{43}$$

the solution of which is

$$A(T_2) = A \exp\!\left[-\mathrm{i}\omega^{(2)}_\alpha T_2\right], \quad \omega^{(2)}_\alpha = -\sum_{\beta\neq\alpha} \frac{\bar{\mathcal{D}}_{\alpha\beta}\bar{\mathcal{D}}_{\beta\alpha}}{\omega_\beta - \omega_\alpha} - \sum_\beta C_{\alpha\beta\beta\alpha}\,. \tag{44}$$

Therefore the eigenfrequency of the coherent oscillations in the turbulent flow is shifted with respect to the eigenfrequency of the background laminar flow by a correction

$$\Delta\omega_\alpha = -\epsilon \bar{\mathcal{D}}_{\alpha\alpha} - \epsilon^2 \sum_{\beta\neq\alpha} \frac{\bar{\mathcal{D}}_{\alpha\beta}\bar{\mathcal{D}}_{\beta\alpha}}{\omega_\beta - \omega_\alpha} - \epsilon^2 \sum_\beta C_{\alpha\beta\beta\alpha}\,. \tag{45}$$

5 DISCUSSION AND CONCLUSIONS

In this note, effects of turbulence on oscillations of rotating flow have been examined. Starting from the ideal MHD equations, we derived IWE describing excitation and damping of the oscillations. Using decomposition into normal modes we obtained general formulae for amplitudes of random oscillations [equation (36)] and for the frequency shifts of the coherent oscillations [equation (45)]. If they are imaginary, these frequency shifts may describe damping or instabilities induced by the turbulence. Further exploration of this issue needs a specific model of the turbulence and is left for a further work.

ACKNOWLEDGEMENTS

This work was supported by Grant Agency of the Czech Republic (ref. P209/11/2004).

REFERENCES

Arras, P., Blaes, O. and Turner, N. J. (2006), Quasi-periodic Oscillations from Magnetorotational Turbulence, *Astrophys. J. Lett.*, **645**, pp. L65–L68, arXiv: `arXiv:astro-ph/0602275`.

Brandenburg, A. (2005), Turbulence and its parameterization in accretion discs, *Astronomische Nachrichten*, **326**, pp. 787–797, arXiv: `arXiv:astro-ph/0510015`.

Glampedakis, K. and Andersson, N. (2007), Lagrangian perturbation theory for rotating magnetic stars, **377**, pp. 630–644, arXiv: `arXiv:astro-ph/0702382`.

Goldreich, P. and Keeley, D. A. (1977), Solar seismology. II - The stochastic excitation of the solar p-modes by turbulent convection, **212**, pp. 243–251.

Goldreich, P. and Kumar, P. (1990), Wave generation by turbulent convection, **363**, pp. 694–704.

Houdek, G. (2006), Stochastic excitation and damping of solar-type oscillations, *ArXiv Astrophysics e-prints*, arXiv: `arXiv:astro-ph/0612024`.

Kato, Y. (2004), 2:3 Twin Quasi-Periodic Oscillations in Magnetohydrodynamic Accretion Flows, **56**, pp. 931–937, arXiv: `arXiv:astro-ph/0408018`.

Lighthill, M. J. (1952), On Sound Generated Aerodynamically. I. General Theory, *Royal Society of London Proceedings Series A*, **211**, pp. 564–587.

Reynolds, C. S. and Miller, M. C. (2009), The Time Variability of Geometrically Thin Black Hole Accretion Disks. I. The Search for Modes in Simulated Disks, **692**, pp. 869–886, arXiv: `0805.2950`.

Samadi, R. and Goupil, M.-J. (2001), Excitation of stellar p-modes by turbulent convection. I. Theoretical formulation, **370**, pp. 136–146, arXiv: `arXiv:astro-ph/0101109`.

Schenk, A. K., Arras, P., Flanagan, É. É., Teukolsky, S. A. and Wasserman, I. (2002), Nonlinear mode coupling in rotating stars and the r-mode instability in neutron stars, *Phys. Rev. D*, **65**(2), pp. 024001–+, arXiv: `arXiv:gr-qc/0101092`.

Proceedings of *RAGtime 10–13, 15–17/20–22/15–17/14–16 September, 2008/2009/2010/2011, Opava, Czech Republic*
Z. Stuchlík, G. Török and T. Pecháček, editors, Silesian University in Opava, 2014, pp. 61–74

The gyraton solutions on generalized Melvin universe with cosmological constant

Hedvika Kadlecová[a] and Pavel Krtouš[b]

Institute of Theoretical Physics, Faculty of Mathematics and Physics, Charles University, V Holešovičkách 2, 180 00 Prague, Czech Republic.
[a]hedvika.kadlecova@centrum.cz
[b]Pavel.Krtous@utf.mff.cuni.cz

ABSTRACT
We present and analyse new exact gyraton solutions of algebraic type II on generalized Melvin universe of type D which admit non-vanishing cosmological constant Λ. We show that it generalizes both, gyraton solutions on Melvin and on direct product spacetimes. When we set $\Lambda = 0$ we get solutions on Melvin spacetime and for $\Sigma = 1$ we obtain solutions on direct product spacetimes. We demonstrate that the solutions are member of the Kundt family of spacetimes as its subcases. We show that the Einstein equations reduce to a set of equations on the transverse 2-space. We also discuss the polynomial scalar invariants which are non-constant in general but constant for sub-solutions on direct product spacetimes.

Keywords: Gyraton solutions – Melvin universe – cosmological constant – Kundt family – direct product spacetimes – constant polynomial scalar invariants – Einstein equations

1 INTRODUCTION

In Kadlecová et al. (2009) and Kadlecová and Krtouš (2010) we have investigated the gyraton solutions on direct product spacetimes and gyraton solutions on Melvin universe. These solutions are of algebraic type II. In this work we present the gyraton solutions on Melvin universe with the cosmological constant.

We present our ansatz for the gyraton metric on generalized Melvin universe and the generalized electromagnetic tensor. We briefly review the derivation of the Einstein–Maxwell equations. The source-free Einstein equations determine the functions Σ and S, in particular, there exists a relation between them. Next we derive the non-trivial source equations. The Einstein–Maxwell equations do decouple for the gyraton metric on generalized Melvin universe as for its subcase solutions on Melvin and on direct product spacetimes. Next, we focus on interpretation of our solutions. Especially, we discuss the geometry of the transverse metric of the generalized Melvin universe in detail for different values of the cosmological constant. We show explicitly that the Melvin universe and direct product spacetimes are special cases of our solutions. We also discuss the properties of the scalar polynomial invariants which are functions of ρ but for subcase solutions on direct product spacetimes ($\Sigma = 1$) the invariants are constant.

978-80-7510-125-9

2 THE ANSATZ FOR THE GYRATONS ON GENERALIZED MELVIN UNIVERSE

The ansatz for the gyraton metric on the generalized Melvin spacetime is the following,

$$\mathbf{g} = -2\Sigma^2 H\, \mathrm{d}u^2 - \Sigma^2\, \mathrm{d}u \vee \mathrm{d}v + \mathbf{q} + \Sigma^2 \mathrm{d}u \vee \mathbf{a}\,, \tag{1}$$

where we have introduced the 2-dimensional transversal metric $\mathbf{q}$ on transverse spaces $u,\ v = \text{constant}$ as

$$\mathbf{q} = \Sigma^2\, \mathrm{d}\rho^2 + \frac{S(\rho)^2}{\Sigma^2}\, \mathrm{d}\phi^2\,. \tag{2}$$

We have assumed that the metric (1) belongs to the Kundt class of spacetimes and that the transversal metric $\mathbf{q}$ has one Killing vector $\mathcal{L}_{\partial/\partial\phi}\mathbf{q} = 0$. The metric (1) represents gyraton propagating on the background which is formed by generalized Melvin spacetime. The metric (1) generalizes only the transversal metric therefore the algebraical type is II as for the gyraton on the Melvin spacetime Kadlecová and Krtouš (2010), the NP quantities are listed in Kadlecová (2013).

We have generalized the transversal metric for the Melvin universe by assuming general function $S = S(\rho)$ instead of the simple coordinate ρ in front of the term $\mathrm{d}\phi^2$, see Kadlecová and Krtouš (2010). We will show that these general functions $\Sigma(\rho)$ and $S(\rho)$ are determined by the Einstein–Maxwell equations and have proper interpretation. The presence of cosmological constant Λ is not allowed for the solution on pure Melvin background Kadlecová and Krtouš (2010).

The transverse space is covered by two spatial coordinates x^i $(i = \rho, \phi)$ and it is convenient to introduce suitable notation on it, technical details can be found in Kadlecová (2013). The function $H(u, v, \mathbf{x})$ in the metric (1) can depend on all coordinates, but the functions $a(u, \mathbf{x})$ are v-independent.

The derivation of the Einstein–Maxwell equations is almost identical with the previous paper Kadlecová and Krtouš (2010) therefore we will describe the derivation of Einstein–Maxwell equations very briefly.

The metric should satisfy the Einstein equations with cosmological constant Λ and with a stress-energy tensor generated by the electromagnetic field of the background Melvin spacetime $\mathbf{T}^{\mathrm{EM}}$ and the gyratonic source $\mathbf{T}^{\mathrm{gyr}}$ as[1]

$$\mathbf{G} + \Lambda\, \mathbf{g} = \varkappa\big(\mathbf{T}^{\mathrm{EM}} + \mathbf{T}^{\mathrm{gyr}}\big)\,. \tag{3}$$

We assume the electromagnetic field is given by

$$\mathbf{F} = E\, \mathrm{d}v \wedge \mathrm{d}u + \frac{B}{\Sigma^2}\boldsymbol{\epsilon} + \mathrm{d}u \wedge \big(E\, \mathbf{s} - B{*}(\mathbf{s} - \mathbf{a})\big)\,, \tag{4}$$

[1] $\varkappa = 8\pi G$ and ε_0 are gravitational and electromagnetic constants. There are two general choices of geometrical units: the gaussian with $\varkappa = 8\pi$ and $\varepsilon_0 = 1/4\pi$, and SI-like with $\varkappa = \varepsilon_0 = 1$.

where E and B are parameters of electromagnetic field. The self-dual complex form of the Maxwell[2] tensor is

$$\mathcal{F} = \mathcal{B}\left(\mathrm{d}v \wedge \mathrm{d}u - \frac{i}{\Sigma^2}\boldsymbol{\epsilon} + \mathrm{d}u \wedge \left[\mathbf{s} + i{*}(\mathbf{s} - \boldsymbol{a})\right]\right), \tag{5}$$

for details see Kadlecová and Krtouš (2010).

We have denoted the complex constant $\mathcal{B} = E + iB$, and we have introduced a constant ϱ_{EM},

$$\varrho_{\mathrm{EM}} = \frac{\varkappa\varepsilon_{\mathrm{o}}}{2}\left(E^2 + B^2\right). \tag{6}$$

We define the gyratonic matter only on a phenomenological level as

$$\varkappa\, \mathbf{T}^{\mathrm{gyr}} = j_u\, \mathrm{d}u^2 + \mathrm{d}u \vee \mathbf{j}\,, \tag{7}$$

where the source functions $j_u(v, u, \mathbf{x})$ and $j(v, u, \mathbf{x})$. We assume that the gyraton stress-energy tensor is locally conserved,

$$\nabla \cdot \mathbf{T}^{\mathrm{gyr}} = 0\,. \tag{8}$$

To conclude, the fields are characterized by functions Σ, S, H, $\mathbf{a}$, and $\mathbf{s}$ which must be determined by the field equations and the gyraton sources j_u and $\mathbf{j}$ and the constants E and B of the background electromagnetic field are prescribed.

3 THE EINSTEIN–MAXWELL FIELD EQUATIONS

First, we will start to solve the Maxwell equations, it is sufficient to calculate the cyclic Maxwell equation for the self-dual Maxwell tensor (5)

$$0 = \mathrm{d}\mathcal{F} = \mathcal{B}\left\{\partial_v\big(\mathbf{s} + i{*}(\mathbf{s} - \mathbf{a})\big)\, \mathrm{d}v \wedge \mathrm{d}u \wedge \mathrm{d}\mathbf{x} - \left[\mathrm{rot}\,\mathbf{s} + i\,\mathrm{div}(\mathbf{s} - \mathbf{a})\right] \mathrm{d}u \wedge \boldsymbol{\epsilon}\right\}. \tag{9}$$

From the real part we immediately get that the 1-forms $\mathbf{s}$ is v-independent, and rotation free $\mathrm{rot}\,\mathbf{s} = 0$. From imaginary part it follows that the 1-form $\mathbf{a}$ is also independent and it satisfies $\mathrm{div}(\mathbf{s} - \mathbf{a}) = 0$.

3.1 The trivial Einstein–Maxwell equations – determining the function Σ and S

Next we will derive the Einstein–Maxwell equations from the Einstein tensor and the electromagnetic stress-energy tensor, which are listed in Kadlecová (2013).

First we will solve the equations which are source free and we will be able to determine the analytic formula for the functions Σ and S.

---

[2] We will follow the notation of Stephani et al. (2003). Namely, $\mathcal{F} \equiv \mathbf{F} + i{\star}\mathbf{F}$ is complex self-dual Maxwell tensor, where the 4-dimensional Hodge dual is ${\star}F_{\mu\nu} = \varepsilon_{\mu\nu\rho\sigma}F^{\rho\sigma}/2$. The self-dual condition reads ${\star}\mathcal{F} = -i\mathcal{F}$. The orientation of the 4-dimensional Levi–Civita tensor is fixed by the sign of the component $\varepsilon_{vu\rho\phi} = S\Sigma^2$. The energy-momentum tensor of the electromagnetic field is given by $T_{\mu\nu} = \varepsilon_{\mathrm{o}}\mathcal{F}_{\mu}^{\ \rho}\overline{\mathcal{F}}_{\nu\rho}/2$.

The first equation we obtain from the vu-component,

$$-\frac{(\Sigma_{,\rho})^2}{\Sigma^2}+2\frac{\Sigma_{,\rho}}{\Sigma}\frac{S_{,\rho}}{S}-\frac{S_{,\rho\rho}}{S}=\Lambda\Sigma^2+\frac{\varrho_{\mathrm{EM}}}{\Sigma^2}\,, \tag{10}$$

the next two equations we get from the transverse diagonal components $\rho\rho$ and $\phi\phi$,

$$-\frac{(\Sigma_{,\rho})^2}{\Sigma^2}+2\frac{\Sigma_{,\rho}}{\Sigma}\frac{S_{,\rho}}{S}+\partial_v^2H=-\Lambda\Sigma^2+\frac{\varrho_{\mathrm{EM}}}{\Sigma^2}\,, \tag{11}$$

$$-\frac{(\Sigma_{,\rho})^2}{\Sigma^2}+2\frac{\Sigma_{,\rho\rho}}{\Sigma}+\partial_v^2H=-\Lambda\Sigma^2+\frac{\varrho_{\mathrm{EM}}}{\Sigma^2}\,. \tag{12}$$

When we compare the equation (11) and (12) we immediately get the relation between the functions Σ and S, as $\Sigma_{,\rho}S_{,\rho}/S=\Sigma_{,\rho\rho}$, and thus we are able to determine their explicit relation ($\Sigma_{,\rho}\neq 0$) as

$$\Sigma_{,\rho}=\gamma S\,, \tag{13}$$

where γ is an integration constant.

After substituting the relation (13) into Eq. (10) then we get equation

$$-\frac{(\Sigma_{,\rho})^2}{\Sigma^2}+2\frac{\Sigma_{,\rho\rho}}{\Sigma}+\frac{\Sigma_{,\rho\rho\rho}}{\Sigma_{,\rho}}=\Lambda\Sigma^2+\frac{\varrho_{\mathrm{EM}}}{\Sigma^2}\,, \tag{14}$$

which will be useful later.

To determine the function H it is useful to substitute (13) into the Eq. (12) and then multiply it by $\Sigma/2\Sigma_{,\rho}$, we get

$$\frac{1}{2}\big(\partial_v^2H\big)_{,\rho}\frac{\Sigma}{\Sigma_{,\rho}}-2\frac{\Sigma_{,\rho\rho}}{\Sigma}+\frac{\big(\Sigma_{,\rho}\big)^2}{\Sigma^2}+\frac{\Sigma_{,\rho\rho\rho}}{\Sigma_{,\rho}}=-\Lambda\Sigma^2-\frac{\varrho_{\mathrm{EM}}}{\Sigma^2}\,. \tag{15}$$

Now, we add the Eq. (10) to (15) and obtain, $(\partial_v^2H)_{,\rho}\Sigma/2\Sigma_{,\rho}=0$, then for $\Sigma_{,\rho}\neq 0$ we can write that $\partial_v^2H=-\alpha$, where α is a constant.

Thus the metric function H has a structure

$$H=-\frac{1}{2}\alpha v^2+g\,v+h\,, \tag{16}$$

where we have introduced v-independent functions $g(u,\mathbf{x})$ and $h(u,\mathbf{x})$.

In the following we want to determine an analytical expression for Σ, in order to do that we substitute the result (16) into (12),

$$2\frac{\Sigma_{,\rho\rho}}{\Sigma}-\frac{\big(\Sigma_{,\rho}\big)^2}{\Sigma^2}=-\Lambda\Sigma^2+\frac{\varrho_{\mathrm{EM}}}{\Sigma^2}+\alpha\,. \tag{17}$$

When we add the expression (14) to (17), we obtain that

$$\Sigma_{,\rho\rho\rho}=-2\Lambda\Sigma^2\Sigma_{,\rho}+\alpha\Sigma_{,\rho}\,. \tag{18}$$

We can rewrite the previous equation as $\Sigma_{,\rho\rho\rho} = -2\Lambda(\Sigma^3)_{,\rho}/3 + \alpha\Sigma_{,\rho}$ to be able to integrate it again as

$$\Sigma_{,\rho\rho} = -\frac{2}{3}\Lambda\Sigma^3 + \alpha\Sigma + \frac{1}{2}\beta\,, \tag{19}$$

which we can rewrite as

$$\frac{1}{2}\big[(\Sigma_{,\rho})^2\big]_{,\rho} = -\frac{1}{6}\Lambda\big(\Sigma^4\big)_{,\rho} + \alpha\big(\Sigma^2\big)_{,\rho} + \frac{1}{2}\beta\Sigma_{,\rho}\,. \tag{20}$$

After another integration we get the final formula for the derivative of the function Σ,

$$\big(\Sigma_{,\rho}\big)^2 = -\frac{1}{3}\Lambda\Sigma^4 + \alpha\Sigma^2 + \beta\Sigma + c\,, \tag{21}$$

and it can be rewritten using (13) as

$$\gamma S = \left[-\frac{1}{3}\Lambda\Sigma^4 + \alpha\Sigma^2 + \beta\Sigma + c\right]^{1/2}\,, \tag{22}$$

where α, β and c are integration constants which should be determined.

Furthermore, we are able to determine the constant c explicitly. When we substitute the result (21) and (19) into (17) we immediately obtain that $c = -\varrho_{\mathrm{EM}}$. The constants α and β will be determined in the Section 4.1.

3.2 The Einstein–Maxwell equations for the sources

The remaining nontrivial components of the Einstein equations are those involving the gyraton source (7). To write the source equation we have to evaluate the component G_{uv} using the expressions for derivatives of Σ. Then the component G_{uv} has the explicit form

$$G_{uv} = \Lambda\Sigma^2 + \frac{\varrho_{\mathrm{EM}}}{\Sigma^2}\,. \tag{23}$$

The ui-components give equations related to $\mathbf{j}$,

$$\Sigma^2\,\mathbf{j} = \frac{1}{2}\mathrm{rot}\left(\Sigma^4\,b\right) + \Sigma^2\mathrm{d}g - \alpha\Sigma^2\mathbf{a} + 2\varrho_{\mathrm{EM}}(\mathbf{s}-\mathbf{a})\,, \tag{24}$$

where $b = \mathrm{rot}\ \mathbf{a}$.

It is useful to split the source equation into divergence and rotation parts:

$$\mathrm{div}\left(\Sigma^2\,\mathbf{j}\right) = \mathrm{div}\ \Sigma^2(\mathrm{d}g - \alpha\,\mathbf{a})\,, \tag{25}$$

$$\mathrm{rot}\left(\Sigma^2\mathbf{j}\right) = -\frac{1}{2}\triangle\left(\Sigma^4 b\right) + \mathrm{rot}\left(\Sigma^2\mathrm{d}g\right) - \alpha\mathrm{rot}\left(\Sigma^2\mathbf{a}\right) - 2\varrho_{\mathrm{EM}}\,b\,. \tag{26}$$

These are coupled equations for g and $\mathbf{a}$. We will return to them below.

The condition (8) for the gyraton source gives, that the sources $\mathbf{j}$ must be v-independent and j_u has the structure

$$j_u = v\ \mathrm{div}\big(\Sigma^2\mathbf{j}\big) + \iota\,, \tag{27}$$

where $\iota(u, \mathbf{x})$ is v-independent function, see Kadlecová and Krtouš (2010) Eq. (2.51). The gyraton source (7) is therefore determined by three v-independent functions $\iota(u, \mathbf{x})$ and $j(u, \mathbf{x})$.

The uu-component of the Einstein equation gives

$$j_u = v\Big[\operatorname{div}\big(\Sigma^2 \mathrm{d}g\big) - \alpha \operatorname{div}\big(\Sigma^2 \mathbf{a}\big)\Big] + \Sigma^2\Big(\triangle h - \big(\Sigma^{-2}\big)_{,\rho} h_{,\rho}\Big) \\ + \frac{1}{2}\Sigma^4 b^2 + 2\Sigma^2 \mathbf{a}\cdot \mathrm{d}g + (\partial_u + g)\operatorname{div}\big(\Sigma^2\mathbf{a}\big) - \alpha\Sigma^2\mathbf{a}^2 - 2\varrho_{\mathrm{EM}}\,(\mathbf{s}-\mathbf{a})^2 . \quad (28)$$

Then we can compare the coefficient in front of v with (25) and we get consistent structure with (27). The nontrivial v-independent part of (28) gives the equation for the metric function h,

$$\Sigma^2\Big(\triangle h - \big(\Sigma^{-2}\big)_{,\rho} h_{,\rho}\Big) = \iota - \frac{1}{2}\Sigma^4 b^2 - 2\Sigma^2\mathbf{a}\cdot\mathrm{d}g \\ - (\partial_u + g)\operatorname{div}\big(\Sigma^2\mathbf{a}\big) + \alpha\Sigma^2\mathbf{a}^2 + 2\varrho_{\mathrm{EM}}\,\big(\mathbf{s}-\mathbf{a}\big)^2 . \quad (29)$$

Now, let us return to solution of Eqs. (25) and (26). The first equation simplifies if we use gauge condition

$$\operatorname{div}\big(\Sigma^2\mathbf{a}\big) = 0 . \quad (30)$$

It can be satisfied due to gauge freedom $v \to v - \chi$, $\mathbf{a} \to \mathbf{a} - \mathrm{d}\chi$, cf. the discussion in Kadlecová and Krtouš (2010). Such a condition implies the existence of a potential $\tilde{\lambda}$, as $\Sigma^2\,\mathbf{a} = \operatorname{rot}\tilde{\lambda}$.

The equation (25) now reduces to

$$\operatorname{div}\big(\Sigma^2\mathrm{d}g - \Sigma^2\mathbf{j}\big) = 0 . \quad (31)$$

It guarantees the existence of a scalar ω such that

$$\mathrm{d}g = \mathbf{j} + \Sigma^{-2}\operatorname{rot}\omega . \quad (32)$$

However, we have to enforce the integrability conditions

$$\operatorname{rot}\,\mathrm{d}g = 0 , \quad (33)$$

which turns out to be the equation for ω:

$$\operatorname{div}\big(\Sigma^{-2}\mathrm{d}\omega\big) = \operatorname{rot}\mathbf{j} . \quad (34)$$

We thus obtained the decoupled Eqs. (32) and (34) which determine the metric function g.

Substituting $\Sigma^2\mathbf{a} = \operatorname{rot}\tilde{\lambda}$ and (32) to (26), and using identity $b = \operatorname{rot}\big(\Sigma^{-2}\operatorname{rot}\tilde{\lambda}\big)$, we get the decoupled equation for $\tilde{\lambda}$:

$$\frac{1}{2}\triangle\Big(\Sigma^4\operatorname{rot}\big(\Sigma^{-2}\operatorname{rot}\tilde{\lambda}\big)\Big) + 2\varrho_{\mathrm{EM}}\operatorname{rot}\big(\Sigma^{-2}\operatorname{rot}\tilde{\lambda}\big) - \alpha\triangle\tilde{\lambda} = -\triangle\omega . \quad (35)$$

It is a complicated equation of the forth order. It can be simplified to an ordinary differential equation if we assume the additional symmetry properties of the fields, e.g. the rotational symmetry around the axis. The potential $\tilde{\lambda}$ then determines the metric 1-form $\mathbf{a}$ through $\Sigma^2\mathbf{a} = \mathrm{rot}\,\tilde{\lambda}$.

After finding $\mathbf{a}$ one can solve the field equations for $\mathbf{s}$. The potential equations give immediately that

$$\mathbf{s} = \mathrm{d}\varphi\,. \tag{36}$$

Substituting to the condition $\mathrm{div}(\mathbf{s} - \mathbf{a}) = 0$ we get the Poisson equation for φ:

$$\triangle\,\varphi = \mathrm{div}\,\mathbf{a}\,. \tag{37}$$

Finally, the remaining metric function h is determined by the Eq. (29).

4 THE INTERPRETATION OF THE SOLUTIONS

4.1 The geometries of the transversal spacetime

In this section we will investigate the geometry of the transversal metric $\mathbf{q}$ (the wave fronts) (2) and we will determine the constants α, β in the final Eq. (21). Subsequently, we will discuss the various geometries of $\mathbf{q}$ in proper parametrization and we will determine the meaning of the parameter γ.

We impose conditions to the derivatives of Σ (i.e. S) (21), (19) and (18) while using the relation (13) between $\Sigma_{,\rho}$ and S to determine α and β.

First, we impose conditions at the axis $\rho = 0$. We assume that S and $\Sigma_{,\rho}$ vanish at the axis $\rho = 0$, $S = 0$, $\Sigma_{,\rho} = 0$, second, we can always rescale the metric (2) to get $\Sigma|_{\rho=0} = 1$, third, we want no conical singularities there, therefore we assume $\Sigma_{,\rho\rho}|_{\rho=0} = \gamma$, which we can be justified by computation of the ratio of the circumference o divided by 2π times radius in limit $\rho \to 0$,

$$\frac{o}{2\pi r} = \frac{2\pi\,\frac{S}{\Sigma}}{2\pi\int\Sigma\,\mathrm{d}\rho} = \frac{1}{\Sigma}\left(\frac{S}{\Sigma}\right)_{,\rho} = \frac{1}{\gamma}\,\frac{\Sigma_{,\rho\rho}\Sigma - \left(\Sigma_{,\rho}\right)^2}{\Sigma^3} = 1\,. \tag{38}$$

Applying the conditions from last paragraph, we obtain

$$-\frac{1}{3}\Lambda + \alpha + \beta - \varrho_{\mathrm{EM}} = 0\,, \quad -\frac{2}{3}\Lambda + \alpha + \frac{1}{2}\beta = \gamma\,. \tag{39}$$

We can then determine the constants α and β explicitly in terms of the cosmological constant Λ, the density of electromagnetic field ϱ_{EM} and the parameter γ,

$$\alpha = \Lambda - \varrho_{\mathrm{EM}} + 2\gamma\,, \quad \beta = -\frac{2}{3}\Lambda + 2\varrho_{\mathrm{EM}} - 2\gamma\,. \tag{40}$$

We can conveniently rewrite (13),

$$\left(\gamma S\right)^2 = \left(\Sigma_{,\rho}\right)^2 = \left[-\frac{1}{3}\frac{\Lambda}{\gamma^2}\left(\Sigma^2 - 2\right)\Sigma - \frac{\varrho_{\mathrm{EM}}}{\gamma^2}(\Sigma - 1) + \frac{2}{\gamma}\Sigma\right](\Sigma - 1)\,. \tag{41}$$

Now we know explicitly the constants in the derivative of Σ and we can investigate the interpretation of the generalized Melvin spacetime. It is convenient to introduce new coordinate x as

$$\Sigma = 1 + \gamma x\,, \tag{42}$$

then we can write that

$$S = x_{,\rho}\,, \quad \Sigma_{,\rho} = \gamma x_{,\rho}\,. \tag{43}$$

The transversal metric $\mathbf{q}$ (2) then can be rewritten as

$$\mathbf{q} = \left(\frac{\Sigma}{S}\right)^2 \mathrm{d}x^2 + \left(\frac{S}{\Sigma}\right)^2 \mathrm{d}\phi^2 = \frac{1}{G}\,\mathrm{d}x^2 + G\mathrm{d}\phi^2\,, \tag{44}$$

where we can express the new function G as

$$G = \left(\frac{S}{\Sigma}\right)^2 = -\frac{1}{3}\frac{\Lambda}{\gamma^2}\Sigma^2 + \frac{\alpha}{\gamma^2} + \frac{\beta}{\gamma^2}\frac{1}{\Sigma} - \frac{\varrho_{\mathrm{EM}}}{\gamma^2}\frac{1}{\Sigma^2}\,, \tag{45}$$

and

$$S^2 = \mp\ell^2\gamma^2x^4 \mp \ell^2\gamma x^3 + \big(\mp 3\ell^2 - \varrho_{\mathrm{EM}} + 2\gamma\big)x^2 + 2x, \tag{46}$$

where we denoted $\mp\ell^2 = \Lambda/3$ where $\pm = \operatorname{sign}\Lambda$.

Before we will discuss the possible geometries given by the transversal metric $\mathbf{q}$ (2) and interpret them accordingly we introduce important characteristics for the generalized Melvin spacetime.

The radial radius is then defined as

$$r = \int_0^x \frac{1}{\sqrt{G}}\,\mathrm{d}x\,, \tag{47}$$

the circumference radius is simply given by the function G, $R = \sqrt{G}$. Interestingly, the ratio of the radia is then determined by the derivative of G,

$$\frac{\mathrm{d}R}{\mathrm{d}r} = \sqrt{G}\,\frac{\mathrm{d}\sqrt{G}}{\mathrm{d}x} = \frac{1}{2}G_{,x}\,. \tag{48}$$

The scalar curvature of $\mathbf{q}$ can be also written as

$$\mathcal{R} = -G_{,xx} = -\frac{2}{\Sigma^4}\left[3\Sigma_{,\rho} + \frac{2}{3}\Lambda\Sigma^4 - 3\alpha\Sigma^2 - 2\beta\Sigma\right]. \tag{49}$$

The geometries of the transversal spacetime $\mathbf{q}$ can be illustrated by investigating the function G and its roots when we consider different values of Λ, ϱ_{EM} and of the parameter γ.

First, we consider positive cosmological constant $\Lambda > 0$ for any ϱ_{EM} and γ we obtain *closed space* where $\rho \in (0, \rho_*)$ and ρ_* represents the first positive root of G where in fact the spacetime closes itself. The other characteristics are: the radial radius tends to a finite

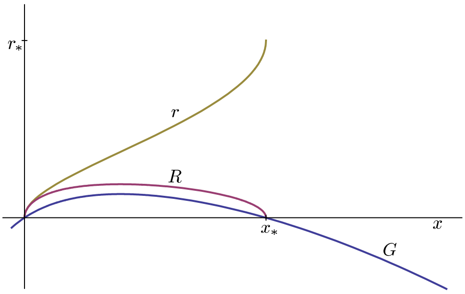

Figure 1. The case when $\Lambda > 0$ which represents closed spacetime. The function G is visualized for any value of ϱ_{EM} and γ. The coordinate ρ ranges $\rho \in (0, \rho_*)$ where the ρ_* is the first root of G where the spacetime closes.

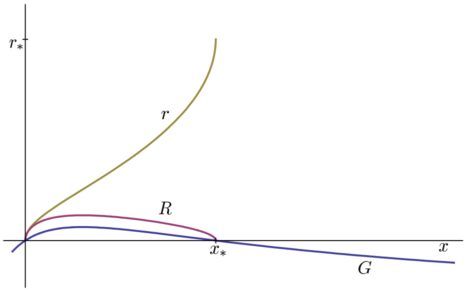

Figure 2. The case when $\Lambda = 0$ and $\varrho_{\mathrm{EM}} > 2\gamma$ represents the closed spacetime. The function G is visualized for $\varrho_{\mathrm{EM}} > 2\gamma$ and the coordinate ρ ranges $\rho \in (0, \rho_*)$ where the ρ_* is the root of G where the spacetime closes.

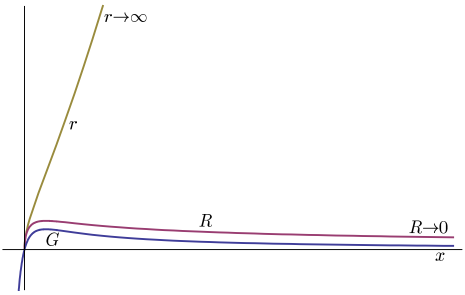

Figure 3. The case when $\Lambda = 0$ and $\varrho_{\mathrm{EM}} = 2\gamma$ then represents the closed spacetime with an infinite peak. The function G is visualized for $\varrho_{\mathrm{EM}} = 2\gamma$ and the coordinate ρ ranges $\rho \to \infty$.

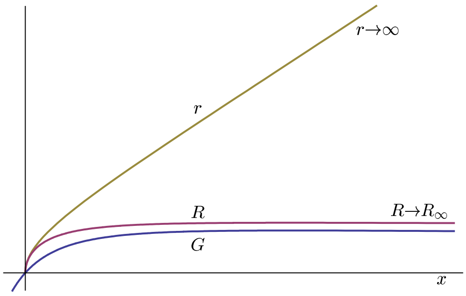

Figure 4. The case when $\Lambda = 0$ and $\varrho_{\mathrm{EM}} < 2\gamma$ then represents the open spacetime. The function G is visualized for $\varrho_{\mathrm{EM}} < 2\gamma$ and the coordinate ρ ranges $\rho \to \infty$.

value $r \to r_*$ at the ρ_* and the circumference radius vanishes $R \to 0$ when $\rho \to \rho_*$. This special case is visualized in the Fig. 1.

For the vanishing cosmological constant $\Lambda = 0$ we obtain three possible spacetimes according to the values of ϱ_{EM} and γ.

When $\varrho_{\mathrm{EM}} > 2\gamma$ then we get *closed space* where the range of the coordinate ρ goes again as $\rho \in (0, \rho_*)$ and ρ_* is then the root of G and it is the closing point of the universe. The radia are then $r \to r_*$ and $R \to 0$ when $\rho \to \rho_*$, see the Fig. 2.

When $\varrho_{\mathrm{EM}} = 2\gamma$ then we obtain *closed space with and infinite peak* for $\rho \to \infty$. Therefore, when $\rho \to \infty$ the radial radius tends to infinity $r \to \infty$ and the circumference radius goes to zero $R \to 0$, see the Fig. 3. This case represents the pure Melvin spacetime Bonnor (1954); Melvin (1965) which we discussed in Kadlecová and Krtouš (2010).

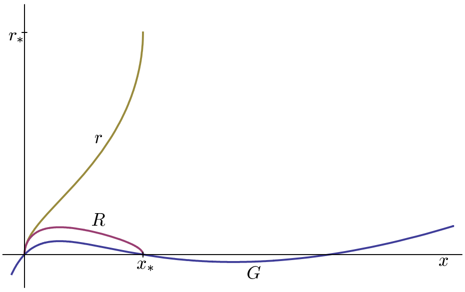

Figure 5. The case when $\Lambda < 0$ and $\gamma < \gamma_{cr}$ represents the closed spacetime. The coordinate ρ ranges $\rho \in (0, \rho_*)$ where the ρ_* is the root of G where the spacetime closes.

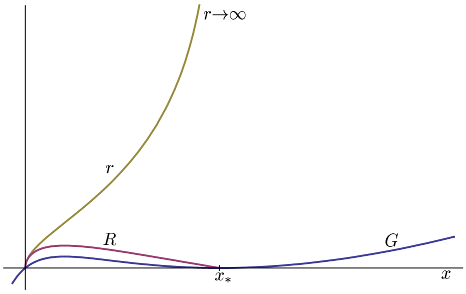

Figure 6. The case when $\Lambda < 0$ and $\gamma = \gamma_{cr}$ represents the asymptotically closed spacetime. The coordinate ρ ranges $\rho \in (0, \rho_*)$ where the ρ_* is the root of G. The radial distance tends to infinity and the circumference shrinks to zero.

Table 1. Possible geometries of the transversal spacetime **q**. Here Λ is a cosmological constant, ϱ_{EM} is energy density of the electromagnetic field and γ is the parameter of 'Melviniztion' of the spacetime. Critical value $\gamma_{cr}(\Lambda, \varrho_{\text{EM}})$ is determined by the condition that the function G has degenerated root at ρ_*.

Λ	$\varrho_{\text{EM}},\gamma$	transversal spacetime	ρ	$r\vert_{\rho\to\rho_*}$	$R\vert_{\rho\to\rho_*}$
$\Lambda > 0$	any	closed space	$(0, \rho_*)$	r_*	0
$\Lambda = 0$	$\gamma < \varrho_{\text{EM}}/2$	closed space	$(0, \rho_*)$	r_*	0
	$\gamma = \varrho_{\text{EM}}/2$	Melvin universe	$\mathbb{R}^+$	∞	0
	$\gamma > \varrho_{\text{EM}}/2$	open space	$\mathbb{R}^+$	∞	R_∞
$\Lambda < 0$	$\gamma < \gamma_{cr}$	closed space	$(0, \rho_*)$	r_*	0
	$\gamma = \gamma_{cr}$	closed with ∞ peak	$(0, \rho_*)$	∞	0
	$\gamma > \gamma_{cr}$	open space	$\mathbb{R}^+$	∞	∞

When $\varrho_{\text{EM}} < 2\gamma$ then we obtain *an open space* for $\rho \in (0, \infty)$. When $\rho \to \infty$, the radial radius tends to infinity $r \to \infty$; however, the circumference radius goes to a finite value, $R \to R_\infty$, see the Fig. 4.

When we consider the negative cosmological constant $\Lambda < 0$ we obtain three possible spacetimes according to the values of γ. For γ smaller than certain critical value γ_{cr} (which depends on Λ and ϱ_{EM}), we get *closed space* where the range of the coordinate ρ goes again as $\rho \in (0, \rho_*)$ and ρ_* is then the root of G and the closing point of the universe. The radia are then $r \to r_*$ and $R \to 0$ when $\rho \to \rho_*$, see the Fig. 5.

When $\gamma = \gamma_{cr}$, we obtain *closed space with and infinite peak* where the range of the coordinate ρ goes as $\rho \in (0, \rho_*)$ and ρ_* is the root of G. The radia are then $r \to \infty$ and $R \to 0$ when $\rho \to \rho_*$, see the Fig. 6.

When $\gamma > \gamma_{cr}$, we obtain *open space* for $\rho \in (0, \infty)$. For $\rho \to \infty$, $r \to \infty$, and $R \to R_\infty$, see the Fig. 7.

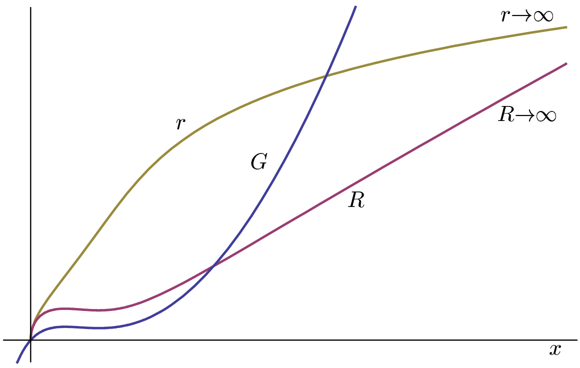

Figure 7. The case when $\Lambda < 0$ and $\gamma > \gamma_{cr}$ represents the open spacetime. The coordinate ρ takes positive real values. For $\rho \to \infty$, $r \to \infty$, and $R \to R_\infty$, see the Fig. 7.

We have summarized our resulting geometries arising from the generalized Melvin universe in a Table 1.

To conclude this section, we have investigated the transversal spacetime of the generalized Melvin universe. We have identified the constants α and β, interpreted them in terms of the cosmological constant Λ, ϱ_{EM} and γ. After suitable parametrization of the transversal spacetime we have discussed all possible cases of universes which are contained in the generalized Melvin universe. The Melvin universe occurs as a special case. We have visualized these cases in figures and summarized them in the Table 1.

The parameter γ changes the character of the influence of the electromagnetic field on the geometry. With larger γ the influence is stronger and for $\Lambda \leq 0$ it can even change the global structure of the spacetime, what exactly happens for the critical value γ_{cr} (for $\Lambda = 0$ $\gamma_{cr} = \varrho_{\mathrm{EM}}/2$).

4.2 The backgrounds for our solutions

The background spacetimes are defined as a limit when $h = g = 0$ and $\mathbf{a} = 0$, then the metric (1) reduces to

$$\mathbf{g} = \mathbf{q} - \Sigma^2\, \mathrm{d}u \vee \mathrm{d}v + \alpha v^2 \Sigma^2 \mathrm{d}u^2 \,. \tag{50}$$

The metric (50) admits one killing vector ∂_ϕ which corresponds to cylindrical symmetry.

Using the adapted null tetrad $\mathbf{k} = \partial_v$, $\mathbf{l} = \Sigma^{-2}(\partial_u + \alpha v^2 \partial_v/2)$, $\mathbf{m} = (\Sigma^{-1}\partial_\rho - i\,\Sigma S^{-1}\partial_\phi)/\sqrt{2}$, the only non-vanishing components of Weyl and Ricci tensors are,

$$\Psi_2 = \frac{1}{2\Sigma^4}\left(\beta\Sigma - 2\varrho_{\mathrm{EM}}\right) \,, \qquad \Phi_{11} = \frac{1}{2\Sigma^4}\varrho_{\mathrm{EM}} \,. \tag{51}$$

This demonstrates that the generalized Melvin universe is a non-vacuum solution of type D, except the points where $\Psi_2 = 0$.

Table 2. Some of possible background spacetimes in the case $\gamma = 0$ which represents the direct product of two 2-spaces of constant curvature. The parameter $\Lambda_+ = \Lambda + \varrho_{\mathrm{EM}}$ gives the geometry of the wave front and $\Lambda_- = \Lambda - \varrho_{\mathrm{EM}}$ determines the conformal structure of the background.

Λ_+	Λ_-	geometry	background	Λ	ϱ_{EM}
0	0	$E^2 \times M_2$	Minkowski	$= 0$	$= 0$
Λ	Λ	$S^2 \times dS_2$	Nariai	> 0	$= 0$
Λ	Λ	$H^2 \times AdS_2$	anti-Nariai	< 0	$= 0$
ϱ_{EM}	$-\varrho_{\mathrm{EM}}$	$S^2 \times AdS_2$	Bertotti–Robinson	$= 0$	> 0
2Λ	0	$S^2 \times M_2$	Plebański–Hacyan	> 0	$= \Lambda$
0	2Λ	$E^2 \times AdS_2$	Plebański–Hacyan	< 0	$= \lvert\Lambda\rvert$

The background metric (50) contains several sub-solutions. For $\Lambda = 0$ and $\varrho_{\mathrm{EM}} = 2\gamma$ we obtain the Melvin universe which serves as a background in Kadlecová and Krtouš (2010) and the the only non-vanishing Weyl and curvature scalars are

$$\Phi_2 = -\frac{\varrho_{\mathrm{EM}}}{2\Sigma^4}(2-\Sigma) = \frac{1}{2}\frac{\varrho_{\mathrm{EM}}}{\Sigma^4}\left(-1 + \frac{1}{4}\varrho_{\mathrm{EM}}\rho^2\right), \quad \Psi_{11} = \frac{1}{2\Sigma^4}\varrho_{\mathrm{EM}}\,, \tag{52}$$

where we have used the $\Sigma = 1 + \varrho_{\mathrm{EM}}\rho^2/4$ which specifies the Melvin spacetime. The scalar curvature of the transversal spacetime $\mathbf{q}$ (49) then becomes

$$\mathcal{R} = 0\,, \tag{53}$$

which agrees with Kadlecová and Krtouš (2010).

For $\Sigma = 1$ we get the direct product background spacetimes, the metric (50) reduces to

$$\mathbf{g} = \mathbf{q} - \mathrm{d}u \vee \mathrm{d}v + \alpha v^2\, \mathrm{d}u^2\,, \tag{54}$$

the only non-vanishing Weyl and curvature scalars then are

$$\Psi_2 = \tfrac{1}{2}\,(\beta - 2\varrho_{\mathrm{EM}}) = -\tfrac{\Lambda}{3}\,, \quad \Phi_{11} = \tfrac{1}{2}\varrho_{\mathrm{EM}}\,. \tag{55}$$

The scalar curvature of the transversal spacetime $\mathbf{q}$ (49) then becomes

$$\mathcal{R} = 2(\Lambda + \varrho_{\mathrm{EM}})\,, \tag{56}$$

which agrees with Kadlecová et al. (2009).

To summarize the background metric (50) generalizes the metric for the pure Melvin universe and the direct product spacetimes into one background metric and combines their properties.

5 THE SCALAR POLYNOMIAL INVARIANTS

The scalar invariants are important characteristics of gyraton spacetimes. The gyratons in the Minkowski spacetime Frolov et al. (2005) have vanishing invariants (VSI) Pravda et al. (2002), the gyratons in the AdS Frolov and Zelnikov (2005) and direct product spacetimes

Kadlecová et al. (2009) have all invariants constant (CSI) Coley et al. (2006). The invariants are independent of all metric functions a_i which characterize the gyraton, and have the same values as the corresponding invariants of the background spacetime. We have shown that similar property is valid also for the gyraton on Melvin spacetime Kadlecová and Krtouš (2010), but the invariants are functions of the coordinate ρ and depend on the constant density ϱ_{EM}.

In these cases, the invariants are independent of all metric functions which characterize the gyraton, and have the same values as the corresponding invariants of the background spacetime. We observed that similar property is valid also for the gyraton on Melvin spacetime and it is valid also for its generalization with Λ, however, in this case the invariants are generally *non-constant*, namely, they depend on the coordinate ρ. This property is a consequence of general theorem holding for the relevant subclass of Kundt solution, see Theorem II.7 in Coley et al. (2010). For more details, see Kadlecová (2013).

6 CONCLUSION

Our work generalizes the studies of the gyraton on the Melvin universe Kadlecová and Krtouš (2010). Namely we have generalized the transversal background metric for the pure Melvin universe where instead of the coordinate ρ we have assumed general function S dependent only on the coordinate ρ. This change enabled us to find new solutions with possible non-zero cosmological constant. This is not allowed for the pure Melvin background spacetime. We were able to derive relation between metric functions Σ and S from the source free Einstein–Maxwell equations. The derivative of the function $\Sigma_{,\rho}$ is then polynomial in the function Σ itself and contains four parameters. We have showed that these parameters can be expressed using constants Λ, ϱ_{EM} and γ.

The Einstein–Maxwell equations reduce again to the set of linear equations on the 2-dimensional transverse spacetime which has non-trivial geometry given by the generalized Melvin spacetime (2). Fortunately, these equations do decouple and they can be solved least in principle for any distribution of the matter sources.

In detail, we have studied the transversal geometries of generalized Melvin spacetime (2). We have discussed the various possible values of constants Λ, ϱ_{EM} and γ. It occurs that for $\Lambda > 0$ the transversal geometry represents only one type of space, the case $\Lambda = 0$ includes three different spaces, one of them corresponds to the Melvin spacetime as a special case. The case $\Lambda < 0$ also describes three types of spaces. We have visualized them in several figures in Section 4 and summarized them in the Table 1. Thanks to this discussion we were able to interpret the parameter γ as the parameter which makes the electromagnetic field of the direct product spacetimes stronger.

We have investigated the polynomial scalar invariants. In this generalized case, the invariants are again not constant and they are functions of the metric function Σ and the full gyratonic metric has the same invariants as the background metric.

ACKNOWLEDGEMENTS

The present work was supported by the grant GAUK 12209 by the Czech Ministry of Education, the project SVV 261301 of the Charles University in Prague and the LC06014 project of the Center of Theoretical Astrophysics.

REFERENCES

Bonnor, W. B. (1954), The Equations of Motion in the Non-Symmetric Unified Field Theory, *Proc. Roy. Soc. London A*, **67**(225).

Coley, A. A., Hervik, S. and Pelavas, N. (2006), On spacetimes with constant scalar invariants, *Class. Quant. Gravity*, **23**, pp. 3053–3074.

Coley, A. A., Hervik, S. and Pelavas, N. (2010), Lorentzian manifolds and scalar curvature invariants, *Class. Quant. Gravity*.

Frolov, V. P., Israel, W. and Zelnikov, A. (2005), Gravitational field of relativistic gyratons, *Phys. Rev. D*, **72**, p. 084031.

Frolov, V. P. and Zelnikov, A. (2005), Relativistic gyratons in asymptotically AdS spacetime, *Phys. Rev. D*, **72**, p. 104005.

Kadlecová, H. (2013), *Gravitational field of gyratons on various background spacetimes*, Ph.D. thesis, Charles University in Prague, Faculty of Mathematics and Physics, arXiv:1308.5008.

Kadlecová, H. and Krtouš, P. (2010), Gyratons on Melvin spacetime, *Phys. Rev. D*, **82**, p. 044041.

Kadlecová, H., Zelnikov, A., Krtouš, P. and Podolský, J. (2009), Gyratons on direct–product spacetimes, *Phys. Rev. D*, **80**, p. 024004.

Melvin, M. A. (1965), Dynamics of Cylindrical Electromagnetic Universes, *Phys. Rev.*, **139**, pp. B225–B243.

Pravda, V., Pravdova, A., Coley, A. and Milson, R. (2002), All spacetimes with vanishing curvature invariants, *Class. Quant. Gravity*, **19**, pp. 6213–6236.

Stephani, H., Kramer, D., Maccallum, M., Hoenselaers and Herlt, E. (2003), *Exact Solutions of Einstein's Field Equations*, Cambridge University Press, Cambridge.

Proceedings of *RAGtime 10–13, 15–17/20–22/15–17/14–16 September, 2008/2009/2010/2011, Opava, Czech Republic*
Z. Stuchlík, G. Török and T. Pecháček, editors, Silesian University in Opava, 2014, pp. 75–92

An introduction to relativistic magnetohydrodynamics. II. Case of stationary electro-vacuum fields around black holes

Vladimír Karas[a]

Astronomical Institute, Academy of Sciences, Boční II 1401, CZ-14100 Prague, Czech Republic
[a]vladimir.karas@cuni.cz

ABSTRACT
This is the second lecture of 'RAGtime' series on electrodynamical effects near black holes. We will summarize the basic equations of relativistic electrodynamics in terms of spin-coefficient (Newman–Penrose) formalism.

The aim of the lecture is to present important relations that hold for exact electro-vacuum solutions and to exhibit, in a pedagogical manner, some illustrative solutions and useful approximation approaches. First, we concentrate on weak electromagnetic fields and we illustrate their structure by constructing the magnetic and electric lines of force. Gravitational field of the black hole assumes axial symmetry, whereas the electromagnetic field may or may not share the same symmetry. With these solutions we can investigate the frame-dragging effects acting on electromagnetic fields near a rotating black hole. These fields develop magnetic null points and current sheets. Their structure suggests that magnetic reconnection takes place near the rotating black hole horizon. Finally, the last section will be devoted to the transition from test-field solution to exact solutions of coupled Einstein-Maxwell equations.

New effects emerge within the framework of exact solutions: the expulsion of the magnetic flux out of the black-hole horizon depends on the intensity of the imposed magnetic field.

Keywords: Black holes – Electromagnetic fields – Relativity

1 INTRODUCTION

Electromagnetic fields play an important role in astrophysics. Near rotating compact bodies, such as neutron stars and black holes, the field lines are deformed by an interplay of rapidly moving plasma and strong gravitational fields. Here we will illustrate purely gravitational effects by exploring simplified vacuum solutions in which the influence of plasma is ignored but the presence of strong gravity is taken into account.

In the first lecture of this workshop series (Karas, 2005, Paper I) we summarized the basic equations of relativistic magnetohydrodynamics (MHD). In that paper we employed standard tensorial notation and we focused our attention on situations when the plasma motion is governed by MHD and gravitational effects are competing with each other in the vicinity of a black hole. We limited our discussion to axially symmetric and stationary flows. The latter assumption will be still maintained in the present talk. In fact, we will restrict ourselves to purely electro-vacuum solution, however, we will discuss them in greater depth and, more importantly, we will employ the elegant formalism of null tetrads. We do not derive new solutions or technique in these lectures, instead, we summarise useful relations in the form of brief notes paying special attention to effects of strong gravity.

One new point is mentioned in conclusion: with *exact solutions* of Einstein–Maxwell electrovacuum fields, an aligned magnetic flux becomes expelled from a rotating black hole as an interplay between the shape of magnetic lines of force (which become pushed out of the horizon) and the concentration of the magnetic flux tube toward the rotation axis (which becomes more concentrated for strong magnetic fields because of their own gravitational effect). This is, however, important only for *very strong* magnetic fields only, where 'very strong' means that the magnetic field contributes to the space-time metric.

2 DEFINITIONS, NOTATION, AND BASIC RELATIONS

Field equations

We start with Einstein's equations which, in the notation of Paper I, take a familiar form of a set of coupled partial differential equations (e.g. Chandrasekhar, 1983),

$$R_{\mu\nu} - \frac{1}{2} R g_{\mu\nu} = 8\pi T_{\mu\nu} \, , \tag{1}$$

where the right-hand side source terms $T_{\mu\nu}$ are of purely electromagnetic origin,

$$T^{\alpha\beta} \equiv T^{\alpha\beta}_{\mathrm{EMG}} = \frac{1}{4\pi} \left(F^{\alpha\mu} F^{\beta}_{\mu} - \frac{1}{4} F^{\mu\nu} F_{\mu\nu} g^{\alpha\beta} \right) , \tag{2}$$

$$T^{\mu\nu}{}_{;\nu} = -F^{\mu\alpha} j_{\alpha} \, , \qquad F^{\mu\nu}{}_{;\nu} = 4\pi j^{\mu} \, , \qquad {}^{\star}F^{\mu\nu}{}_{;\nu} = 4\pi \mathcal{M}^{\mu} \, . \tag{3}$$

where ${}^{\star}F_{\mu\nu} \equiv \varepsilon_{\mu\nu}{}^{\rho\sigma} F_{\rho\sigma}/2$. We assume that the electromagnetic test-fields reside in a curved background of a rotating black hole. Such solutions can be found by solving for the electromagnetic field in a fixed background geometry of Kerr metric (Thorne et al., 1986; Gal'Tsov, 1986). Here we study classical solutions for (magnetised) Kerr–Newman black holes that possess a horizon. Higher-dimensional black holes and black rings in external magnetic fields were explored by, e.g. Ortaggio (2005); Yazadjiev (2006), and references cited therein, whereas an extension to the case of naked singularity has been discussed recently by Adámek and Stuchlík (2013).

Killing vectors generate a test-field solution

The presence of Killing vectors corresponds to the symmetry of the spacetime (Chandrasekhar, 1983; Wald, 1984), such as stationarity and axial symmetry.

Killing vectors satisfy the well-known equation,

$$\xi_{\mu;\nu} + \xi_{\nu;\mu} = 0 \, , \tag{4}$$

where coordinate system is selected in such a way that the following condition is satisfied: $\xi^{\mu} = \delta^{\mu}_{\rho}$. One can check that Killing vectors obey a sequence of relations:

$$0 = \xi_{\mu;\nu} + \xi_{\nu;\mu} = \xi_{\mu,\nu} - \Gamma^{\lambda}_{\mu\nu}\xi_{\lambda} + \xi_{\nu,\mu} - \Gamma^{\lambda}_{\mu\nu}\xi_{\lambda} = g_{\mu\nu,\rho} \, . \tag{5}$$

The last equality (5) states that because of symmetry the metric tensor does not depend x^{ρ} coordinate.

The electromagnetic field may or may not conform to the same symmetries as the gravitational field. Naturally, the problem is greatly simplified by assuming axial symmetry and stationarity for both fields. In a vacuum spacetime, Killing vectors generate a test-field solution of Maxwell equations. We *define* the electromagnetic field by associating it with the Killing vector field,

$$F_{\mu\nu} = 2\xi_{\mu;\nu} \, . \tag{6}$$

Then

$$F_{\mu\nu} = 2\xi_{\mu;\nu} = -2\xi_{\nu;\mu} = -F_{\nu\mu} \, , \tag{7}$$

$$F_{\mu\nu} = \xi_{\mu;\nu} - \xi_{\nu;\mu} \equiv \xi_{[\mu;\nu]} \, . \tag{8}$$

By employing the Killing equation and the definition of Riemann tensor, i.e. the relations $\xi_{\mu;\nu;\sigma} - \xi_{\mu;\sigma;\nu} = -R_{\lambda\mu\nu\sigma}\xi^{\lambda}$, and $R_{\lambda[\mu\nu\sigma]\mathrm{cycl}} = 0$, we find:

$$\xi_{\mu;\nu;\sigma} = R_{\lambda\sigma\mu\nu}\xi^{\lambda} \, , \qquad \xi^{\mu;\nu}{}_{;\nu} = R^{\mu}{}_{\lambda}\xi^{\lambda} \, . \tag{9}$$

The right-hand side vanishes in vacuum, hence

$$F^{\mu\nu}{}_{;\nu} = 0 \, . \tag{10}$$

It follows that the well-known field invariants are given by relations

$$\boldsymbol{E}.\boldsymbol{B} = \frac{1}{4}\,{}^{\star}F_{\mu\nu}F^{\mu\nu} \, , \qquad B^2 - E^2 = \frac{1}{2}F_{\mu\nu}F^{\mu\nu} \, . \tag{11}$$

Magnetic and electric charges

We start from the axial and temporal Killing vectors, existence of which is guaranteed in any axially symmetric and stationary spacetime,

$$\xi^{\mu} = \frac{\partial}{\partial t}, \qquad \tilde{\xi}^{\mu} = \frac{\partial}{\partial \phi} \, . \tag{12}$$

In the language of differential forms (e.g. Wald, 1984),

$$\underbrace{\tfrac{1}{2}F_{\mu\nu}\,\mathrm{d}x^{\mu} \wedge \mathrm{d}x^{\nu}}_{\mathbf{F}} = \underbrace{\xi_{\mu,\nu}\,\mathrm{d}x^{\mu} \wedge \mathrm{d}x^{\nu}}_{\mathbf{d}\boldsymbol{\xi}} \, . \tag{13}$$

The above-given equations allow us to introduce the magnetic and electric charges in the form of integral relations,

$$\text{Magnetic charge:} \qquad 4\pi\mathcal{M} = \int_{\mathcal{S}} \mathbf{F} = \int_{\mathcal{S}} \mathbf{d}\boldsymbol{\xi} = 0\,. \tag{14}$$

$$\text{Electric charge:} \qquad 4\pi Q = \int_{\mathcal{S}} {}^{\star}\boldsymbol{F} = \int_{\mathcal{S}} {}^{\star}\mathbf{d}\boldsymbol{\xi} = -8\pi M\,, \tag{15}$$

$$= \int_{\mathcal{S}} {}^{\star}\mathbf{d}\tilde{\boldsymbol{\xi}} = 16\pi J\,, \tag{16}$$

where M has a meaning of mass and J is angular momentum of the source. Here, integration is supposed to be carried out far from the source, i.e. in spatial infinity of Kerr metric in our case. For example for the electric charge we obtain

$$4\pi Q = \int_{\mathcal{S}} {}^{\star}\boldsymbol{F} = \int_{\mathcal{S}} {}^{\star}F_{\mu\nu}\,\mathrm{d}\sigma^{\mu\nu} = \int_{\mathcal{V}} 2F^{\tau\alpha}{}_{;\alpha}\,\mathrm{d}\mathcal{V}\,, \tag{17}$$

where $\mathrm{d}\sigma^{\mu\nu} = \mathrm{d}_1 x^{\mu} \wedge \mathrm{d}_2 x^{\nu} = \mathrm{d}\theta\ \mathrm{d}\phi$.

Wald's field

In an asymptotically flat spacetime, ∂_{ϕ} generates uniform magnetic field, whereas the field vanishes asymptotically for ∂_t. These two solutions are known as the Wald's field (Wald, 1974; King et al., 1975; Bičák and Dvořák, 1980; Nathanail and Contopoulos, 2014):

$$F = \frac{1}{2}B_0\left(\mathrm{d}\tilde{\xi} + \frac{2J}{M}\,\mathrm{d}\xi\right)\,. \tag{18}$$

Magnetic flux surfaces:

$$4\pi\Phi_{\mathcal{M}} = \int_{\mathcal{S}} \boldsymbol{F} = \mathrm{const}\,. \tag{19}$$

Magnetic and electric Lorentz force are then given by equations

$$m\dot{\boldsymbol{u}} = q_{\mathrm{m}}{}^{\star}\boldsymbol{F}.\boldsymbol{u}\,, \qquad m\dot{\boldsymbol{u}} = q_{\mathrm{e}}\boldsymbol{F}.\boldsymbol{u}\,. \tag{20}$$

Finally, magnetic field lines (in the axisymmetric case):

$$\frac{\mathrm{d}r}{\mathrm{d}\theta} = \frac{B_r}{B_{\theta}}\,, \tag{21}$$

Magnetic field lines lie in surfaces of constant magnetic flux (see below).

3 SPIN-COEFFICIENT FORMALISM OF NULL TETRADS FOR ELECTROMAGNETIC FIELDS

The spin-coefficient formalism (Newman and Penrose, 1962) is a special case of the tetrad formalism where tensors are projected onto a complete vector basis at each point in spacetime. The vector basis is chosen as a complex null tetrad, l^{μ}, n^{μ}, m^{μ}, $\bar{m}^{\mu}$, satisfying conditions

$$l_\nu n^\nu = 1\,, \qquad m_\nu \bar{m}^\nu = -1\,, \tag{22}$$

and zero all other combinations. A natural correspondence with an orthonormal tetrad reads

$$e_{(0)} = \frac{l+n}{\sqrt{2}}\,, \quad e_{(1)} = \frac{l-n}{\sqrt{2}}\,, \quad e_{(2)} = \frac{m+\bar{m}}{\sqrt{2}}\,, \quad e_{(3)} = \frac{m-\bar{m}}{\Im\sqrt{2}}\,. \tag{23}$$

Null tetrads are not unambiguous, as the following three transformations maintain the tetrad properties:

(i) $l \to l, m \to m + al, n \to n + a\bar{m} + \bar{a}m + a\bar{a}l$;
(ii) $n \to n, m \to m + bm, l \to l + b\bar{m} + \bar{b}m + b\bar{b}n$;
(iii) $l \to \zeta l, n \to \zeta^{-1}l, m \to e^{\Im\psi}m$;

with $\zeta, \psi \in \Re$.

Instead of six real components of $F_{\mu\nu}$, the framework of the null tetrad formalism describes the electromagnetic field by three independent complex quantities,

$$\Phi_0 = F_{\mu\nu} l^\mu m^\nu\,, \tag{24}$$
$$\Phi_1 = \tfrac{1}{2} F_{\mu\nu}\big(l^\mu n^\nu + \bar{m}^\mu m^\nu\big)\,, \tag{25}$$
$$\Phi_2 = F_{\mu\nu} \bar{m}^\mu n^\nu\,. \tag{26}$$

It can be checked that the backward transformation has a form

$$F_{\mu\nu} = \Phi_1\left(n_{[\mu} l_{\nu]} + m_{[\mu}\bar{m}_{\nu]}\right) + \Phi_2 l_{[\mu} m_{\nu]} + \Phi_0 \bar{m}_{[\mu} n_{\nu]} + c.c. \tag{27}$$

The Newman–Penrose formalism defines the following differential operators:

$$D \equiv l^\mu \partial_\mu\,, \quad \delta \equiv m^\mu \partial_\mu\,, \quad \bar{\delta} \equiv \bar{m}^\mu \partial_\mu\,, \quad \Delta \equiv n^\mu \partial_\mu\,. \tag{28}$$

Furthermore, one introduces a set of spin coefficients (Ricci rotations symbols),

$$\alpha = -\tfrac{1}{2}\left(n_{\mu;\nu} l^\mu \bar{m}^\nu - \bar{m}_{\mu;\nu} m^\mu \bar{m}^\nu\right)\,, \tag{29}$$
$$\beta = \tfrac{1}{2}\left(l_{\mu;\nu} n^\mu m^\nu - m_{\mu;\nu} \bar{m}^\mu m^\nu\right)\,, \tag{30}$$
$$\gamma = -\tfrac{1}{2}\left(n_{\mu;\nu} l^\mu n^\nu - \bar{m}_{\mu;\nu} m^\mu m^\nu\right)\,, \tag{31}$$
$$\epsilon = \tfrac{1}{2}\left(l_{\mu;\nu} n^\mu l^\nu - m_{\mu;\nu} \bar{m}^\mu l^\nu\right)\,, \tag{32}$$
$$\kappa = l_{\mu;\nu} m^\mu l^\nu\,, \qquad \lambda = -n_{\mu;\nu} \bar{m}^\mu \bar{m}^\nu\,, \tag{33}$$
$$\rho = l_{\mu;\nu} m^\mu \bar{m}^\nu\,, \qquad \mu = -n_{\mu;\nu} \bar{m}^\mu m^\nu\,, \tag{34}$$
$$\sigma = l_{\mu;\nu} m^\mu m^\nu\,, \qquad \nu = -n_{\mu;\nu} \bar{m}^\mu n^\nu\,, \tag{35}$$
$$\tau = l_{\mu;\nu} m^\mu n^\nu\,, \qquad \pi = -n_{\mu;\nu} \bar{m}^\mu l^\nu\,. \tag{36}$$

Despite a seemingly large number of variables we will find this notation very useful and practical later on. However, first it will be useful to give an explicit example.

Example of the null tetrad for Schwarzschild metric

The metric is written in the form

$$\mathrm{d}s^2 = \left(1 - \frac{2M}{r}\right)\mathrm{d}t^2 - \left(1 - \frac{2M}{r}\right)^{-1}\mathrm{d}r^2 - r^2\,\mathrm{d}\theta^2 - r^2\sin^2\theta\,\mathrm{d}\phi^2\,. \tag{37}$$

The appropriate null tetrad is then given by

$$l^\mu = \Big([1-2M/r]^{-1}, 1, 0, 0\Big)\,, \tag{38}$$

$$n^\mu = \Big(\tfrac{1}{2}, \tfrac{1}{2}[1-2M/r], 0, 0\Big)\,, \tag{39}$$

$$m^\mu = \frac{1}{\sqrt{2}\,r}\Big(0, 0, 1, \Im\sin^{-1}\theta\Big)\,. \tag{40}$$

An arbitrary type-D spacetime (e.g. the Schwarszchild metric) allows to set $\kappa = \sigma = \nu = \lambda = 0$. In particular, for the Schwarzschild metric the explicit form of non-vanishing spin coefficients is:

$$\rho = -\frac{1}{r}\,, \quad \mu = -\frac{1}{2r}\frac{1}{1-2M/r}\,, \quad \alpha = -\beta = -\sqrt{2}\,r\cot\frac{\theta}{2}\,, \quad \gamma = \frac{M}{2r^2}\,. \tag{41}$$

Maxwell's equations

Maxwell's equations adopt the form

$$(D - 2\rho + 2\epsilon)\Phi_1 - (\bar{\delta} + \pi - 2\alpha)\Phi_0 = 2\pi J_l\,, \tag{42}$$

$$(\delta - 2\tau)\Phi_1 - (\Delta + \mu - 2\gamma)\Phi_0 = 2\pi J_m\,, \tag{43}$$

$$(D - \rho + 2\epsilon)\Phi_2 - (\bar{\delta} + 2\pi)\Phi_1 = 2\pi J_{\bar{m}}\,, \tag{44}$$

$$(\delta - \tau + 2\beta)\Phi_2 - (\Delta + 2\mu)\Phi_1 = 2\pi J_n \tag{45}$$

with

$$J_l = l_\mu\big(j^\mu + \Im\mathcal{M}^\mu\big)\,, \qquad J_m = m_\mu\big(j^\mu + \Im\mathcal{M}^\mu\big)\,, \tag{46}$$

$$J_{\bar{m}} = \bar{m}_\mu\big(j^\mu + \Im\mathcal{M}^\mu\big)\,, \qquad J_n = n_\mu\big(j^\mu + \Im\mathcal{M}^\mu\big)\,. \tag{47}$$

These are four equations for three complex variables.

Teukolsky's equations

Teukolsky (1973) derived the following form of Maxwell equations:

$$\begin{gathered}
\Big[\big(D\epsilon + \bar{\epsilon} - 2\rho - \bar{\rho}\big)\big(\Delta + \mu - 2\gamma\big) - \big(\delta - \beta - \bar{\alpha} - 2\tau + \bar{\pi}\big)\big(\bar{\delta} + \pi - 2\alpha\big)\Big]\Phi_0 = 2\pi J_0\,,\\
\Big[\big(D + \epsilon + \bar{\epsilon} - \rho - \bar{\rho}\big)\big(\Delta + 2\mu\big) - \big(\delta + \beta - \bar{\alpha} - \tau + \bar{\pi}\big)\big(\bar{\delta} + 2\pi\big)\Big]\Phi_1 = 2\pi J_1\,,\\
\Big[\big(\Delta + \gamma - \bar{\gamma} + 2\mu + \bar{\mu}\big)\big(D - \rho + 2\epsilon\big) - \big(\bar{\delta} + \alpha + \bar{\beta} - \bar{\tau} + 2\pi\big)\big(\delta - \tau + 2\beta\big)\Big]\Phi_2 = 2\pi J_2
\end{gathered} \tag{48}$$

with

$$J_0 = \big(\delta - \beta - \bar{\alpha} - 2\tau + \bar{\pi}\big) J_l - \big(D - \epsilon + \bar{\epsilon} - 2\rho - \bar{\rho}\big) J_m \,, \tag{49}$$
$$J_1 = \big(\delta + \beta - \bar{\alpha} - \tau + \bar{\pi}\big) J_{\bar{m}} - \big(D + \epsilon + \bar{\epsilon} - \rho - \bar{\rho}\big) J_n \,, \tag{50}$$
$$J_2 = \big(\Delta + \gamma - \bar{\gamma} + 2\mu + \bar{\mu}\big) J_{\bar{m}} - \big(\bar{\delta} + \alpha + \bar{\beta} + 2\pi - \bar{\tau}\big) J_n \,. \tag{51}$$

Clearly this is an extremely useful form: noticed that the above-given differential equations are entirely decoupled.

Example – Maxwell's equations in Schwarzschild metric

$$\left[\frac{\partial}{\partial r} + \frac{2}{r}\right] \Phi_1 + \frac{1}{\sqrt{2}r} {}^\star\bar{\partial} \Phi_0 = 2\pi J_l \,, \tag{52}$$
$$-\frac{1}{\sqrt{2}r} {}^\star\partial \Phi_1 + \frac{1}{2}\left[\left(1 - \frac{2M}{r}\right)\frac{\partial}{\partial r} + \frac{1}{r}\right] \Phi_0 = 2\pi J_m \,, \tag{53}$$
$$\left[\frac{\partial}{\partial r} + \frac{1}{r}\right] \Phi_2 + \frac{1}{\sqrt{2}r} {}^\star\bar{\partial} \Phi_1 = 2\pi J_{\bar{m}} \,, \tag{54}$$
$$-\frac{1}{\sqrt{2}r} {}^\star\partial \Phi_2 + \frac{1}{2}\left(1 - \frac{2M}{r}\right)\left[\frac{\partial}{\partial r} + \frac{2}{r}\right] \Phi_1 = 2\pi J_n \,, \tag{55}$$

where the "edth" operator acts on a spin weight s quantity η is the following manner:

$${}^\star\partial \eta = -\left\{\sin^s\theta \left[\frac{\partial}{\partial\theta} + \frac{\Im}{\sin\theta}\frac{\partial}{\partial\phi}\right] \sin^{-s}\theta\right\} \eta \,. \tag{56}$$

Spin weight is defined by by the transformation property $\eta \to e^{\Im s \psi}\eta$ under the transformation $m \to e^{\Im\psi} m$. Φ_0, Φ_1, Φ_2 have spin weights $s = 1, 0, -1$, respectively.

Spin harmonics

Spin harmonics form a complete set of orthonormal functions

$${}_sY_{lm}(\theta,\phi) = \begin{cases} \sqrt{\frac{(l-s)!}{(l+s)!}}\, {}^\star\partial^s Y_{lm}(\theta,\phi) & \text{for } 0 \le s \le l \,, \\ (-1)^s \sqrt{\frac{(l+s)!}{(l-s)!}}\, {}^\star\partial^{-s} Y_{lm}(\theta,\phi) & \text{for } -l \le s \le 0 \end{cases} \tag{57}$$

with the orthogonality relation

$$\int_0^{2\pi}\int_0^{\pi} {}_sY_{lm}(\theta,\phi)\; {}_sY_{l'm'}(\theta,\phi)\; \sin\theta\, \mathrm{d}\theta\, \mathrm{d}\phi = \delta_{ll'}\delta_{mm'} \,. \tag{58}$$

A general stationary vacuum electromagnetic test field can be expanded in terms of spin-s spherical harmonics.

3.1 Test fields in Schwarzschild spacetime

Bičák and Dvořák (1980) use the following expansion:

$$\Phi_0 = \sum_{l=1}^{\infty} \sum_{m=-l}^{l} {}^0R_{lm}(r)\, {}_1Y_{lm}(\theta, \phi)\,, \tag{59}$$

$$\Phi_1 = \sum_{l=0}^{\infty} \sum_{m=-l}^{l} {}^1R_{lm}(r)\, {}_0Y_{lm}(\theta, \phi)\,, \tag{60}$$

$$\Phi_2 = \sum_{l=1}^{\infty} \sum_{m=-l}^{l} {}^2R_{lm}(r)\, {}_{-1}Y_{lm}(\theta, \phi)\,. \tag{61}$$

Then the equations for radial functions take a form

$$r(r-2M)\, {}^0R''_{lm} + 4(r-M)\, {}^0R'_{lm} - (l-1)(l+2)\, {}^0R_{lm} = -4\pi\, {}^0J_{lm}\,, \tag{62}$$

$$r(r-2M)\, {}^1R''_{lm} + 2(2r-3M)\, {}^1R'_{lm} - (l-1)(l+2)\, {}^1R_{lm} = -4\pi\, {}^1J_{lm}\,, \tag{63}$$

$$r(r-2M)\, {}^2R''_{lm} + 4(r-2M)\, {}^2R'_{lm} - \left[(l-1)(l+2) + 4M/r\right] {}^2R_{lm} = -4\pi\, {}^2J_{lm}\,, \tag{64}$$

where

$${}^0J_{lm}(r) = \int J_0(r, \theta, \phi)\, {}_1\bar{Y}_{lm}(\theta, \phi)\, r^2\, \mathrm{d}\Omega\,, \tag{65}$$

$${}^1J_{lm}(r) = \int J_1(r, \theta, \phi)\, {}_0\bar{Y}_{lm}(\theta, \phi)\, r^2\, \mathrm{d}\Omega\,, \tag{66}$$

$${}^2J_{lm}(r) = \int J_2(r, \theta, \phi)\, {}_{-1}\bar{Y}_{lm}(\theta, \phi)\, r^2\, \mathrm{d}\Omega\,. \tag{67}$$

A vacuum field solution is given by a Fuchsian-type equation (Bičák and Dvořák, 1980)

$$x(x-1)\frac{\mathrm{d}^2\, {}^1R_{lm}}{\mathrm{d}x^2} + (4x-3)\frac{\mathrm{d}\, {}^1R_{lm}}{\mathrm{d}x} - (l-1)(l+2)\, {}^1R_{lm} = 0\,, \tag{68}$$

with $x \equiv r/(2M)$.

Two independent solutions can be found:

$$\left.\begin{aligned} {}^1R_l^{(I)} &= F(1-l, l+2, 3; x), \\ {}^1R_l^{(II)} &= (-x)^{-l-2}\, F\big(l, l+2, 2l+2; x^{-1}\big) \end{aligned}\right\} \quad \text{for } l \neq 0, \tag{69}$$

$$\left.\begin{aligned} {}^1R_0^{(I)} &= \tfrac{1}{x^2}\ln(x-1) + \tfrac{1}{x} \\ {}^1R_0^{(II)} &= \tfrac{1}{x^2} \end{aligned}\right\} \quad \text{for } l = 0. \tag{70}$$

A general solution reads ${}^1R_{lm} = a_{lm}\, {}^1R_l^{(I)} + b_{lm}\, {}^1R_l^{(II)}$, $a_{lm},\ b_{lm} = \text{const}$. Inserting the solution for ${}^1R_{lm}$ in Maxwell equations Bičák and Dvořák (1980) find

$${}^0R_{lm} = a_{lm}\, {}^0R_l^{(I)} + b_{lm}\, {}^0R_l^{(II)} = \sqrt{\frac{2}{l(l+1)}}\frac{1}{r}\frac{\mathrm{d}}{\mathrm{d}r}\left(r^2\, {}^1R_{lm}\right)\,, \tag{71}$$

$${}^2R_{lm} = a_{lm}\, {}^2R_l^{(I)} + b_{lm}\, {}^2R_l^{(II)}\,, \tag{72}$$

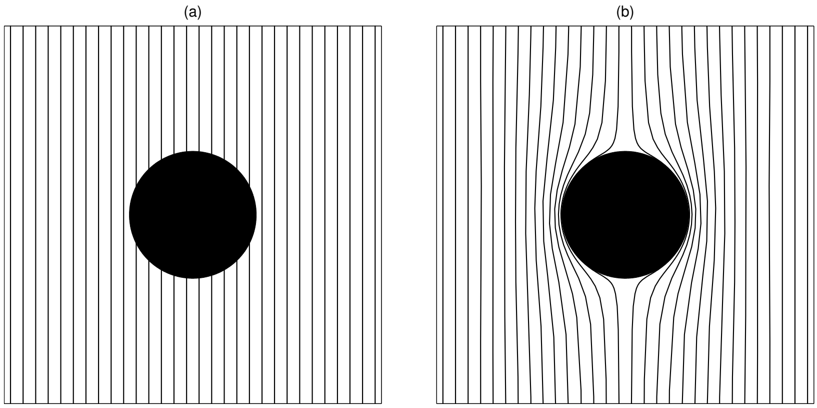

Figure 1. An axisymmetric case: *(a)* $a = 0$ (static black hole), and *(b)* $a = M$ (maximally rotating black hole).

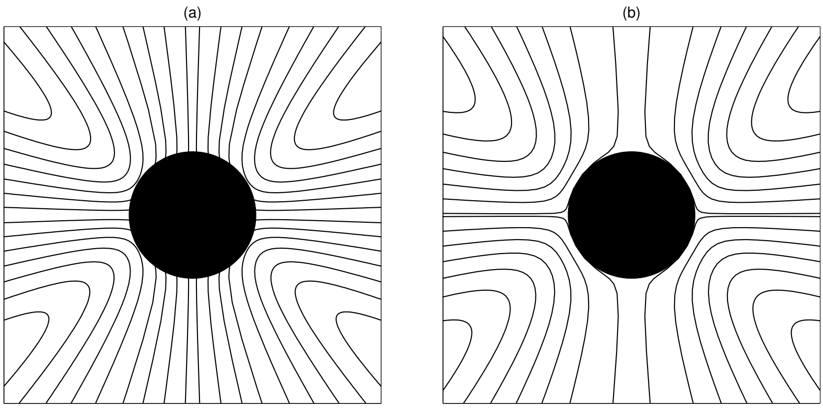

Figure 2. The case of *(a)* uniform aligned magnetic field near a fast rotating black hole ($a = 0.95\,M$); *(b)* near the maximally rotating hole ($a = M$).

where

$$ {}^{0}R_l^{(I)} = \frac{2\sqrt{2}}{\sqrt{l(l+1)}}\, F(1-l, l+2, 2; x)\,, \tag{73}$$

$$ {}^{0}R_l^{(II)} = -\sqrt{\frac{2l}{l+1}}\,(-x)^{-l-2} F\big(l+1, l+2, 2l+2; x^{-1}\big)\,, \tag{74}$$

$$ {}^{2}R_l^{(I)} = -\sqrt{\frac{2}{l(l+1)}}\, x^{-1} F(-l, l+1, 2; x)\,, \tag{75}$$

$$ {}^{2}R_l^{(II)} = -\sqrt{\frac{l}{2(l+1)}}\,(-x)^{-l-2} F\big(l+1, l, 2l+2; x^{-1}\big)\,. \tag{76}$$

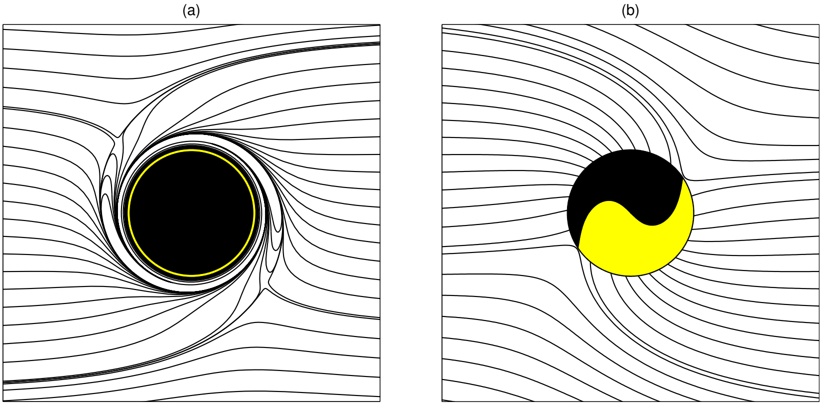

Figure 3. Equatorial plane is shown as viewed from top, i.e. along rotation axis, *(a)* in the frame of zero angular momentum observers orbiting at constant radius; *(b)* in the frame of freely falling observers. In the panel *(b)*, two regions of ingoing/outgoing lines are distinguished by different levels of shading of the horizon. The hole rotates counter-clockwise ($a = M$). Based on Karas (1989); Dovčiak et al. (2000).

We can select a physically appropriate solution by assuming a source between r_1 and r_2 ($r_+ \leq r_1 \leq r_2 \leq \infty$). By seeking a well-behaved solution on horizon that vanishes at infinity, we find

$$\left.\begin{aligned} \Phi_0 &= \textstyle\sum_{l,m} a_{l,m}\, {}^0R_l^{(I)}\, {}_1Y_{lm} \\ \Phi_1 &= \textstyle\sum_{l,m} a_{l,m}\, {}^1R_l^{(I)}\, {}_0Y_{lm} + \frac{E_\mathrm{a}}{r^2}\, {}_0Y_{00} \\ \Phi_2 &= \textstyle\sum_{l,m} a_{l,m}\, {}^2R_l^{(I)}\, {}_{-1}Y_{lm} \end{aligned}\right\} \quad \text{for } 2M \leq r < r_1\,, \tag{77}$$

$$\left.\begin{aligned} \Phi_0 &= \textstyle\sum_{l,m} b_{l,m}\, {}^0R_l^{(II)}\, {}_1Y_{lm} \\ \Phi_1 &= \textstyle\sum_{l,m} b_{l,m}\, {}^1R_l^{(II)}\, {}_0Y_{lm} + \frac{E_\mathrm{b}}{r^2}\, {}_0Y_{00} \\ \Phi_2 &= \textstyle\sum_{l,m} b_{l,m}\, {}^2R_l^{(II)}\, {}_{-1}Y_{lm} \end{aligned}\right\} \quad \text{for } r > r_2\,. \tag{78}$$

Two examples

First, a spherically symmetric electric field. A unique solution that is well-behaving both at $r = r_+$ and at $r \to \infty$: ${}^1R_0^{(II)}$. This term describes a weakly charged Reissner–Nordström black hole.

Second, an asymptotically uniform magnetic field:

$$F_{\mu\nu} \to B_0\boldsymbol{e}_z + B_1\boldsymbol{e}_x\,, \tag{79}$$

$$\text{i.e. } F_{r\theta} \to -B_1\, r \sin\phi\,, \tag{80}$$

$$F_{r\phi} \to B_0\, r\, \sin^2\theta - B_1\, r\, \sin\theta\, \cos\theta\, \cos\phi\,, \tag{81}$$

$$F_{\theta\phi} \to B_0\, r^2\, \sin\theta \cos\theta + B_1\, r^2\, \sin^2\theta\, \cos\phi\,. \tag{82}$$

3.2 Magnetic and electric lines of force near a rotating black hole

Lorentz force acts on electric/magnetic monopoles residing at rest with respect to a locally non-rotating frame,

$$\frac{\mathrm{d}u^\mu}{\mathrm{d}\tau} \propto {}^\star F^\mu_\nu \, u^\nu \,, \qquad \frac{\mathrm{d}u^\mu}{\mathrm{d}\tau} \propto F^\mu_\nu \, u^\nu \,. \tag{83}$$

Magnetic lines are defined (Christodoulou and Ruffini, 1973):

$$\frac{\mathrm{d}r}{\mathrm{d}\theta} = -\frac{F_{\theta\phi}}{F_{r\phi}} \,, \qquad \frac{\mathrm{d}r}{\mathrm{d}\phi} = \frac{F_{\theta\phi}}{F_{r\theta}} \,. \tag{84}$$

In an axially symmetric case the magnetic flux is:

$$\Phi_{\mathrm{m}} = \pi B_0 \left[r^2 - 2Mr + a^2 + \frac{2Mr}{r^2 + a^2 \cos^2\theta} \left(r^2 - a^2\right) \right] \sin^2\theta = \mathrm{const}\,. \tag{85}$$

Notice: $\Phi_{\mathrm{m}} = 0$ for $r = r_+$ and $a = M$. The flux is expelled out of the horizon (Meissner effect; Bičák and Ledvinka (2000); Penna (2014)).

The electric fluxes and field lines can be introduced in a similar manner, one only needs to interchange the electromagnetic field tensor by its dual, the magnetic charge by the electric charge, and vice versa wherever they appear in the above-given formulae. It should be evident that the induced electric field vanishes in the non-rotating case. Based on the classical analogy with a rotating sphere, one would perhaps expect a quadrupole-type component, but here the leading term of the electric field arises due to gravomagnetic interaction which is a purely general-relativistic effect, and this electric field falls off radially as r^{-2}.

Magnetic field lines reside in surfaces of constant magnetic flux, and this way the lines of force are defined in an invariant way (see Fig. 1). Electric field is induced by the gravito-magnetic influence of the black hole. The resulting field lines are shown in Fig. 2. An asymptotic form of the electric field-lines reads

$$\frac{\mathrm{d}r}{\mathrm{d}\lambda} = \frac{B_0 a M}{r^2} \left(3\cos^2\theta - 1\right) + \frac{3B_\perp a M}{r^2} \sin\theta\, \cos\theta\, \cos\phi + \mathcal{O}\left(r^{-3}\right) \,, \tag{86}$$

$$\frac{\mathrm{d}\theta}{\mathrm{d}\lambda} = \mathcal{O}\left(B_\perp r^{-3}\right) \,, \qquad \frac{\mathrm{d}\phi}{\mathrm{d}\lambda} = \mathcal{O}\left(B_\perp r^{-3}\right) \,. \tag{87}$$

As mentioned above, an aligned magnetic field produces an asymptotically radial electric field, rather than a quadrupole field, expected under these circumstances in the classical electrodynamics. This difference is due to rotation of the black hole.

Figure 3 shows the structure of a uniform magnetic field perpendicular to the black hole rotation axis (Bičák and Karas, 1989; Karas and Kopáček, 2009; Karas et al., 2012, 2013, 2014). We notice the enormous effect of frame-dragging which acts on field lines and distorts them in the sense of black hole rotation. Nevertheless, some field lines still enter the horizon and bring the magnetic flux into the black hole (naturally, the same magnetic flux has to emerge out of the horizon, so that the total flux through the black hole vanishes and its magnetic charge is equal zero).

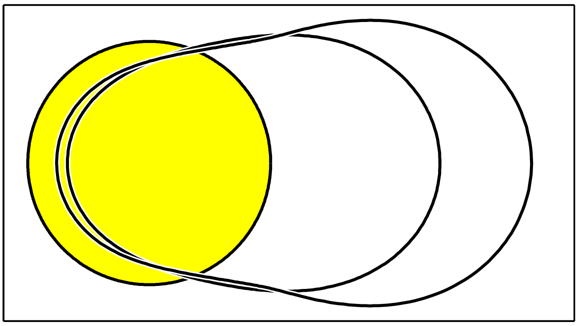

Figure 4. Cross-sectional area for the capture of magnetic flux by a rotating black hole. The three curves correspond to different values of the black-hole angular momentum: $a = 0$ (cross-section is the circle; its projection coincides with the black-hole horizon, indicated by yellow colour), $a = 0.95\,M$, and $a = M$. The enclosed area contains the field lines of the asymptotically perpendicular magnetic field which eventually enter into the black hole horizon. From the graph we notice that this area grows with the black hole spin and its shape is distorted by the gravitomagnetic interaction.

We notice that magnetic null points emerge near the black hole, suggesting that magnetic reconnection can be initiated by the purely gravitomagnetic effect of the rotating black hole. Indeed, this new reconnection mechanism has been only recently proposed (Karas and Kopáček, 2009) in the context of particle acceleration processes near magnetized black holes. The capture of magnetic field lines is further illustrated in Fig. 4 where we plot the black hole effective cross sectional area.

Surface charge on the horizon

Surface charge is formally defined by the radial component of electric field in non-singular coordinates (Thorne et al., 1986),

$$\sigma_{\rm H} = \frac{B_0 a}{4\pi\,\Sigma_+}\left[r_+\sin^2\theta - \frac{M}{\Sigma_+}\left(r_+^2 - a^2\cos^2\theta\right)\left(1+\cos^2\theta\right)\right] + \frac{B_\perp a}{4\pi\,\Sigma_+}\,\sin\theta\,\cos\theta\left[\frac{Mr_+}{\Sigma_+}+1\right]\left[a\sin\psi - r_+\cos\psi\right], \tag{88}$$

with

$$\psi = \phi + \frac{a}{r_+ - r_-}\,\ln\frac{r-r_+}{r-r_-}\;\propto\ln(r-r_+)\,. \tag{89}$$

For $a \ll M$,

$$\sigma_{\rm H} = \frac{a}{16\pi M}\left[B_0\left(1-3\cos^2\theta\right) + 3B_\perp\sin\theta\,\cos\theta\,\cos\psi\right]. \tag{90}$$

It should be obvious that $\sigma_{\rm H}$ does not represent any kind of a real charge distribution. Instead, it is introduced only by pure analogy with junction conditions for Maxwell's equations in classical electrodynamics. The classical problem was treated in original works by Faraday, Lamb, Thomson and Hertz, and more recently in Bullard (1949); Elsasser (1950). It is quite enlightening to pursue this similarity to greater depth (see e.g. Karas and Budinová, 2000 and references cited therein) despite the fact that this is purely a formal analogy, as pointed out by Punsly (2008).

4 ON THE WAY FROM TEST FIELDS TO EXACT SOLUTIONS OF EINSTEIN–MAXWELL EQUATIONS

So far we discussed test-field solutions of Einstein equations which reside in a prescribed (curved) spacetime. In the rest of this lecture we will briefly outline a way to construct *exact* solutions of mutually couple (vacuum) Einstein–Maxwell equations. Because this task is very complicated, astrophysically realistic results can be only obtained by numerical approaches. However, important insight can be gained by simplified analytic solutions. We will thus explore the latter approach.

The spacetime metric

Let us first assume a static spacetime metric in the form

$$\mathrm{d}s^2 = f^{-1}\left[e^{2\gamma}\left(\mathrm{d}z^2 + \mathrm{d}\rho^2\right) + \rho^2\,\mathrm{d}\phi^2\right] - f\,(\mathrm{d}t - \omega\,\mathrm{d}\phi)^2\ , \tag{91}$$

with f, ω, and γ being functions of z and ρ only. We consider coupled Einstein–Maxwell equations under the following constraints: (i) electrovacuum case containing a black hole, (ii) axial symmetry and stationarity, (iii) *not* necessarily asymptotically flat (see Kramer et al. (1980); Alekseev and Garcia (1996); Ernst and Wild (1976); Karas and Vokrouhlický (1991), and references cited therein).

As explained in various textbooks and, namely, in the above-mentioned works, one can proceed in the following way to find the three unknown metric functions:

- Standard approach: $g_{\mu\nu} \rightarrow \Gamma^{\mu}_{\nu\lambda} \rightarrow R^{\alpha}_{\beta\gamma\delta} \rightarrow G_{\mu\nu}$.
- Exterior calculus: $e^{\mu}_{(\lambda)} \rightarrow \omega_{\mu\nu}\Omega_{\mu\nu} \rightarrow R^{\hat{\alpha}}_{\hat{\beta}\hat{\gamma}\hat{\delta}} \rightarrow G_{\hat{\mu}\hat{\nu}}$.
- Variation principle: $\mathcal{L} = -\frac{1}{2}\rho f^{-2}\nabla f\cdot\nabla f + \frac{1}{2}\rho^{-1}f^2\nabla\omega\cdot\nabla\omega$.

We denoted nabla operator, $\nabla\cdot\left(\rho^{-1}\boldsymbol{e_\phi}\times\nabla\varphi\right) = 0\ \forall\varphi \equiv \varphi(\rho, z)$. Now, the vacuum field equations (without electromagnetic field) can be written in the form:

$$f\nabla^2 f = \nabla f\cdot\nabla f - \rho^{-2}f^4\nabla\omega\cdot\nabla\omega\,, \quad \nabla\cdot\left(\rho^{-2}f^2\nabla\omega\right) = 0\,. \tag{92}$$

Let us define functions $\varphi(\rho, z)$, $\omega(\rho, z)$ by the prescription

$$\rho^{-1}f^2\nabla\omega = \boldsymbol{e_\phi}\times\nabla\varphi\,,$$
$$f^{-2}\nabla\varphi = -\rho^{-1}\boldsymbol{e_\phi}\times\nabla\omega\,.$$

By applying $\nabla\cdot$ operator on the both sides of the last equation, the relation for φ comes out, $\nabla\cdot\left(f^{-2}\nabla\varphi\right)=0$. Let us further define $\mathcal{E}\equiv f+\Im\varphi$. Then, both field equations can be written in the form

$$(\Re\mathcal{E})\nabla^2\mathcal{E}=\nabla\mathcal{E}\cdot\nabla\mathcal{E}\,. \tag{93}$$

Now we can proceed to adding the electromagnetic field:

$$\mathcal{L}'=\mathcal{L}+2\rho f^{-1}A_0\left(\nabla A\right)^2-2\rho^{-1}f\left(\nabla A_3-\omega\nabla A_0\right)^2. \tag{94}$$

Functions f, ω, A_0, and A_3 are constrained by the variational principle. Define $\Phi\equiv\Phi(A_0,A_3)$, $\mathcal{E}\equiv f-|\Phi|^2+\Im\varphi$:

$$\left(\Re\mathcal{E}+|\Phi|^2\right)\nabla^2\mathcal{E}=\left(\nabla\mathcal{E}+2\bar{\Phi}\nabla\Phi\right)\cdot\nabla\mathcal{E}\,, \tag{95}$$

$$\left(\Re\mathcal{E}+|\Phi|^2\right)\nabla^2\Phi=\left(\nabla\mathcal{E}+2\bar{\Phi}\nabla\Phi\right)\cdot\nabla\Phi\,. \tag{96}$$

Let us assume $\mathcal{E}\equiv\mathcal{E}(\Phi)$ to be an analytic function which satisfies

$$\left(\Re\mathcal{E}+\Phi^2\right)\frac{\mathrm{d}^2\mathcal{E}}{\mathrm{d}\Phi^2}\nabla\Phi\cdot\nabla\Phi=0\,. \tag{97}$$

Assume further a linear relation,

$$\mathcal{E}=1-2\frac{\Phi}{q}\,,\qquad q\in\mathrm{C} \tag{98}$$

and a new variable ξ,

$$\mathcal{E}\equiv\frac{\xi-1}{\xi+1}\,,\qquad \Phi=\frac{q}{\xi+1}\,, \tag{99}$$

$$\left[\xi\bar{\xi}-\left(1-q\bar{q}\right)\right]\nabla^2\xi=2\bar{\xi}\nabla\xi\cdot\nabla\xi\,. \tag{100}$$

Generating "new" solutions

We introduce new variables by relations

$$\xi_0\to\xi=(1-q\bar{q})\xi_0\,, \tag{101}$$

$$\left[\xi_0\bar{\xi}_0-1\right]\nabla^2\xi_0=2\bar{\xi}_0\nabla\xi_0\cdot\nabla\xi_0\,, \tag{102}$$

i.e.

$$(\Re\mathcal{E}_0)\nabla^2\mathcal{E}_0=\nabla\mathcal{E}_0\cdot\nabla\mathcal{E}_0\,,\qquad \mathcal{E}_0\equiv\frac{\xi_0-1}{\xi_0+1}\,. \tag{103}$$

where $\mathcal{E}_0$ has a meaning of an "old" vacuum solution.

Theorem. Let (Φ, $\mathcal{E}$, $\gamma_{\alpha\beta}$) be a solution of Einstein–Maxwell electrovaccum equations with anisotropic Killing vector field. Then there is another solution (Φ', $\mathcal{E}'$, $\gamma'_{\alpha\beta}$), related to the old one by transformation

$$
\begin{aligned}
&\mathcal{E}' = \alpha\bar{\alpha}\mathcal{E}\,, && \Phi' = \alpha\Phi\,, \quad \ldots\text{dual rotation, } {}^\star F_{\mu\nu} \to \sqrt{\alpha/\bar{\alpha}}\,{}^\star F_{\mu\nu}\,,\\
&\mathcal{E}' = \mathcal{E} + \Im b\,, && \Phi' = \Phi\,, \quad \ldots\text{calibration, no change in } F_{\mu\nu}\,,\\
&\mathcal{E}' = \mathcal{E} - 2\bar{\beta}\Phi - \beta\bar{\beta}\,, && \Phi' = \Phi + \beta\,, \quad \ldots\text{calibration}\ldots,\\
&\mathcal{E}' = \mathcal{E}(1 + \Im c\mathcal{E})^{-1}\,, && \Phi' = (1 + \Im c\mathcal{E})^{-1}\,,\\
&\mathcal{E}' = \mathcal{E}\underbrace{(1 - 2\bar{\gamma}\Phi - \gamma\bar{\gamma}\mathcal{E})}_{\Lambda = 1 - B_0\Phi - \frac{1}{4}B_0^2\mathcal{E}}{}^{-1}\,, && \Phi' = (\Phi + \gamma\mathcal{E})(1 - 2\bar{\gamma}\Phi - \gamma\bar{\gamma}\mathcal{E})^{-1}\,.
\end{aligned}
$$

$$
\mathcal{E} \to \mathcal{E}' = \Lambda^{-1}\mathcal{E}\,, \qquad f \to f' = |\Lambda|^{-2} f\,, \qquad \omega \to \omega' = ?\,, \tag{104}
$$

$$
\Phi \to \Phi' = \Lambda^{-1}\big(\Phi - \tfrac{1}{2}B_0\mathcal{E}\big)\,, \quad \nabla\omega' = |\Lambda|^2\nabla\omega + \rho f^{-1}(\bar{\Lambda}\nabla\Lambda - \Lambda\nabla\bar{\Lambda})\,. \tag{105}
$$

Examples

Example 1. Minkowski spacetime → Melvin universe.

$$
\mathrm{d}s^2 = \Big[\mathrm{d}z^2 + \mathrm{d}\rho^2 - \mathrm{d}t^2\Big] + \rho^2\,\mathrm{d}\phi^2\,. \tag{106}
$$

$$
\begin{aligned}
&f = -\rho^2\,, \quad \omega = 0\,, \quad \Phi = 0\,, \quad \mathcal{E} = -\rho^2\,, \quad \varphi(\omega) = 0\,,\\
&f' = -\Lambda^{-2}\rho^2\,, \quad \omega' = 0\,, \quad \Phi' = \tfrac{1}{2}\Lambda^{-1}B_0\rho^2\,,\\
&B_z = \Lambda^{-2}B_0\,, \quad B_\rho = B_\phi = 0\,,
\end{aligned} \tag{107}
$$

$$
\mathrm{d}s^2 = \Lambda^2\Big[\mathrm{d}z^2 + \mathrm{d}\rho^2 - \mathrm{d}t^2\Big] + \Lambda^{-2}\rho^2\,\mathrm{d}\phi^2\,. \tag{108}
$$

Gravity of the magnetic field in balance with the Maxwell pressure. Cylindrical symmetry along z-axis.

Example 2. Schwarzschild BH → Schwarzschild–Melvin black hole.

$$
\mathrm{d}s^2 = \left[\left(1 - \frac{2M}{r}\right)^{-1}\mathrm{d}r^2 - \left(1 - \frac{2M}{r}\right)\mathrm{d}t^2 + r^2\,\mathrm{d}\theta^2\right] + r^2\sin^2\theta\,\mathrm{d}\phi^2\,, \tag{109}
$$

$$
\begin{aligned}
&f = -r^2\sin^2\theta\,, \quad \omega = 0\,, \quad \rho = \sqrt{r^2 - 2Mr}\,\sin\theta\,,\\
&B_r = \Lambda^{-2}B_0\cos\theta\,, \quad B_\theta = -\Lambda^{-2}B_0(1 - 2M/r)\sin\theta\,,
\end{aligned} \tag{110}
$$

$$
\mathrm{d}s^2 = \Lambda^2\Big[\ldots\Big] + \Lambda^{-2}r^2\sin^2\theta\,\mathrm{d}\phi^2\,. \tag{111}
$$

There the following limits of the magnetized Schwarzschild–Melvin black hole: (i) $B_0 = 0$ ... Schwarzschild solution, (ii) $r/M \to \infty$ ... Melvin solution, (iii) $|B_0M| \ll 1$ ... Wald's test field in the region $2M \ll r \ll B_0^{-1}$.

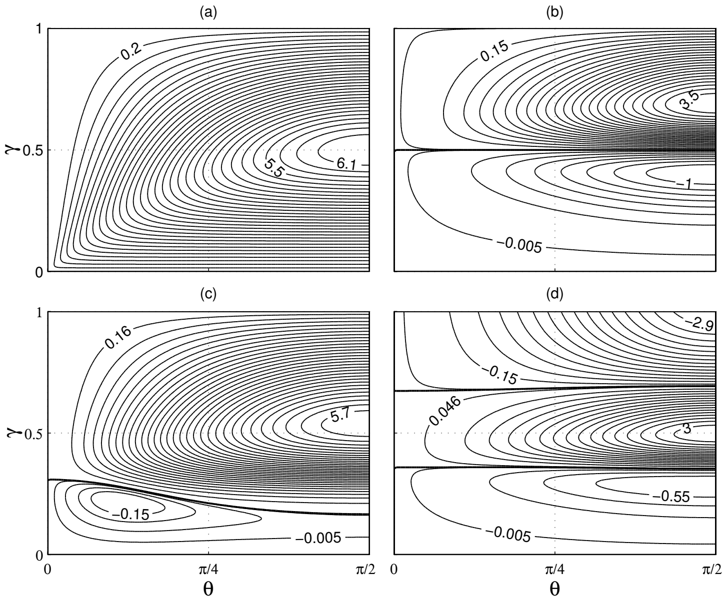

Figure 5. Contours of magnetic flux across a cap on the horizon (latitude angle θ is measured from the rotation axis) of a magnetized black hole: (a) $a = e = 0$; (b) $a = 1$, $e = 0$; (c) $a = 0.2$, $e = 0$; (d) $a = -e = 1/\sqrt{2}$ (electric charge and spin of the black hole). Here, $\gamma \equiv (1+\beta)^{-1}$, $\beta \equiv B_0 M$. This figure from Karas and Budinová (2000) illustrates strong-gravity effects on magnetic fields that do not occur in weak-magnetic (test) field approximation, namely, the expulsion of the magnetic flux as a function of the intensity of the imposed magnetic field.

Example 3. Magnetized Kerr-Newman BH.

$$g = |\Lambda|^2 \Sigma \Big(\Delta^{-1}\,\mathrm{d}r^2 + \,\mathrm{d}\theta^2 - \Delta A^{-1}\,\mathrm{d}t^2\Big) + |\Lambda|^{-2} \Sigma^{-1} A \sin^2\theta \big(\mathrm{d}\phi - \omega\,\mathrm{d}t\big)^2\,, \tag{112}$$

$\Sigma = r^2 + a^2\cos^2\theta$, $\Delta = r^2 - 2Mr + a^2 + e^2$, $A = (r^2+a^2)^2 - \Delta a^2 \sin^2\theta$ are functions from the Kerr–Newman metric.

$\Lambda = 1 + \beta\Phi - \beta^2\mathcal{E}/4$ is given in terms of the Ernst complex potentials $\Phi(r,\theta)$ and $\mathcal{E}(r,\theta)$:

$$\begin{aligned}\Sigma\Phi &= ear\sin^2\theta - \Im e\big(r^2+a^2\big)\cos\theta\,,\\ \Sigma\mathcal{E} &= -A\sin^2\theta - e^2\big(a^2 + r^2\cos^2\theta\big)\\ &\quad + 2\Im a\Big[\Sigma\big(3-\cos^2\theta\big) + a^2\sin^4\theta - re^2\sin^2\theta\Big]\cos\theta\,.\end{aligned}$$

The electromagnetic field can be written in terms of orthonormal LNRF components,

$$\begin{aligned}H_{(r)} + \mathrm{i}E_{(r)} &= A^{-1/2}\sin^{-1}\theta\,\Phi'_{,\theta}\,,\\ H_{(\theta)} + \mathrm{i}E_{(\theta)} &= -\,(\Delta/A)^{1/2}\sin^{-1}\theta\,\Phi'_{,r}\,,\end{aligned}$$

where $\Phi'(r,\theta) = \Lambda^{-1}\,(\Phi - \beta\mathcal{E}/2)$.

The horizon is positioned at $r \equiv r_+ = 1 + \sqrt{(1 - a^2 - e^2)}$, independent of β. As in the non-magnetized case, the horizon exists only for $a^2 + e^2 \leq 1$.

There is an issue with this solution, namely, the range of angular coordinates *versus* the problem of conical singularity: $0 \leq \theta \leq \pi$, $0 \leq \phi < 2\pi|\Lambda_0|^2$, where

$$|\Lambda_0|^2 \equiv |\Lambda(\sin\theta = 0)|^2 = 1 + \frac{3}{2}\beta^2 e^2 + 2\beta^3 ae + \beta^4\left(\frac{1}{16}e^4 + a^2\right) . \tag{113}$$

The total electric charge Q_H and the magnetic flux $\Phi_\mathrm{m}(\theta)$ across a cap in axisymmetric position on the horizon (with the edge defined by $\theta = \mathrm{const}$):

$$Q_\mathrm{H} = -|\Lambda_0|^2\, \Im\mathrm{m}\, \Phi'\,(r_+, 0)\,,$$
$$\Phi_\mathrm{m} = 2\pi|\Lambda_0|^2\, \Re\mathrm{e}\, \Phi'\left(r_+, \bar{\theta}\right)\Big|_{\bar{\theta}=0}^{\theta} .$$

The magnetic flux across the black hole hemisphere in the exact magnetized black hole solution is shown in Fig. 5.

ACKNOWLEDGEMENTS

The author acknowledges continued support from the Czech Science Foundation grant No. 13-00070J.

REFERENCES

Adámek, K. and Stuchlík, Z. (2013), Magnetized tori in the field of Kerr superspinars, *Classical Quantum Gravity*, **30**(20), 205007.

Alekseev, G. A. and Garcia, A. A. (1996), Schwarzschild black hole immersed in a homogeneous electromagnetic field, *Phys. Rev. D*, **53**, pp. 1853–1867.

Bičák, J. and Ledvinka, T. (2000), Electromagnetic fields around black holes and Meissner effect, *Nuovo Cimento B*, **115**, p. 739, arXiv: `gr-qc/0012006`.

Bičák, J. and Dvořák, L. (1980), Stationary electromagnetic fields around black holes. III. General solutions and the fields of current loops near the Reissner-Nordström black hole, *Phys. Rev. D*, **22**, pp. 2933–2940.

Bičák, J. and Karas, V. (1989), The influence of black holes on uniform magnetic fields, in D. G. Blair and M. J. Buckingham, editors, *Proceedings of the 5th Marcel Grossmann Meeting on General Relativity*, p. 1199, Singapore: World Scientific.

Bullard, E. C. (1949), Electromagnetic Induction in a Rotating Sphere, *Royal Society of London Proceedings Series A*, **199**, pp. 413–443.

Chandrasekhar, S. (1983), *The mathematical theory of black holes*, Clarendon Press/Oxford University Press, Oxford/New York.

Christodoulou, D. and Ruffini, R. (1973), *On the electrodynamics of collapsed objects*, Gordon and Breach Science Publishers, New York.

Dovčiak, M., Karas, V. and Lanza, A. (2000), Magnetic fields around black holes, *European J. Phys.*, **21**, pp. 303–315.

Elsasser, W. M. (1950), The Earth's Interior and Geomagnetism, *Rev. Modern Phys.*, **22**, pp. 1–35.

Ernst, F. J. and Wild, W. J. (1976), Kerr black holes in a magnetic universe, *J. Math. Phys.*, **17**, pp. 182–184.

Gal'Tsov, D. V. (1986), *Particles and fields in the vicinity of black holes*, Moscow University Press, Moscow.

Karas, V. (1989), Asymptotically uniform magnetic field near a Kerr black hole, *Phys. Rev. D*, **40**, pp. 2121–2123.

Karas, V. (2005), An introduction to relativistic magnetohydrodynamics I. The force-free approximation, in Hledík, S. and Stuchlík, Z., editor, *Proceedings of RAGtime 6/7: Workshops on black holes and neutron stars, Opava, 16–18/18–20 September 2004/2005*, pp. 71–80, Silesian University in Opava, Opava, ISBN 80-7248-334-X.

Karas, V. and Budinová, Z. (2000), Magnetic Fluxes Across Black Holes in a Strong Magnetic Field Regime, *Phys. Scripta*, **61**, pp. 253–256.

Karas, V. and Kopáček, O. (2009), Magnetic layers and neutral points near a rotating black hole, *Classical Quantum Gravity*, **26**(2), 025004, arXiv: `0811.1772`.

Karas, V., Kopáček, O. and Kunneriath, D. (2012), Influence of frame-dragging on magnetic null points near rotating black holes, *Classical Quantum Gravity*, **29**(3), 035010.

Karas, V., Kopáček, O. and Kunneriath, D. (2013), Magnetic Neutral Points and Electric Lines of Force in Strong Gravity of a Rotating Black Hole, *International Journal of Astronomy and Astrophysics*, **3**, pp. 18–24, arXiv: `1303.7251`.

Karas, V., Kopáček, O., Kunneriath, D. and Hamerský, J. (2014), Oblique magnetic fields and the role of frame dragging near rotating black hole, *Acta Polytechnica*, in press, arXiv: `1408.2452`.

Karas, V. and Vokrouhlický, D. (1991), On interpretation of the magnetized Kerr-Newman black hole., *J. Math. Phys.*, **32**, pp. 714–716.

King, A. R., Lasota, J. P. and Kundt, W. (1975), Black holes and magnetic fields, *Phys. Rev. D*, **12**, pp. 3037–3042.

Kramer, D., Stephani, H., Maccalum, M. and Herlt, E. (1980), *Exact solutions of the Einstein's field equations*, Deutscher Verlag der Wissenschaften, Berlin.

Nathanail, A. and Contopoulos, I. (2014), Black Hole Magnetospheres, *Astrophys. J.*, **788**, p. 186, arXiv: `1404.0549`.

Newman, E. and Penrose, R. (1962), An Approach to Gravitational Radiation by a Method of Spin Coefficients, *J. Math. Phys.*, **3**, pp. 566–578.

Ortaggio, M. (2005), Higher dimensional black holes in external magnetic fields, *Journal of High Energy Physics*, **5**, 048, arXiv: `gr-qc/0410048`.

Penna, R. F. (2014), Black hole Meissner effect and Blandford-Znajek jets, *Phys. Rev. D*, **89**(10), 104057, arXiv: `1403.0938`.

Punsly, B. (2008), *Black Hole Gravito-hydromagnetics*, Springer-Verlag, Berlin.

Teukolsky, S. A. (1973), Perturbations of a Rotating Black Hole. I. Fundamental Equations for Gravitational, Electromagnetic, and Neutrino-Field Perturbations, *Astrophys. J.*, **185**, pp. 635–648.

Thorne, K. S., Price, R. H. and Macdonald, D. A. (1986), *Black Holes: The Membrane Paradigm*, Yale University Press, New Haven.

Wald, R. M. (1974), Black hole in a uniform magnetic field, *Phys. Rev. D*, **10**, pp. 1680–1685.

Wald, R. M. (1984), *General Relativity*, University of Chicago Press, Chicago.

Yazadjiev, S. S. (2006), Magnetized black holes and black rings in the higher dimensional dilaton gravity, *Phys. Rev. D*, **73**(6), 064008, arXiv: `gr-qc/0511114`.

Proceedings of *RAGtime 10–13, 15–17/20–22/15–17/14–16 September, 2008/2009/2010/2011, Opava, Czech Republic*
Z. Stuchlík, G. Török and T. Pecháček, editors, Silesian University in Opava, 2014, pp. 93–102

Revealing general relativity effects from accretion events near a supermassive black hole

Vladimír Karas,[1†] Michal Dovčiak,[1] Andreas Eckart,[2,3]
Devaky Kunneriath[1] and Mohammad Zamaninasab[2,3]

[1]Astronomical Institute, Academy of Sciences, Boční II 1401, CZ-14131 Prague, Czech Republic
[2]I.Physikalisches Institut, Universität zu Köln, Zülpicher Str. 77, D-50937 Köln, Germany
[3]Max-Planck-Institut für Radioastronomie, Auf dem Hügel 69, D-53121 Bonn, Germany
[†]E-mail: `vladimir.karas@cuni.cz`

ABSTRACT
Accretion onto black holes often proceeds via an accretion disc or a temporary disc-like pattern. Variability features, observed in the light curves of such objects, and theoretical models of accretion flows suggest that inner accretion discs are inhomogeneous and clumpy. We discuss the general relativity effects acting on the radiation signal from the inner accretion flow. To this end we consider the radiation flux and polarization properties originating from a blob of gas near a rotating black hole. The predicted observed polarization at infinity is changed from its local value due to strong gravity and fast orbital motion. Different processes can produce the observed pattern: in the context of Sgr A* flares, the synchrotron mechanism and the inverse Compton upscattering appear to be the most likely mechanisms. The energy dependence of the changing degree and angle of polarization should allow us to discriminate between rotating (Kerr) and a non-rotating (Schwarzschild) black hole.

Keywords: Black holes – Galactic Center – Relativity

1 INTRODUCTION

Polarization of light originating from different regions of a black hole accretion disc and detected by a distant observer is influenced by strong gravitational field near a central black hole. A ‘spotted’ accretion disc is a useful model of an interface of such an inhomogeneous medium, assuming that there is a well defined boundary between the disc interior and the outer, relatively empty space. Relativistic corrections to a signal from orbiting spots can lead to large rotation in the plane of observed X-ray polarization. When integrated over an extended surface of the source, this can diminish the observed degree of polarization. Such effects are potentially observable and can be used to distinguish among different models of the source geometry and the radiation mechanisms responsible for the origin of the polarized signal. The polarization features show specific energy and time dependencies which can indicate whether a black hole is present in a compact X-ray source.

978-80-7510-125-9

Practical implementation of the idea, originally proposed in the late 1970s (Connors and Stark, 1977; Pineault, 1977), is a challenging task because the polarimetric investigations need a high signal-to-noise ratio. Also, the interpretation of the model results is often very sensitive to the assumptions about the radiation transfer in the source and the geometrical shape and orientation of the emission region. Nevertheless, the technology has achieved significant advances since the 1980s and reached a mature state.

We assume that the gravitational field is described by a rotating black hole, and so the Kerr metric is the right model for the gravitational field. Using a constant of motion along null geodesics in the Kerr metric (Walker and Penrose, 1970), one can determine the change of polarization angle along light rays. While the polarization degree is scalar and the gravitational influence of the black hole does not change it along the null geodesic (which is identical with the light ray path in the geometrical optics approximation), the observed polarization angle is affected. The calculations show that general-relativistic effects can cause large rotation of the polarization angle and produce significant fluctuations in the degree of observed polarization due to gravitational bending.

Although the geometrical effects of strong gravitational fields act on photons independently of their energy, the intrinsic emissivity of accretion discs and the influence of turbulent magnetic fields, intervening via Faraday rotation, are indeed energy dependent. As a result, the variability amplitudes of both the polarization degree the polarization angle must be energy dependent quantities as well. Furthermore, the signal resolved with respect to both energy and polarization (i.e. the spectro-polarimetric information) can probe different regions of the accretion disc due to radially varying temperature.

These dependencies suffer from some degeneracy, which can be avoided with time-resolved observations. Namely, if the source is an orbiting spot near a black hole, the time variation of the observed signal reflects the presence of strong gravity effects (Connors et al., 1980; Bao et al., 1997; Murphy et al., 2009). A related problem of spots rotating on the surface of a compact star was also investigated (Viironen and Poutanen, 2004).

On the whole, there are some similarities as well as differences between the expected manifestation of GR polarization changes in X-rays and in other spectral bands, such as the infrared region. We will mention these interrelations and point out that the near-infrared polarization measurements of the radiation flares from the immediate vicinity of the horizon are already now available for Sagittarius A* supermassive black hole in the Galaxy center (Meyer et al., 2006; Zamaninasab et al., 2008).

2 POLARIZATION FROM BLACK HOLE ACCRETION DISCS

It was realized some four decades ago that X-ray polarization studies could provide decisive clues to the physics of accreting compact objects (Angel 1969; Bonometto et al. 1970; Lightman and Shapiro 1975; Rees 1975). In the non-relativistic regime, a conceptually similar problem was discussed by Rudy (1978) and Fox (1994), who studied the polarization of star light caused by an ionized circumstellar shell of free electrons.

Wave fronts of light propagating near a rotating black hole do exhibit the frame dragging effect. On the other hand, the wave fronts do not depend on polarization (in geometrical optics approximation). Therefore, the impact of strong gravity on observed polarization comes in a somewhat complicated manner, through the interplay of light-bending, aberration and the Doppler effect.

In the context of accretion discs the effect of electron scattering atmosphere has been also often invoked. Further, polarization of the Comptonized radiation of accretion discs was examined as a function of various model parameters, such as the optical thickness of the disc medium, energy of scattered photons and directional angle of the emission (Stark 1981; Williams 1984; Sunyaev and Titarchuk 1985).

Two basic schemes were proposed as being relevant for the X-ray polarization from the inner accretion disc. Firstly, the accretion disc surface lies below the scattering atmosphere and acts as a source of seed photons. Polarization of thermal radiation from a black hole accretion disc was also studied (Laor et al., 1990). The reason for polarization is that photons from the disc are scattered by electrons within the disc atmosphere. Linear polarization should arise in the disc local co-rotating reference frame. This situation is expected to be particularly relevant for Galactic black hole candidates whose discs exhibit phases of strong multi-blackbody thermal radiation dominating over other spectral components. The early investigations were recently put forward by several groups (Dovčiak et al., 2008; Li et al., 2009). Secondly, Matt (1993) and Dovčiak et al. (2004) examined the polarimetric consequences of a specific model of a lamp-post illuminated accretion disc. Within this scheme the number of reflected (polarized) photons is proportional to the incident flux arriving from the primary source.

Relativistic effects would be even more prominent and unique if one could include the higher-order, gravitationally bent light rays (Horák and Karas 2006) and the effects of disc self-irradiation (Schnittman and Krolik, 2009). In fact, the latter authors argue that the self-irradiation effects can be surprisingly important for polarization measurements.

3 TIME-VARYING POLARIZATION FROM AN ORBITING SPOT

The model of an orbiting bright spot (e.g. Cunningham and Bardeen, 1972; Broderick and Loeb, 2006; Meyer et al., 2006; Noble et al., 2007) has been fairly successful in explaining the observed modulation of various accreting black hole sources. Certainly not all variability patterns can be explained in this way, however, the scheme is general enough to be able to capture also the effects of spiral waves and similar kind of transient phenomena that are expected to occur in the disc (Tagger et al. 1990, 2006; Karas et al. 2001). It can be argued that the spot lightcurves can be phenomenologically understood as a region of enhanced emission that performs a co-rotational motion near above the innermost stable circular orbit (ISCO). For example, within the framework of the flare-spot model (Czerny et al., 2004) the spots are just regions of enhanced emission on the disc surface rather than massive clumps that could suffer from fast decay due to shearing motion in the disc. The observed signal is modulated by relativistic effects. According to this idea, Doppler and gravitational lensing influence the observed radiation flux and this can be computed by ray-tracing methods. Such an approach has been extended to compute also strong gravity effects acting on polarization properties (Dovčiak et al., 2004).

To summarize our model, we assumed a Keplerian geometrically thin and optically thick disc around Kerr black hole. A spot is supposed to be intrinsically polarized by different mechanisms – either by reflection of a primary flare on the disc surface or by synchrotron

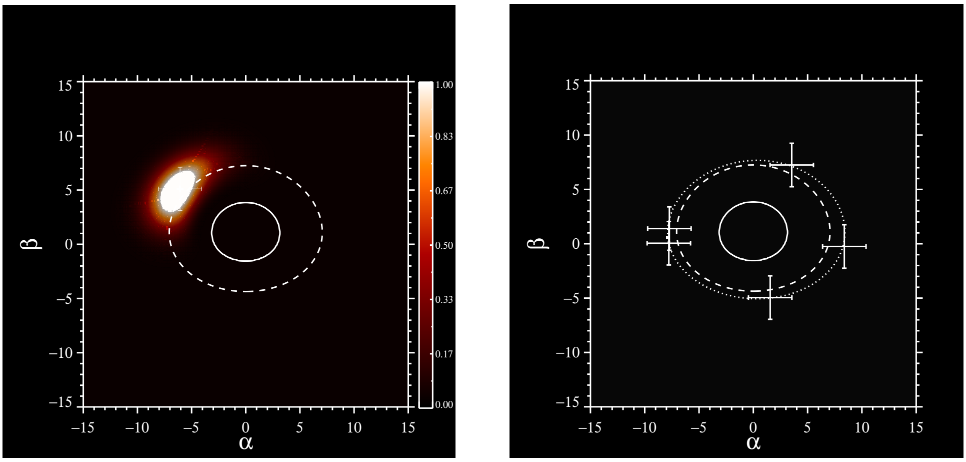

Figure 1. *Left*: A snapshot of a spot orbiting at constant radius $r = 1.1\,r_{\rm ISCO}$. The image is shown in the observer plane (α, β), for a non-rotating black hole observed at a moderate view angle, $\theta_{\rm o} = 45$ deg. The horizon radius (*solid curve*) and the ISCO (*dashed curve*) are shown for the reference. *Right*: Trajectory of the image centroid during one revolution of the spot. The wobbling position of the image centroid is indicated by crosses at different moments along the image track (*dotted curve*).

emission originating from an expanding blob, as detailed below, or within the framework of the accretion–ejection scheme (see also Melrose, 1971; Eckart et al., 2008; Huang et al., 2008 and references cited therein). The blob represents a rotating surface feature in the accretion flow. It shares the bulk orbital motion of the underlying medium at sufficiently large radii above the ISCO, gradually decaying due to differential rotation of the disc.

We have applied different prescriptions for the local polarization (see Dovčiak et al., 2006; Meyer et al., 2006; Zamaninasab et al., 2008 for the detailed description of the model set-up in the individual cases that we investigated). For example, one set of models assumes the local emission to be polarized either in the direction normal to the disc plane, or perpendicular to the toroidal magnetic field. Obviously, in the case of partial local polarization the observed polarization signal will be diluted by an unpolarized fraction, and so the polarization degree of the final signal will be proportionally diminished. In another set of models we assumed a lamp-post illuminated spot as the source of spot polarization by reflection. For the spot shape we first assumed the spot does not change its shape during its orbit, but then we also consider the spot decay with time. The relativistic effects can be clearly identified and understood with these simple (and astrophysically unrealistic) toy models, as they produce visible signatures in the observed polarization properties.

General relativistic effects present in our model can be split into two categories. Firstly, it is the symmetry breaking between the approaching and the receding part of the spot orbit. Doppler beaming as well as the light focusing contribute to the change of the observed flux, especially at high view angles when the spot orbit is seen almost edge-on. Notice that the Doppler boosting effect is off phase with respect to the light focusing effect, roughly by 0.25 of the full orbit at the corresponding radius. Here, the precise number depends on the

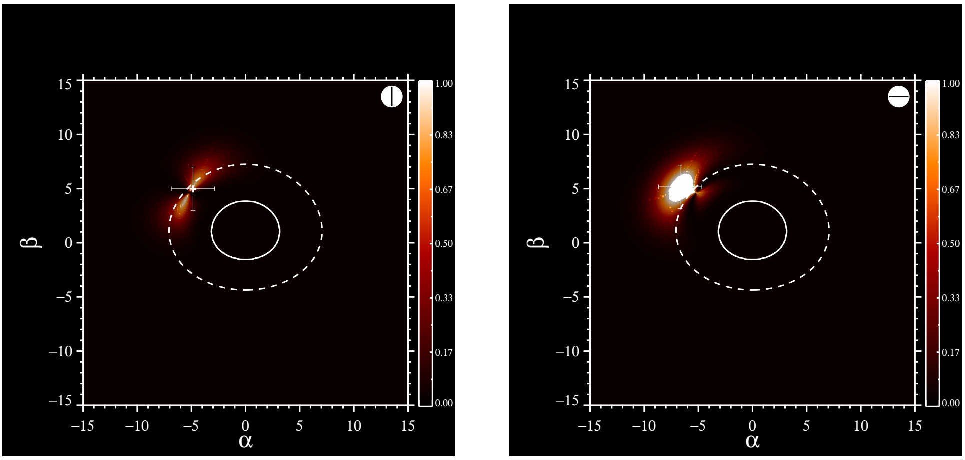

Figure 2. As in the left panel of the previous figure, but now the spot emission is assumed to be intrinsically polarized and recorded in two polarization channels, rotated by 90 degrees with respect to each other (Zamaninasab et al., 2010).

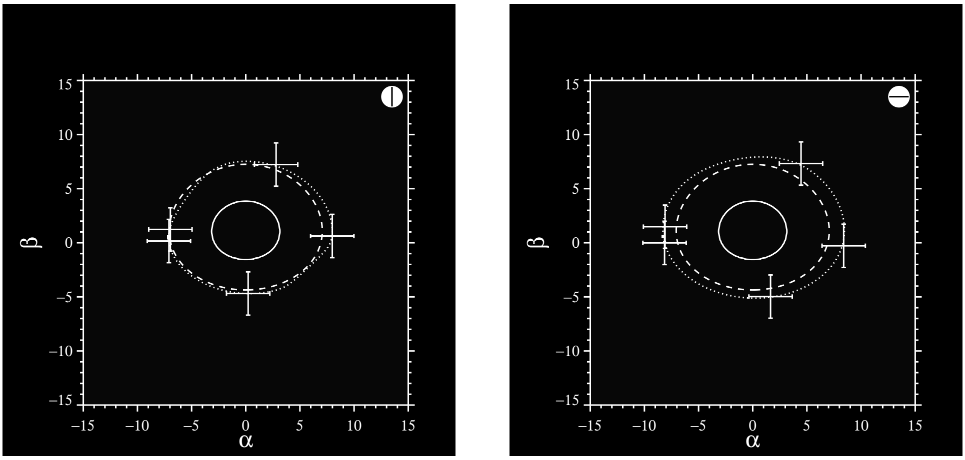

Figure 3. Trajectory of the image centroid during one revolution of the spot corresponding to the previous figure.

black hole spin; it also depends on the inclination through the finite light-travel time from different parts of the spot orbit towards the observer. Also, higher order images could be important in case of almost edge-on view of the spot.

Secondly, rotation of the polarization plane along the photon trajectory also plays a role. This effect is particularly strong for small radii of the spot orbit, in which case a critical point occurs (Dovčiak et al., 2008). The observed polarization angle exhibits just a small wobbling around its principal direction when the spot radius is above the critical point, whereas it starts turning around the full circle once the radius drops below the critical

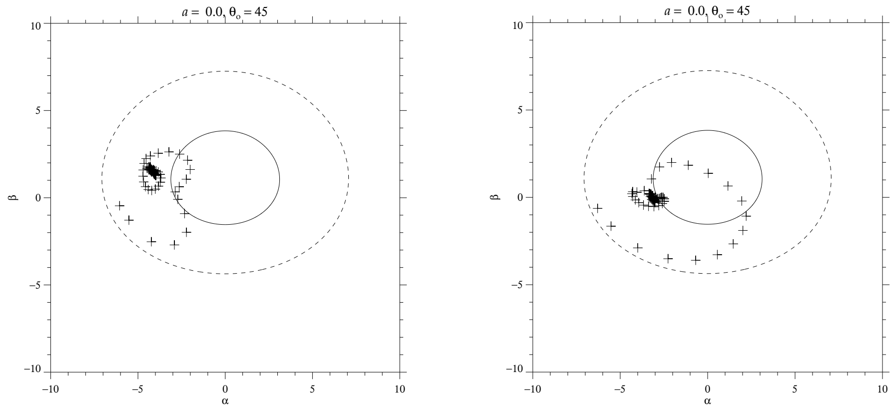

Figure 4. Similar to Fig. 3, but now the spot is supposed to become elongated and eventually decay due to the shearing motion in the accretion disc. Also the disc itself also to part of the emitted radiation in this example. The case of a rotating black hole, $a = 0.5\,M$, seen at $\theta_\mathrm{o} = 45$ deg. The final track of the centroid image was extracted, taking into account both the spot and the underlying disc contributions. As a result of this model set-up, the centroid wobbles slightly off the actual center of the system, and the centroid motion evolves as the spot gradually disappears. Each orbit remains just above the ISCO and the image of the corresponding track settles down within one or two full orbits.

one. Notice that the exact location of the critical point depends on the black hole angular momentum, in principle allowing us to determine its value.

However, a caveat (and a third point on the list) is caused by sensitivity of the critical radius to the special relativistic aberration effects, especially at small view angles (i.e. when the spot is seen almost along the rotation axis). This means that the moment when the observed polarization angle starts rotating is sensitive to the underlying assumption of a perfectly planar geometry of the disc surface.

Obviously the turbulent magnetic fields will play a role in diminishing the observed polarization degree, and that part has been neglected in the present contribution. It is worth noticing, however, that the impact of Faraday rotation on the observed polarization decreases with the square of photon energy, and hence it is less restricting in the X-ray band.

By combining the above-mentioned effects together, Dovčiak et al. (2006) have shown that the observed polarization degree is expected to decrease (in all their models) mainly in that part of the orbit where the spot moves close to the region where the photons are emitted perpendicularly to the disc. In this situation the polarization angle changes rapidly. The decrease in the observed polarization degree for the local polarization perpendicular to the toroidal magnetic field happens also in those parts of the orbit where the magnetic field points approximately along light ray.

However, for the more realistic models the resulting polarization shows a much more complex behaviour. Among persisting features is the peak in polarization degree for the extreme Kerr black hole for large inclinations, caused by the lensing effect at a particular position of the spot in the orbit where the polarization angle is changed. This is not visible in the Schwarzschild case.

The X-ray polarization lightcurves and spectra are still to be taken by future missions, but one may envision even a more challenging goal connected with imaging of the inner regions of accreting black hole sources. Obviously this is a truly distant future: imaging a black hole shadow would require order of ten microsecond angular resolution. However, what might be realistically foreseen is the tracking of the wobbling image centroid that a spot is supposed to produce (Hamaus et al., 2009; Zamaninasab et al., 2010). With the polarimetric resolution, the wobbling could provide an excellent evidence proving the presence of the orbiting feature. See Figures 1–4 for examples of the expected form of the spot images and the corresponding centroid tracks in a simplified case of a model spot endowed with an intrinsic polarization that remains constant in the co-orbiting frame.

Figure 1 assumes a spot rotating rigidly at constant radius near above the ISCO. Figure 2 corresponds to the case of intrinsically polarized spot radiation of which is recorded behind the polarization filter. Orientation of the filter is fixed and indicated in the top-right corner of the plot. Correspondingly, Fig. 3 shows the tracks of the image centroid. Albeit the tracks are not identical in the two orientations of the polarization filter, the difference is rather subtle. Notice that the project of detecting the centroid motion does not necessarily have to be limited to the X-ray domain. In view of recent results on Sagittarius A* flares, which have been reported in X-rays as well as in the near infrared, submillimiter and the radio spectral bands (Eckart et al., 2008), the immediate vicinity of the black hole can be probed by various techniques. The simultaneous time-dependent measurements equipped with the polarimetric resolution seem to be a final goal of this effort.

In Figure 4, the contribution from a time-evolving evolving spot and the (axially symmetric and stationary) background disc are taken into account. When put in this way, the spot represents a travelling disturbance in the disc medium, while the effect of the background disc causes a small but persisting offset of the centroid track towards the Doppler enhanced side of the disc. The changes predicted for the observed signal are now visibly larger and they are caused by the interplay between the relativistic effects and the shearing decay of the spot.

It may be worth reminding the reader that the KY code, employed in our computations, is publicly available, either as a part of the XSPEC package or directly from the authors (Dovčiak et al., 2004). The current version allows the user to include the polarimetric resolution and to compute the observational consequences of strong-gravity effects from a Kerr black hole accretion disc. Within the XSPEC notation, this polarimetric resolution is encoded by a switch defining which of the four Stokes parameters is returned in the photon count array at the moment of the output from the model evaluation. This way one can test and combine various models, and pass the resulting signal through the response matrices of different instruments.

4 CONCLUSIONS

The task of detecting the relativistic effects and in this way determining the physical parameters of the black hole systems seems to be feasible in near future. Among possible ways to reach the goal, time-dependent polarization profiles, such as those expected from orbiting spots, play an important role. In our work, the adopted approach is based on mapping the Kerr black hole equatorial plane onto the observer's plane at radial infinity. Off equatorial features are first projected onto the disc plane, hence imposing the vertically averaged approximation. A conceptually similar problem of a vertically thick oscillating torus has been studied recently by Horák and Bursa (2010), who employed a new three-dimensional code and with its help examined different modes of the torus oscillation.

To conclude, the strong gravity effects can be revealed as the observable direction of polarization is changed upon light propagation near a black hole. This may be relevant not only for the inner regions of active galactic nuclei, for which we assumed the X-ray reflection as a mechanism producing spectral and polarimetric features, but also for the radiation coming from individual blobs of gas orbiting near the Galaxy Center, where an interplay between synchrotron and inverse Compton mechanisms is expected to play a role. Spots are among viable models capable to explain the occurrence about once per day of flares from within a few milli-arcseconds of the supermassive black hole, Sagittarius A*. Because of short time-scales the flares cannot be understood in terms of viscous processes in the standard accretion disc with some appreciable accretion rate. It has been widely known that the flares from the very vicinity of the black hole are highly polarized in near-infrared, however, we are still lacking any polarimetric information on this object in X-rays.

ACKNOWLEDGEMENTS

We acknowledge support from Czech Science Foundation – Deutsche Forschungsgemeinschaft collaboration project No. 13-00070J.

REFERENCES

Angel, J. R. P. (1969), Polarization of Thermal X-Ray Sources, *Astrophys. J.*, **158**, p. 219.

Bao, G., Hadrava, P., Wiita, P. J. and Xiong, Y. (1997), Polarization Variability of Active Galactic Nuclei and X-Ray Binaries, *Astrophys. J.*, **487**, pp. 142–152.

Bonometto, S., Cazzola, P. and Saggion, A. (1970), Polarization in Inverse Compton Effect, *Astronomy and Astrophysics*, **7**, p. 292.

Broderick, A. E. and Loeb, A. (2006), Imaging optically-thin hotspots near the black hole horizon of Sgr A* at radio and near-infrared wavelengths, *Monthly Notices Roy. Astronom. Soc.*, **367**, pp. 905–916, arXiv: `astro-ph/0509237`.

Connors, P. A. and Stark, R. F. (1977), Observable gravitational effects on polarised radiation coming from near a black hole, *Nature*, **269**, p. 128.

Connors, P. A., Stark, R. F. and Piran, T. (1980), Polarization features of X-ray radiation emitted near black holes, *Astrophys. J.*, **235**, pp. 224–244.

Cunningham, C. T. and Bardeen, J. M. (1972), The Optical Appearance of a Star Orbiting an Extreme Kerr Black Hole, *Astrophys. J. Lett.*, **173**, p. L137.

Czerny, B., Różańska, A., Dovčiak, M., Karas, V. and Dumont, A.-M. (2004), The structure and radiation spectra of illuminated accretion disks in AGN. II. Flare/spot model of X-ray variability, *Astronomy and Astrophysics*, **420**, pp. 1–16, arXiv: `astro-ph/0402394`.

Dovčiak, M., Karas, V., Martocchia, A., Matt, G. and Yaqoob, T. (2004), An XSPEC model to explore spectral features from black-hole sources, in S. Hledík and Z. Stuchlík, editors, *Proceedings of RAGtime 4/5: Workshops on black holes and neutron stars, Opava, 14–16/13–15*

October 2002/2003, pp. 33–73, Silesian University in Opava, Opava, ISBN 80-7248-242-4, arXiv: astro-ph/0408092.

Dovčiak, M., Karas, V. and Matt, G. (2004), Polarization signatures of strong gravity in active galactic nuclei accretion discs, *Monthly Notices Roy. Astronom. Soc.*, **355**, pp. 1005–1009, arXiv: astro-ph/0409356.

Dovčiak, M., Karas, V. and Matt, G. (2006), X-ray spectra and polarization from accreting black holes: polarization from an orbiting spot, *Astronom. Nachr.*, **327**, p. 993.

Dovčiak, M., Muleri, F., Goosmann, R. W., Karas, V. and Matt, G. (2008), Thermal disc emission from a rotating black hole: X-ray polarization signatures, *Monthly Notices Roy. Astronom. Soc.*, **391**, pp. 32–38, arXiv: 0809.0418.

Eckart, A., Baganoff, F. K., Zamaninasab, M., Morris, M. R., Schödel, R., Meyer, L., Muzic, K., Bautz, M. W., Brandt, W. N., Garmire, G. P., Ricker, G. R., Kunneriath, D., Straubmeier, C., Duschl, W., Dovciak, M., Karas, V., Markoff, S., Najarro, F., Mauerhan, J., Moultaka, J. and Zensus, A. (2008), Polarized NIR and X-ray flares from Sagittarius A*, *Astronomy and Astrophysics*, **479**, pp. 625–639, arXiv: 0712.3165.

Fox, G. K. (1994), The theoretical polarization of pure scattering axisymmetric circumstellar envelopes, *Astrophys. J.*, **435**, pp. 372–378.

Hamaus, N., Paumard, T., Müller, T., Gillessen, S., Eisenhauer, F., Trippe, S. and Genzel, R. (2009), Prospects for Testing the Nature of Sgr A*'s Near-Infrared Flares on the Basis of Current Very Large Telescope and Future Very Large Telescope Interferometer–Observations, *Astrophys. J.*, **692**, pp. 902–916, arXiv: 0810.4947.

Horák, J. and Bursa, M. (2010), Polarization from the oscillating magnetized accretion torus, in R. Bellazzini, E. Costa, G. Matt and G. Tagliaferri, editors, *X-ray Polarimetry: A New Window in Astrophysics*, p. 182, Cambridge University Press, ISBN 9780521191845.

Horák, J. and Karas, V. (2006), On the role of strong gravity in polarization from scattering of light in relativistic flows, *Monthly Notices Roy. Astronom. Soc.*, **365**, pp. 813–826, arXiv: astro-ph/0510532.

Huang, L., Liu, S., Shen, Z.-Q., Cai, M. J., Li, H. and Fryer, C. L. (2008), Linearly and Circularly Polarized Emission in Sagittarius A*, *Astrophys. J. Lett.*, **676**, pp. L119–L122, arXiv: 0802.3561.

Karas, V., Martocchia, A. and Subr, L. (2001), Variable Line Profiles Due to Non-Axisymmetric Patterns in an Accretion Disc around a Rotating Black Hole, *Publications of the Astronomical Society of Japan*, **53**, pp. 189–199, arXiv: astro-ph/0102460.

Laor, A., Netzer, H. and Piran, T. (1990), Massive thin accretion discs. II - Polarization, *Monthly Notices Roy. Astronom. Soc.*, **242**, pp. 560–569.

Li, L.-X., Narayan, R. and McClintock, J. E. (2009), Inferring the Inclination of a Black Hole Accretion Disk from Observations of its Polarized Continuum Radiation, *Astrophys. J.*, **691**, pp. 847–865, arXiv: 0809.0866.

Lightman, A. P. and Shapiro, S. L. (1975), Spectrum and polarization of X-rays from accretion disks around black holes, *Astrophys. J. Lett.*, **198**, pp. L73–L75.

Matt, G. (1993), X-ray polarization properties of a centrally illuminated accretion disc, *Monthly Notices Roy. Astronom. Soc.*, **260**(3), pp. 663–674.

Melrose, D. B. (1971), On the Degree of Circular Polarization of Synchrotron Radiation, *Astrophys. and Space Sci.*, **12**, pp. 172–192.

Meyer, L., Eckart, A., Schödel, R., Duschl, W. J., Mužić, K., Dovčiak, M. and Karas, V. (2006), Near-infrared polarimetry setting constraints on the orbiting spot model for Sgr A* flares, *Astronomy and Astrophysics*, **460**, pp. 15–21, arXiv: astro-ph/0610104.

Murphy, K. D., Yaqoob, T., Karas, V. and Dovčiak, M. (2009), On the Prospect of Constraining Black Hole Spin Through X-ray Spectroscopy of Hotspots, *Astrophys. J.*, **701**, pp. 635–641, arXiv: 0906.4713.

Noble, S. C., Leung, P. K., Gammie, C. F. and Book, L. G. (2007), Simulating the emission and outflows from accretion discs, *Classical Quantum Gravity*, **24**, pp. S259–S274, arXiv: astro-ph/0701778.

Pineault, S. (1977), Polarized radiation from a point source orbiting a Schwarzschild black hole, *Monthly Notices Roy. Astronom. Soc.*, **179**, pp. 691–697.

Rees, M. J. (1975), Expected polarization properties of binary x-ray sources, *Monthly Notices Roy. Astronom. Soc.*, **171**(3), pp. 457–465.

Rudy, R. J. (1978), Polarization from thomson scattering of the light of a spherical, limb-darkened star, *Publications of the Astronomical Society of the Pacific*, **90**(538), pp. 688–691.

Schnittman, J. D. and Krolik, J. H. (2009), X-ray Polarization from Accreting Black Holes: The Thermal State, *Astrophys. J.*, **701**, pp. 1175–1187, arXiv: 0902.3982.

Stark, R. F. (1981), The radiative polarization transfer equations in hot comptonizing electron scattering atmospheres including induced scattering, *Monthly Notices Roy. Astronom. Soc.*, **195**(2), pp. 115–126.

Sunyaev, R. A. and Titarchuk, L. G. (1985), Comptonization of low-frequency radiation in accretion disks Angular distribution and polarization of hard radiation, *Astronomy and Astrophysics*, **143**, pp. 374–388.

Tagger, M., Henriksen, R. N., Sygnet, J. F. and Pellat, R. (1990), Spiral waves and instability in magnetized astrophysical disks, *Astrophys. J.*, **353**, pp. 654–657.

Tagger, M. and Melia, F. (2006), A Possible Rossby Wave Instability Origin for the Flares in Sagittarius A*, *Astrophys. J. Lett.*, **636**, pp. L33–L36, arXiv: astro-ph/0511520.

Viironen, K. and Poutanen, J. (2004), Light curves and polarization of accretion- and nuclear-powered millisecond pulsars, *Astronomy and Astrophysics*, **426**, pp. 985–997, arXiv: astro-ph/0408250.

Walker, M. and Penrose, R. (1970), On quadratic first integrals of the geodesic equations for type $\{22w\}$ spacetimes, *Comm. Math. Phys.*, **18**, pp. 265–274.

Williams, A. C. (1984), Polarization of Comptonized photons, *Astrophys. J.*, **279**, pp. 401–412.

Zamaninasab, M., Eckart, A., Meyer, L., Schödel, R., Dovčiak, M., Karas, V., Kunneriath, D., Witzel, G., Gießübel, R., König, S., Straubmeier, C. and Zensus, A. (2008), An evolving hot spot orbiting around Sgr A*, *Journal of Physics Conference Series*, **131**(1), 012008, arXiv: 0810.0138.

Zamaninasab, M., Eckart, A., Witzel, G., Dovciak, M., Karas, V., Schödel, R., Gießübel, R., Bremer, M., García-Marín, M., Kunneriath, D., Mužić, K., Nishiyama, S., Sabha, N., Straubmeier, C. and Zensus, A. (2010), Near infrared flares of Sagittarius A*. Importance of near infrared polarimetry, *Astronomy and Astrophysics*, **510**, A3, arXiv: 0911.4659.

Z. Stuchlík, G. Török and T. Pecháček, editors, Silesian University in Opava, 2014, pp. 103–111

String loop chaotic scattering in the field of Schwarzschild black hole

Martin Kološ[a] and Zdeněk Stuchlík[b]

Institute of Physics, Faculty of Philosophy & Science, Silesian University in Opava, Bezručovo nám. 13, CZ-746 01 Opava, Czech Republic
[a]`Martin.Kolos@fpf.slu.cz`
[b]`Zdenek.Stuchlik@fpf.slu.cz`

ABSTRACT
Relativistic current-carrying string loop moving axisymmetrically along the axis of a Schwarzschild black hole is investigated as model of relativistic jet formation. Acceleration of the string loop along its axis of symmetry shows regular and also irregular dependence on initial conditions. We will apply the theory of chaotic scattering on this problem.

Keywords: string loop – relativistic jets – chaotic scattering – Schwarzschild – black holes

1 INTRODUCTION

Current-carrying string loop model is relativistic string with circular shape threaded on to black hole axis. Tension of such string loops prevents their expansion beyond some radius, while their worldsheet current introduces an angular momentum barrier preventing them from collapsing into the black hole. The string loop oscillates in the x-z plane propagating simultaneously in the y-direction. Such model could in a simplified way represent plasma that exhibits associated string-like behaviour via dynamics of the magnetic field lines in the plasma (Semenov et al., 2004) or due to thin isolated flux tubes of magnetized plasma that could be described by an one-dimensional string (Spruit, 1981; Semenov and Bernikov, 1991).

From the astrophysical point of view, one of the most relevant applications of the axisymmetric string loop motion is the possibility of strong acceleration of the linear translational string loop motion due to the transmutation process in the strong gravity of extremely compact objects that could well mimic acceleration of relativistic jets in Active Galactic Nuclei (AGN) and microquasars (Jacobson and Sotiriou, 2009). Due to chaotic nature of string loop equation of motion (Frolov and Larsen, 1999), the resulting acceleration in the terms of the translational velocity or gamma factor shows strong dependence on the initial conditions (Stuchlík and Kološ, 2009). In this article we would like to address this problem from the point of view of chaotic scattering theory as it is presented in Chapter 5 of Ott (1993) and Chapter 8 in Tél and M. (2006).

978-80-7510-125-9

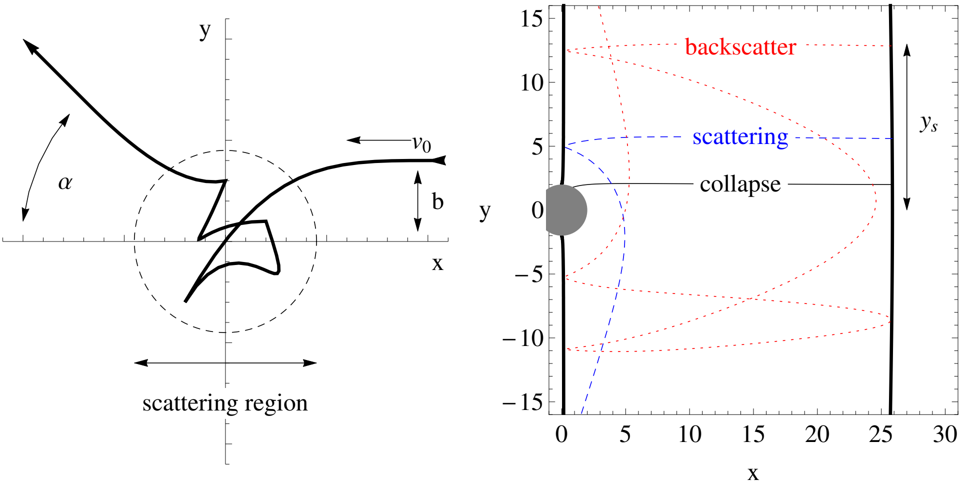

Figure 1. Schematic picture of standard chaotic scattering of particle moving towards scattering region of effective potential (*left*) and chaotic scattering of string loop on Schwarzschild black hole (*right*). On the right, in the case of string loop, we assumed axial symmetry which allows to investigate only one point of the loop; one point path can represent whole string loop movement. Trajectory of the loop is then represented by the black curve on the picture, given in 2D x-y plot. If the string loop is in equatorial plane $y = 0$, its overall loop circle will be seen in x-z plane.

Let us we have a particle with impact parameter b, entering some part of effective potential (scattering region), and let's the particle can escape the scattering region with some scattering angle α, see Fig. 1 (left). We can define scattering angle (scattering function) $\alpha(b)$ as a function depending on impact parameter b. Chaotic scattering theory is dealing with the properties of scattering function $\alpha(b)$, especially when $\alpha(b)$ shows some "strange" (chaotic behaviour). In our system of string loop winding around black hole, we will shoot string loops from some position y_s giving initial distance from the equatorial plane (impact parameter), towards to the black hole (effective potential) and we will measure final gamma factor γ (scattering angle), see Fig. 1 (right). Properties of the scattering function $\gamma(y_s)$ for string loop dynamics in the vicinity of Schwarzschild black hole are examined in this report.

2 CURRENT-CARRYING STRING LOOP

We study a string loop motion in the field of a black hole described by the Schwarzschild metric

$$\mathrm{d}s^2 = -A(r)\,\mathrm{d}t^2 + A^{-1}(r)\,\mathrm{d}r^2 + r^2\big(\mathrm{d}\theta^2 + \sin^2\theta\,\mathrm{d}\phi^2\big), \qquad A(r) = 1 - \frac{2M}{r}\,. \tag{1}$$

We use the geometric units with $c = G = 1$ and the Schwarzschild coordinates. In order to properly describe the string loop motion, it is useful to use the Cartesian coordinates

$$x = r\,\sin(\theta), \qquad y = r\,\cos(\theta)\,. \tag{2}$$

The string loop is threaded on to an axis of the black hole chosen to be the y-axis. Due to the assumed axisymmetry of the string motion one point path can represent whole movement of the string. Trajectory of the string can be represented by a curve in the 2D x-y plane, see Fig. 1 (right). The string loop can oscillate, changing its radius in the x-z plane, while propagating in the y direction.

The string loop motion is governed by barriers given by the string tension and the worldsheet current determining the angular momentum – these barriers are modified by the gravitational field. Dynamics of the string is described by the action

$$S = \int \mathrm{d}^2\sigma \sqrt{-h}\left(\mu + h^{ab}\varphi_{,a}\varphi_{,b}\right) , \tag{3}$$

where $\varphi_{,a} = j_a$ determines current of the string and $\mu > 0$ reflects the string tension. Axisymmetry of the string loop means that the scalar field $\varphi = j_\sigma \sigma + j_\tau \tau$, where j_σ and j_τ are constant components of the current.

The worldsheet stress-energy tensor density $\tilde{\Sigma}^{ab}$ can be expressed in the form (Jacobson and Sotiriou, 2009)

$$\tilde{\Sigma}^{\tau\tau} = \frac{J^2}{g_{\phi\phi}} + \mu\,, \quad \tilde{\Sigma}^{\sigma\sigma} = \frac{J^2}{g_{\phi\phi}} - \mu\,, \quad \tilde{\Sigma}^{\sigma\tau} = \frac{-2 j_\tau j_\sigma}{g_{\phi\phi}}\,, \quad J^2 \equiv j_\sigma^2 + j_\tau^2\,. \tag{4}$$

As demonstrated in (Larsen, 1993; Carter and Steer, 2004), the string loop motion in spherically symmetric spacetime can be described by the Hamiltonian

$$H = \frac{1}{2} g^{rr} P_r^2 + \frac{1}{2} g^{\theta\theta} P_\theta^2 + \frac{1}{2} g_{\phi\phi} \left(\Sigma^{\tau\tau}\right)^2 + \frac{1}{2} g^{tt} E^2\,. \tag{5}$$

The equations of motion are given by the Hamilton equations

$$\frac{\mathrm{d}X^\mu}{\mathrm{d}\zeta} = \frac{\partial H}{\partial P_\mu}\,, \quad \frac{\mathrm{d}P_\mu}{\mathrm{d}\zeta} = -\frac{\partial H}{\partial X^\mu}\,. \tag{6}$$

Due to symmetries of metrics (1) we have conserved quantities string loop energy E and string loop angular momentum L, given by

$$-E = P_t = g_{tt} \tilde{\Sigma}^{\tau\tau} X^t_{|\tau}\,, \quad L = P_\phi = g_{\phi\phi} \tilde{\Sigma}^{\sigma\tau} = -2 j_\tau j_\sigma\,. \tag{7}$$

Hamiltonian is constant of the motion $H = 0$. The loci where the string loop has zero velocity ($\dot{r} = 0, \dot{\theta} = 0$) form boundary of the string motion

$$E = E_{\mathrm{b}}(r, \theta) = \sqrt{-g_{tt} g_{\phi\phi}}\, \tilde{\Sigma}^{\tau\tau}\,. \tag{8}$$

There are four different types of the behaviour of the energy boundary function for the string loop dynamics in the Schwarzschild BH spacetime represented by the characteristic $E =$ const. sections of the $E_{\mathrm{b}}(r, \theta)$ function in dependence on parameter J (Jacobson and Sotiriou, 2009). We can distinguish them according to two properties: possibility of the string loop to escape to infinity in the y-direction, and possibility to collapse to the black hole. A detailed discussion can be found in Kološ and Stuchlík (2010).

The first case corresponds to no inner and outer boundary – the string loop can be captured by the black hole or escape to infinity. The second case corresponds to the situation with an outer boundary – the string loop must be captured by the black hole. The third case corresponds to the situation when both inner and outer boundary exist – the string loop is trapped in some region forming a potential "lake" around the black hole. The fourth case corresponds to an inner boundary – the string loop cannot fall into the black hole but it must escape to infinity, see Fig. 2 in Stuchlík and Kološ (2009). For our following discussion only the first and fourth case, corresponding to the possibility of the string loop to escape to infinity in the y-direction, will be relevant.

3 STRING LOOP ASYMPTOTICAL EJECTION SPEED

Since the Schwarzschild spacetime is asymptotically flat, we will discuss the string loop motion in the flat spacetime that enables clear definition of the acceleration process. The energy of the string loop (8) in the flat spacetime, expressed in the Cartesian coordinates, reads

$$E^2 = \dot{y}^2 + \dot{x}^2 + \left(\frac{J^2}{x} + x\right)^2 = E_{\mathrm{y}}^2 + E_{\mathrm{x}}^2 \,, \tag{9}$$

where dot denotes derivative with respect to the affine parameter ζ. The energy related to the motion in the x- and y-directions are given by the relations

$$E_{\mathrm{y}}^2 = \dot{y}^2, \quad E_{\mathrm{x}}^2 = \dot{x}^2 + \left(\frac{J^2}{x} + x\right)^2 = (x_{\mathrm{i}} + x_{\mathrm{o}})^2 = E_0^2 \tag{10}$$

where x_i (x_o) represent the inner (outer) limit of the oscillatory motion. The energy E_0 representing the internal energy of the string loop is minimal when the inner and the outer radii coincide, leading to the relation

$$E_{0(\mathrm{min})} = 2J \tag{11}$$

that determines the minimal energy necessary for escaping of the string loop to infinity. Clearly, $E_{\mathrm{x}} = E_0$ and E_{y} are constants of the string loop motion and no transformation between these energy modes is possible in the flat spacetime. However, in strong gravity in vicinity of black holes or naked singularities, the internal kinetic energy of the oscillating string can be transmitted into the kinetic energy of the translational linear motion (or vice versa) due to the chaotic character of the string loop dynamics (Jacobson and Sotiriou, 2009; Stuchlík and Kološ, 2012a).

In order to get a strong acceleration in the Schwarzschild spacetime, the string loop has to pass the region of strong gravity near the black hole horizon (scattering region), where the string transmutation effect $E_{\mathrm{x}} \leftrightarrow E_{\mathrm{y}}$ can occur. All energy of the transitional (E_{y}) energy mode can be transmitted to the oscillatory (E_{x}) energy mode – oscillations of the string loop in the x-direction and the internal energy of the string will increase maximally in such a situation, while the string will stop moving in the y-direction. However, all energy of

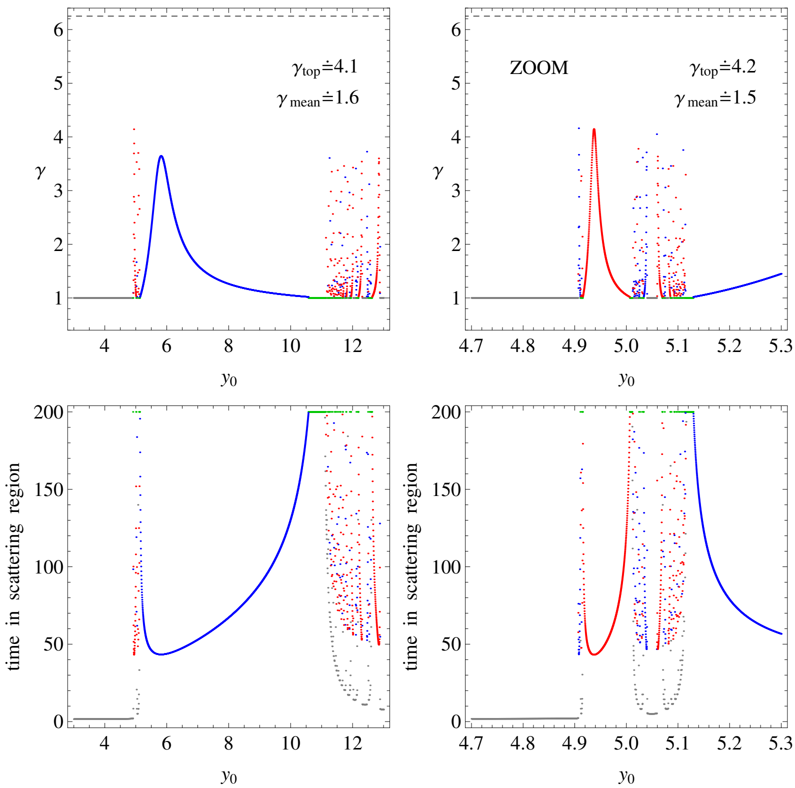

Figure 2. Scattering function $\gamma(y_s)$ (Lorentz factor at infinity) and time spend by the string loop in the region close to the black hole horizon (scattering region) is calculated for energy $E = 25$ and current $J = 2$. All trajectories starting from the rest with different initial position $y_0 \in (3, 13)$ while x_0 is calculated from E_b condition (8). Gray points correspond to the string loops collapsed to the black hole, blue to the scattered and red backscattered string loops. Green are trajectories which were not able to reach numerical infinity located at $r = 1000$ in given maximal integration time $\zeta = 200$. Examples of individual trajectories trajectories can be found in Fig. 1. Maximal acceleration for this case (13) gives us the limiting gamma factor $\gamma_{max} = 6.25$ (*dashed line*). We show the topical gamma factor that is numerically found in the sample, γ_{top}, and also the mean value γ_{mean} from the sample. Figure on the left is only zoom in to the figure on the right for values $y_0 \in (4.7, 5.3)$ (first chaotic band).

the E_x mode cannot be transmitted into the E_y energy mode – there remains inconvertible internal energy of the string, $E_{0(min)} = 2J$, being the minimal potential energy hidden in the E_x energy mode.

The final Lorentz factor of the transitional motion of an accelerated string loop as observed in the asymptotically flat region of the Schwarzschild spacetime is, due to (10), determined by the relation (Jacobson and Sotiriou, 2009; Stuchlík and Kološ, 2012a)

$$\gamma = \frac{E}{E_0} = \frac{E}{x_i + x_o}, \tag{12}$$

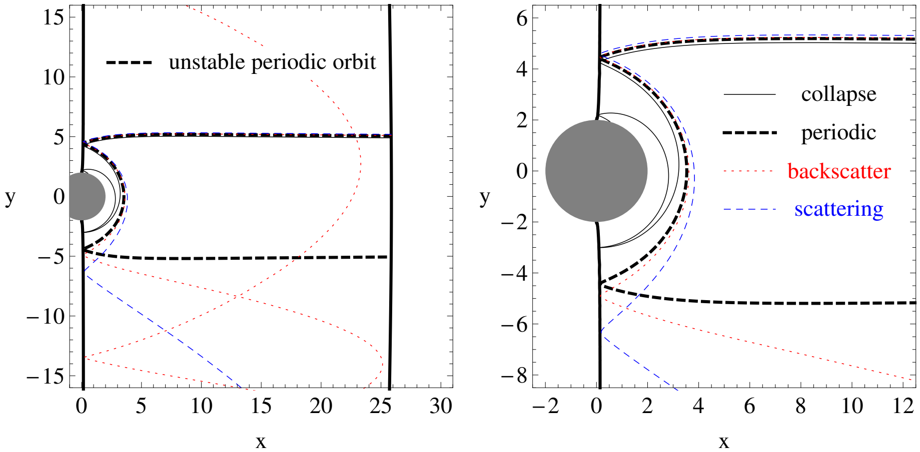

Figure 3. String loop unstable periodic orbit (UPO) compared to orbits obtained by slight change in UPO initial conditions. Presented UPO, with initial starting position $y_s \doteq 5.05905$, is responsible for first chaotic band on left Fig. 2.

where E is the total energy of the string loop moving with the internal energy E_0 in the y-direction with the velocity corresponding to the Lorentz factor γ.

To see how the acceleration of the string loop in the field of Schwarzschild black hole works, we will start to "shoot" string loops from position $x_s \sim 25$, $y_s \in (3, 13)$ with energy $E = 25$ and current $J = 2$, see Fig. 1 (right). Maintaining the string loop energy $E = 25$ constant for all trajectories of $y_s \in (3, 13)$ sample, we must calculate the starting coordinate x_s from energy condition (8). For every starting position y_s (impact parameter) we will measure final gamma factor, γ given by (12) and hence obtaining the gamma factor $\gamma(y_s)$ (scattering function) as function of starting position.

As can be seen from Fig. 2., the scattering function $\gamma(y_s)$ have some regular scattering regions, example is the region $y_s \in (6, 10)$, where the final γ factor is changing continuously with initial starting position y_s. Such behaviour is expected by common sense, because it is observed in many normal (non chaotic) scatterings. But for chaotic scattering there are also chaotic regions (chaotic bands), example is the region $y_s \in (5.0, 5.1)$, where it is not possible to predict final γ factor output from neighbouring initial starting points $y_s \pm \delta$ – the scattering function $\gamma(y_s)$ is not continuous.

To find the origin of chaotic bands in our system, we can compare the scattering function $\gamma(y_s)$ (upper row of pictures in Fig. 2) with the the integration time which the string loop is spending in region close to the black hole horizon (scattering region) before escaping to the infinity (lower row of pictures in Fig. 2). Now it is obvious, that trajectories from chaotic bands are spending large amount of time in region close to the black hole; many time crossing the equatorial plane in attempt to decide in which direction to go. The origin of such string loop motion lies in the existence of the unstable periodic orbits (UPOs) in the system, (Ott, 1993; Tél and M., 2006).

String loop at an unstable periodic orbit (UPO) will forever periodically oscillate close to black hole horizon and never leave it, even if there is possibility for escape to infinity from the energetic point of view (energy boundary function E_b is open to infinity in y

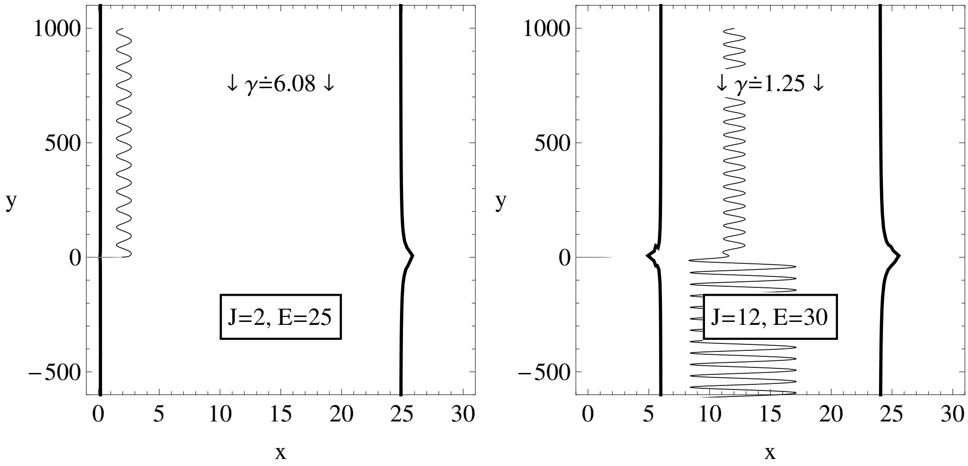

Figure 4. Particle is coming from infinity with almost maximal speed $\gamma \sim \gamma_{\max}$. On the left we have the case of motion for small values of current parameter $J = 2$ (1st type of energy boundary) when the sting loop can collapse to the black hole, while on the right we have $J = 12$ (4th type of energy boundary) when the string loop collapse is prohibited.

direction), see Fig. 3. But if the initial conditions for UPO are only sightly changed, the string loop trajectory are completely different, see Fig. 3. We can not predict final output from neighbouring initial conditions.

4 MAXIMAL EJECTION SPEED

During the acceleration, the energy of the oscillatory mode E_{x} is transmitted into translational energy E_y, but there always remains inconvertible internal energy of the string, $E_{0(\min)} = 2J$ (11), in the E_{x} mode. This gives limit on string loop maximal acceleration, there exist the maximal Lorentz factor for string loop ejection speed as shown in (Stuchlík and Kološ, 2012a)

$$\gamma_{\max} = \frac{E}{2J} \,. \tag{13}$$

From this equation we see that large ratio of the string loop energy E versus its angular momentum given by the current parameter J is needed for ultra-relativistic acceleration. We can use small values of parameter J or large string loop energy E.

We have calculated 3000 trajectories for string loops with energy $E = 25$ and current $J = 2$, with limiting gamma factor $\gamma_{\max} = 6.25$ (13), but observed top accelerated string loop has only $\gamma_{\mathrm{top}} \doteq 4.2$, see Fig. 2. No trajectory with extreme acceleration $\gamma \sim \gamma_{\max}$ was found.

To see for better resolution in Fig. 2, if there can exist an extremely accelerated string loop, hidden somewhere in the chaotic bands, we will examine more closely how such trajectory will looks like. For $\gamma = \gamma_{\max}$ the string loop will stop oscillating in the x

direction and moves only along the y axis, with constant radius $x_\mathrm{i} = x_\mathrm{o} = J$, see (12). Since the string loop motion is time reversible $t \leftrightarrow -t$, instead of escape, we will consider string loop with $\gamma \sim \gamma_\mathrm{max}$ coming from the infinity towards to the black hole.

Now we can have different situations, depending on the value of the current parameter J, see Fig. 4. If J is quite small, $J \sim 3$ or smaller, the string loop will collapse to the black hole horizon. Loops with $\gamma \sim \gamma_\mathrm{max}$ have very tiny oscillations in x direction and hence can't "jump over" black hole. Obviously this is the reason why we do not see extremely accelerated string loop $\gamma \sim \gamma_\mathrm{max}$ in Fig. 2 – such a trajectory had to be started from the black hole. However, such a situation can occur on the naked-singularity spacetimes (Stuchlík and Kološ, 2012b), where the region of strong gravity is not hidden by the event horizon, and $\gamma \sim \gamma_\mathrm{max}$ can be obtained (Kološ and Stuchlík, 2013). If parameter J is large, typically $J > 10$, extremely accelerated trajectories can not collapse to the black hole (it is prevented by energetic conditions) but they are also too far from gravity well where the string loop transmutation process occur.

5 CONCLUSIONS

The existence of chaotic bands in the scattering function $\gamma(y_\mathrm{s})$ is given by presence of unstable periodic orbit in the system. There exists energetic limit on the maximal string loop acceleration γ_max. Large string acceleration along the y-axis can occurs only for large $E/2J$ ratios. It is easy to observe extremely accelerated string loop $\gamma \sim \gamma_\mathrm{max}$ in the case of naked singularity spacetime, where the horizon is missing.

It should be stressed that rotation of the black hole (naked singularity) is not a relevant ingredient of the acceleration of the string loop motion due to the transmutation effect (Stuchlík and Kološ, 2012a), contrary to the Blandford–Znajek effect (Blandford and Znajek, 1977) usually considered in modelling acceleration of jet-like motion in AGN and microquasars.

ACKNOWLEDGEMENTS

The authors would like to thank the EU grant Synergy CZ.1.07./2.3.00/20.0071, the internal student grant SGS/23/2013 of the Silesian University, and the Albert Einstein Centre for gravitation and astrophysics supported by the Czech Science Foundation Grant No. 14-37086G.

REFERENCES

Blandford, R. D. and Znajek, R. L. (1977), Electromagnetic extraction of energy from Kerr black holes, *Monthly Notices of the Royal Astronomical Society* , **179**, pp. 433–456.

Carter, B. and Steer, D. A. (2004), Symplectic structure for elastic and chiral conducting cosmic string models, *Phys. Rev. D* , **69**(12), 125002, arXiv: `hep-th/0307161`.

Frolov, A. V. and Larsen, A. L. (1999), Chaotic scattering and capture of strings by a black hole, *Classical and Quantum Gravity*, **16**, pp. 3717–3724, arXiv: `gr-qc/9908039`.

Jacobson, T. and Sotiriou, T. P. (2009), String dynamics and ejection along the axis of a spinning black hole, *Phys. Rev. D* , **79**(6), 065029, arXiv: `0812.3996`.

Kološ, M. and Stuchlík, Z. (2010), Current-carrying string loops in black-hole spacetimes with a repulsive cosmological constant, *Phys. Rev. D* , **82**(12), 125012, arXiv: `1103.4005`.

Kološ, M. and Stuchlík, Z. (2013), Dynamics of current-carrying string loops in the Kerr naked-singularity and black-hole spacetimes, *Phys. Rev. D* , **88**(6), 065004, arXiv: `1309.7357`.

Larsen, A. L. (1993), Dynamics of cosmic strings and springs; a covariant formulation, *Classical and Quantum Gravity*, **10**, pp. 1541–1548, arXiv: `hep-th/9304086`.

Ott, E. (1993), *Chaos in dynamical systems*.

Semenov, V., Dyadechkin, S. and Punsly, B. (2004), Simulations of Jets Driven by Black Hole Rotation, *Science*, **305**, pp. 978–980, arXiv: `astro-ph/0408371`.

Semenov, V. S. and Bernikov, L. V. (1991), Magnetic flux tubes - Nonlinear strings in relativistic magnetohydrodynamics, *Astrophysics and Space Science* , **184**, pp. 157–166.

Spruit, H. C. (1981), Equations for thin flux tubes in ideal MHD, *Astronomy and Astrophysics* , **102**, pp. 129–133.

Stuchlík, Z. and Kološ, M. (2009), Ejection of string loop from region near black hole horizon, in *Proceedings of RAGtime 11: Workshops on Black Holes and Neutron Stars*, pp. 185–193, in this proceedings.

Stuchlík, Z. and Kološ, M. (2012a), Acceleration of string loops in the Schwarzschild-de Sitter geometry, *Phys. Rev. D* , **85**(6), 065022, arXiv: `1206.5658`.

Stuchlík, Z. and Kološ, M. (2012b), String loops in the field of braneworld spherically symmetric black holes and naked singularities, *Journal of Cosmology and Astroparticle Physics* , **10**, 008, arXiv: `1309.6879`.

Tél, T. and M., G. (2006), *Chaotic Dynamics: An Introduction Based on Classical Mechanics*.

Z. Stuchlík, G. Török and T. Pecháček, editors, Silesian University in Opava, 2014, pp. 113–122

Transition from regular to chaotic string loop motion

Martin Kološ[a] and Zdeněk Stuchlík[b]

Institute of Physics, Faculty of Philosophy & Science, Silesian University in Opava, Bezručovo nám. 13, CZ-746 01 Opava, Czech Republic
[a]Martin.Kolos@fpf.slu.cz
[b]Zdenek.Stuchlik@fpf.slu.cz

ABSTRACT
We study transition from regular to chaotic motion in the neighbourhood of stable equilibrium point of a relativistic current-carrying string-loop located around Schwarzschild black hole. We demonstrate successive transfer from the purely regular, periodic motion through quasi-periodic motion to purely chaotic motion of the string loop, with increasing of its energy. We also calculated quasi-periodic fundamental frequencies, which are important for survival of corresponding KAM tori. Using maximal Lyapunov exponent we show how the chaoticity of the string loop motion changes with increase of the string loop energy.

Keywords: chaos and regularity – string loop – Schwarzschild – black holes – Lyapunov exponent

1 INTRODUCTION

Relativistic current-carrying strings moving axisymmetrically along the axis of a Kerr black hole have been studied in (Jacobson and Sotiriou, 2009) where it has been proposed that such a string loop configuration can be used as a model of jet formation and acceleration in the field of black holes in microquasars or active galactic nuclei. Tension of such string loops prevents their expansion beyond some radius, while their worldsheet current introduces an angular momentum barrier preventing them from collapsing into the black hole. It has bee shown that string loop model could in a simplified way represent plasma that exhibits associated string-like behaviour via dynamics of the magnetic field lines in the plasma (Christensson and Hindmarsh, 1999; Semenov et al., 2004) or due to thin isolated flux tubes of magnetized plasma that could be described by an one-dimensional string (Spruit, 1981; Semenov and Bernikov, 1991; Cremaschini and Stuchlík, 2013).

The astrophysical applications of the current carrying string loops have been focused on the problem of acceleration of string loops due to the transmutation process (Jacobson and Sotiriou, 2009), the role of the cosmic repulsion in the string loop motion has been investigated for the Schwarzschild–de Sitter (SdS) spacetime in (Kološ and Stuchlík, 2010a). Since the string loops can be accelerated to ultra-relativistic velocities in the deep gravitational potential well of compact objects (Stuchlík and Kološ, 2009; Kološ and Stuchlík, 2010b; Stuchlík and Kološ, 2012a,b), the string loop transmutation can be well considered as a

978-80-7510-125-9

process of formation of ultra-relativistic jets, along with the standard model based on the Blandford–Znajek process (Blandford and Znajek, 1977). Here we concentrate out attention on the inverse situation of small oscillations of string loops in vicinity of stable equilibrium points in the equatorial plane of black holes that was proposed as a possible model of HF QPOs observed in black hole and neutron star binary systems (Stuchlík and Kološ, 2012b).

2 CURRENT-CARRYING STRING LOOP MOTION

We study a string loop motion in the field of a black hole described by the Schwarzschild metric

$$\mathrm{d}s^2 = -A(r)\,\mathrm{d}t^2 + A^{-1}(r)\,\mathrm{d}r^2 + r^2(\mathrm{d}\theta^2 + \sin^2\theta\,\mathrm{d}\phi^2), \quad A(r) = 1 - \frac{2M}{r}\,. \tag{1}$$

We use the geometric units with $c = G = 1$ and the Schwarzschild coordinates. In order to properly describe the string loop motion, it is useful to use the Cartesian coordinates

$$x = r\sin(\theta), \quad y = r\cos(\theta)\,. \tag{2}$$

The string loop is threaded on to an axis of the black hole chosen to be the y-axis. Due to the assumed axisymmetry of the string motion one point path can represent whole movement of the string. Trajectory of the string can be represented by a curve in the 2D x-y plane. The string loop can oscillate, changing its radius in x-z plane, while propagating in y direction.

The string loop motion is governed by barriers given by the string tension and the worldsheet current determining the angular momentum – these barriers are modified by the gravitational field. Dynamics of the string is described by the action

$$S = \int \mathrm{d}^2\sigma\sqrt{-h}(\mu + h^{ab}\varphi_{,a}\varphi_{,b})\,, \tag{3}$$

where $\varphi_{,a} = j_a$ determines current of the string and $\mu > 0$ reflects the string tension.

The worldsheet stress-energy tensor density $\tilde{\Sigma}^{ab}$ can be expressed in the form (Jacobson and Sotiriou, 2009)

$$\tilde{\Sigma}^{\tau\tau} = \frac{J^2}{g_{\phi\phi}} + \mu\,, \quad \tilde{\Sigma}^{\sigma\sigma} = \frac{J^2}{g_{\phi\phi}} - \mu\,, \quad \tilde{\Sigma}^{\sigma\tau} = \frac{-2j_\tau j_\sigma}{g_{\phi\phi}}\,, \quad J^2 \equiv j_\sigma^2 + j_\tau^2\,. \tag{4}$$

We shall use for simplicity the dimensionless radial coordinate $r/M \to r$, dimensionless time coordinate $t/M \to t$, and we make the rescaling $E_\mathrm{b}/\mu \to E_\mathrm{b}$ and $J/\sqrt{\mu} \to J$.

As demonstrated in (Larsen, 1993), the string loop motion in spherically symmetric spacetimes can be described by the Hamiltonian

$$H = \frac{1}{2}g^{rr}\,P_r^2 + \frac{1}{2}g^{\theta\theta}\,P_\theta^2 + \frac{1}{2}g_{\phi\phi}\left(\Sigma^{\tau\tau}\right)^2 + \frac{1}{2}g^{tt}\,E^2\,. \tag{5}$$

The motion of string loops is given by the Hamilton equations in the form

$$\frac{\mathrm{d}X^\mu}{\mathrm{d}\zeta} = \frac{\partial H}{\partial P_\mu}\,, \quad \frac{\mathrm{d}P_\mu}{\mathrm{d}\zeta} = -\frac{\partial H}{\partial X^\mu}\,, \tag{6}$$

where X^μ is 4-position, P^μ is the 4-momentum and ζ is the affine parameter.

Due to symmetries of metric (1), conserved quantities occur for the string loop motion, being the energy E and string the axial angular momentum L, given by

$$-E = P_t = g_{tt}\tilde{\Sigma}^{\tau\tau}X^t_{|\tau}\,, \quad L = P_\phi = g_{\phi\phi}\tilde{\Sigma}^{\sigma\tau} = -2j_\tau j_\sigma\,. \tag{7}$$

The components of the current, j_τ, j_σ, give the angular momentum of the string loop (Stuchlík and Kološ, 2012a).

Hamiltonian is constant of the motion, $H = 0$. The loci where the string loop has zero velocity ($\dot{r} = 0, \dot{\theta} = 0$) form boundary of the string motion

$$E = E_\mathrm{b}(r,\theta) = \sqrt{-g_{tt}g_{\phi\phi}}\,\tilde{\Sigma}^{\tau\tau}\,. \tag{8}$$

Function $E_\mathrm{b}(r,\theta)$ is playing the role of effective potential, see discussion in (Stuchlík and Kološ, 2012a), its shape is determined by current parameter $J^2 = j_\tau^2 + j_\sigma^2$.

There are four different types of the behaviour of the energy boundary function for the string loop dynamics in the Schwarzschild BH spacetime represented by the characteristic $E = \mathrm{const}$ sections of the function $E_\mathrm{b}(r,\theta)$ in dependence on parameter J (Jacobson and Sotiriou, 2009). We can distinguish them according to two properties: possibility of the string loop to escape to infinity in the y-direction, and possibility to collapse to the black hole. A detailed discussion can be found in Kološ and Stuchlík (2010a), here we shortly summarize the results.

The first case corresponds to no inner and outer boundary – the string loop can be captured by the black hole or escape to infinity. The second case corresponds to the situation with an outer boundary – the string loop must be captured by the black hole. The third case corresponds to the situation when both inner and outer boundary exist – the string loop is trapped in some region forming a potential "lake" around the black hole. The fourth case corresponds to an inner boundary – the string loop cannot fall into the black hole but it must escape to infinity, see Fig. 2. in Stuchlík and Kološ (2009). For our following discussion only the third case, corresponding to the string loop trapped in toroidal space along black hole, will be relevant.

3 SMALL OSCILLATIONS AROUND MINIMA OF THE "EFFECTIVE POTENTIAL"

It is convenient to examine systems which are constructed from regular part, H_0, plus some small non-linear perturbation, H_p,

$$H = H_0 + \epsilon H_\mathrm{p}\,. \tag{9}$$

As the non-linear parameter ϵ increases, it causes a non-linearity in the system. This "regular+perturbation" separation in not possible in every given Hamiltonian, examples can be given by string loop model (5), or by charged particles moving in combined magnetic and gravitational field, (Kopáček et al., 2010).

However the "regular+perturbation" separation (9) of the Hamiltonian can be done in the neighbourhood of any elliptic point of the Hamiltonian, (Arnold, 1978; Tabor, 1989). The equilibrium points of the Hamiltonian (5) correspond to the local minima at $X_0^\alpha = (r_0, \theta_0)$

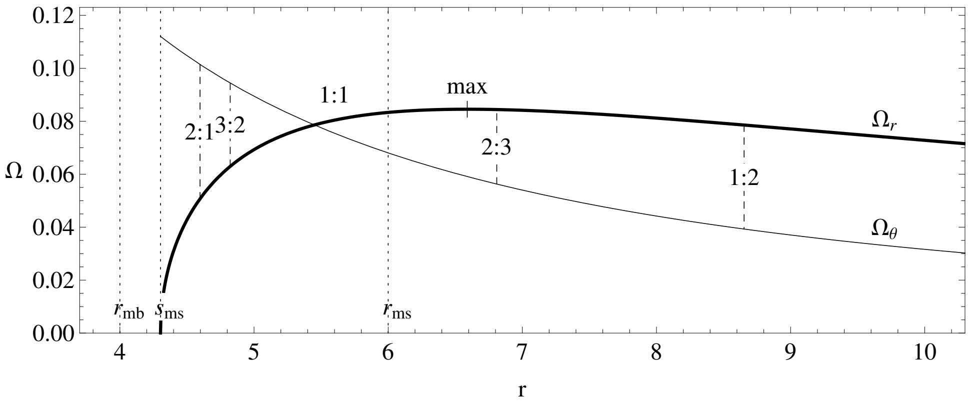

Figure 1. Fundamental frequencies $\Omega_{\rm r}(r)$ and $\Omega_\theta(r)$, as function of radial coordinate r, for string loop oscillations in equatorial plane of Schwarzschild BH. Resonant and another important radii, such as marginally stable $r_{\rm ms} = 6$, marginally bound $r_{\rm mb} = 4$ orbit for particle motion and marginally stable $s_{\rm ms} \doteq 4.3$ string loop position, are also given.

of the energy boundary function $E_{\rm b}(r, \theta)$, (Arnold, 1978). It is useful to rewrite the Hamiltonian in the form

$$H = H_{\rm D} + H_{\rm P} = \frac{1}{2} g^{rr} P_r^2 + \frac{1}{2} g^{\theta\theta} P_\theta^2 + H_P(r, \theta) \tag{10}$$

where we split H into the "dynamical" $H_{\rm D}$ and the "potential" $H_{\rm P}$ parts. Introducing a small parameter $\epsilon \ll 1$, we can rescale coordinates and momenta by the relations

$$X^\alpha = X_0^\alpha + \epsilon \hat{X}^\alpha \,, \quad P_\alpha = \epsilon \hat{P}_\alpha \,, \tag{11}$$

applied for the coordinates $\alpha \in \{r, \theta\}$. We can make polynomial expansion of the Hamiltonian into the Taylor series and express it in separated parts according to the power of ϵ

$$H\left(\hat{P}_\alpha, \hat{X}^\alpha\right) = H_0 + \epsilon H_1\left(\hat{X}^\alpha\right) + \epsilon^2 H_2\left(\hat{P}_\alpha, \hat{X}^\alpha\right) + \epsilon^3 H_3\left(\hat{P}_\alpha, \hat{X}^\alpha\right) + \cdots \,, \tag{12}$$

where H_k is a homogeneous part of the Hamiltonian of degree k considered for the momenta $\hat{P}_\alpha$ and coordinates $\hat{X}^\alpha$. Recall that P_α occurs in the quadratic form in (5) and appears in H_k only for $k \geq 2$. If the string loop is located at a local minimum of the $E_{\rm b}(x, y)$ function, we have $H_{\rm D} = 0$ and hence $H_0 = 0$. The local extrema of the $E_{\rm b}$ function, given by (6), imply also $H_1(\hat{X}^\alpha) = 0$.

We can divide (12) by the factor ϵ^2 (remember $H = 0$) expressing the Hamiltonian in the vicinity of the local minimum in the "regular" plus "perturbation" form

$$H = H_2\left(\hat{P}_\alpha, \hat{X}^\alpha\right) + \epsilon H_3\left(\hat{P}_\alpha, \hat{X}^\alpha\right) + \ldots \tag{13}$$

If $\epsilon = 0$, we arrive to an integrable Hamiltonian

$$H = H_2\left(\hat{P}_\alpha, \hat{X}^\alpha\right) = \frac{1}{2} \sum_\alpha \left[g^{\alpha\alpha} \left(\hat{P}_\alpha\right)^2 + \tilde{\omega}_\alpha^2 \left(\hat{X}^\alpha\right)^2 \right] \tag{14}$$

representing two uncoupled harmonic oscillators. This "perturbation" approach corresponds to the linearisation of the motion Eqs. (6) in the neighbourhood of local minima of the function $E_{\mathrm{b}}(r, \theta)$.

For the string loop motion represented by coordinates $r = r_0 + \delta r$, $\theta = \theta_0 + \delta\theta$ we obtain the periodic harmonic oscillations determined by the equations

$$\ddot{\delta r} + \omega_{\mathrm{r}}^2 \, \delta r = 0 \,, \quad \ddot{\delta\theta} + \omega_{\theta}^2 \, \delta\theta = 0 \,, \tag{15}$$

where the locally measured frequencies of the oscillatory motion are given by

$$\omega_{\mathrm{r}}^2 = \frac{1}{g_{rr}} \frac{\partial^2 H_{\mathrm{P}}}{\partial r^2} \,, \quad \omega_{\theta}^2 = \frac{1}{g_{\theta\theta}} \frac{\partial^2 H_{\mathrm{P}}}{\partial \theta^2} \,. \tag{16}$$

The locally measured angular frequencies

$$\omega_{(\mathrm{r},\theta)} = \frac{\mathrm{d} f_{(\mathrm{r},\theta)}}{\mathrm{d}\zeta} \tag{17}$$

are connected to the angular frequencies related to distant observers, Ω, by the gravitational redshift transformation

$$\Omega_{(\mathrm{r},\theta)} = \frac{\mathrm{d} f_{(\mathrm{r},\theta)}}{\mathrm{d}t} = \frac{\omega_{(\mathrm{r},\theta)}}{P^t} \,, \tag{18}$$

where $P^t = \mathrm{d}\,t \,/\, \mathrm{d}\,\zeta = -g^{tt} E$. If the angular frequencies $\Omega_{(\mathrm{r},\theta)}$, or frequencies $\nu_{(\mathrm{r},\theta)}$, of the string loop oscillation are expressed in the physical units, their dimensionless form has to be extended by the factor c^3/GM. Then the frequencies of the string loop oscillations measured by the distant observers are given by

$$\nu_{(\mathrm{r},\theta)} = \frac{1}{2\pi} \frac{c^3}{GM} \, \Omega_{(r,\theta)} \,. \tag{19}$$

Notice that this is the same factor as the one occurring in the case of the orbital and epicyclic frequencies of the geodetical motion in the black hole spacetimes, (Török and Stuchlík, 2005). Therefore, the order of magnitude and scaling of the frequencies of the radial and vertical oscillations due to the mass of the central object is the same for both current-carrying string loops and test particles.

In the Schwarzschild spacetime the harmonic oscillations have frequencies (16) relative to distant observers given by expressions relatively very simple for both string loops and test particles. Therefore, we can give the frequencies in dimensional form, as an example. In the case of string loops they read

$$\Omega_{\mathrm{r}}^2(r) = \frac{3M^2 - 5Mr + r^2}{r^4} \,, \quad \Omega_{\theta}^2(r) = \frac{M}{r^3} \,, \tag{20}$$

while for the epicyclic motion of test particles there is

$$\Omega_{\mathrm{r(geo)}}^2(r) = \frac{M(r - 6M)}{r^4} \,, \quad \Omega_{\theta(\mathrm{geo})}^2(r) = \frac{M}{r^3} \,. \tag{21}$$

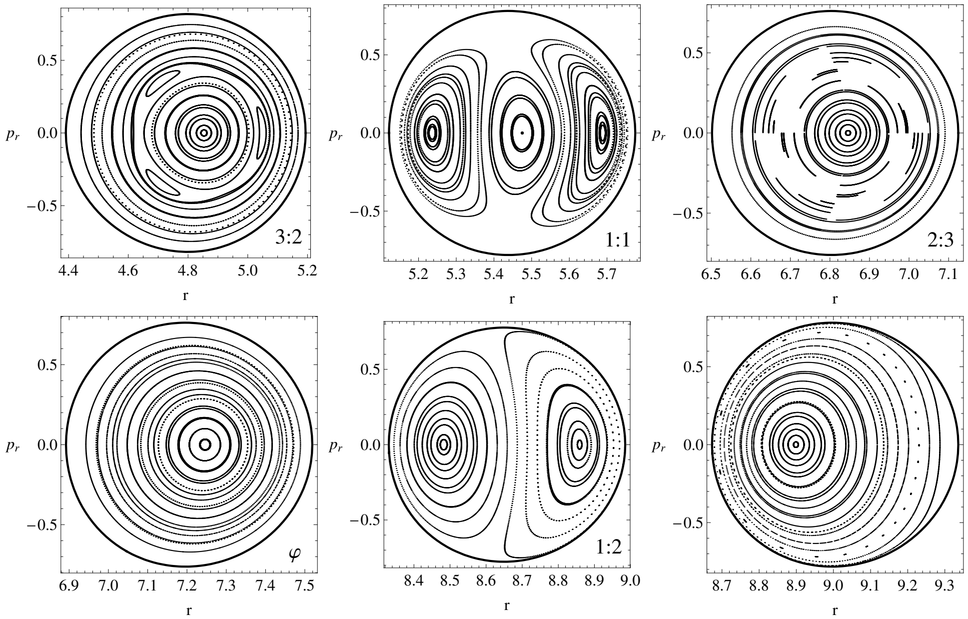

Figure 2. Poincare surface of section r/p_r ($\theta = \pi/2$) for string loop trajectories in the neighbourhood of minima of $E_b(r, \theta)$ function. Resonant (3:2, 1:1, 2:3, 1:2) and nonresonant (1:φ, $r_0 = 9$) radii for $\Omega_\theta(r) : \Omega_r(r)$ frequency ratios are depicted. Every picture contains multiple trajectories and every (regular) trajectory is forming a ring. Trajectories are differing in initial conditions r, P_r, P_θ, but has the same energy E and parameter J. They are bounded by the E_b function, see thick curve. We see destruction of the initial tori for 1:1 and 1:2 and formation of new ones on $P_r = 0$ line. For another resonances and also for nonresonant radii, the initial tori are preserved. The most resilient tori exist for golden frequency ratio 1:φ.

It is quite interesting that the latitudinal frequency of the string loop oscillations in the Schwarzschild or other spherically symmetric spacetimes equals to the latitudinal frequency of the epicyclic geodetical motion as observed by distant observers – for details see (Stuchlík and Kološ, 2012b).

The radial profiles of the string loop oscillations qualitatively differ from those related to the radial oscillations of the geodesic, test particle motion in the Schwarzschild geometry, especially there is a crossing point of the radial and vertical frequencies in the Kerr black hole spacetimes for the string loop oscillation, while for the test particle oscillations such a crossing is possible only in the Kerr naked singularity spacetimes, (Török and Stuchlík, 2005; Stuchlík and Schee, 2012).

4 TRANSITION FROM REGULAR TO CHAOTIC MOTION

According to the Kolmogorov–Arnold–Moser (KAM) theory (Arnold, 1978), a string loop will oscillate in a regular quasi-periodic motion, if the parameter ϵ remains small. The trajectory of such regular motion, restricted by energy (8) in its phase space r, θ, P_r, P_θ,

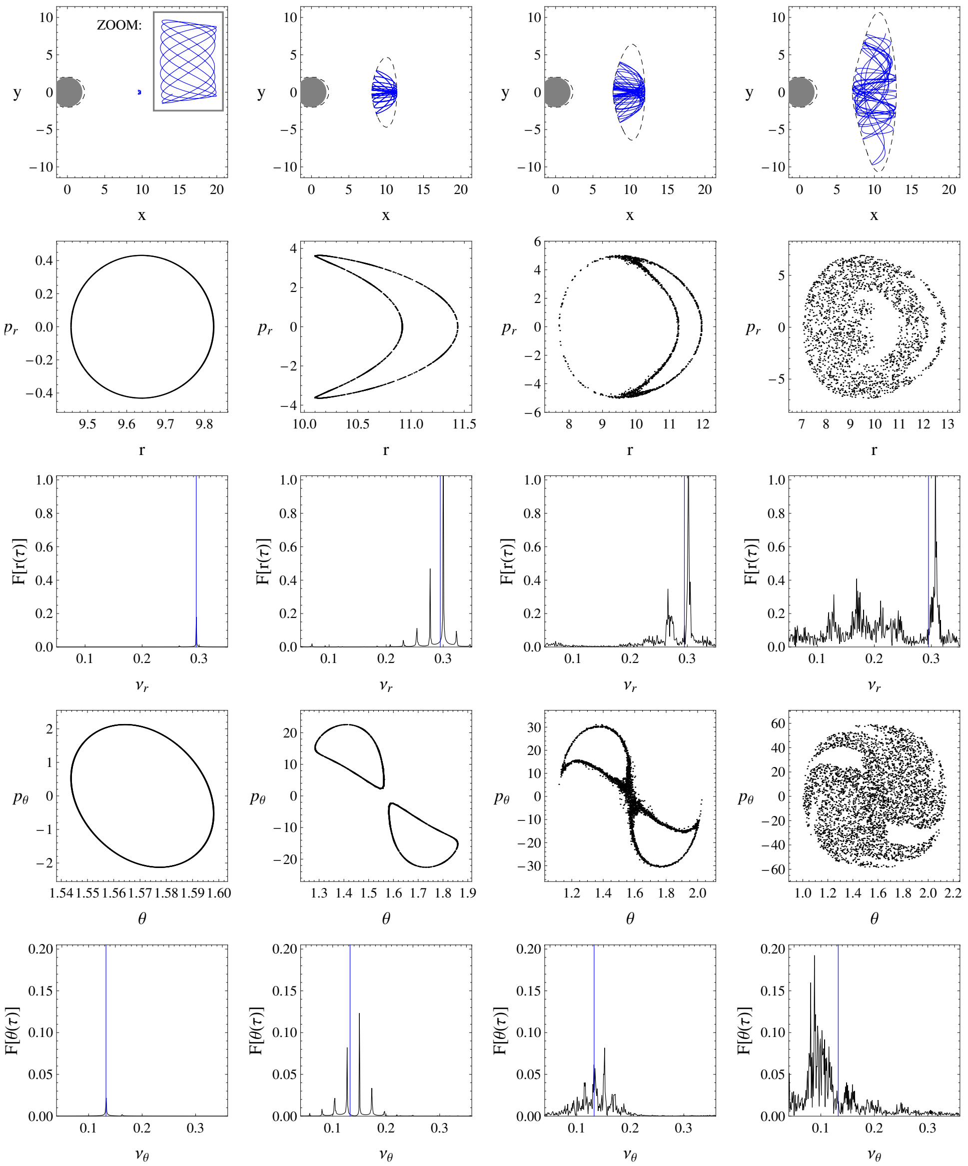

(a) $E = 19.8$ (b) $E = 20$ (c) $E = 20.15$ (d) $E = 20.5$

Figure 3. Transition from the regular to the chaotic regime of the string loop motion. The string loop is starting from the rest near the local minimum located (for the string parameter $J = 11$) at $r_0 \doteq 9.64, \theta_0 = \pi/2$, with successively increasing energy E. For every energy level we plotted the string loop trajectory, the Poincare surface sections (r, P_r),(θ, P_θ) and the Fourier spectrum for both coordinates r and θ (Ott, 1993). The vertical lines in the Fourier spectra are the frequencies $\omega_r/(2\pi), \omega_\theta/(2\pi)$.

will lies on so called KAM torus. As the parameter ϵ grows, the condition $\epsilon \ll 1$ becomes violated, the nonlinear parts in the Hamiltonian become stronger, and the string loop enters the nonlinear, chaotic regime of its motion.

The Birkhoff theorem, ensuring the existence of a canonical transformation (11) putting a Hamiltonian system into normal form (13) up to a remainder of a given order, is violated, if for our two degrees of freedom (2 DOF) (5)

$$k_1 \omega_1 + k_2 \omega_2 = 0 , \quad k_1 + k_2 < 4 . \tag{22}$$

So for resonances 1:1, 1:2, 2:1 we can not construct normal forms, with frequencies ω_1, ω_2. It does not mean that at resonant radii the motion in the vicinity of minima will not be regular, we still have regular motion close to the minima of E_b, but the former KAM tori are destroyed for 1:1, 1:2, 2:1, see Fig. 2.

Increase of non-linearity and chaoticity of a system moving in vicinity of its local stable equilibrium point is caused by increase of its energy. We demonstrate successive transfer from the purely regular, periodic motion through quasi-periodic motion to purely chaotic motion of a string loop in Fig. 3. The Poincare surface sections in the phase space and the Fourier transforms of the oscillatory motion in the radial and latitudinal direction clearly represent the transfer to the chaotic motion. Of course, in the entering phase of the motion with lowest energy, the string loop motion is fully regular and periodic and is represented by appropriate Lissajousse figures.

It is convenient to represent the transfer to the chaotic system by an appropriate Lyapunov coefficient. The chaotic systems are sensitive to initial conditions and we can follow two string loop trajectories separated at the initial time t_0 by a small phase-space distance d_0. As the system evolves, the two orbits will be separated at an exponential rate if the motion of the string loops is in the chaotic regime. The Lyapunov exponent (Ott, 1993)

$$\lambda_\mathrm{L} = \lim_{\substack{d_0 \to 0 \\ t \to \infty}} \left(\frac{1}{t} \ln \left(\frac{d(t)}{d_0} \right) \right) \tag{23}$$

is describing the two orbits separation and hence the measure of chaos. The transition from the regular to the chaotic regime of the string loop motion is clearly visible due to the evolution of the maximal Lyapunov exponent (Ott, 1993) demonstrated in Fig. 4. We clearly see strongly increasing measure of chaos with increasing energy of the moving string loop when some critical energy is crossed. This effect is genuine to the dynamical systems and we observed it also for the string loops in the spherically symmetric braneworld spacetimes, (Stuchlík and Kološ, 2012b).

5 CONCLUSIONS

System will oscillate in a quasi-periodic motion, if the parameter ϵ remains small. As the parameter ϵ grows, the condition $\epsilon \ll 1$ becomes violated, the nonlinear parts in the Hamiltonian become stronger, and we enter the nonlinear, chaotic regime of its motion. Increase of non-linearity of a system moving in vicinity of its local stable equilibrium point (minimum) is caused by increase of its energy. The transition from the regular to the chaotic regime of the motion is the solution to the "focusing" problem of the string loop trajectories discussed in (Jacobson and Sotiriou, 2009).

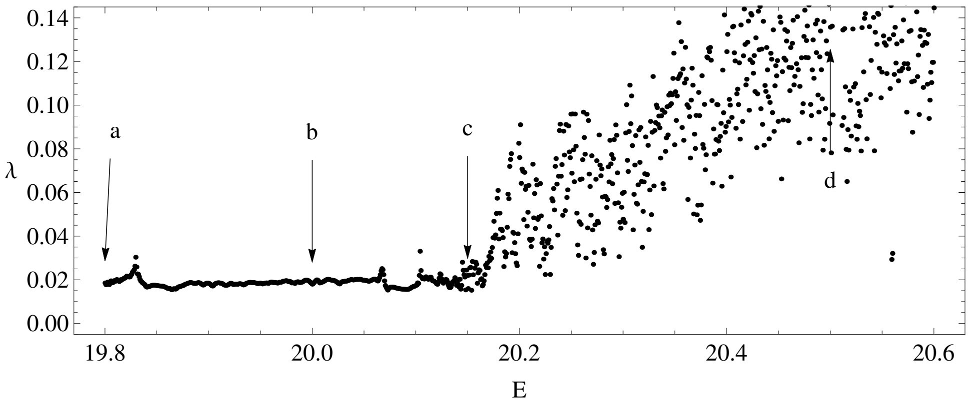

Figure 4. Evolution of the maximal Lyapunov exponent in dependence of on the string loop energy, related to Fig. 3. For small energies the motion is regular, for bigger energies the motion is chaotic – this is manifestation of the KAM theorem. The transition between the regular/chaotic regimes occurs approximately at $E \sim 20.15$. Letters denote the individual cases in Fig. 3.

ACKNOWLEDGEMENTS

The authors would like to thank the EU grant Synergy CZ.1.07./2.3.00/20.0071, the internal student grant SGS/23/2013 of the Silesian University, and the Albert Einstein Centre for gravitation and astrophysics supported by the Czech Science Foundation Grant No. 14-37086G.

REFERENCES

Arnold, V. I. (1978), *Mathematical methods of classical mechanics*, New York: Springer.

Blandford, R. D. and Znajek, R. L. (1977), Electromagnetic extraction of energy from Kerr black holes, *Monthly Notices of the Royal Astronomical Society* , **179**, pp. 433–456.

Christensson, M. and Hindmarsh, M. (1999), Magnetic fields in the early universe in the string approach to MHD, *Phys. Rev. D* , **60**(6), 063001, arXiv: `astro-ph/9904358`.

Cremaschini, C. and Stuchlík, Z. (2013), Magnetic loop generation by collisionless gravitationally bound plasmas in axisymmetric tori, *Phys. Rev. E* , **87**(4), 043113.

Jacobson, T. and Sotiriou, T. P. (2009), String dynamics and ejection along the axis of a spinning black hole, *Phys. Rev. D* , **79**(6), 065029, arXiv: `0812.3996`.

Kološ, M. and Stuchlík, Z. (2010a), Current-carrying string loops in black-hole spacetimes with a repulsive cosmological constant, *Phys. Rev. D* , **82**(12), 125012, arXiv: `1103.4005`.

Kološ, M. and Stuchlík, Z. (2010b), String loop chaotic scattering in the field of Schwarzschild black hole, in *Proceedings of RAGtime 11: Workshops on Black Holes and Neutron Stars*, pp. 103–111, in this proceedings.

Kopáček, O., Karas, V., Kovář, J. and Stuchlík, Z. (2010), Transition from Regular to Chaotic Circulation in Magnetized Coronae near Compact Objects, *The Astrophysical Journal* , **722**, pp. 1240–1259, arXiv: `1008.4650`.

Larsen, A. L. (1993), Dynamics of cosmic strings and springs; a covariant formulation, *Classical and Quantum Gravity*, **10**, pp. 1541–1548, arXiv: `hep-th/9304086`.

Ott, E. (1993), *Chaos in dynamical systems*.

Semenov, V., Dyadechkin, S. and Punsly, B. (2004), Simulations of Jets Driven by Black Hole Rotation, *Science*, **305**, pp. 978–980, arXiv: `astro-ph/0408371`.

Semenov, V. S. and Bernikov, L. V. (1991), Magnetic flux tubes - Nonlinear strings in relativistic magnetohydrodynamics, *Astrophysics and Space Science* , **184**, pp. 157–166.

Spruit, H. C. (1981), Equations for thin flux tubes in ideal MHD, *Astronomy and Astrophysics* , **102**, pp. 129–133.

Stuchlík, Z. and Kološ, M. (2009), Ejection of string loop from region near black hole horizon, in *Proceedings of RAGtime 11: Workshops on Black Holes and Neutron Stars*, pp. 185–193, in this proceedings.

Stuchlík, Z. and Kološ, M. (2012a), Acceleration of string loops in the Schwarzschild-de Sitter geometry, *Phys. Rev. D* , **85**(6), 065022, arXiv: `1206.5658`.

Stuchlík, Z. and Kološ, M. (2012b), String loops in the field of braneworld spherically symmetric black holes and naked singularities, *Journal of Cosmology and Astroparticle Physics* , **10**, 008, arXiv: `1309.6879`.

Stuchlík, Z. and Schee, J. (2012), Observational phenomena related to primordial Kerr superspinars, *Classical and Quantum Gravity*, **29**(6), 065002.

Tabor, M. (1989), *Chaos and Integrability in Nonlinear Dynamics: An Introduction*, Wiley-Interscience.

Török, G. and Stuchlík, Z. (2005), Radial and vertical epicyclic frequencies of Keplerian motion in the field of Kerr naked singularities. Comparison with the black hole case and possible instability of naked-singularity accretion discs, *Astronomy and Astrophysics* , **437**, pp. 775–788, arXiv: `astro-ph/0502127`.

Proceedings of *RAGtime 10–13, 15–17/20–22/15–17/14–16 September, 2008/2009/2010/2011, Opava, Czech Republic*
Z. Stuchlík, G. Török and T. Pecháček, editors, Silesian University in Opava, 2014, pp. 123–132

Application of a symplectic integrator in a non-integrable relativistic system

Ondřej Kopáček,[1,2,a] Vladimír Karas,[1] Jiří Kovář[3] and Zdeněk Stuchlík[3]

[1] Astronomical Institute of the Academy of Sciences of the Czech Republic, Boční II 1401/1a, CZ-141 31 Prague, Czech Republic
[2] Faculty of Mathematics and Physics of Charles University, Ke Karlovu 3, CZ-121 16 Prague, Czech Republic
[3] Institute of Physics, Faculty of Philosophy & Science, Silesian University in Opava, Bezručovo nám. 13, CZ-746 01 Opava, Czech Republic
[a] kopacek@ig.cas.cz

ABSTRACT
We present a detailed comparison of several integration schemes applied to the dynamic system consisting of a charged particle on the Kerr background endowed with the axisymmetric electromagnetic test field. In particular, we compare the performance of the symplectic integrator with several non-symplectic routines and discuss under which circumstances we should choose the symplectic one and when we should switch to some other scheme. We are basically concerned with two crucial, yet opposing aspects – accuracy of the integration and CPU time consumption. The latter is generally less critical in our application while the highest possible accuracy is strongly demanded.

Keywords: black hole physics – test particle dynamics – magnetic fields – symplectic integrators – deterministic chaos

1 INTRODUCTION

In our recent study of the test particle dynamics (Kopáček et al., 2010; Kovář et al., 2010) we faced the problem of numerical integration of relativistic dynamic system described by the non-integrable equations of motion. Such system generally allows for both regular and chaotic orbits. We first applied several standard 'all-purpose' integration routines to realize that they are unable to provide sufficiently accurate results concerning the long-term integration. Seeking for the scheme which would better fit our problem and provide more reliable results we finally employed symplectic integrators which are specifically designed for the integration of Hamiltonian systems.

In this contribution we compare performance of a symplectic routine with several non-symplectic integrators. We treat separately the case of regular and chaotic motion because we may expect different results. Particular system which we employ in the survey consists

978-80-7510-125-9

of a charged test particle orbiting above the outer horizon of the Kerr black hole which is immersed into the asymptotically uniform magnetic field aligned with the rotation axis (Wald, 1974). Specification of this system along with the detailed study of the charged particle dynamics is given by Kopáček et al. (2010). Current paper is based on the results previously published in the Ph.D. thesis of one of the authors (Kopáček, 2011).

We recall that in the given system the particle of rest mass m is characterized by its specific angular momentum $\tilde{L} \equiv L/m$, specific energy $\tilde{E} \equiv E/m$ and specific charge $\tilde{q} \equiv q/m$. Black hole of mass M is described by the spin parameter a and specific test charge $\tilde{Q} \equiv Q/M$. Background magnetic field is specified by its asymptotic strength B_0. Inspecting the equations of motion we reveal that $\tilde{q}$, $\tilde{Q}$ and B_0 are not independent variables and we only need to specify values of products $\tilde{q}\tilde{Q}$ and $\tilde{q}B_0$ to characterize the system. We use standard Boyer–Lindquist coordinates $x^{\mu} = (t,\ r,\ \theta,\ \varphi)$ and denote the canonical four-momentum as $\pi_{\mu} = (\pi_t, \pi_r, \pi_{\theta}, \pi_{\varphi})$. Standard kinematical four-momentum p^{μ} and canonical four-momentum are related as follows $p^{\mu} = \pi^{\mu} - qA^{\mu}$ where A^{μ} stands for the electromagnetic four-potential. Integration variable is affine parameter λ defined as $\lambda \equiv \tau/m$ where τ denotes the proper time of the particle. We use geometrized units $G = c = 1$ and scale all quantities by the mass of the black hole M.

We are dealing with the integration of the autonomous Hamiltonian system[1] whose equations of motion form a specific subclass of first order ordinary differential equations (ODEs). Two fundamental characteristics of the Hamiltonian flow should be highlighted

- conservation of the net energy (Hamiltonian) of the system
- conservation of the symplectic 2-form $\boldsymbol{\omega} = \mathbf{d}\pi_{\mu} \wedge \mathbf{d}x^{\mu}$.

Here $\mathbf{d}$ stands for the exterior derivative and $\wedge$ denotes the wedge product.

In the classical mechanics the natural choice of the generalized coordinates leads to the Hamiltonian which may be interpreted as a net energy of the system. This is true even for the system of a charged particle in the external electromagnetic field where the generalized momenta-dependent potential is introduced (Goldstein et al., 2002, Chap. 8). Time-independence of the Hamiltonian is thus equivalent to the conservation of the net energy of the system. In the general relativistic version of this system, however, we employ super-hamiltonian formalism (Misner et al., 1973, Chap. 21) in which the energy of the particle E, as a negatively taken time component of the canonical momentum $E \equiv -\pi_t$, is conserved by virtue of the Hamilton's equations it selves providing that the super-hamiltonian doesn't depend on the coordinate time t. On the other hand the value of the super-hamiltonian $\mathcal{H} = p_{\mu}p^{\mu}/2$ is by construction equal to $-m^2/2$ where m is the rest mass of the particle. Conservation of the super-hamiltonian in the system is thus equivalent to the conservation of the rest mass of the particle.

[1] Equations of motion may be equivalently expressed in terms of Lorentz force (Misner et al., 1973, p. 898) which leads to the set of four second order ODEs. Numerical experiments, however, led us to the conclusion that this formulation is computationally less effective compared to the Hamiltonian formalism. Generally for a given numerical scheme with the same parameters (resulting in similar accuracy of the integration) the integration of Hamilton's equations was roughly two times faster. Moreover, the symplectic methods may only be applied in the Hamiltonian formulation of the problem.

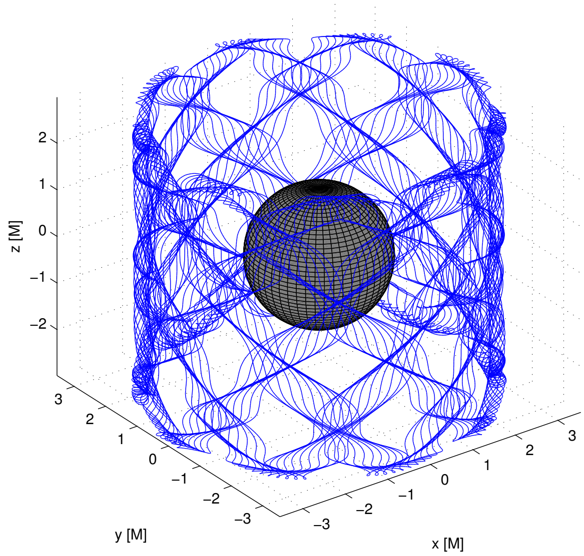

Figure 1. Regular trajectory of a charged test particle ($\tilde{q}\tilde{Q} = 1$, $\tilde{L} = 6\,M$ and $\tilde{E} = 1.6$) on the Kerr background ($a = 0.9\,M$) with Wald magnetic field $\left(\tilde{q}B_0 = 1M^{-1}\right)$. The particle is launched at $r(0) = 3.68\,M$, $\theta(0) = 1.18$ with $u^r(0) = 0$.

By conservation of the symplectic 2-form $\boldsymbol{\omega}$ we mean that its components $\omega_{\alpha\beta}$ in the basis $\left(\mathbf{d}t(\lambda), \mathbf{d}r(\lambda), \mathbf{d}\theta(\lambda), \mathbf{d}\varphi(\lambda), \mathbf{d}\pi_t(\lambda), \mathbf{d}\pi_r(\lambda), \mathbf{d}\pi_\theta(\lambda), \mathbf{d}\pi_\varphi(\lambda)\right)$ do not change during the evolution of the system and for arbitrary value of the affine parameter λ (i.e. at each point of the phase space trajectory) we obtain

$$\omega_{\alpha\beta} = \begin{pmatrix} 0 & -\mathbb{I} \\ \mathbb{I} & 0 \end{pmatrix}, \tag{1}$$

where $\mathbb{I}$ stands for the four-dimensional identity submatrix and 0 is the null submatrix of the same dimension. Conservation of the symplectic structure expresses in the abstract geometrical language the fact that the evolution of the system is governed by the Hamilton's canonical equations. See Arnold (1978) for details on the geometric formulation of the Hamiltonian dynamics.

It would be highly desirable to use such integration scheme which would conserve both quantities which are conserved by the original system. It appears, however, that this is not possible for non-integrable systems and one has to decide whether he employs the scheme which conserves energy or rather the integrator which keeps the symplectic structure. The latter are referred to as symplectic integrators and by many accounts provide most reliable results in numerical studies involving Hamiltonian systems. See Yoshida (1993) for a comprehensive review on symplectic methods.

We list all the schemes we employ in this survey specifying their basic properties. We shall actually compare one symplectic method with several standard integrators. Code names we use for the schemes are those which denote the routines in the MATLAB system.

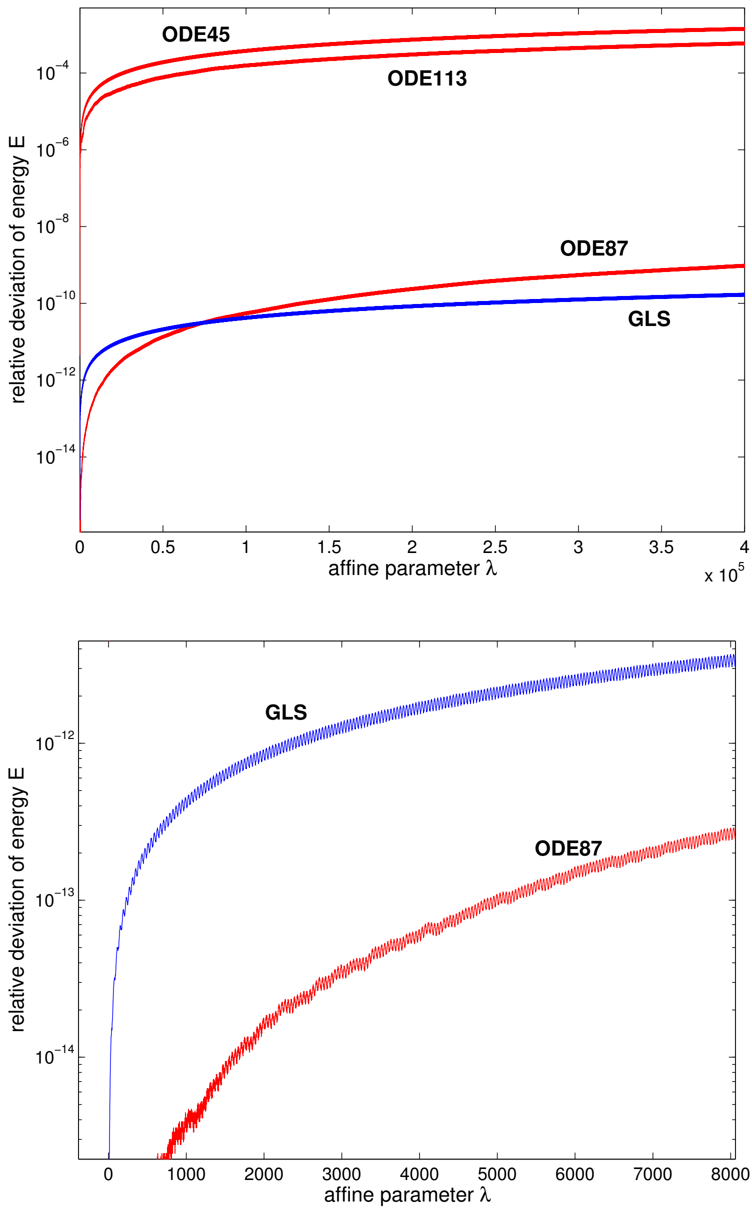

Figure 2. Comparison of the integrators in the case of regular trajectory. Symplectic GLS provides the most reliable results for $\lambda \gtrsim 10^5$. *Bottom* panel shows that besides secular drift in energy (artificial excitation or dumping of the system; plot shows absolute values, however) it also oscillates on the short time scale.

- GLS – Gauss–Legendre symplectic solver, s-stage implicit Runge–Kutta (RK) method, crucial control parameter: stepsize h.
- ODE87 – Dormand–Prince 8th-7th order explicit RK scheme, the most precise RK method $\big($local error of order $O\big(h^8\big)\big)$, adaptive stepsize – RelTol is set to control the local truncation error.
- ODE113 – multistep Adams–Bashforth–Moulton solver, based on the predictor-corrector method (PECE), RelTol is set.
- ODE45 – Dormand–Prince seven stage 5th-4th order method of explicit RK family, adaptive stepsize, default integration method in MATLAB and GNU OCTAVE, error is controlled by RelTol.

Apart from ODE113 all other routines are single-step (Runge–Kutta like) methods which means that they express the value of the solution in the next step in terms of a single preceding step. They may be related explicitly or implicitly. Multistep methods in contrast employ more preceding steps to calculate the solution at the succeeding point. RelTol (relative tolerance) is a parameter which specifies the highest allowed relative error in each step of integration (local truncation error) when the adaptive stepsize methods are used. In the case of exceeding the RelTol the stepsize is reduced automatically to decrease the error.

We comment that for general non-separable Hamiltonians only implicit symplectic schemes may be found. Explicit methods exist for separable Hamiltonians and for some special forms of non-separable ones (Chin, 2009). Besides other implications of the usage of the implicit methods we note that they necessarily involve some type of iterative scheme which is typically of a Newton's type and thus requires to supply Jacobian of the right hand sides of the equations of motion which is the Hessian matrix of the second derivatives of the super-hamiltonian $\mathscr{H}$ in our case.

integrator	$\Delta\lvert E\rvert/\lvert E\rvert$	$t_{\mathrm{comp}}[h]$	RelTol	stepsize h
GLS	$\approx 10^{-10}$	14	N/A	0.25
ODE87	$\approx 10^{-9}$	14	10^{-14}	adaptive
ODE113	$\approx 10^{-3}$	1/3	10^{-14}	adaptive
ODE113	$\approx 10^{-3}$	1/4	10^{-6}	adaptive
ODE45	$\approx 10^{-3}$	1/4	10^{-14}	adaptive

Table 1. Comparison of the performance of several integration schemes for the regular trajectory integrated up to $\lambda = 4 \times 10^5$ (see Fig. 2). Quantity t_{comp} expresses the CPU time in hours.

Another inconvenience connected with the symplectic methods is their failure to conserve the symplectic structure once the adaptive stepsize method would be used (Skeel and Gear, 1992). Therefore the stepsize has to be set rigidly for a given integration segment when using symplectic method. Several workarounds have been suggested to combine benefits of symplectic solvers and variable stepsize algorithms – e.g. Hairer's symplectic meta-algorithm (Hairer, 1997) which is, however, only applicable to the separable Hamiltonians. In our context one would considerably suffer from the fixed timestep only in the case of highly eccentric orbits.

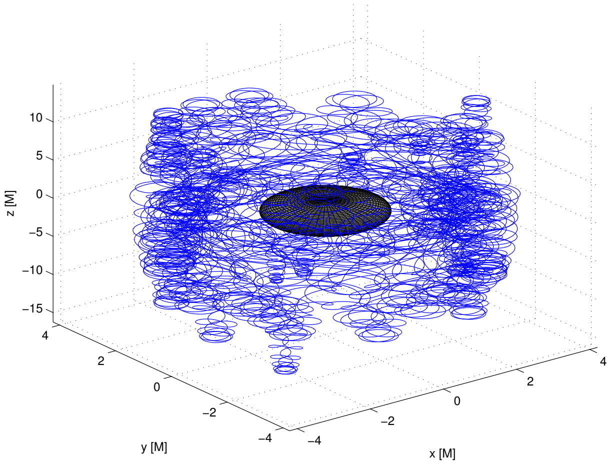

Figure 3. Chaotic trajectory of a charged test particle ($\tilde{q}\tilde{Q} = 1$, $\tilde{L} = 6\,M$ and $\tilde{E} = 1.8$) on the Kerr background ($a = 0.9\,M$) with Wald magnetic field ($\tilde{q}B_0 = 1M^{-1}$). The particle is launched at $r(0) = 3.68\,M$, $\theta(0) = 1.18$ with $u^r(0) = 0$.

2 PERFORMANCE OF THE INTEGRATORS

First we integrate the cross-equatorial regular trajectory depicted in Fig. 1. Comparison of the performance of the integrators is plotted in Fig. 2. We plot relative deviation of the particle's specific energy $\tilde{E}$ from its initial value rather than the error in super-hamiltonian because the discussion of motion in Kopáček et al. (2010) was mostly held in terms of $\tilde{E}$ whose impact upon the trajectory is thus more familiar to us. We calculate the current value of $\tilde{E}$ from the super-hamiltonian $\mathscr{H}$, while the value of π_t remains truly constant regardless the integrator since the Hamilton's equation for its evolution is simply $\mathrm{d}\pi_t/\mathrm{d}\lambda = 0$.

Stepsize of GLS is set in such a way that the integration consumes roughly the same amount of the CPU time as it does for ODE87 with RelTol $= 10^{-14}$ to make the results comparable. The global accuracy of the GLS solver could be further increased by reducing the stepsize while decreasing the RelTol hardly improves the secular accuracy of non-symplectic methods here (we have compared RelTol $= 10^{-6}$ and RelTol $= 10^{-14}$ results for ODE113 obtaining global errors of the same orders in both cases).

integrator	$\lvert\Delta E\rvert/\lvert E\rvert$	t_{comp} $[h]$	RelTol	stepsize h
GLS	$\approx 10^{-9}$	14	N/A	0.25
ODE87	$\approx 10^{-6}$	14	10^{-14}	adaptive
ODE113	$\approx 10^{-3}$	1/6	10^{-14}	adaptive
ODE113	$\approx 10^{-3}$	1/6	10^{-6}	adaptive
ODE45	$\approx 10^{-3}$	1/2	10^{-14}	adaptive

Table 2. Comparison of the performance of several integration schemes for the chaotic trajectory integrated up to $\lambda = 4 \times 10^5$ (see Fig. 4).

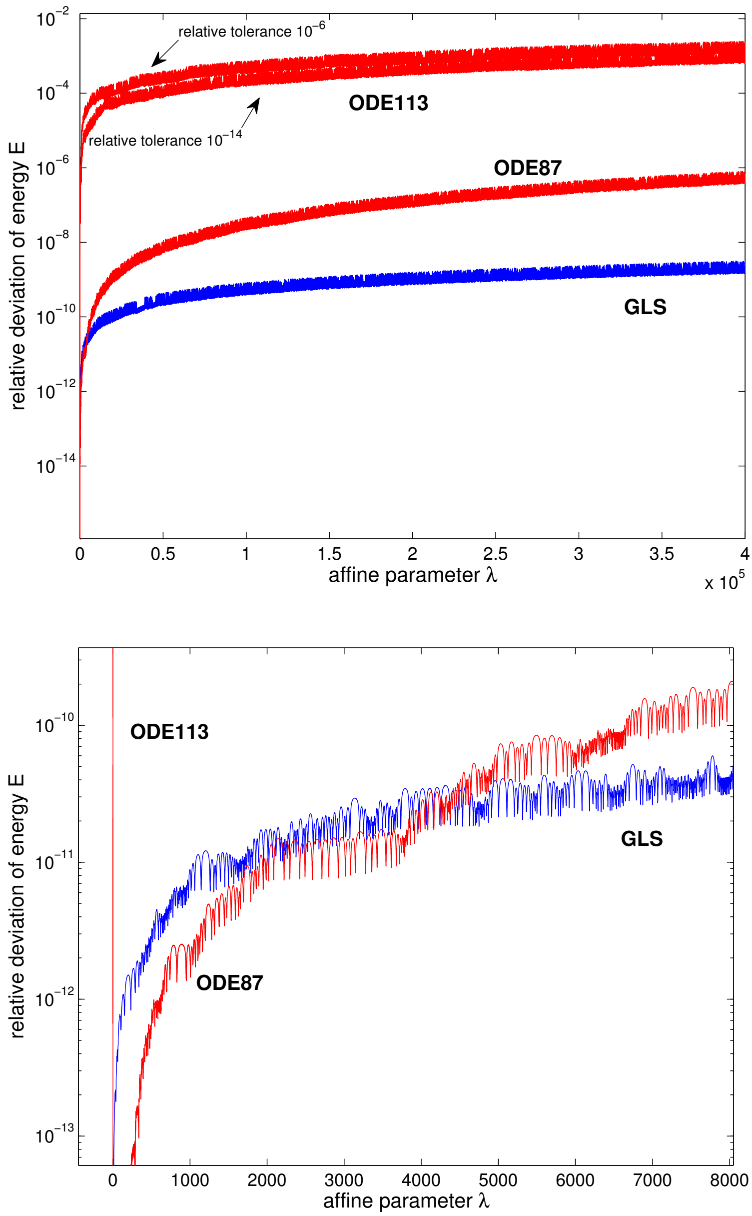

Figure 4. Comparison of the integrators in the case of chaotic trajectory. For $\lambda \gtrsim 5 \times 10^3$ the GLS dominates in accuracy over other schemes with the difference rising steadily. In the *upper* panel we compare ODE113's outcome for two distinct values of the RelTol parameter. ODE45 is not shown to avoid overlapping of its plot with ODE113 curves.

We observe that the error of GLS rises steeply at the beginning and ODE87 is considerably better for some amount of time. However then the error of GLS almost saturates while ODE87's error keeps growing significantly. For $\lambda \gtrsim 10^5$ which corresponds to ≈ 1000 revolutions around the center[2] the GLS scheme becomes more accurate than ODE87 with the difference further rising steadily. We conclude that in the case of regular trajectory ODE87 is appropriate for short-term accurate integration and GLS for any longer accurate integrations. On the other hand for fast, though inaccurate computations one employs ODE113 on all time scales. See Table 1 for the summary.

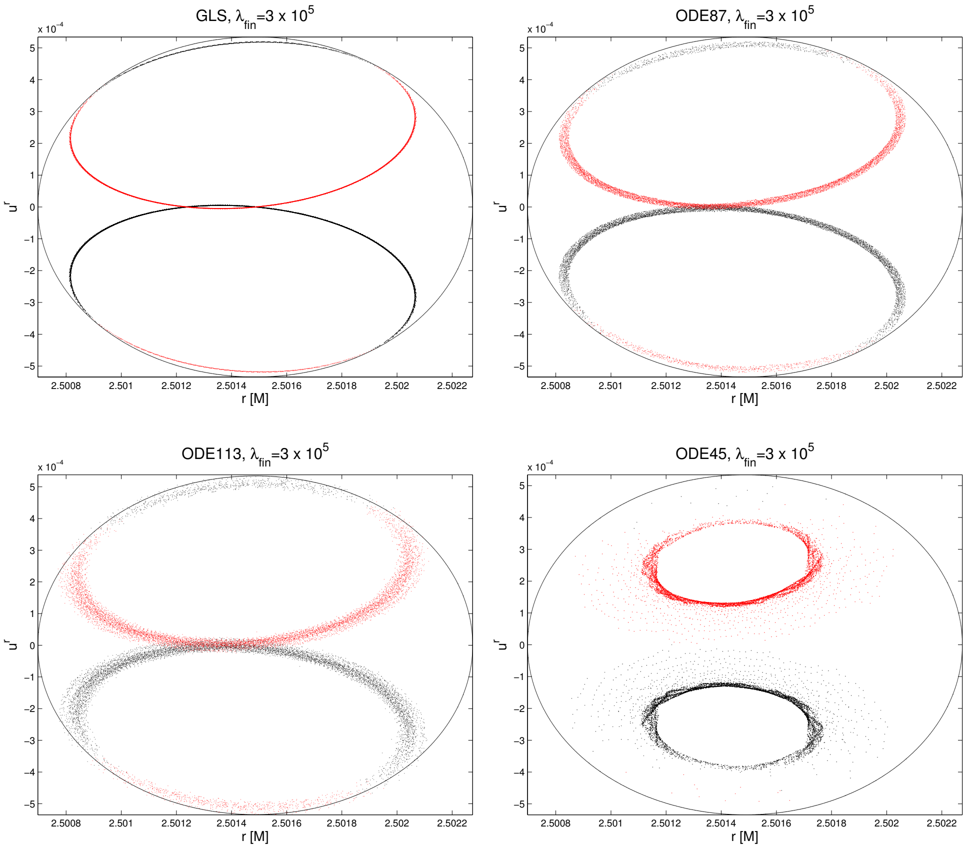

Figure 5. We show how the accuracy of the integration crucially affects the appearance of the Poincarè surfaces of section of a single regular trajectory with $\tilde{q}\tilde{Q} = 1.76$, $\tilde{L} = 4.02\,M$ and $\tilde{E} = 1.619855$ on the Kerr background $a = 0.55\,M$ with Wald magnetic field $\tilde{q}B_0 = 1.92\,M^{-1}$. Particle is launched at $r(0) = 2.5012\,M$, $\theta(0) = 1.0447$ with $u^r(0) = 0$. We distinguish downward crossing with $u^\theta \geq 0$ (black point) from the upward crossing with $u^\theta < 0$ (red point) in the surfaces of section.

[2] For instance for $M = 10^6\,M_\odot$ the azimuthal proper period of a given particle reads $T_\varphi \approx 10^3$ s in SI.

In the case of the chaotic trajectory (depicted in Fig. 3) the dynamics changes in favour of symplectic solver GLS. In Fig. 4 we observe that in this case the symplectic scheme is superior to the others in even more convincing manner than it was in the regular case. Although the initial phase when the error induced by GLS rises more steeply than that of ODE87 is also present, it turns over very quickly and for $\lambda \gtrsim 5 \times 10^3$ ($\approx$ 50 azimuthal revolutions) the GLS turns out to be more accurate. The difference then rises much faster compared to the regular case.

Experiments with ODE113 reveal that here we obtain distinct (though not sharply) errors by changing the RelTol. Difference of eight orders of magnitude in RelTol resulted in roughly one order difference in global error. We also note that chaotic regime induces disorder in short-time oscillations of the global error (see bottom panel of Fig. 4). We summarize that the chaotic regime accents the supremacy of the symplectic scheme which is to be applied on all time scale here (except very short integrations where ODE87 dominates) to obtain the most accurate results. For fast though inaccurate calculation one would switch to ODE113 as before. Results for the chaotic orbit are summarized in Table 2.

From a practical point of view we demand high accuracy of the long-term integration when constructing Poincarè surfaces of section. By theory the intersection points with regular trajectory form one-dimensional curve in the section plane. In Fig. 5 we observe, however, that the points may be dispersed over the considerable area if the global error in energy rises causing artificial excitation/dumping of the system. Symplectic integrator GLS provides the most reliable outcome, with ODE87 the curve is blurred significantly but the interpretation remains unambiguous. With ODE113 the curve is further blurred and using ODE45 solver we obtain completely unreliable outcome which could easily lead to the incorrect interpretation of a trajectory as a chaotic one. We note that we intentionally chose such trajectory which is highly sensitive to the relative errors in dynamic quantities since it itself spans small range of coordinate and momenta values.

3 CONCLUSIONS

We confirm that the symplectic integrators are the method of choice in the case of long-term integration of the Hamiltonian system which in our case consists of a charged test particle orbiting around the Kerr black hole with stationary and axisymmetric electromagnetic test field. Its supremacy over non-symplectic methods is even more apparent in the case of chaotic orbits, where the global accuracy of non-symplectic methods decreases rapidly. The accuracy of the symplectic integrator could be further increased by reducing the stepsize (at the cost of the computational time). On the other hand the performance of the non-symplectic solvers is not considerably affected by reducing the local error (controlled by the RelTol parameter in our case) across the wide range of the values. Once the integrator does not fit the problem (= is not symplectic) there is no effective way to control the global error and even the extremely small local truncation errors do not ensure reliable outcome on a long time scale.

We suggest that our results are not problem-specific and may be generalized to the broad class of the systems. In particular, we suppose that symplectic integrators provide outstanding results in the chaotic regime of any non-integrable Hamiltonian system.

ACKNOWLEDGEMENTS

The present work was supported by the Grant Agency of Charles University (project GAUK 119210/2010) and Charles University research project SVV-263301. Authors also acknowledge the support from the Czech Science Foundation (project No. 205/09/H033) and the COST Action MP1304.

REFERENCES

Arnold, V. I. (1978), *Mathematical methods of classical mechanics*, Springer, New York.

Chin, S. A. (2009), Explicit symplectic integrators for solving nonseparable Hamiltonians, **80**(3), pp. 037701–+.

Goldstein, H., Poole, C. and Safko, J. (2002), *Classical mechanics*, Addison-Wesley, San Francisco.

Hairer, E. (1997), Variable time step integration with symplectic methods, *Appl. Numer. Math.*, **25**, pp. 219–227.

Kopáček, O. (2011), Transition from regular to chaotic motion in black hole magnetospheres, *ArXiv e-prints*, arXiv: 1110.4553.

Kopáček, O., Karas, V., Kovář, J. and Stuchlík, Z. (2010), Transition from Regular to Chaotic Circulation in Magnetized Coronae near Compact Objects, *The Astrophysical Journal*, **722**, pp. 1240–1259, arXiv: 1008.4650.

Kovář, J., Kopáček, O., Karas, V. and Stuchlík, Z. (2010), Off-equatorial orbits in strong gravitational fields near compact objects–II: halo motion around magnetic compact stars and magnetized black holes, *Classical Quantum Gravity*, **27**(13), pp. 135006–+, arXiv: 1005.3270.

Misner, C. W., Thorne, K. S. and Wheeler, J. A. (1973), *Gravitation*, W.H. Freeman and Co., San Francisco.

Skeel, R. D. and Gear, C. W. (1992), Does variable step size ruin a symplectic integrator?, *Physica D Nonlinear Phenomena*, **60**, pp. 311–313.

Wald, R. M. (1974), Black hole in a uniform magnetic field, *Phys. Rev. D*, **10**, pp. 1680–1685.

Yoshida, H. (1993), Recent Progress in the Theory and Application of Symplectic Integrators, *Celestial Mechanics and Dynamical Astronomy*, **56**, pp. 27–43.

Proceedings of *RAGtime 10–13, 15–17/20–22/15–17/14–16 September, 2008/2009/2010/2011, Opava, Czech Republic*
Z. Stuchlík, G. Török and T. Pecháček, editors, Silesian University in Opava, 2014, pp. 133–141

Pseudo-Newtonian gravitational potential of Schwarzschild black hole in the presence of quintessence

Jiří Kovář[a], Zdeněk Stuchlík and Petr Slaný

Institute of Physics, Faculty of Philosophy & Science, Silesian University in Opava, Bezručovo nám. 13, CZ-746 01 Opava, Czech Republic
[a]jiri.Kovar@fpf.slu.cz

ABSTRACT
We introduce a pseudo-Newtonian gravitational potential describing the gravitational field of Schwarzschild black hole surrounded by a quintessential field. We also show, how the geodesic motion reflected in behaviour of general relativistic effective potential can be alternatively described by the pseudo-Newtonian one.

Keywords: Schwarzschild black hole – quintessence – geodesic motion – pseudo-Newtonian potential

1 INTRODUCTION

Starting in late seventies, the conception of the so-called pseudo-Newtonian (PN) gravitational potential came up in astrophysics (Abramowicz, 2009). Those days, the observational 'discover' of the black hole Cygnus-X seemed to be widely accepted in astrophysics. Consequently, general relativity started to play its role in investigation of astrophysical processes. Even these days, however, many astrophysicists neglect the effects of general relativity, being focused on processes relatively far from sources of gravity, where the general relativistic effects can be assumed as small corrections to Newtonian calculations only. On the other hand, coming closer to the objects, like compact objects (black holes, neutron stars, etc.) are, the Newtonian calculations lose its validity and general relativity approach must be applied. Accretions discs (toroidal fluid structures) circling round black holes represent the impressive example of this. The accretion disc treated within Newtonian theory does not exhibit the cusp, through which the matter flows onto the black hole. Just the application of general relativistic description shows up the existing cusp (Abramowicz et al., 1978, 1980) Thus, in dependence on studied problems, it is crucial to decide correctly, which approach to apply. The exact and general, but complex general relativistic one, or the approximative, simpler and perhaps more intuitive Newtonian one, but failing in strong gravity very close to compact objects.

In 1980, however, B. Paczyński and P. Wiita introduced the gravitational potential of spherically symmetric static object – the source of strong gravity (e.g. Schwarzschild black hole) $\psi_{\mathrm{PW}} = -1/(r - 2GM/c^2)$ in the paper (Paczyński and Wiita, 1980). Being used

978-80-7510-125-9

instead of the standard Newtonian one $\psi_{\rm N} = -GM/r$ in the Newtonian theory, such a gravitational potential 'helps' the Newtonian approach to describe also some features of processes taking place close to Schwarzschild black holes.

There is a variety of different approaches in defining the PN gravitational potential describing different kinds of black holes and various aspects of their spacetime structure (Paczyński and Wiita, 1980; Chakrabarti and Khanna, 1992; Nowak and Wagoner, 1991; Artemova et al., 1996; Semerák and Karas, 1999; Mukhopadhyay, 2002; Mukhopadhyay and Misra, 2003; Ghosh and Mukhopadhyay, 2007; Abramowicz, 2009). In the case of Schwarzschild spacetimes, it seems (Artemova et al., 1996) that to reflect the accretion disc properties, the most convenient is the original Paczyński–Wiita gravitational potential $\psi_{\rm PW}$. It enables us to calculate positions of the marginally stable and bound circular orbits at the same radii as follow from the general relativistic calculations.

Originally, the Paczyński–Wiita potential was introduced by a guess, when attempting to include the Schwarzschild radius $r = 2GM/c^2$ into the Newtonian gravity. There is, however, a simple heuristic method for derivation of the PN potentials that yields the Paczyński–Wiita potential. The same method was used for the derivation of the PN gravitational potential for the equatorial plane of rotating Kerr black hole as well (Mukhopadhyay, 2002). Then the position of the marginally stable circular orbit corresponds to the position determined by using the general relativistic approach, and differences in positions of marginally bound circular orbit determined in both the ways are relatively small.

Standardly, this kind of approach, i.e. using the common Newtonian routines and formulas, but with the PN gravitational potential is called the PN approach. The gravity, however, is not the only widely manifesting force in the universe influencing the astrophysical processes. Cosmological observations of distant Ia-type supernova explosions indicate an accelerating universe. Starting at the cosmological redshift $z \approx 1$, the accelerated expansion should be generated by some appropriate form of the so-called dark energy (S. Perlmutter *et al.*, 1999; Riess and *et al.*, 2004). These results are in accord with a large variety of cosmological tests including gravitational lensing, galaxy number counts, etc. (Ostriker and Steinhardt, 1995). The recent detailed studies of the cosmic microwave background (CMB) anisotropies indicate that the energy content of the dark energy represents $\sim 74.5\%$ of the energy content in the observable universe, and the sum of energy densities is very close to the critical energy density $\rho_{\rm crit}$, corresponding to almost flat universe (Spergel D. N. *et al.*, 2003, 2007).

A large variety of possible candidates for the dark energy is discussed these days. First of all, there is the standard possibility represented by the cosmological constant Λ. Its Lorentz invariant form enables interpretation in terms of a ground state or vacuum energy of quantum fields (Dolgov et al., 1988). The energy density ρ_Λ, which can be associated with the cosmological constant, remains unchanged during the cosmic expansion, and its pressure to energy density ratio (equation of state) is $w = p_\Lambda/\rho_\Lambda = -1$.

Further, there is a variety of scalar fields evolving outside of their energy minimum, called quintessence, which possess a time varying energy density and equation of state with $-1 < w < -1/3$ (Zlatev et al., 1999). Such a scenario can be realised by light scalar field coming from modified $f(R)$ gravity (Nojiri and Odintsov, 2003), string-inspired cosmologies (Tsujikawa and Sami, 2001), cosmology with extra dimensions (Neupane, 2004), or by k-essence being a scalar field with a non-canonical kinetic term (Armendariz-

Picon et al., 1999). Similar behaviour is exhibited by the coupled dark energy, i.e. a scalar field coupled to the dark matter. For example, Chaplygin gas or its generalization called quartessence explain both dark energy and dark matter from an unified physical origin (Kamenshchik et al., 2001).

Several years ago, trying to have an effective PN tool even for processes with the dark energy, we constructed the PN gravitational potential describing the gravitational field of Schwarzschild black hole in the universe with the cosmological constant Λ (Stuchlík and Kovář, 2008; Stuchlík et al., 2009). The general relativistic description of such a configuration is represented by the Schwarzschild–de Sitter spacetimes (Stuchlík, 1990; Stuchlík et al., 2000; Stuchlík, 2005). Here we follow this kind of investigation, introducing the PN gravitational potential for the gravitational field of Schwarzschild black hole immersed in a quintessence, representing an alternative explanation of the dark energy.

2 SCHWARSCHILD BLACK HOLE SURROUNDED BY QUINTESSENCE IN GENERAL RELATIVITY

In the standard Schwarzschild coordinates (t, r, θ, ϕ) and the geometric system of units $(c = G = 1)$, the spacetime of Schwarzschild black hole surrounded by a quintessence field is determined by the static and spherically symmetric Kiselev solution of the Einstein equations (Kiselev, 2003)

$$\mathrm{d}s^2 = -g(r)\,\mathrm{d}t^2 + \frac{\mathrm{d}r^2}{g(r)} + r^2\big(\mathrm{d}\theta^2 + \sin^2\theta\,\mathrm{d}\phi^2\big)\,, \tag{1}$$

with the lapse function

$$g(r) = 1 - \frac{2M}{r} - \frac{\alpha}{r^{3w+1}}\,, \tag{2}$$

where M is the mass parameter of the spacetime, w is the quintessential state parameter and α is the normalization factor. The quintessential parameter relates the quintessence pressure p and density ρ in the equation of state $p = w\rho$ and takes values from $-1 < w < -1/3$, whereas the limiting value $w = -1$ corresponds to the dark energy not being quintessence but the vacuum energy (cosmological constant). Moreover, in that case of $\alpha = \Lambda/3$, where Λ is the cosmological constant, the solution (1) reduces exactly to the Schwarzschild–de Sitter solution. Comparison of both the solutions is given in the paper (Fernando, 2013).

In the following, we focus on the exemplary case $w = -2/3$, when the metric lapse function takes a simple form

$$g(r) = 1 - \frac{2M}{r} - \alpha r\,. \tag{3}$$

Singularities of the lapse function giving the black-hole and cosmological horizons are determined by the equation $r - 2M - \alpha r^2 = 0$ and are located at

$$r_{\mathrm{bh}} = \frac{1-\sqrt{1-8\alpha M}}{2\alpha}\,, \quad r_{\mathrm{c}} = \frac{1+\sqrt{1-8\alpha M}}{2\alpha}\,. \tag{4}$$

Both the horizons exist for $1 - 8\alpha M > 0$, separating the spacetimes into two dynamic regions and one static region between $r_{\rm bh}$ and $r_{\rm c}$. For $M = 1/(8\alpha)$, both the horizons coalesce at the radius $r_{\rm bh} = r_{\rm c} = 1/(2\alpha)$.

The heuristic method (see, e.g. Mukhopadhyay (2002)), enabling us to define the PN gravitational potential is based on the knowledge of exact general relativistic relations for the angular momentum per particle mass $L_{\rm c}$ and energy per particle mass $E_{\rm c}$ of particles moving along circular geodesics. Then, we have to realize that in Newtonian physics, the Newtonian gravitational potential $\psi_{\rm N}$ for central gravitational fields is related to the Newtonian angular momentum per particle mass $l_{\rm N,c}$ of free particles moving along circular orbits by the relation $\mathrm{d}\psi_{\rm N}/\mathrm{d}r = l^2_{\rm N,c}/r^3$. Now, the main idea in definition of the PN gravitational potential ψ is in the transposition $l_{\rm N,c} \to L_{\rm c}/E_{\rm c} \equiv l_{\rm c}$,[1] thus we define the potential by the relation

$$\psi = \int \frac{L_{\rm c}^2}{E_{\rm c}^2\, r^3}\, \mathrm{d}r\,. \tag{5}$$

Note that the described method of PN determination works quite well in spherically symmetric (non-rotating) spacetimes, or in the equatorial plane of axially symmetric (rotating, e.g. Kerr or KdS) spacetimes. However, it is much more complicated task to find a PN potential for regions outside the equatorial plane of the rotating spacetimes, because of a non-trivial influence of the dragging of inertial frames. There is a need to upgrade this method (Ghosh and Mukhopadhyay, 2007) or use completely different way of the gravitational potential definition (Semerák and Karas, 1999).

3 CIRCULAR GEODESICS IN GENERAL RELATIVITY

In general relativity, the circular geodesics at $r_{\rm c}$ correspond to extrema of the effective potential, given in the equatorial plane of static and spherically symmetric spacetimes in terms of the metric coefficients $g_{\phi\phi}$ and g_{tt}, and the angular momentum L, by the relation (Misner et al., 1973)

$$V^2_{\rm eff} = -g_{tt}\left(1 + \frac{L^2}{g_{\phi\phi}}\right), \tag{6}$$

thus, for the Schwarzschild-quintessential spacetime, it is given by the relation

$$V^2_{\rm eff} = \left(1 - \frac{2M}{r} - \alpha r\right)\left(1 + \frac{L^2}{r^2}\right). \tag{7}$$

[1] The quantity $l_{\rm c} = L_{\rm c}/E_{\rm c}$ plays its role only when the PN (e.g., Paczyński–Wiita) gravitational potential is defined. Later, standard Newtonian quantities in Newtonian theory are used along with the PN gravitational potential.

The extrema condition for this effective potential, $\partial_r V_{\mathrm{eff}}|_{r_{\mathrm{c}}} = 0$, enables us to determine the constants of motion related to the circular geodesic orbits in the form

$$L_{\mathrm{c}}^2 = \frac{r_{\mathrm{c}}^2\left(\alpha r_{\mathrm{c}}^2 - 2M\right)}{\alpha r_{\mathrm{c}}^2 - 2r_{\mathrm{c}} + 6M}\,, \tag{8}$$

$$E_{\mathrm{c}}^2 = -\frac{2\left(\alpha r_{\mathrm{c}}^2 - r_{\mathrm{c}} + 2M\right)^2}{r_{\mathrm{c}}\left(\alpha r_{\mathrm{c}}^2 - 2r_{\mathrm{c}} + 6M\right)}\,. \tag{9}$$

Dropping now the subscript 'c', the PN gravitational potential (5) can be written in the form

$$\psi = -\frac{r}{2\left(r - 2M - \alpha r^2\right)} + \mathcal{K}\,, \tag{10}$$

where $\mathcal{K}$ is an integration constant having no physical meaning, but enabling to specify a proper form of the potential ψ. Here, we demand that for $\alpha = 0$ expression (11) takes the form of the Paczyński–Wiita potential. This corresponds to the choice $\mathcal{K} = 1/2$ and the PN gravitational potential can be then written in its final form

$$\psi = -\frac{2M + \alpha r^2}{2\left(r - 2M - \alpha r^2\right)}\,. \tag{11}$$

We can see that the potential diverges at the radii of horizons and reflects the position of the static radius r_{s} (corresponding to the local maximum of this potential) of the Kiselev spacetime (see Fig. 1).

Along with the horizons, the static radius is the crucial feature of the Kiselev spacetime. It is the radius where the gravitational attraction of the central black hole is balanced by the cosmic repulsion caused by the quintessence matter. In more details, test particle can stay at rest at that radius – its angular momentum must vanish, $L_{\mathrm{c}} = \alpha r_{\mathrm{c}}^2 - 2M = 0$, which determines the static radius as

$$r_{\mathrm{s}} = \sqrt{2M/\alpha}\,. \tag{12}$$

4 TEST-PARTICLE MOTION IN THE PN POTENTIAL

In the case of central gravitational fields, test-particle motion is confined to central planes (e.g. to the equatorial plane). Following the Newtonian physics, the radial equation of the Keplerian equatorial motion can be written in the form

$$\frac{1}{2}\left(\frac{\mathrm{d}r}{\mathrm{d}t}\right)^2 = e - v_{\mathrm{eff}}\,, \tag{13}$$

where e is the total PN energy per particle mass (energy hereafter) and v_{eff} is the PN effective potential per particle mass (effective potential in the following) defined by the standard relation

$$v_{\mathrm{eff}} = \psi + \frac{l^2}{2r^2}\,. \tag{14}$$

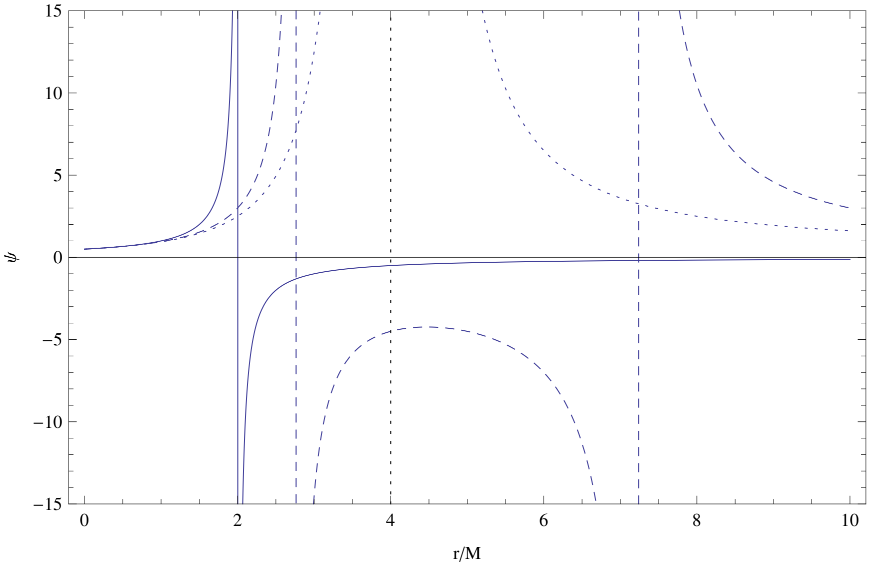

Figure 1. Pseudo-Newtonian gravitational potential for the gravitational field of Schwarzschild black hole surrounded by the quintessence with $w = 2/3$. The solid curve represents the behaviour of the limit case $\alpha = 0$ of the potential, the dashed curve shows its behaviour for $\alpha = 1/10\,\mathrm{M}^{-1}$, while the dotted curve represents the limit case $\alpha = 1/8\,\mathrm{M}^{-1}$, when the horizons coalesce at the radius $r = 4\,\mathrm{M}$.

Here, ψ is the PN gravitational potential (11) and l is the PN angular momentum per particle mass (angular momentum hereafter) defined in Section 2. The circular Keplerian orbits (geodesics) correspond to the effective potential extrema.[2] Thus, their angular momentum is governed by the function

$$l_{\mathrm{c}}^2 = -\frac{r^3\left(\alpha r^2 - 2M\right)}{2\left(\alpha r^2 - r + 2M\right)^2}\,, \tag{15}$$

and the corresponding energy (effective potential extreme) is governed by the function

$$e_{\mathrm{c}} = \frac{2\left(\alpha r^2 + 2M\right)^2 - r\left(3\alpha r^2 + 2M\right)}{4\left(\alpha r^2 - r + 2M\right)^2}\,. \tag{16}$$

[2] Keplerian circular motion can be equivalently given also directly from the PN gravitational potential (11) using relations for orbital and angular velocities, and for the angular momentum and energy

$$v = \left(r\frac{\mathrm{d}\psi}{\mathrm{d}r}\right)^{1/2},\ \Omega = \left(\frac{1}{r}\frac{\mathrm{d}\psi}{\mathrm{d}r}\right)^{1/2},\ l_{\mathrm{c}} = \left(r^3\frac{\mathrm{d}\psi}{\mathrm{d}r}\right)^{1/2},\ e_{\mathrm{c}} = \frac{1}{2}v^2 + \psi\,.$$

However, in some sense, the method of effective potential (Misner et al., 1973), combining the gravitational potential and potential of centrifugal forces, is more general, illustrative and convenient for our case.

5 CONCLUSION

In general, the PN gravitational potential, being used instead of the Newtonian one in the Newtonian approach represents very useful tool to describe the test particle motion (and not only that problem, as we show, e.g. in (Stuchlík et al., 2009)) within the Newtonian physics, taking into account some of the most important features following from general relativity effects when strong gravitational field is present. It also enables us to simply incorporate cosmic repulsive forces (caused by the cosmological constant, quintessence matter, etc.) into our consideration, having an impact on astrophysical phenomena as well.

Few years ago, we presented the construction of the PN gravitational potential for the gravitational field of Schwarzschild black hole in the universe with cosmological constant (Schwarzschild–de Sitter spacetime) and tested its accuracy. We showed that the PN gravitational potential defined for the Schwarzschild–de Sitter spacetimes reflects precisely the existence of the static radius, diverges at both the black-hole and cosmological horizons, and predicts locations of both the inner and outer marginally stable and marginally bound circular orbits at the same radii as those following from the full general relativity (Stuchlík and Kovář, 2008). The energy difference between the inner and outer marginally stable circular orbit, which plays a crucial role in the theory of thin discs, has been shown very close to the relativistic result. We also demonstrated that the PN potential can be well applied even for description of thick discs orbiting Schwarzschild–de Sitter black holes; it provides exact determination of the equipressure (equipotential) surfaces governing the shape of toroidal discs in equilibrium configuration (Stuchlík et al., 2009).

Here, we have presented the construction of the PN gravitational potential describing the gravitational field of a Schwarzschild black hole surrounded by a quintessence representing source of the accelerated expansion of the universe. We have presented its form that reduces to the well-known Paczyński–Wiita gravitational potential (describing the gravitational field of the pure Schwarzschild black hole) when the quintessence parameter α tends to zero (the quintessence is not present). The PN gravitational potential diverges on both the horizons and reflects the position of the static radius as well.

In the future, we plan to deeply go through the testing of accuracy of the presented potential in the same way as we have done for the case of the PN gravitational potential for the Schwarzschild black hole gravitational field and cosmological constant, summarized above.

ACKNOWLEDGEMENTS

The authors acknowledge the project Synergy CZ.1.07/2.3.00/20.0071 supporting the international collaboration of Institute of Physics, Silesian University in Opava, and the Albert Einstein Centre of Gravitation and Astrophysics supported by the Czech Science Foundation Grant No. 14-37086G.

REFERENCES

Abramowicz, M. A. (2009), The Paczyński-Wiita potential. A step-by-step "derivation". commentary on: Paczyński B. and Wiita P J., 1980, AA, 88, 23, *Astronomy and Astrophysics*, **500**, p. 213.

Abramowicz, M. A., Calvani, M. and Nobili, L. (1980), Thick accretion disks with super-eddington luminosities, *The Astrophysical Journal*, **242**, p. 772.

Abramowicz, M. A., Jaroszyński, M. and Sikora, M. (1978), Relativistic accreting disks, *Astronomy and Astrophysics*, **63**, p. 221.

Armendariz-Picon, C., Damour, T. and Mukhanov, V. (1999), k-inflation, *Physical Letters B*, **458**, p. 209.

Artemova, I. V., Björnsson, G. and Novikov, I. D. (1996), Modified newtonian potentials for the description of relativistic effects in accretion disks around black holes, *The Astrophysical Journal*, **461**, p. 565.

Chakrabarti, S. K. and Khanna, R. (1992), A newtonian description of the geometry around a rotating black hole, *Monthly Notices of the Royal Astronomical Society*, **256**, p. 300.

Dolgov, A. D., Zel'dovich, Y. B. and Sazhin, M. V. (1988), *Kosmologiya rannej vselennoj (Cosmology of the early universe)*, Izdatel'stvo Moskovskogo universiteta, Moscow.

Fernando, S. (2013), Nariai black holes with quintessence, *Modern Physics Letters A*, **28**, p. 50189.

Ghosh, S. and Mukhopadhyay, B. (2007), Generalized pseudo-newtonian potential for studying accretion disk dynamics in off-equatorial planes around rotating black holes: Description of a vector potential, *The Astrophysical Journal*, **667**, p. 367.

Kamenshchik, A., Moschella, U. and Pasquier, V. (2001), An alternative to quintessence, *Physical Letters B*, **511**, p. 265.

Kiselev, V. V. (2003), Quintessence and black holes, *Classical and Quantum Gravity*, **20**, p. 1187.

Misner, C. W., Thorne, K. S. and Wheeler, J. A. (1973), *Gravitation*, Freeman, San Francisco.

Mukhopadhyay, B. (2002), Description of pseudo-newtonian potential for the relativistic accretion disk around kerr black holes, *The Astrophysical Journal*, **581**, p. 427.

Mukhopadhyay, B. and Misra, R. (2003), Pseudo-newtonian potentials to describe the temporal effects on relativistic accretion disk around rotating black holes and neutron stars, *The Astrophysical Journal*, **582**, p. 347.

Neupane, I. P. (2004), Accelerating cosmologies from exponential potentials, *Classical and Quantum Gravity*, **21**, p. 4383.

Nojiri, S. and Odintsov, S. D. (2003), Modified gravity with negative and positive powers of curvature: Unification of inflation and cosmic acceleration, *Physical Review D*, **68**, p. 123512.

Nowak, M. A. and Wagoner, R. V. (1991), Diskoseismology: Probing accretion disks I. Trapped adiabatic oscillations, *The Astrophysical Journal*, **378**, p. 656.

Ostriker, J. P. and Steinhardt, P. J. (1995), The observational case for a low density universe with a non-zero cosmological constant, *Nature*, **377**, p. 600.

Paczyński, B. and Wiita, P. (1980), Thick accretion disks and supercritical luminosities, *Astronomy and Astrophysics*, **88**, p. 23.

Riess, A. G. and *et al.* (2004), Type ia supernova discoveries at $z > 1$ from the hubble space telescope: Evidence for past deceleration and constraints on dark energy evolution, *The Asytrophysical Journal*, **607**, p. 665.

S. Perlmutter *et al.* (1999), Measurements of ω and λ from 42 high-redshift supernovae, *Monthly Notices of the Royal Astronomical Society*, **517**, p. 565.

Semerák, O. and Karas, V. (1999), Pseudo-newtonian models of a rotating black hole field, *Astronomy and Astrophysics*, **343**, p. 325.

Spergel D. N. *et al.* (2003), First year wilkinson microwave anisotropy probe (wmap) observations: Determination of cosmological parameters, *The Astrophysical Journal*, **148**, p. 175.

Spergel D. N. *et al.* (2007), Three-year wilkinson microwave anisotropy probe (wmap) observations: Implications for cosmology, *The Astrophysical Journal*, **170**, p. 377.

Stuchlík, Z. (1990), Note on the properties of the schwarzschild-de sitter spacetime, *Bull. Astronom. Inst. Czechoslovakia*, **41**, p. 341.

Stuchlík, Z. (2005), Influence of the relic cosmological constant on accretion discs, *Modern Physics Letters A*, **20**, p. 561.

Stuchlík, Z. and Kovář, J. (2008), Pseudo-newtonian gravitational potential for schwarzschild–de sitter spacetimes, *International Journal of Modern Physics D*, **17**, p. 2089.

Stuchlík, Z., Slaný, P. and Hledík, S. (2000), Equilibrium configurations of perfect fluid orbiting schwarzschild–de sitter black holes, *Astronomy and Astrophysics*, **363**, p. 425.

Stuchlík, Z., Slaný, P. and Kovář, J. (2009), Pseudo-newtonian and general relativistic barotropic tori in schwarzschild-de sitter spacetimes, *Classical and Quantum Gravity*, **26**, p. 215013.

Tsujikawa, S. and Sami, M. (2001), String-inspired cosmology: a late time transition from a scaling matter era to a dark energy universe caused by a gauss-bonnet coupling, *Journal of Cosmology and Astroparticle Physics*, **01**, p. 006.

Zlatev, I., Wang, L. and Steinhardt, P. J. (1999), Quintessence, cosmic coincidence and the cosmological constant, *Physical Review Letters*, **82**, p. 896.

Proceedings of *RAGtime 10–13, 15–17/20–22/15–17/14–16 September, 2008/2009/2010/2011, Opava, Czech Republic*
Z. Stuchlík, G. Török and T. Pecháček, editors, Silesian University in Opava, 2014, pp. 143–154

Programming models used on Many-Core architectures

Jan Novotný

Institute of Physics, Faculty of Philosophy & Science, Silesian University in Opava,
Bezručovo nám. 13, CZ-746 01 Opava, Czech Republic

ABSTRACT
The time in which we live is characterized by an ever-increasing amount of data that we are able to explore and acquire. In all fields of science we could find some examples. Processing large volumes of information thus brings the requirement for engaging computational science. With increasing demands on data processing is advantageous to use new technology and start using parallel computation. Effective use of current technology requires from programmers new knowledge and skills. They meet with the countless new programming models and tools. In this article, we summarize the most commonly used programming models and points which good programming model should meet. The article also try to highlight the reasons why one should use a structured parallel programming.

Keywords: patterns – parallel computing – many-core systems – heterogeneous systems – programming models – parallel software development

1 INTRODUCTION

There is constantly increasing number of sold devices (smartphones, tablets, etc.) which enable parallelized applications. Not only availability of these systems is on the rise, also computational demands of applications are increasing that leads to the development and usage of certain methods. We are at a time when multi-core or many-core architectures are becoming mainstream.

In physics, the need to begin using the accelerated calculations appears in several areas. For example, the arrival of new types of radio telescopes such as the SKA (Square Kilometre Array) requires use of High Performance Computing (HPC). HPC is also often needed in areas of research such as cosmology (mostly real-time processing area) and galaxy evolution, pulsars, star and planet formation, etc.

Computational science where a massive amounts of calculations are processed is no longer a domain of supercomputers or distributed platforms. For scientific computations is now possible to use besides CPU specified coprocessors (e.g. Xeon Phi) and the graphic cards. Each of these devices has its own advantages and disadvantages. The choice either to use the CPU or many-core coprocessors is not easy and is often dependent on a computing problem.

It turns out that to get better performance, it is necessary to abandon the serial programming and start from the beginning using the parallel program development approach. Generally, it appears as the best to use a so-called heterogeneous approach. That is a division of the algorithm into several parts and calculations, which are distributed among different computational units (hosts and devices).

Nevertheless, the programmer should keep in mind that his main goal is to write scalable code, i.e. code should be able to use any amount of available parallel hardware.

Software engineers designing parallel programs have several options how to proceed. Their choice is often dependent on their skills, experience and intended objective of the application itself.

One of the easiest way is to rewrite few lines of the existing serial program or add specific lines (e.g. Directives) and use compilers ability of auto-parallelization. The other way is to use structured patterns of parallelism. The use of these patterns has it's advantages, such as ease of readability, scalability, extensibility and so on. Most patterns avoid non-deterministic behaviour as well as the serial programming, which is deterministic by nature.

Using current programming tools may nevertheless lead to worse results because of unnecessary serialization. Among programmers, this is known as a serial trap. Recognition and avoidance is perhaps the hardest part of parallel programming.

For example imagine you have two workers and four tasks. One worker take the first two tasks and the second worker the rest. The two workers can run in parallel as long as there is no dependency between the four tasks. But if there is some, like the third task need results from the first task, the system need to run serially. Moreover sometimes you can find that each task can take different time to process. If you cannot divide further then the total running time of the program is the sum of the dependent tasks or the task that takes longest. This is the *span* of example above.

We are in an era in which to get any enhancements in application performance we must use *parallel thinking*. Together with the above mentioned patterns finding serial traps is deemed as a first step to think parallel.

2 MOTIVATION

Hardware is parallel by nature because of several techniques like instruction level parallelism (ILP), pipelining, vector instructions, hyperthreading, etc. but CPU architects and designers made it so that CPU seemed serial on the outside. CPUs started to use implicit parallel operations long ago without programmers explicitly telling them to do so. That is so-called *serial illusion*. More about this problem could be found in literature.(McCool et al., 2008) Programmers depended on this illusion for a long time and now this approach does not lead to any significant improvement as is shown in the right bottom of the Fig. 1. Moreover the performance of serial program will not grow over time as show dark blue and green color in the figure.

To achieve improvement programmer can either rewrite the sequential code with special directives or use the compiler's automatic parallelization tools. However it is not universally working and mostly it comes with no significant improvements as is shown in the Fig. 1. The right bottom part of the figure indicates that the individual benchmark tests are rather

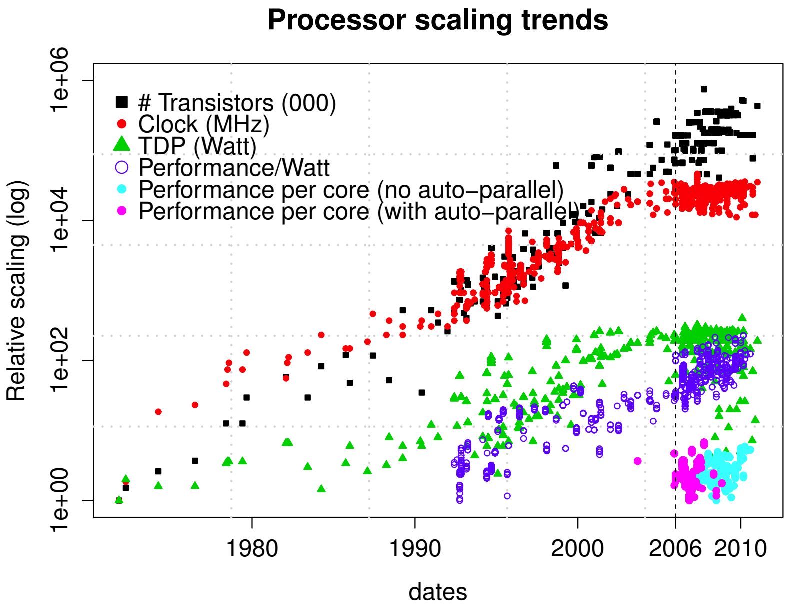

Figure 1. The figure is showing the trends over the years with emphasizing of the year 2006 when the multi-core era comes. The number of transistors is raising with accordance to the Moore law on the other hand clock rates nowadays are stalling. Data comes from CPU DB.(Stanford VLSI Group, 2014)

flat when the auto-parallelization is allowed.[1] The gain in performance per core using auto-parallelization over the years is not particularly a trend and therefore exploitation of the parallel nature of the hardware generally leads to the need of using the explicit parallel programming.(Herb Sutter, 2005) We are not saying to not use the benefits coming of the rather easy way to run application quicker. We want only stress that auto-parallelization is not always the best choice and in time scale not most effective.

Data in the Fig. 1 come from CPU DB (Danowitz et al., 2012) which gather information about CPU performance since 1973. In the figure could be observed several trends. Firstly we can see that since 1975 until 2006 the clock rate is exponentially increasing. In past the increase of clock rate was enough to improve performance of CPU until it reached so-called *power wall*, *memory wall*[2] and *ILP wall*[3]. In the figure since year 2006 can be spotted continual stagnation of clock rate, thermo-design power and performance per Watt. Still

[1] The CPU2006 Spec is an industry standard benchmark providing data on CPU performance since beginning of the multicore era around year 2006. To fully understand the nature of these benchmarks we address to read (Stanford Performance Evaluation Corporation, 2014; Subcommittee, 2006).

[2] The growth of off-chip memory is not as fast as the on-chip memory. The programmer nowadays cannot ignore the overall data rate (bandwidth) and the time between submitted and satisfied request (latency).

[3] The hardware is parallel in nature and for example if two close instructions do not depend on each other, they can be ran parallelly. However the useful limit for most real problems is around six instructions.

according to Moore law the amount of transistors in CPU is growing exponentially and that is why the performance per Watt is slightly going up as demonstrate dark blue color in the Fig. 1.

Secondly, we can see that around year 2004 the increase in thermal design power (green dots) gets to its maximum that can be effectively air-cooled (power wall). That was the most severe issue which appeared and led to creation of multi-core architectures.

Nevertheless, the theoretical performance continues to grow. It is clear that a programmer to obtain better results need to move from just rewriting the serial algorithm (*refactoring*[4]) and using the auto-parallelization. Nowadays to improve the code and be able to scale it in time developers must explicitly specify parallel algorithms.

In many cases the way to *think parallel* and use new programming models seems the best solution. However with that more problems arises: knowledge of new models, finding the most time consuming chain of tasks which needs to be run serially (*span*[5]), etc.

Finally learning parallel programming side by side with serial programming is not the best approach. Teaching how to think parallel needs to be done from the beginning and alone to avoid certain serial assumptions. Structured approach to parallel programming is essential and it is one of the best strategies for writing effective scalable program. Using a set of patterns with standard names help to design such programs and also aid in readability.

3 PARALLEL SOFTWARE DEVELOPMENT

The process of software development today provides various methodologies that have been proven over time. Their structure often helps to set a few questions that are advised to answer before starting programming, or before refactoring. (Figure 2 shows the three most commonly used methods).

These questions may specify for example, exactly what do we want from the application? On which architectures will it run or which hardware is available (this decision is mostly set during the design phase, see 2)? Where are the input data and what type of data have we available? These are the types of questions that will assist us in the software development process and possibly help us find the span of the program.

During the implementation phase, it is also preferable to use development environments and tools such as profilers, debuggers, etc. This fact is highlighted in documentation from nVidia (best practice guide).(nVidia, 2014)

In its essence nVidia best practice guide introduces four elements: assess, parallelize, optimize and deploy (APOD cycle) which is very similar to the spiral methodology. There should be emphasized that this is a cyclical process and it is always necessary to verify the results with a control test in the verification phase.

Finally, McCool et al. (2008) highlight problems that must be discussed in process of parallel algorithm design:

---

[4] It is true that this is sometimes sufficient, and certainly one of the simplest ways to parallelize code.(Fowler et al., 1999)

[5] Span refers to the longest set of tasks that must run serially. This chain in computer science is known as a critical path.

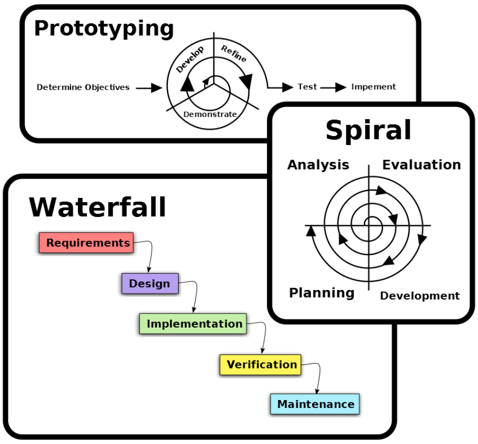

Figure 2. The three basic approaches applied to software development methodology frameworks.(Wikimedia Foundation, 2014)

- “Total amount of computational work.
- Critical path (span).
- Total amount of communication.”

In question of amount of computational work we believe in heterogeneous approach, i.e. systems with different kind of units. Every programmable unit has its own specifics and it is favourable to use certain kind depending on its abilities.

Critical path refers to recognition and finding chains of instruction which needs to be run serially as mentioned above in Section 2.

The last mentioned concerns the fact that memory access and communication between cores costs time. How much time it costs depends on the location of the work unit (locality). Relatively low cost are threads which run on the same core, more cost those which share an on-chip memory and even more cost those in another socket. It may indicate that the problem is memory bandwidth limited and not computational limited.[6] Finally we can say that finding the bottleneck of the program is the most critical problem.

4 PROGRAMMING MODELS AND PATTERNS

Effective management of communication and redistribution of work is required for meaningful parallel programming. Usage of patterns should facilitate both. Programming models that enable effective implementation of patterns are also necessary.

Unfortunately none of the most widely used programming languages are adapted for needs of parallel programming. However, if we look at the amount of serial code already written, it would be a shame not to reuse it. For this reason, most parallel models are in fact an extension of the current programming practices and tools.

[6] In the case of heterogeneous systems must be also taken into account the bandwidth of the PCI Express bus.

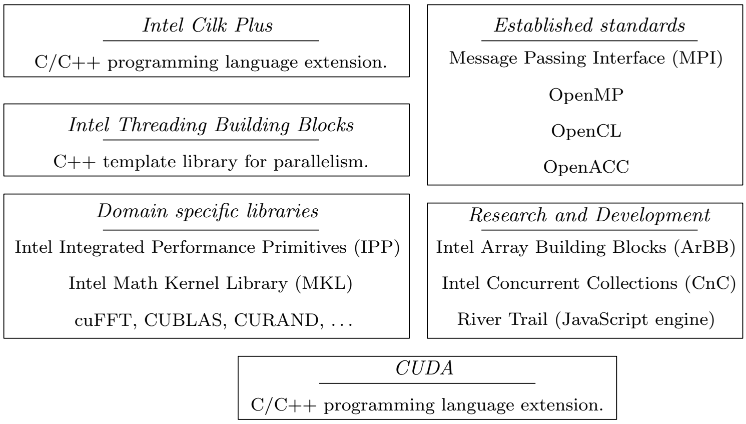

Figure 3. Examples of most frequently used programming models and libraries for parallel programming.(McCool et al., 2008)

In Figure 3 are examples of most frequently used extensions and libraries in industry and science. Despite the fact that each of them has its advantages and disadvantages, it is important to know that the models have the following properties:

- performance,
- productivity,
- portability.

For portability there is need to extend functionality and performance across operating systems and compilers. Programming languages like Java, C and C++ are portable and most of the programming models in the Fig. 3 too. Just CUDA language does not fulfil this criteria. To be able to compile the CUDA code you need to use nVidia compiler and for running the program a CUDA enabled graphics card is required.

In general, using abstractions like elemental functions or array operations is preferable. This approach is better in general than a program specifically suited to concrete hardware although such a program is very efficient. For example each Intel's processor today can support different vector instruction set extension, that is why using abstraction to specify vectorization[7] instead of vector intrinsic[8] is better. However, we must keep in mind that in some cases programming for the specific pieces of hardware is desired.

In terms of productivity models we should make it possible to debug and maintain programs as well as easily implement a range of suitable algorithms and maintain composability. By that we mean the ability to use a feature regardless to other features used in the linked library or elsewhere in the code. Consider a case where this is not true and using `for` statement somewhere in the code meant that you cannot use `if` statement anywhere. It's something we do not want, but unfortunately can happen.

[7] Vectorization is a concrete form of parallelism enabling simultaneous computing using vector hardware by instructions such as MMX, SSE, and AVX.

[8] Intrinsics seems like a function in programming language but are supported directly by the compiler.

Oversubscription is another quite common problem, i.e. each use of parallelism could define a new set of threads and so exceed the number of threads that system can handle.

To obtain reasonable improvement of performance we must sustain scalability. In other words, generating more parallelism when the problem grows larger is crucial. This can be achieved by so called data parallelism and each programming model in the figure is supporting it. For example Cilk Plus has a "special" array notation extensions for C and C++ (see, algorithm 1) which explicitly specify data parallelism operations. The ArBB has even simpler solution as long as the data are stored in the appropriate containers. Such abstractions built in the models make possible to use regular data parallelism[9] explicitly and not rely only on the compilers.

Algorithm 1: Examples of vector addition in different programming models.

Serial vector addition in C:

for $i \leftarrow 0$ **to** 100000 **do**
| a[i] = b[i] + c[i];
end

Parallel vector addition in Cilk Plus:

a[0:100000] = b[0:100000] + c[0:100000];

Parallel vector addition in ArBB:

input : a
output: b, c

a = b + c;

Above mentioned models and usage of elementary functions or compiler directives such as `pragma`, are helping to vectorize the code and work in the context of regular data parallelism. At last, sometimes to support vectorization, change of the data layout (array of structures or structure of arrays) is preferable.

Selecting the programming model is not an easy task, despite the fact that some models overlap its functionality, but not portability. Next factor may be the hardware on which will the application run. Other may be the requirement for fine control of architecture or vice versa ease of implementation (see Fig. 4).

Structured programming using patterns is now commonly used and proven method of development of applications in various fields such as natural language learning (Kamiya, 2012), software architectures (Buschmann et al., 1996; Schmidt et al., 2000) and so on. Perhaps that is why they have became best practice tool among the software engineers.(Gamma et al., 1994)

In computer science there are three different strategies: Design Patterns, Implementation Patterns and Algorithmic Strategy Patterns. The first two mentioned have rather abstract character. The first of them can be classified as a high level and the second as a low level

[9] That is a subcategory of data parallelism which is mapped onto vector instruction of the hardware.

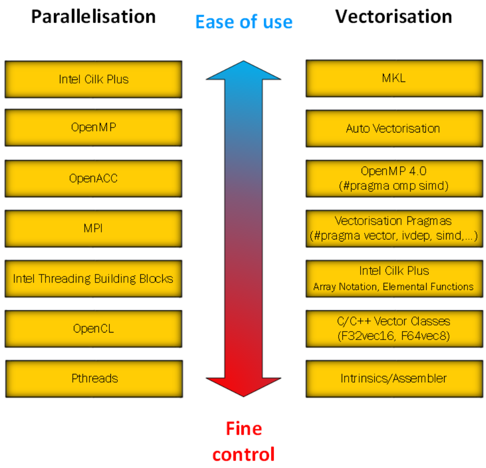

Figure 4. Here is shown the relevance between easy of implementation and fine control from different models provided by Leibnitz Supercomputing Centre in their guide for users.(Leibnitz Supercomputing Centre, Bavarian Academy of Sciences and Humanities, 2014-07-21)

(tied to specific hardware). Algorithmic Strategy pattern lies somewhere between these two, and thanks to it's semantic behaviour and ease of implementation appears to be best choice for most of the cases. Because they affect how your algorithms are organized, we strongly believe that algorithmic strategy patterns are good for learning and teaching parallel thinking. These design in literature are usually so-called algorithmic skeletons.(Cole, 1989; Aldinucci and Danelutto, 2007)

Lots of Algorithmic Strategic Patterns nowadays are already implemented in the programming models and often knowledge of these patterns helps to teach programming languages. Still, knowledge and use of algorithmic skeletons exceeds certain programming languages and models in being more general.

Examples of the three most useful and frequently used patterns are: nesting, mapping and fork-join. Nesting is often used in sequential programming and is important for a modular approach. Yet its transfer to the parallel programme is a challenge. The key to implement map pattern is a division of the problem into smaller tasks and run those parallelly. This is called embarrassing parallelism. Problems where this pattern can be used are well scalable and lead to efficient vectorization. Last pattern: fork-join divide tasks recursively into simpler ones and combines them later. In fact, it is one of the pillars of the strategy divide and conquer in computational science.

All these mentioned patterns highlight that to get good scalable code we need to pay attention to the data parallelism method. In other words, dividing problems into smaller ones with possibility to grow with increasing overall problem size.

Generally, the programmer should use a structured approach for better readability, debugability and scalability of the code. Patterns should be used as basic building blocks. They also become a common vocabulary when discussing ways of how to solve computational problems. In addition, patterns are independent of the usage of a particular programming model, programming language or even computing architecture.

5 SHORT OVERVIEW OF PARALLEL PROGRAMMING MODELS

The following paragraphs briefly describe selected programming models satisfying above mentioned properties.

Cilk Plus

Cilk Plus is an extension of the programming languages C and C++ it supports task and data parallelism. It is very easy to use and compared to sequential code it differs only in adding keywords (i.e. `cilk_sync`) and array section notation. This characteristic is mainly due to the fact that Cilk Plus is embedded into most compilers. In fact if you run Cilk Plus program with one thread it will act as the special keywords are ignored (serial illusion). Other features are:

- "Fork-join to support irregular programming patterns and nesting." (McCool et al., 2008)
- Parallel loops to support patterns such as map.
- Explicit vectorization by using array section like `pragma simd`.
- "Load balancing via work-stealing." (McCool et al., 2008)

For more information and specification see Intel (2014a).

Threading Building Blocks (TBB)

This is a C++ library under development by Intel. Because it is not a language extension it is supported by all standard (ISO C++) compilers. In order to run the blocks of code in parallel TBB requires the use of functors.

Just as Cilk Plus TBB supports parallelism based on the tasking model. In other words, the individual operations are considered as tasks and are dynamically allocated to each core using the library run-time engine and automating efficient use of the CPU cache.

TBB provides following features:

- "Template library supporting regular and irregular parallelism." (McCool et al., 2008)
- Support for certain pattern (fork-join, scan, reduction).
- Load balancing via work-stealing.

Advantage of TBB is in algorithms that are written with respect to the minimum assumption of data structure. The literature describes TBB as part of generic programming and C++ standard template library (STL) is a good example of its philosophy.

Commonly seen in practice are the use of the individual components of TBB with other programming models such as OpenMP and Cilk Plus. For more information and specification see Intel (2014b).

Open Multi-Processing (OpenMP)

OpenMP is a standard developed by a consortium of major brands in hardware and software. This is an application programming interface (API) that supports shared memory multiprocessing programming. OpenMP is based on using a set of compilation directives or pragmas in Fortran, C and C++.

In its essence OpenMP is based on multi-threading model, i.e. the main thread divide and run multiple threads sub-dividing the task among them. This property is especially beneficial for certain types of algorithms and memory hierarchy platforms often seen in high-performance computing (HPC). The main problem of the explicit threading model is mentioned oversubscription.

One of the advantages over Cilk Plus and TBB is the ability to explicitly manage threads using the thread ID and the number of threads to control how the work is mapped to threads. This feature is often used by HPC programmers. On the other hand, it is a limiting factor too. It prevents system to determine the load balancing.

In summary OpenMP interface provides following features:

- "A tasking model that supports execution by an explicit group of threads.
- Creations of group of threads that jointly execute a block of code.
- Support for atomic operations and locks."(McCool et al., 2008)

For more information and specification see OpenMP Architecture Review Board (2014).

Array Building Blocks (ArBB)

ArBB is compiler independent C++ library supporting data parallelism on different architectures such as multi-core processors, graphics processing unit (GPU), Intel Many Integrated Core Architecture (MIC). The parallelization is mediated by a set of operations which operate on a group of data. It provides following features:

- "High level programming language with elemental functions and vector operations.
- Offloading to attached many-core architectures without changing source code." (McCool et al., 2008)
- Safe by default: preventing parallel programming bugs such as deadlocks and data races.

This programming model is classified as a high-level programming language. It was developed by Intel as experimental library. During October 2012 was announced discontinuation of development in favour of Cilk Plus and TBB.(Intel, 2011)

Open Computing Language (OpenCL)

OpenCL is an open standard maintained by the Khronos group and is used for writing programs that can execute on heterogeneous machines such as CPUs, GPUs, field-programmable gate arrays (FPGAs) and others.

OpenCL framework divides computing system into two parts: CPU (host) and accelerators (devices). Therefore, it includes a kernel language[10] and an API for data management and execution of the kernels on the devices from the host.

As a low-level language is primarily designed for performance programming. This fact requires more effort from programmers to specify computations into detail and often write different versions of kernel for each class of devices.

Although OpenCL is not considered as mainstream among programmers as the previous models, we believe that it has it's place among others and should not be ignored. For more information and specification see OpenMP Architecture Review Board (2014).

[10] The language is a standard C99 including certain features.

Compute Unified Device Architecture (CUDA)

CUDA is a parallel computing platform using primarily GPUs. It is developed by NVIDIA Corporation and its implemented on graphics cards of their brand.

For software engineers CUDA is programming model accessible through a set of accelerated libraries, compilation directives (OpenACC) and as an extension of C/C++ and Fortran languages with using specific compilers.

Despite this programming model does not comply the requirement for portability and works only on certain devices, is it highly extended and used in computational science. For example third party wrappers are available for Python, Java, Perl, MATLAB, and also software Mathematica have its native support.

In addition to OpenCL, CUDA is for beginning programmers a little easier and has very good documentation on the Web (nVidia, 2014-08-01). This and the above mentioned are arguments why it should be one of the options in deciding which programming model to use.

CONCLUSION

Mainstream computers and other electronic devices around us are changing in its essence and to be able to get better performance and scalability of old or new software we need to switch to a new concept of thinking. Furthermore, as we have shown in Section 2 programmers cannot rely on so-called serial illusion any-more. We reached the three walls: power wall, memory wall and ILP wall. Because of that we are driven by the need to change to the explicit parallel programming.

Today in computer science and in science in general are increasingly used heterogeneous systems, i.e. systems based on multi-core and many-core computational units. To make better use of these machines, it is good to use parallel programming models. Some examples of programming models and their properties we described in Section 5.

Furthermore, to achieve effective programming, it is the best practice to use parallel patterns. They are easily scalable, debugable and among computational scientists settle basic vocabulary. That is why we want to stress that usage of parallel patterns and models is for a computational scientist inevitable.

ACKNOWLEDGEMENTS

I would like to express my special thanks to Karel Adámek and Anna Janíková for their valuable and constructive suggestions during writing this paper and for many consultations. The presented work was supported by EU grant Synergy CZ.1.07./2.3.00/20.0071

REFERENCES

Aldinucci, M. and Danelutto, M. (2007), Skeleton-based parallel programming: Functional and parallel semantics in a single shot, *Computer Languages, Systems & Structures*, **33**(3-4), pp. 179–192, ISSN 14778424.

Buschmann, F., Meunier, R., Rohnert, H., Sommerlad, P. and Stal, M. (1996), *Pattern-Oriented Software Architecture Volume 1: A System of Patterns*, Wiley, Chichester ; New York, ISBN 9780471958697.

Cole, M. I. (1989), *Algorithmic Skeletons: Structural Management of Parallel Computation*, The MIT Press, London : Cambridge, Mass, ISBN 9780262530866.

Danowitz, A., Kelley, K., Mao, J., Stevenson, J. P. and Horowitz, M. (2012), CPU DB: recording microprocessor history, *Communications of the ACM*, **55**(4), pp. 55–63, URL `http://dl.acm.org/citation.cfm?id=2133822`.

Fowler, M., Beck, K., Brant, J., Opdyke, W. and Roberts, D. (1999), *Refactoring: Improving the Design of Existing Code*, Addison-Wesley Professional, Reading, MA, 1st edition, ISBN 9780201485677.

Gamma, E., Helm, R., Johnson, R. and Vlissides, J. (1994), *Design Patterns: Elements of Reusable Object-Oriented Software*, Addison-Wesley Professional, Reading, Mass, 1st edition, ISBN 9780201633610.

Herb Sutter (2005), The free lunch is over: A fundamental turn toward concurrency in software, *Dr. Dobbs Journal*, **30**(3), URL `http://www.gotw.ca/publications/concurrency-ddj.htm`.

Intel (2011), Intel® Array Building Blocks, URL `https://software.intel.com/en-us/articles/intel-array-building-blocks`.

Intel (2014a), Intel® Cilk™ Plus, URL `https://software.intel.com/en-us/node/522579`.

Intel (2014b), Intel® Threading Building Blocks (Intel® TBB) User Guide, URL `https://software.intel.com/en-us/node/506045`.

Kamiya, T. (2012), *Japanese Sentence Patterns for Effective Communication: A Self-Study Course and Reference*, Kodansha USA, New York, ISBN 9781568364209.

Leibnitz Supercomputing Centre, Bavarian Academy of Sciences and Humanities (2014-07-21), LRZ: SuperMIC - intel xeon phi cluster, URL `http://www.lrz.de/services/compute/supermuc/supermic/`.

McCool, M., Reinders, J. and Robison, A. (2008), *Structured Parallel Programming: Patterns for Efficient Computation*, Morgan Kaufmann, Amsterdam, 1st edition, ISBN 9780124159938.

nVidia (2014), CUDA C programming guide, URL http://docs.nvidia.com/cuda/cuda-c-programming-guide/index.html.

nVidia (2014-08-01), CUDA toolkit documentation, URL `http://docs.nvidia.com/cuda/index.html`.

OpenMP Architecture Review Board (2014), OpenMP.org, URL `http://openmp.org/wp/`.

Schmidt, D., Stal, M., Rohnert, H. and Buschmann, F. (2000), *Pattern-Oriented Software Architecture Volume 2: Patterns for Concurrent and Networked Objects*, Wiley, Chichester England ; New York, ISBN 9780471606956.

Stanford Performance Evaluation Corporation (2014), SPEC - standard performance evaluation corporation, URL `http://www.spec.org/`.

Stanford VLSI Group (2014), CPU DB - looking at 40 years of processor improvements | a complete database of processors for researchers and hobbyists alike., cPUDBv1.2-11-30-gcbf16c8, URL `http://cpudb.stanford.edu/`.

Subcommittee, S. C. (2006), SPEC CPU2006 benchmark descriptions, *ACM SIGARCH Computer Architecture News*, **34**(4), pp. 1–17, URL `http://dl.acm.org/citation.cfm?id=1186737`.

Wikimedia Foundation (2014), Software development process, URL `http://en.wikipedia.org/w/index.php?title=Software_development_process&oldid=627519437`.

Proceedings of *RAGtime 10–13, 15–17/20–22/15–17/14–16 September, 2008/2009/2010/2011, Opava, Czech Republic*
Z. Stuchlík, G. Török and T. Pecháček, editors, Silesian University in Opava, 2014, pp. 155–163

Comparison of the CDM halo and MOND models of the Magellanic Cloud motion in the field of Milky Way

Jan Schee and Zdeněk Stuchlík

Institute of Physics, Faculty of Philosophy & Science, Silesian University in Opava, Bezručovo nám. 13, CZ-746 01 Opava, Czech Republic

ABSTRACT
There is an explanation of the rotation curves in the periphery of spiral galaxies based on MOdified Newtonian Dynamics (MOND). Considering the motion of Magellanic Clouds in the gravitational field of Milky Way, we compare predictions of the CDM halo model with the cosmic repulsion term included to those obtained in the framework of the MOND theory. Our results demonstrate that the predictions of the CDM halo and MOND models differ very substantially, especially in the case of the Large Magellanic Cloud motion.

Keywords: MOND – galactic motion – Milky Way – Magellanic Clouds

1 INTRODUCTION

An alternative to the model of Cold Dark Matter (CDM) explanation of the rotation curves in the periphery of spiral galaxies, based on MOdified Newtonian Dynamics (MOND) (Milgrom, 1983), is realized on the Newtonian level, modifying the Newton dynamic law by introducing an additional term depending on the ratio of acceleration and some critical acceleration a_0 below which the Newton second law in not valid. The MOND dynamic law relating the acceleration a of a test particle with mass m and the acting force F takes the general form

$$m\mu(x)a = F\,, \quad x = \frac{a}{a_0}\,, \tag{1}$$

where we assume that the modification is given by the function $\mu(x)$ such that $\mu(x) \sim 1$ for $x \gg 1$ and $\mu(x) \sim x$ for $x \ll 1$. In the MOND regime the gravitational acceleration is proportional to $1/r$ and its fall is much slower in comparison with the standard Newtonian dependence $1/r^2$. The MOND is successful in explaining the rotation curves of spiral galaxies by putting $a_0 \sim 10^{-8}\mathrm{cm}\cdot\mathrm{s}^{-2}$ (Milgrom, 1983). Various interpolation formulae has been proposed to cover the transition between the Newton and MOND regime, but it seems that the simplest one that will be used later works quite well (Famaey and Binney,

978-80-7510-125-9

2005; Iorio, 2009). The compatibility of MOND with data from Solar System was discussed in a number of works (Sereno and Jetzer, 2006; Iorio, 2008). However, it is of high relevance to test its predictions in the case of the motion of satellite galaxies.

A relativistic covariant formulation of the MOND theory was discussed by (Bekenstein and Milgrom, 1984; Bruneton and Esposito-Farèse, 2007; Zhao, 2007; Milgrom, 2008). There are some other non-standard approaches to explanation of the galactic rotation curves without using the CDM (Iorio, 2009). Of special interest is MOdified Gravity (MOG) – a fully covariant gravity theory where a massive vector field coupled to matter exists, giving a Yukava-like modification of gravity (Moffat and Toth, 2009), but here we restrict our attention to the MOND theory.

It is of high interest to test the gravitational influence of the Milky Way on its close companions. For example, the motion of the tidal debris of the Sagittarius dwarf at 17.4 kpc from the Milky Way center was studied (Read and Moore, 2005). However, there is another important possibility for such testing due to the closest galaxies to the Milky Way, namely the Magellanic Clouds. They have their total mass much smaller than the Milky Way total mass – their mass is estimated to be smaller than $(1/10)M_{\rm MW}$. Further, their distance from the Milky Way exceeds substantially its dimension. Therefore, the Magellanic Clouds can be well approximated as test particles moving in the gravitational field of the Galaxy.

Quite recently it has been shown that the cosmic repulsion inferred from the cosmological observations (Riess et al., 2004) seems to be very important for determining the character of the satellite galaxy motion and their trajectories in the standard framework of the Galaxy model with the CDM halo (Stuchlík and Schee, 2011). The effects of the cosmological constant are on the 10 per cent level or higher, if we consider the binding mass of Milky Way relative to SMC and LMC through their initial positions and velocities. The results of the models of the motion put serious doubts on the binding of the LMC to the Milky Way if the CDM halo model is the relevant one – see also Besla et al. (2007). Nevertheless, the problem of LMC binding remains to be open due to uncertainties in determination of the initial velocity due to the Galaxy rotation velocity (Shattow and Loeb, 2009; Stuchlík and Schee, 2011). We compare here the predictions of the CDM halo model of the Galaxy gravitational field to those given by the MOND model of the satellite galaxy motion. Since the role of the cosmological constant has been shown to be important in the CDM halo model, we add the cosmic repulsion potential in the Newtonian limit

$$U_\Lambda = -\frac{\Lambda c^2}{6} r^2 \,, \tag{2}$$

to the CDM halo model – see Stuchlík and Schee (2011). On the other hand, we do not include the effects of the cosmic repulsion into the MOND model, since the trajectories predicted by the model are much closer to the Galaxy, being limited to regions where the role of the cosmic repulsion has to be suppressed. The Galaxy gravitational field is reflected by the (ellipsoidal) potential of the Galaxy disc and (spherical) potential of the Galactic bulge (Binney and Tremaine, 1987). For simplicity these can be substituted by a spherical Newtonian potential of a point source located at the Galaxy centre and having total mass of the visible Galaxy, since the motion of Magellanic Clouds is restricted to regions distant to the visible Galaxy.

2 THE GALAXY GRAVITATIONAL FIELD

The Galaxy is represented by its visible, baryonic parts, i.e. by the disk and the bulge that could be considered as central point sources, neglecting the non-sphericity of the Galaxy disc. The recent estimate of the total baryonic mass of the Galaxy is

$$M = 6.5 \times 10^{10}\, M_{\odot} \tag{3}$$

with the composition given by $M_{\rm disc} = 5 \times 10^{10}\, M_{\odot}$ and $M_{\rm bulge} = 1.5 \times 10^{10}\, M_{\odot}$ (McGaugh, 2008; Xue et al., 2008; Iorio, 2009).

The elliptical gravitational potential of the Galactic disk reads

$$U_{\rm disc} = -\frac{\xi G M_{\rm disc}}{\sqrt{x^2 + y^2 + \left(k + \sqrt{z^2 + b^2}\right)^2}}\,, \tag{4}$$

while the galactic bulge potential is simulated by

$$U_{\rm bulge} = -\frac{G M_{\rm bulge}}{r + c}\,, \tag{5}$$

where $\xi = 1$, $k = 6.5\,\mathrm{kpc}$, $b = 0.26\,\mathrm{kpc}$, $c = 0.7\,\mathrm{kpc}$. We shall compare, for completeness, the effect of the detailed potential

$$U = U_{\rm disc}(M_{\rm disc}) + U_{\rm bulge}\big(M_{M_{\rm bulge}}\big) \tag{6}$$

and the point Newtonian potential $U_{\rm PN}(M_G)$.

3 THE MOND MODEL OF GRAVITATIONAL INTERACTIONS ON COSMIC SCALES

The MOND is invented in order to enable explanation of matter motion in the outer parts of galaxies, including the Milky Way, where discrepancy between the rotation curves of matter and the gravitational effect of galactic visible matter is observed. Usually, this discrepancy is explained by the effect of an invisible CDM, while MOND is trying to explain it by modification of the Newton dynamical law (Milgrom, 1983), modifying the acceleration of matter at large distances from the galaxy center.

3.1 Modification of the Newton gravitational law

Considering the Newtonian gravitational force, the MOND dynamical law reads

$$m\mu(x)a = -G\frac{Mm}{r^2}\,, \tag{7}$$

where $\mu(x)$ is the modifying acceleration function, $x = a/a_0$ is its argument determining the magnitude of the modification and a_0 is the critical acceleration specifying the limit of validity of the standard Newtonian mechanics. From fitting of rotational curves in the

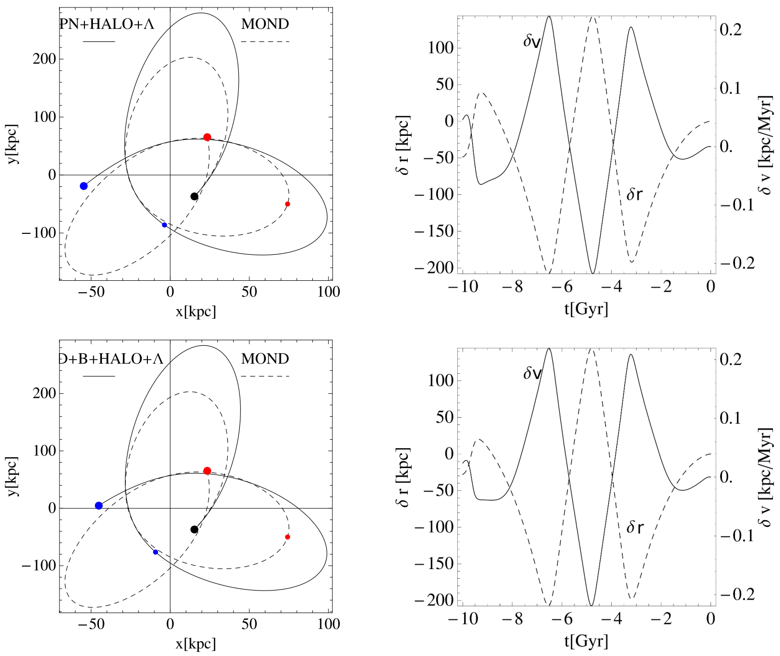

Figure 1. Comparison of MOND model with CDM models with different gravitational potentials $U_{\rm PN} + U_{\rm halo}$ (*top*), $U_{\rm disk} + U_{\rm bulge} + U_{\rm halo} - \Lambda c^2 r^2/6$ (*bottom*) is plotted. On the left the trajectories of SMC are plotted. There are three types of dots in the plot. Big black refers to the time instant $t = 0$, the small dots refer to the time instant $t = 5$ Gyr and big colored dots refer to the time instant $t = 10$ Gyr. The red color dots belong to dashed lines and blue ones to the solid lines. On the right the functions $\delta r = r_1 - r_2$ and $\delta v = v_1 - v_2$ are plotted where index 1 refers to MOND model and index 2 refers to CDM model.

Milky Way and other spiral galaxies the critical acceleration is established to be (Begeman et al., 1991)

$$a_0 = 1.2 \times 10^{-10} \mathrm{m} \cdot s^{-2} \tag{8}$$

giving thus the acceleration scale. Then in terms of the interpolation function $\mu(x)$ the actual acceleration is related to the Newtonian one by $\mathbf{a}_N = \mu(x)\mathbf{a}$ (McGaugh, 2008).

Clearly, for any gravitating mass a critical radius r_0 related to the critical acceleration can be defined by the relation

$$r_0 = \left(\frac{GM}{a_0}\right)^{1/2} \tag{9}$$

that represents a critical distance from the source of the gravitational field beyond which the MOND regime becomes effective. Using the critical value of a_0 determined by fitting the rotational curves of galaxies (8) and the total mass of the visible galactic disc and bulge

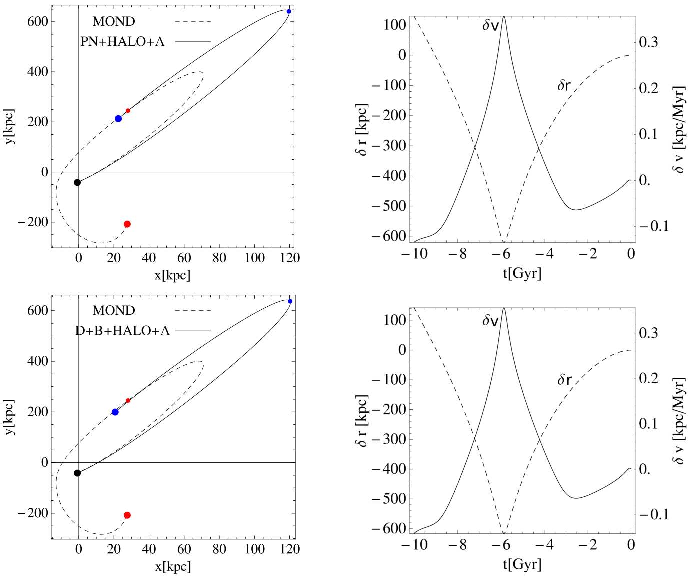

Figure 2. Comparison of MOND model with CDM models with different gravitational potentials $U_{\mathrm{PN}} + U_{\mathrm{halo}}$ (*top*), $U_{\mathrm{disk}} + U_{\mathrm{bulge}} + U_{\mathrm{halo}} - \Lambda c^2 r^2/6$ (*bottom*) is plotted. On the left the trajectories of LMC are plotted. There are three types of dots in the plot. Big black refers to the time instant $t = 0$, the small dots refer to the time instant $t = 5\,\mathrm{Gyr}$ and big colored dots refer to the time instant $t = 10\,\mathrm{Gyr}$. The red color dots belong to dashed lines and blue ones to the solid lines. On the right the functions $\delta r = r_1 - r_2$ and $\delta v = v_1 - v_2$ are plotted where index 1 refers to MOND model and index 2 refers to CDM model.

of the Milky Way ($M \sim 6.5 \times 10^{10}\, M_{\odot}$), we arrive at the characteristic radius relevant for the Milky Way

$$r_0 \sim 2.62 \times 10^{20}\,\mathrm{m} \sim 8.45\,\mathrm{kpc}\,. \tag{10}$$

representing nearly $2/3$ of the visible Galaxy extension.

3.2 The modification function and the critic acceleration

The modification function $\mu(x)$ interpolating transition between the Newtonian and fully MOND regimes was originally given in the form (Bekenstein and Milgrom, 1984)

$$\mu(x) = \frac{x}{\left(1 + x^2\right)^{1/2}}\,. \tag{11}$$

However, there is a simpler possibility (Famaey and Binney, 2005)

$$\mu(x) = \frac{x}{1 + x} \tag{12}$$

that yields better results in fitting the rotation velocity curves in the Milky Way and galaxy NGC 3198 (Zhao and Famaey, 2006; Famaey et al., 2007). The effective MOND “gravitational" acceleration can then be given by (Iorio, 2009)

$$a = \frac{a_N}{2}\left[1 + \left(1 + \frac{4a_0}{a_N}\right)^{1/2}\right]. \tag{13}$$

Using the critical radius r_c, we can express the MOND acceleration in the form

$$a = -\frac{1}{2}\frac{GM}{r^2}\left[1 + \left(1 + \frac{4r^2}{r_0^2}\right)^{1/2}\right]. \tag{14}$$

3.3 Modified gravitational potential and the motion of Magellanic Clouds around Milky Way

The MOND theory can be expressed by a modification of the Newtonian gravitational potential. The form of this modification is determined by the function $\mu(x)$ and using the explicit form of this function (12) we obtain the MOND gravitational potential in the form

$$\Phi_{\mathrm{MOND}} = \frac{GM}{2r} + \frac{GM}{2r}\sqrt{1 + \frac{4r^2}{r_0^2}} - \frac{GM}{r_0}\sinh^{-1}\left(\frac{2r}{r_0}\right). \tag{15}$$

Notice that we assume spherically symmetric source of gravity neglecting thus all the details of the galactic gravitational field; of course, we do not consider the CDM halo gravitational potential. In general (non-relativistic) non-spherical situations the modified Poisson equation (Bekenstein and Milgrom, 1984)

$$\nabla \cdot \left[\mu\left(\frac{|\nabla U|}{a_0}\right)\nabla U\right] = 4\pi G\varrho \tag{16}$$

must be used to determine the MOND potential and, consequently, acceleration. Of course, for our purposes, the gravitational acceleration given by Eq. (15) corresponding to the simplest version of MOND using the spherically symmetric acceleration formula is quite convenient. We consider the point source with $M_G = M_{\mathrm{disk}} + M_{\mathrm{bulge}}$.

4 CDM HALO MODEL

The dark matter halo is assumed spherical and its gravitational potential can be represented by the logarithmic formula of the form (Binney and Tremaine, 1987)

$$U_{\mathrm{halo}} = v_{\mathrm{halo}}^2 \ln\left(r^2 + d^2\right), \tag{17}$$

where $v_{\mathrm{halo}} = 114\,\mathrm{km\cdot s^{-1}}$ and $d = 12\,\mathrm{kpc}$. This halo model implies the halo mass formula

$$M_{\mathrm{halo}} = \frac{2v_{\mathrm{halo}}^2 r^3}{G\left(r^2 + d^2\right)} \tag{18}$$

giving mass of the Galaxy halo (Iorio, 2009)

$$M_{\mathrm{halo}}(r = 60\,\mathrm{kpc}) = 3.5 \times 10^{11}\, M_{\odot} \tag{19}$$

in agreement with value of $M_{\rm halo}(r = 60\,{\rm kpc}) = (4.0 \pm 0.7) \times 10^{11}\,M_\odot$ used in (Xue et al., 2008). For different models of the CDM halo (see, e.g. Einstein, 1939; Lake, 2004; Haager, 1997, 1998; Saxton and Ferreras, 2010).

For halos more extended, crossing the radius of $r \sim 60\,{\rm kpc}$ corresponding approximately to the present positions of both the SMC and LMC, the halo mass and its influence on the motion of the Magellanic Clouds will be higher. For details see Stuchlík and Schee (2011) where the halo extension and its mass are controlled by the so called cut-off radius, assuming the same conditions to be fulfilled at the reference radius of $r \sim 60\,{\rm kpc}$. Here we adopt the results of Xue et al (Xue et al., 2008) giving the CDM halo mass $M_{\rm halo} = 1 \times 10^{12}\,M_\odot$. For simplicity, we do not consider here the role of the dynamical friction Mulder (1983) on the motion of the SMC and LMC through the CDM halo. Of course, the dynamic friction effect is irrelevant for the MOND model since it does not assume any halo.

5 MOTION OF MAGELLANIC CLOUDS AROUND MILKY WAY

The visible Galaxy gravitational field will be common for both the CDM and MOND models. For completeness, we use the detailed and simplified point potential of the visible Galaxy composed with the CDM halo and Λ term.

	x	y	z
x_i	15.3	-36.9	-43.3
v_i	-87± 48	-247± 42	149± 37

Table 1. Galactocentric coordinates (in kpc) and velocity components (in km·s^{-1}) of SMC ($r_0 = 58.9\,{\rm kpc}$, $v_0 = 302 \pm 52\,{\rm km/s}$).

	x	y	z
x_i	-0.8	-41.5	-26.9
v_i	-86± 12	-268± 11	252± 16

Table 2. Galactocentric coordinates (in kpc) and velocity components (in km·s^{-1}) of LMC ($r_0 = 49.5\,{\rm kpc}$, $v_0 = 378 \pm 18\,{\rm km/s}$).

When alternative explanations of galactic rotation velocity curves are considered, based on modified gravitational laws, the CDM halos are not taken into account and only the Galactic mass inferred mainly from the electromagnetic radiation emitted by the baryonic mass is considered.

In the MOND framework only the point source is considered, as the role of the detailed potential is shown to negligible. The recent motion of the Magellanic Clouds is characterized by their position and the velocity relative to the Galaxy plane that are presented in the Table 1 for the Small Magellanic Cloud (SMC) and in Table 2 for the Large Magellanic Cloud (LMC) (Iorio, 2009). These positions and velocities, given in the so called Galactocentric reference system (Shattow and Loeb, 2009) are taken as initial conditions in the integration of the motion equations giving trajectory of SMC and LMC in the field of the Galaxy.

We have confronted the trajectories of both SMC and LMC reflecting the influence of the Galaxy and its CDM Halo combined with the cosmological constant effect that were constructed and in detail discussed in Stuchlík and Schee (2011), with the trajectories obtained by the MOND – therefore, all the external field effects (e.g. those coming from the Andromeda galaxy) are considered as irrelevant. The trajectories are given in Fig. 1 for SMC and Fig. 2 for LMC. Clearly, the differences in the character of the trajectories of the Magellanic Clouds are substantial being of the same order as the extension of the trajectories and could thus serve potentially as an efficient test of the validity of the MOND models. Significant differences of the MOND and CDM halo trajectories have been found, both for the SMC and LMC galaxies. For LMC the differences are bigger than for SMC.

6 CONCLUSIONS

We compared the trajectories constructed using the models including the CDM halo and the cosmological constant to the those based on the MOND, modelling the rotation curves of visible Galaxy without necessity of the CDM halo. The results, shown in Fig. 1 for SMC and in Fig. 2 for LMC galaxy, indicate enormous differences in the predicted trajectories. In the case of SMC trajectories there is $\delta r \sim 100\,\mathrm{kpc}$ and $\delta v \sim 0.2\,\mathrm{kpc/Myr}$. In the case of the LMC trajectories the differences approach even higher values $\delta r \sim 500\,\mathrm{kpc}$ and $\delta v \sim 0.3\,\mathrm{kpc/Myr}$. On the other hand, the detailed description of the gravitational potential of the visible Galaxy is shown to be quite irrelevant for the motion of the Magellanic Clouds. We have found that the trajectories of both SMC and LMC constructed under the model of MOND differ significantly from the trajectories based on the CDM halo models. The CDM halo models were shown to be strongly dependent on the cosmic repulsion represented by the cosmological constant term Stuchlík and Schee (2011). It could be thus interesting to test the role of the cosmic repulsion even in the case of the MOND model. Nevertheless, we expect these effects to be suppressed relative to the CDM model since the closer binding of the SMC and LMC trajectories to the Galaxy.

ACKNOWLEDGEMENTS

The present work was supported by the Czech Grants MSM 4781305903.

REFERENCES

Begeman, K. G., Broeils, A. H. and Sanders, R. H. (1991), Extended rotation curves of spiral galaxies - Dark haloes and modified dynamics, *Monthly Notices Roy. Astronom. Soc.*, **249**, pp. 523–537.

Bekenstein, J. and Milgrom, M. (1984), Does the missing mass problem signal the breakdown of Newtonian gravity?, *Astrophys. J.*, **286**, pp. 7–14.

Besla, G., Kallivayalil, N., Hernquist, L., Robertson, B., Cox, T. J., van der Marel, R. P. and Alcock, C. (2007), Are the Magellanic Clouds on Their First Passage about the Milky Way?, *Astrophys. J.*, **668**, pp. 949–967, arXiv: `astro-ph/0703196`.

Binney, J. and Tremaine, S. (1987), *Galactic dynamics*, Princeton University Press, NJ.

Bruneton, J.-P. and Esposito-Farèse, G. (2007), Field-theoretical formulations of MOND-like gravity, *Phys. Rev. D*, **76**(12), 124012.

Einstein, A. (1939), On a Stationary System with Spherical Symmetry Consisting of Many Gravitating Masses, *Annals of Mathematics*, **40**, pp. 922–936.

Famaey, B. and Binney, J. (2005), Modified Newtonian dynamics in the Milky Way, *Monthly Notices Roy. Astronom. Soc.*, **363**, pp. 603–608, arXiv: `astro-ph/0506723`.

Famaey, B., Gentile, G., Bruneton, J.-P. and Zhao, H. (2007), Insight into the baryon-gravity relation in galaxies, *Phys. Rev. D*, **75**(6), 063002, arXiv: `astro-ph/0611132`.

Haager, G. (1997), Two-component dust in spherically symmetric motion, *Classical and Quantum Gravity*, **14**, pp. 2219–2230, arXiv: `gr-qc/9705002`.

Haager, G. (1998), Voids within the two-component dust model, *Classical and Quantum Gravity*, **15**, pp. 3669–3677.

Iorio, L. (2008), Putting Yukawa-Like Modified Gravity (MOG) on the Test in the Solar System, *Scholarly Research Exchange*, **2008**, p. 8385, arXiv: 0809.3563.

Iorio, L. (2009), Galactic Sun's motion in the cold dark matter, MOdified Newtonian Dynamics and modified gravity scenarios, *Astronomische Nachrichten*, **330**, pp. 857–862, arXiv: 0908.2689.

Lake, K. (2004), Galactic Potentials, *Phys. Rev. Lett.*, **92**(5), 051101, arXiv: gr-qc/0302067.

McGaugh, S. S. (2008), Milky Way Mass Models and MOND, *Astrophys. J.*, **683**, pp. 137–148, arXiv: 0804.1314.

Milgrom, M. (1983), A modification of the Newtonian dynamics as a possible alternative to the hidden mass hypothesis, *Astrophys. J.*, **270**, pp. 365–370.

Milgrom, M. (2008), Marriage à-la-MOND: Baryonic dark matter in galaxy clusters and the cooling flow puzzle, *New Astronomy Reviews*, **51**, pp. 906–915, arXiv: 0712.4203.

Moffat, J. W. and Toth, V. T. (2009), Modified Gravity and the origin of inertia, *Monthly Notices Roy. Astronom. Soc.*, **395**, pp. L25–L28, arXiv: 0710.3415.

Mulder, W. A. (1983), Dynamical friction on extended objects, *Astronomy and Astrophysics*, **117**, pp. 9–16.

Read, J. I. and Moore, B. (2005), Tidal streams in a MOND potential: constraints from Sagittarius, *Monthly Notices Roy. Astronom. Soc.*, **361**, pp. 971–976, arXiv: astro-ph/0501273.

Riess, A. G., Strolger, L.-G., Tonry, J., Casertano, S., Ferguson, H. C., Mobasher, B., Challis, P., Filippenko, A. V., Jha, S., Li, W., Chornock, R., Kirshner, R. P., Leibundgut, B., Dickinson, M., Livio, M., Giavalisco, M., Steidel, C. C., Benítez, T. and Tsvetanov, Z. (2004), Type Ia Supernova Discoveries at z¿1 from the Hubble Space Telescope: Evidence for Past Deceleration and Constraints on Dark Energy Evolution, *Astrophys. J.*, **607**, pp. 665–687, arXiv: astro-ph/0402512.

Saxton, C. J. and Ferreras, I. (2010), Polytropic dark haloes of elliptical galaxies, *Monthly Notices Roy. Astronom. Soc.*, **405**, pp. 77–90, arXiv: 1002.0845.

Sereno, M. and Jetzer, P. (2006), Dark matter versus modifications of the gravitational inverse-square law: results from planetary motion in the Solar system, *Monthly Notices Roy. Astronom. Soc.*, **371**, pp. 626–632, arXiv: astro-ph/0606197.

Shattow, G. and Loeb, A. (2009), Implications of recent measurements of the Milky Way rotation for the orbit of the Large Magellanic Cloud, *Monthly Notices Roy. Astronom. Soc.*, **392**, pp. L21–L25, arXiv: 0808.0104.

Stuchlík, Z. and Schee, J. (2011), Influence of the cosmological constant on the motion of Magellanic Clouds in the gravitational field of Milky Way, *Journal of Cosmology and Astroparticle Physics*, **9**, 018.

Xue, X. X., Rix, H. W., Zhao, G., Re Fiorentin, P., Naab, T., Steinmetz, M., van den Bosch, F. C., Beers, T. C., Lee, Y. S., Bell, E. F., Rockosi, C., Yanny, B., Newberg, H., Wilhelm, R., Kang, X., Smith, M. C. and Schneider, D. P. (2008), The Milky Way's Circular Velocity Curve to 60 kpc and an Estimate of the Dark Matter Halo Mass from the Kinematics of 2400 SDSS Blue Horizontal-Branch Stars, *Astrophys. J.*, **684**, pp. 1143–1158, arXiv: 0801.1232.

Zhao, H. (2007), Coincidences of Dark Energy with Dark Matter: Clues for a Simple Alternative?, *Astrophys. J. Lett.*, **671**, pp. L1–L4, arXiv: 0710.3616.

Zhao, H. S. and Famaey, B. (2006), Refining the MOND Interpolating Function and TeVeS Lagrangian, *Astrophys. J. Lett.*, **638**, pp. L9–L12, arXiv: astro-ph/0512425.

Proceedings of *RAGtime 10–13, 15–17/20–22/15–17/14–16 September, 2008/2009/2010/2011, Opava, Czech Republic*
Z. Stuchlík, G. Török and T. Pecháček, editors, Silesian University in Opava, 2014, pp. 165–171

On radial U-H-E collisions between different mass particles

Jan Schee and Zdeněk Stuchlík

Institute of Physics, Faculty of Philosophy & Science, Silesian University in Opava,
Bezručovo nám. 13, CZ-746 01 Opava, Czech Republic

ABSTRACT

We study the result of the U-H-E collisions of particles radially colliding in the strong gravity of Kerr superspinars. The colliding particles have different masses $m_1 \neq m_2$ and we quantify the outcome of such collision taking place at fixed radius $r = 1$ in the field of Kerr superspinar determined by spin parameter a under assumption of both inelastic and elastic collisions.

1 INTRODUCTION

Recently a wide interest is devoted to the so called Banados–Silk–White (BSW) process (Bañados et al., 2009) where centre of mass energy of colliding particles can be highly ultrarelativistic if they collide in vicinity of the black hole horizon (Zaslavskii, 2010; Harada et al., 2013; Tursunov et al., 2013), or in the strong gravity of naked singularity spacetimes, as those related to the Kerr superspinars (Stuchlík et al., 2011; Stuchlík and Schee, 2012, 2013; Stuchlík et al., 2014). In those processes it is usually assumed that the collisions are inelastic and the rest energy of the colliding particles is transformed into the energy of outgoing particles and photons. Here we shall consider also the possibility when the particles are scattered in an elastic process.

2 SPACETIME GEOMETRY AND EQUATIONS OF MOTION

According to String theory there exist a class of solutions interpreted as spinning object of mass M violating the general relativistic bound of spin of black holes, having $a > 1$. They are called Kerr superspinars which, in the astrophysical area of interest, can be primordial remnants of high energy phase of very early period of evolution of the Universe. It turns out that the geometry generated by Kerr superspinar is the well known Kerr geometry and its line element in Boyer–Lindquist coordinates read

$$\mathrm{d}s^2 = -\left(1 - \frac{2r}{\Sigma}\right)\mathrm{d}t^2 + \frac{\Sigma}{\Delta}\mathrm{d}r^2 + \Sigma\,\mathrm{d}\theta^2 + \frac{A}{\Sigma}\sin^2\theta\,\mathrm{d}\varphi^2 - \frac{4ar\sin^2\theta}{\Sigma}\mathrm{d}t\,\mathrm{d}\varphi\,, \tag{1}$$

where is $\Delta = r^2 - 2r + a^2$, $\Sigma = r^2 + a^2\cos^2\theta$, and $A = (r^2 + a^2)^2 - a^2\Delta\sin^2\theta$.

978-80-7510-125-9

It was shown that the equations of motion are separable and can be found by Hamilton–Jacobi separation process. For the motion in the equatorial plane we have the following set of equations of test particle motion

$$\Sigma\dot{r} = \pm\sqrt{R(r)}\,, \tag{2}$$

$$\Sigma\dot{\varphi} = -\left(aE - L_z\right) + \frac{a}{\Delta}P(r)\,, \tag{3}$$

$$\Sigma\dot{t} = -a\left(aE - L_z\right) + \frac{r^2 + a^2}{\Delta}P(r)\,, \tag{4}$$

where $\dot{} \equiv \mathrm{d}/\mathrm{d}w$ with w being the affine parameter and

$$P(r) = E\left(r^2 + a^2\right) - L_z a\,, \tag{5}$$

$$R(r) = P^2 - \Delta\left[m^2 r^2 + \left(L_z - aE\right)^2\right]\,. \tag{6}$$

There are two constants of motion introduced reflecting temporal and azimuthal symmetries of Kerr spacetime, they are covariant energy $E = -p_t$ and azimuthal angular momentum $L_z = p_\varphi$.

3 LOCALLY NON-ROTATING FRAMES

The collision process is studied in the frames connected with the zero-angular-momentum observers, those with $L_z = 0$. Such frame are commonly named as Locally Non-Rotating Frames (LNRF), and the corresponding tetrad reads

$$\omega^{(r)} = \left\{0, \sqrt{\frac{\Sigma}{\Delta}}, 0, 0\right\}\,, \tag{7}$$

$$\omega^{(\theta)} = \left\{0, 0, \sqrt{\Sigma}, 0\right\}\,, \tag{8}$$

$$\omega^{(t)} = \left\{\sqrt{\frac{\Delta\Sigma}{A}}, 0, 0, 0\right\}\,, \tag{9}$$

$$\omega^{(\varphi)} = \left\{-\Omega_{\mathrm{LNRF}}\sqrt{\frac{A}{\Sigma}}\sin\theta, 0, 0, \sqrt{\frac{A}{\Sigma}}\sin\theta\right\} \tag{10}$$

with the angular frequency of LNRF being

$$\Omega_{\mathrm{LNRF}} = \frac{2ar}{A}\,. \tag{11}$$

4 THE PARTICLES COLLISION

We assume the elastic collision between two particles taking place in the equatorial plane, $\theta = \pi/2$. The constant of motion $Q = 0$ and it takes place at $r_{\mathrm{c}} = 1$. We let collide radially freely falling (1) and radially freely receding (2) particles with constants of motion $E_1 = m_1, L_{z1} = 0, E_2 = m_2,$ and $L_{z2} = 0.$ The only non-zero components of 4-momentum in the LNRF frame are temporal and radial, i.e.

$$P_i^{(\mu)} = \left(P_i^{(t)},\, P_i^{(r)}, 0, 0\right) , \tag{12}$$

which in particular case of our two particles reads

$$P_1^{(\mu)} = \left(m_1\gamma, m_1\gamma v^{(r)}, 0, 0\right) , \tag{13}$$

$$P_2^{(\mu)} = \left(m_2\gamma, -m_2\gamma v^{(r)}, 0, 0\right) . \tag{14}$$

with the radial 3-velocity component $v^{(r)}$ given by relation

$$v^{(r)} = \frac{\omega^{(r)}_\mu U^\mu}{\omega^{(t)}_\mu U^\mu} = \pm\sqrt{\frac{2\left(1+a^2\right)}{\left(1+a^2\right)^2 - \left(1-a^2\right)a^2}} . \tag{15}$$

and $\gamma = (1 - [v^{(r)}]^2)^{-1/2}$.

Just before the collision the total 4-momentum $P^{(\mu)}$ is

$$P^{(\mu)} = P_1^{(\mu)} + P_2^{(\mu)} = \left((m_1+m_2)\gamma, (m_1-m_2)\gamma v^{(r)}, 0, 0\right) . \tag{16}$$

We first assume that masses of particles remain the same after collision, then the corresponding components of 4-momenta of colliding particles after collision follow from conservation principles and from normalization of 4-momentum, i.e.

$$P'^{(t)} = P'^{(t)}_1 + P'^{(t)}_2 = P^{(t)} = (m_1+m_2)\gamma , \tag{17}$$

$$P'^{(r)} = P'^{(r)}_1 + P'^{(r)}_2 = P^{(r)} = (m_1-m_2)\gamma v^{(r)} , \tag{18}$$

$$-m_1^2 = -\left[P'^{(t)}_1\right]^2 + \left[P'^{(r)}_1\right]^2 , \tag{19}$$

$$-m_2^2 = -\left[P'^{(t)}_2\right]^2 + \left[P'^{(r)}_2\right]^2 . \tag{20}$$

Solving this set of equations and using

$$v'^{(r)}_i = \frac{P'^{(r)}_i}{P'^{(t)}_i} , \quad i = 1, 2 \tag{21}$$

the resulting radial 3-velocity of particles after collision read

$$v'^{(r)}_1 = \frac{BD + \sqrt{B^2D^2 - \left(A^2-B^2\right)\left(4A^2m_1^2 - D^2\right)}}{AD - \sqrt{A^2D^2 - \left(A^2-B^2\right)\left(4B^2m_1^2 + D^2\right)}} , \tag{22}$$

$$v'^{(r)}_2 = \frac{2B\left(A^2-B^2\right) - BD - \sqrt{B^2D^2 - \left(A^2-B^2\right)\left(4A^2m_1^2 - D^2\right)}}{2A\left(A^2-B^2\right) - AD + \sqrt{A^2D^2 - \left(A^2-B^2\right)\left(4B^2m_1^2 + D^2\right)}} , \tag{23}$$

where we have introduced $A = (m_1 + m_2)\gamma$, $B = (m_1 - m_2)\gamma v^{(r)}$, and

$$D = (m_1 + m_2)\left[m_1 - m_2 + (m_1 + m_2)\gamma^2\right] - (m_1 - m_2)^2\gamma^2\left[v^{(r)}\right]^2 . \tag{24}$$

In the second case we assume that the mass of collision products are the same having value of m we have

$$-m^2 = -\left[P'^{(t)}_1\right]^2 + \left[P'^{(r)}_1\right]^2 , \tag{25}$$

$$-m^2 = -\left[P'^{(t)}_2\right]^2 + \left[P'^{(r)}_2\right]^2 . \tag{26}$$

From Equations (17), (18), (25), and (26) the resulting radial 3-velocities of collision products are

$$v'^{(r)}_{1\pm} = \frac{B \pm A\sqrt{1-4m^2}}{A \mp \sqrt{2A^2 - B^2\left(1+4m^2\right)}} , \tag{27}$$

$$v'^{(r)}_{2\pm} = \frac{2A - B \mp A\sqrt{1-4m^2}}{2B - A \pm \sqrt{2A^2 - B^2\left(1+4m^2\right)}} . \tag{28}$$

In the third case we asked a question, what are the conditions for masses of colliding particles and the masses of the products if we want the products of the collision to became static just after the collision? In this case we have following set of equations

$$P'^{(t)}_1 + P'^{(t)}_2 = \gamma(m_1 + m_2) , \tag{29}$$

$$\underbrace{P'^{(r)}_1}_{0} + \underbrace{P'^{(r)}_2}_{0} = 0 = \gamma v^{(r)}(m_1 - m_2) . \tag{30}$$

Which imply the masses of particles before collision are same $m_1 = m_2$ and the masses of the products is determined by formula

$$m = \gamma m_1 = \frac{1}{\sqrt{1 - [v^{(r)}]^2}} m_1 . \tag{31}$$

The characteristic parameter of collision is the centre-of-mass energy E_{CM}. It is the total energy of system measured by observer at rest in CM. In the case of two particle collision we have $P_{\mathrm{tot}} = P_1 + P_2$ which imply the energy

$$E^2_{\mathrm{CM}} = -P_{\mathrm{tot}} \cdot P_{\mathrm{tot}} = m_1^2 + m_2^2 - 2g_{\mu\nu}P_1^{\mu}P_2^{\nu} , \tag{32}$$

and, in our particular case, it reads

$$E^2_{\mathrm{CM}} = m_1^2 + m_2^2 + \frac{2}{r^2}\left\{\left[m_1 m_2\left(r^2+a^2\right)^2 + 2r\sqrt{m_1 m_2}\left(r^2+a^2\right)\right]\frac{1}{\Delta} - a^2 m_1 m_2\right\} . \tag{33}$$

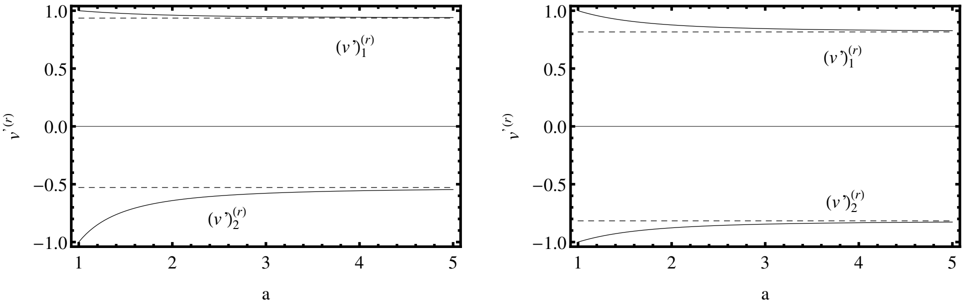

Figure 1. Plots of $v'^{(r)}_1$ and $v'^{(r)}_2$ curves as functions of spin parameter for fixed values of particle masses. Plots on the left (right) are constructed for $m_1 = 2$ and $m_2 = 1$ ($m_1 = 1$ and $m_2 = 2$).

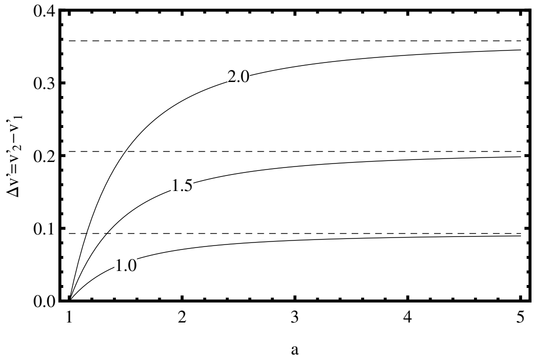

Figure 2. The difference between the magnitude of velocities of two particles collision products gaining after it same mass m. Each curve is plotted for a representative value of collision product masses. Each curve is asymptotically for $a \to \infty$ getting to limiting value which in presented cases are $\Delta v'_{\mathrm{lim}}(m = 1.0) = 0.0928676$, $\Delta v'_{\mathrm{lim}}(m = 1.5) = 0.205702$, and 0.357901.

5 RESULTS

We let collide two particles with $L_z = 0$ at $r = 1$. The particles have distinct masses $m_1 \neq m_2$. With respect to collision products masses we have studied two situations:

- Masses of products do not change during collision. We first study the case of $m_1 = m'_1 = 1$ and $m_2 = m'_2 = 2$ and of $m_1 = m'_1 = 2$ and $m_2 = m'_2 = 1$.
- The masses of products is the same $m'_1 = m'_2 = m$. In our simulations the mass $m = 1$, 1.5, and 2.0.

The outcome of the collision is reflected in the plots of curves $v'^{(r)}_1(a)$ and $v'^{(r)}_2(a)$ in Fig. 1. There are two limiting values as spin $a \to \infty$, $v'^{(r)}_{1\,\mathrm{limit}}=-0.528321$ and $v'^{(r)}_{2\,\mathrm{limit}}=0.935984$ in the first choice of particle masses and $v'^{(r)}_{1\,\mathrm{limit}}=\pm 0.81651$ for the second choice of particle masses. The maximal values of velocities of particles is reached for spins close to extreme Kerr black hole state.

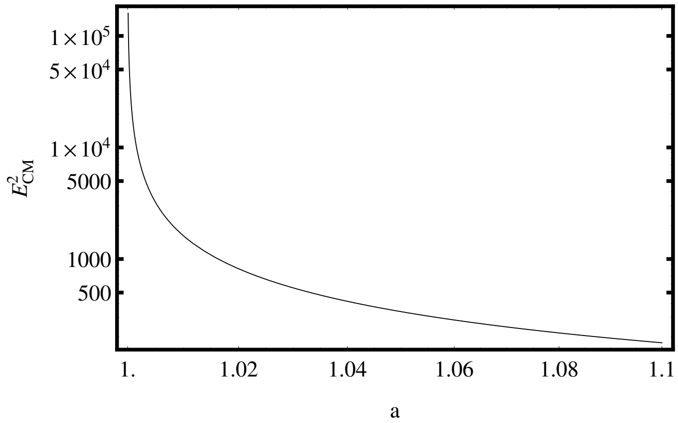

Figure 3. We demonstrate the strength of head on collision of two radially moving test particles with masses $m_1 = 1$ and $m_2 = 2$, which are moving radially, by the square of centre-of-mass energy E^2_{CM}.

The square of centre of mass energy E^2_{CM}, given by formula (33), of collision taking place at $r = 1$ of two radially moving particles with masses $m_1 = 1$ and $m_2 = 2$ is given at Fig. 3.

6 CONCLUSION

We can conclude that in the case of the elastic collisions, the efficiency is largest for near-extreme Kerr superspinars, similarly to the case of the collisions where the rest energy of the colliding particles is transformed into energy of outgoing particles and photons.

ACKNOWLEDGEMENTS

The authors would like to thank the EU grant Synergy CZ.1.07/2.3.00/20.0071. JS and ZS acknowledge the Albert Einstein Centre for gravitation and astrophysics supported by the Czech Science Foundation Grant No. 14-37086G.

REFERENCES

Bañados, M., Silk, J. and West, S. M. (2009), Kerr black holes as particle accelerators to arbitrarily high energy, *Phys. Rev. Lett.*, **103**, p. 111102.

Harada, T., Yoo, C.-M. and Kohri, K. (2013), Threshold of primordial black hole formation, *Phys. Rev. D*, **88**, p. 084051.

Stuchlík, Z., Hledík, S. and Truparová, K. (2011), Evolution of kerr superspinars due to accretion counterrotating thin discs, *Class. and Quant. Grav.*, **28**, p. 155017.

Stuchlík, Z. and Schee, J. (2012), Observational phenomena related to primordial kerr superspinars, *Class. and Quant. Grav.*, **29**, p. 065002.

Stuchlík, Z. and Schee, J. (2013), Ultra-high-energy collisions in the superspinning kerr geometry, *Class. and Quant. Grav.*, **30**, p. 075012.

Stuchlík, Z., Schee, J. and Abdujabbarov, A. (2014), Ultra-high-energy collisions of particles in the field of near-extreme kehagias-sfetsos naked singularities and their appearance to distant observers, *Phys. Rev. D*, **89**, p. 104048.

Tursunov, A., Kološ, M., Abdujabbarov, A., Ahmedov, B. and Stuchlík, Z. (2013), Acceleration of particles in spacetimes of black string, *Phys. Rev. D*, **88**, p. 124001.

Zaslavskii, . B. (2010), Acceleration of particles as a universal property of rotating black holes, *Phys. Rev. D*, **82**, p. 083004.

Z. Stuchlík, G. Török and T. Pecháček, editors, Silesian University in Opava, 2014, pp. 173–183

Aschenbach Effect for Brany Kerr Black Holes and Naked Singularities

Zdeněk Stuchlík[a], Martin Blaschke[b] and Petr Slaný[c]

Institute of Physics, Faculty of Philosophy & Science, Silesian University in Opava,
Bezručovo nám. 13, CZ-746 01 Opava, Czech Republic
[a]Zdenek.Stuchlik@fpf.slu.cz
[b]Martin.Blaschke@fpf.slu.cz
[c]Petr.Slany@fpf.slu.cz

ABSTRACT
We study the non-monotonic Keplerian velocity profiles related to locally non-rotating frames (LNRF) in the field of near-extreme braneworld Kerr black holes and naked singularities in which the non-local gravitational effects of the bulk are represented by a braneworld tidal charge b and the 4D geometry of the spacetime structure is governed by the Kerr–Newman geometry. We show that positive tidal charge has a tendency to restrict the values of the black hole dimensionless spin a admitting existence of the non-monotonic Keplerian LNRF-velocity profiles; the non-monotonic profiles exist in the black hole spacetimes with tidal charge smaller than $b = 0.41005$ (and spin larger than $a = 0.76808$). With decreasing value of the tidal charge (which need not be only positive), both the region of spin allowing the non-monotonicity in the LNRF-velocity profile around braneworld Kerr black hole and the velocity difference in the minimum-maximum parts of the velocity profile increase implying growing astrophysical relevance of this phenomenon.

Keywords: Aschenbach effect – Randall Sundrum – Brane-world

1 INTRODUCTION

Fast rotating black holes play a crucial role in understanding processes observed in quasars and Active Galactic Nuclei (AGN) or in microquasars. It has been shown that supermassive black holes in AGN evolve into states with dimensionless spin $a \sim 1$ due to accretion from thin discs, Volonteri et al. (2005); Shapiro (2005). This statement is supported by analysis of profiled X-ray (Fe56) lines observed in some AGN (e.g. in MCG-6-30-15), Tanaka et al. (1995); Miyakawa et al. (2009); Reynolds et al. (2009) and in some microquasars (e.g. GRS 1915+105), McClintock et al. (2006). Evidence for the existence of near-extreme Kerr black holes comes from high-frequency quasi-periodic oscillations (QPOs) of observed X-ray flux in some microquasars, Török et al. (2005); Steiner et al. (2008). A fast rotating black hole could be also located in the Galaxy center source Sgr A*, Aschenbach (2004); Török (2005); Meyer et al. (2006).

It is widely accepted that the phenomena observed in AGN and microquasars are related to accretion discs orbiting Kerr black holes. However, we can consider also the possibility to explain these phenomena by Kerr superspinars with external field described by the geometry of Kerr naked singularity spacetime, Gimon and Hořava (2009). Then both accretion and related optical effects and the QPOs effects enable us to find clear signature of the Kerr superspinar presence, de Felice (1974, 1978); Stuchlík (1980, 1981); Stuchlík and Schee (2010); Stuchlík et al. (2011).

Properties of accretion discs can be appropriately represented by circular orbits of test particles or fluid elements orbiting black holes (superspinars). The local properties can be efficiently expressed when related to the locally non-rotating frames (LNRF), since these frames corotate with the spacetime in a way that enables to cancel the frame-dragging effects as much as possible, Bardeen et al. (1972). A new phenomenon related to the LNRF-velocity profiles of matter orbiting near-extreme Kerr black holes has been found by B. Aschenbach, Aschenbach (2004, 2008); Stuchlík et al. (2005), namely a non-monotonicity in the velocity profile of the Keplerian motion in the field of Kerr black holes with dimensionless spin $a > 0.9953$. Such a hump in the LNRF-velocity profile of the corotating orbits is a typical and relatively strong feature in the case of Keplerian motion in the field of Kerr naked singularities, but in the case of Kerr black holes it is a very small effect appearing for near-extreme black holes only – see Fig. 1. In the naked singularity case we call the orbits to be of 1st family rather than corotating, since these can be retrograde relative to the LNRF in vicinity of the ring singularity for small values of spin ($a < 5/3$), while they are corotating for larger values of spin, Stuchlík (1980); the humpy character of the LNRF-velocity profile ceases for naked singularities with $a > 4.0014$ – as demonstrated in the Fig. 1. A study of non-Keplerian distribution of specific angular momentum (l = const), related to geometrically thick discs of perfect fluid, has shown that the "humpy" LNRF-velocity profile appears for near-extreme Kerr black holes with $a > 0.9998$, Stuchlík et al. (2005). The humpy LNRF-velocity profile emerges in the ergosphere of near-extreme Kerr black holes, at vicinity of the marginally stable circular orbit. Maximal velocity difference between the local minimum and maximum of the humpy Keplerian velocity profiles is $\Delta v \approx 0.07\,c$ and takes place for $a = 1$, Stuchlík et al. (2007).

Here, we shall study existence of the humpy LNRF-velocity profiles in the field of braneworld rotating black holes considering both negative and positive values of the braneworld tidal charge. Our results related to $b > 0$ are relevant also in the case of the standard Kerr–Newman spacetimes (with $b \to Q^2$), for uncharged particles. We restrict our attention to the Keplerian LNRF-velocity profiles postponing the study of perfect fluid configurations to future work.

2 ORBITAL MOTION IN THE BRANEWORLD KERR SPACETIMES

Motion of test particles in the field of braneworld rotating black holes is given by the geodesic structure of the Kerr–Newman spacetimes with the tidal charge b. The braneworld parameter reflects the tidal effects of the bulk space and has no influence on the motion of charged particles. The geodesic structure given by the Carter equations, Carter (1973) is relevant for both uncharged and charged test particles. The circular test particle orbits of the braneworld

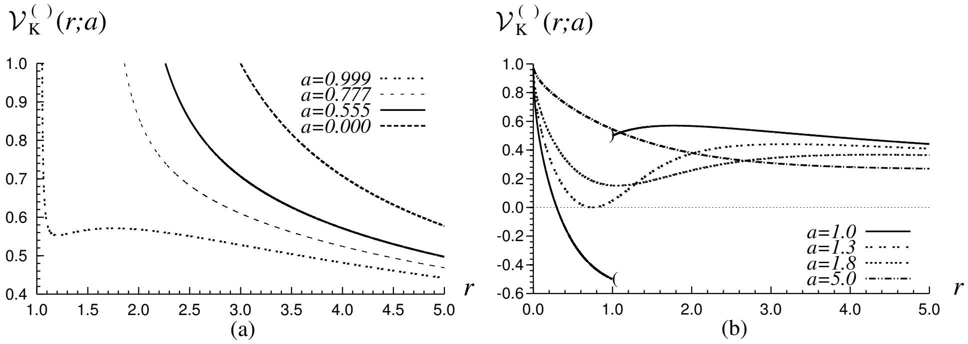

Figure 1. Keplerian velocity profiles related to the LNRF. (a): Kerr black holes – the velocity profiles presented for some values of the black hole spin. The Aschenbach effect appears for near-extreme black holes and is weak. (b): Kerr naked singularities – the velocity profiles are given for some values of the spin, demonstrating existence of Aschenbach effect for orbits with negative valued velocity. For completeness, the velocity profile is given also for extreme black hole, demonstrating velocity jump at $r = 1$.

Kerr black holes are identical to the circular geodesics of the Kerr–Newman spacetime with properly chosen charge parameter.

We shall study the Aschenbach effect, i.e. we look for the non-monotonicity (humps) in the LNRF-velocity profiles of Keplerian discs orbiting near-extreme braneworld Kerr black holes or naked singularities.

2.1 Geometry

Using standard Boyer-Lindquist coordinates (t, r, θ, φ) and geometric units $(c = G = 1)$, we can write the line element of rotating (Kerr) black hole on the 3D-brane in the form

$$\begin{aligned}\mathrm{d}s^2 = &-\left(1 - \frac{2Mr - b}{\Sigma}\right)\mathrm{d}t^2 - \frac{2a(2Mr - b)}{\Sigma}\sin^2\theta\,\mathrm{d}t\,\mathrm{d}\varphi \\ &+ \frac{\Sigma}{\Delta}\mathrm{d}r^2 + \Sigma\,\mathrm{d}\theta^2 + \left(r^2 + a^2 + \frac{2Mr - b}{\Sigma}\,a^2\sin^2\theta\right)\sin^2\theta\,\mathrm{d}\varphi^2\,, \quad (1)\end{aligned}$$

where

$$\Delta = r^2 - 2Mr + a^2 + b\,, \quad (2)$$

$$\Sigma = r^2 + a^2\cos^2\theta\,, \quad (3)$$

M and $a = J/M$ are the mass parameter and the specific angular momentum of the background, while the braneworld parameter b, called "tidal charge", represents the imprint of non-local (tidal) gravitational effects of the bulk space, Aliev and Gümrükçüoğlu (2005). The physical "ring" singularity of the braneworld rotating black holes (and naked singularities) is located at $r = 0$ and $\theta = \pi/2$, as in the Kerr spacetimes.

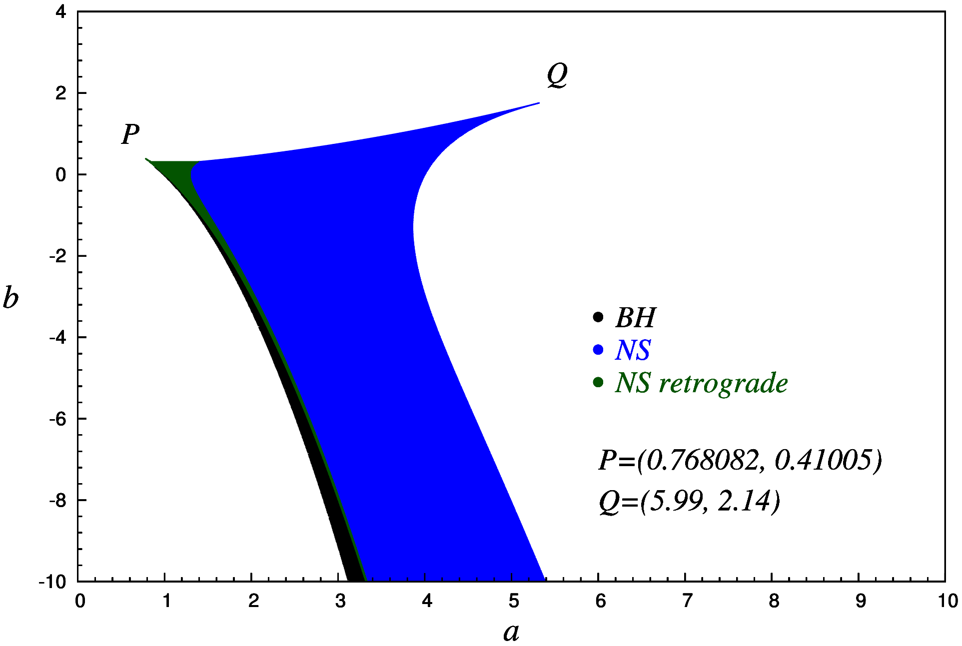

Figure 2. Classification of the braneworld Kerr spacetimes according to existence of the Aschenbach effect. The Aschenbach effect is allowed in the black region representing black holes, dark-grey region representing naked singularities with corotating orbits only, and lighter-grey region representing naked singularities with retrograde motion in the LNRF-velocity profile (corresponding to negative values of the function $\mathcal{V}_{\mathrm{K}}^{(\varphi)}$).

The form of the metric (1) is the same as that of the standard Kerr–Newman solution of the 4D Einstein-Maxwell equations, with tidal charge b being replaced by squared electric charge Q^2, Misner et al. (1973). The stress tensor on the brane $\mathcal{E}_{\mu\nu}$ takes the form

$$\mathcal{E}_t^t = -\mathcal{E}_\varphi^\varphi = -\frac{b}{\Sigma^3}\left[\Sigma - 2\left(r^2 + a^2\right)\right] , \tag{4}$$

$$\mathcal{E}_r^r = -\mathcal{E}_\theta^\theta = -\frac{b}{\Sigma^2} , \tag{5}$$

$$\mathcal{E}_\varphi^t = -\left(r^2 + a^2\right)\sin^2\mathcal{E}_t^\varphi = -\frac{2\,a}{\Sigma^3}\left(r^2 + a^2\right)\sin^2\theta , \tag{6}$$

that is fully analogical ($b \to Q^2$) to components of the electromagnetic energy-momentum tensor of the Kerr–Newmann solution in Einstein's general relativity, Aliev and Gümrükçüoğlu (2005). For negative values of the tidal charge ($b < 0$), the values of the black hole spin $a > M$ are allowed. Such a situation is forbidden for the standard 4D Kerr black holes. In the following, we put $M = 1$ in order to work with completely dimensionless formulae.

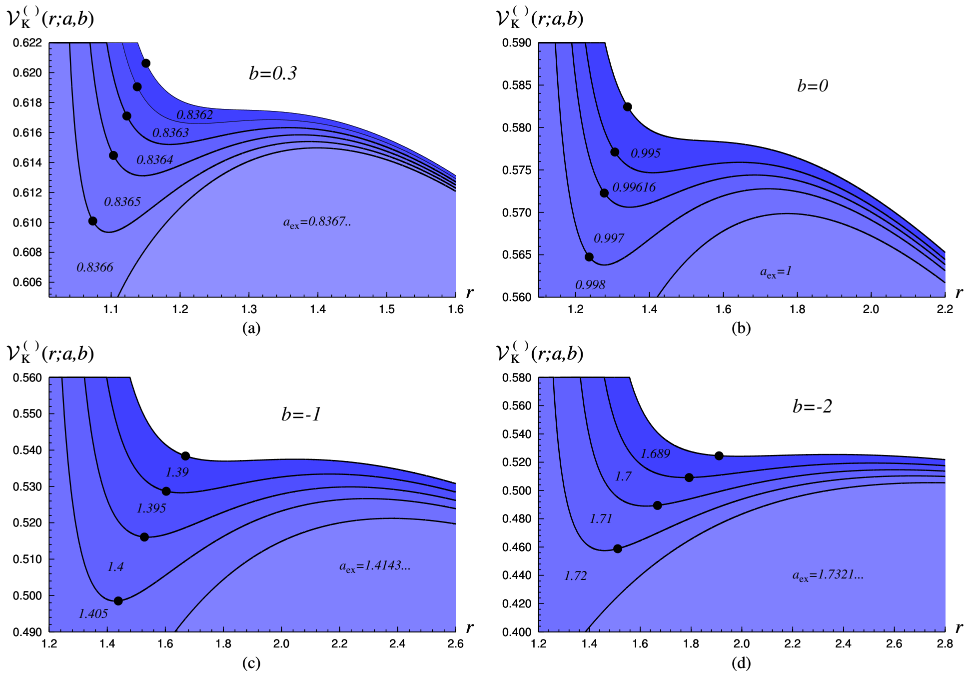

Figure 3. Non-monotonic LNRF-related velocity profiles for braneworld Kerr black hole backgrounds given for some values of the tidal charge b and appropriately chosen values of the a. The black points denote loci of $r_{\rm ms}$.

2.2 Locally non-rotating frames and orbital motion

The orbital velocity of matter orbiting a braneworld Kerr black hole along circular orbits is given by appropriate projections of its 4-velocity $U = (U^t, 0, 0, U^\varphi)$ onto the tetrad of a locally non-rotating frame (LNRF), Bardeen et al. (1972)

$$\mathbf{e}^{(t)} = \left(\omega^2 g_{\varphi\varphi} - g_{tt}\right)^{\frac{1}{2}} \mathbf{d}t \ , \tag{7}$$

$$\mathbf{e}^{(\varphi)} = \left(g_{\varphi\varphi}\right)^{\frac{1}{2}} (\mathbf{d}\varphi - \omega\, \mathbf{d}t) \, , \tag{8}$$

$$\mathbf{e}^{(r)} = \left(\frac{\Sigma}{\Delta}\right)^{\frac{1}{2}} \mathbf{d}r \ , \tag{9}$$

$$\mathbf{e}^{(\theta)} = \Sigma^{\frac{1}{2}} \mathbf{d}\theta \ , \tag{10}$$

where ω is the angular velocity of the LNRF relative to distant observers and reads

$$\omega = -\frac{g_{t\varphi}}{g_{\varphi\varphi}} = \frac{a(2r-b)}{\Sigma\left(r^2+a^2\right) + (2r-b)\, a^2 \sin^2\theta} \, . \tag{11}$$

For the circular motion, the only non-zero component of the 3-velocity measured locally in the LNRF is the azimuthal component that is given by

$$\mathcal{V}^{(\varphi)}_{\mathrm{LNRF}} = \frac{[\Omega - \omega]}{\sqrt{\left((\omega^2 - \frac{g_{tt}}{g_{\varphi\varphi}}\right)}} = \frac{\left[\left(r^2 + a^2\right)^2 - a^2 \Delta \sin^2\theta\right] \sin\theta\,(\Omega - \omega)}{\Sigma\sqrt{\Delta}}\,, \tag{12}$$

where

$$\Omega = \frac{U^{\varphi}}{U^t} = -\frac{l g_{tt} + g_{t\varphi}}{l g_{t\varphi} + g_{\varphi\varphi}} \tag{13}$$

is the angular velocity of the orbiting matter relative to distant observers and

$$l = -\frac{U_{\varphi}}{U_t} \tag{14}$$

is its specific angular momentum; U_t , U_{φ} are the covariant components of the 4-velocity field of the orbiting matter.

Using (1) we arrive to the formula, Stuchlík and Kotrlová (2009)

$$\Omega = \frac{(\Sigma - 2r + b)\, l + a(2r - b)\sin^2\theta}{\left[\Sigma\left(r^2 + a^2\right) + (2r - b)\, a^2 \sin^2\theta\right]\sin^2\theta - la(2r - b)\sin^2\theta}\,. \tag{15}$$

Motion of test particles following circular geodetical orbits in the equatorial plane ($\theta = \pi/2$) is described by the Keplerian distribution of the specific angular momentum, which in the braneworld Kerr backgrounds takes the form:

$$l_{\mathrm{K}\pm} = \pm\frac{\left(r^2 + a^2\right)\sqrt{r - b} \mp a(2r - b)}{r^2 - 2r + b \pm a\sqrt{r - b}}\,, \tag{16}$$

where the signs refer to two distinct families of orbits in the Kerr braneworld spacetimes. Putting all relevant equations together we end up with expression for (φ) component of LNRF 3 orbital Keplerian velocity in the form:

$$\mathcal{V}^{(\varphi)}_{\mathrm{K}\pm} = \pm\frac{\sqrt{r - b}\left(r^2 - a^2\right) \mp a(2r - b)}{\left(r^2 + a\sqrt{r - b}\right)\sqrt{\Delta}}\,. \tag{17}$$

Non-monotonic behaviour of this function can be seen in Fig. 3 and possible combinations of parameters a and b allowing this effect are shown in Fig. 2.

3 ASCHENBACH EFFECT FOR TOROIDAL DISKS

Putting (1), (11) and (15) into (12), and restricting our attention only to equatorial plane ($\theta = \pi/2$) we get the LNRF-velocity profile for $l = \mathrm{const} > 0$ distribution in the form

$$\mathcal{V}^{\varphi}_{\mathrm{LNRF}} = \frac{r^2 \Delta^{1/2} l}{r^2\left(r^2 + a^2\right) + (2r - b)a^2 - a(2r - b)l}\,. \tag{18}$$

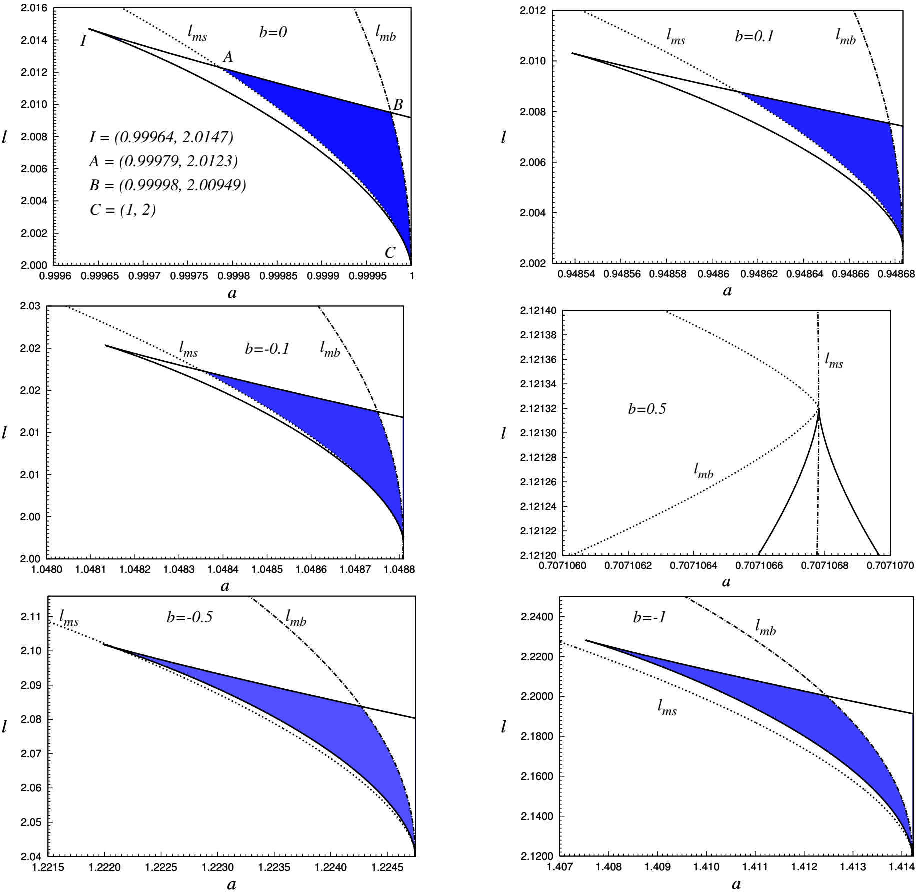

Figure 4. Spacetimes with change of sign of the gradient of LNRF velocity. Function $l_{\mathrm{ex,max}}(a, b)$ (*upper solid curve*), $l_{\mathrm{ex,min}}(a, b)$ (*lower solid curve*), $l_{\mathrm{ms}}(a, b)$ (*dashed thick curve*) and $l_{\mathrm{mb}}(a, b)$ (*dashed curve*).

The radial gradient of the $l = \mathrm{const}$ LNRF-velocity profile reads:

$$\frac{\partial \mathcal{V}^{\varphi}_{\mathrm{LNRF}}}{\partial r} = \frac{\left[2r\Delta + r^2(r-1)\right] K - r^2 \Delta K'}{\Delta^{\frac{1}{2}} K^2} l, \tag{19}$$

where K is denominator of the Eq. (18) and $K' = \partial K/\partial r$. The humpy profiles are determined by condition

$$\frac{\partial \mathcal{V}^{\varphi}_{\mathrm{LNRF}}}{\partial r} = 0 \tag{20}$$

that has to be satisfied for the minimum-maximum structure of the profile; notice however the presence of another maximum of $l = \mathrm{const}$ velocity profiles existing for all $l > 0$ and

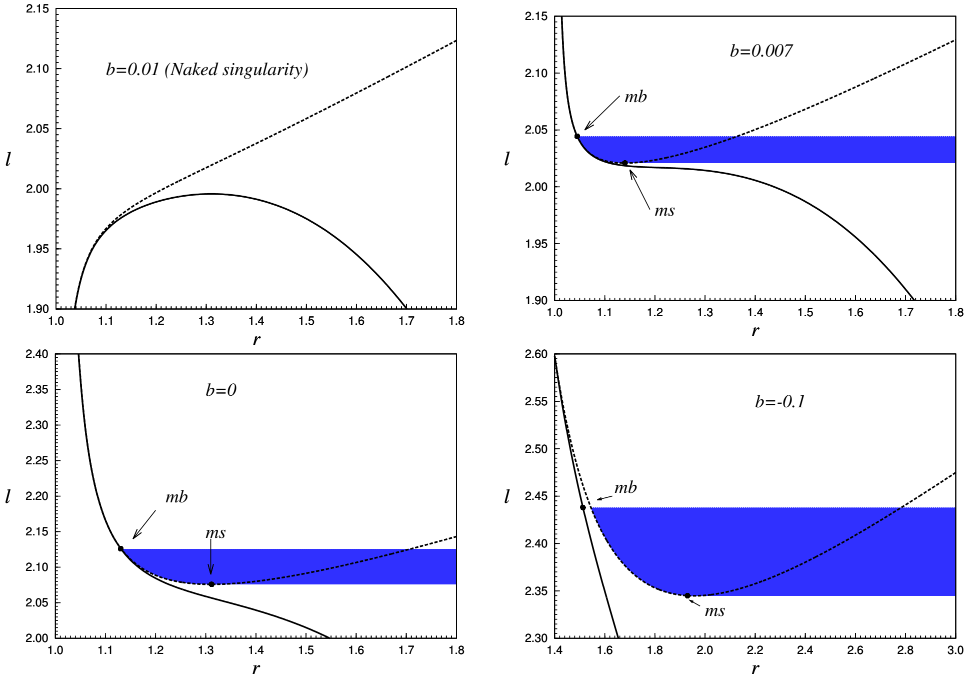

Figure 5. Classifications of the Kerr black-hole spacetimes according to the properties of the function $l_{\rm ex}(r; a, b)$(*solid curve*) and $l_{\rm K}(r; a, b)$(*dashed curves*) for $a = 0.996$. The constant specific angular momentum tori can exist in the shaded region only along $l =$ const. lines.

$a > 0$ in the pure Kerr black holes spacetimes, Stuchlík et al. (2005). Using function (19) we arrive to the relevant conditions that has to satisfied for the extrema of $V^{\varphi}_{\rm LNRF}(r; a, b)$

$$l = l_{\rm ex}(r; a, b) \equiv a - \frac{r^3\left(a^2(1+r) + (r-3)r^2 + 2r\beta\right)}{a\left(4r^3 - 3r^2\beta + 7r\beta - 2a^2\beta - 2\beta^2 - 6r^2 + 2ra^2\right)}\,. \tag{21}$$

From the relation (21) we can create the function $l_{\rm ex}(r; b)$ indicative of extremal value of the specifics momentum l for given r and b, which zeroing term (19). If we now consider rotating disk with constant l, the Aschenbach effect can occur only for

$$l \in \left\langle l_{\rm ex,min}(r; b), l_{\rm ex,max}(r; b)\right\rangle. \tag{22}$$

With the aid of two following equations for $r_{\rm mb}$ and $r_{\rm ms}$

$$r_{\rm mb} : r\left(4r - r^2 - 4b + a^2\right) + b\left(b - a^2\right) \pm 2a(b - 2r)\sqrt{r - b} = 0\,, \tag{23}$$

$$r_{\rm ms} : r\left(6r - r^2 - 9b + 3a^2\right) + 4b\left(b - a^2\right) \mp 8a\,(r - b)^{3/2} = 0\,, \tag{24}$$

we can create two functions $l_{\rm ms}(a, b)$ and $l_{\rm mb}(a, b)$, specific momentum for marginally stable and marginally bound orbits. The figure 4 shows regions where the Aschenbach effect can occur. We see that the positives values of the tidal charge b has repressing influence,

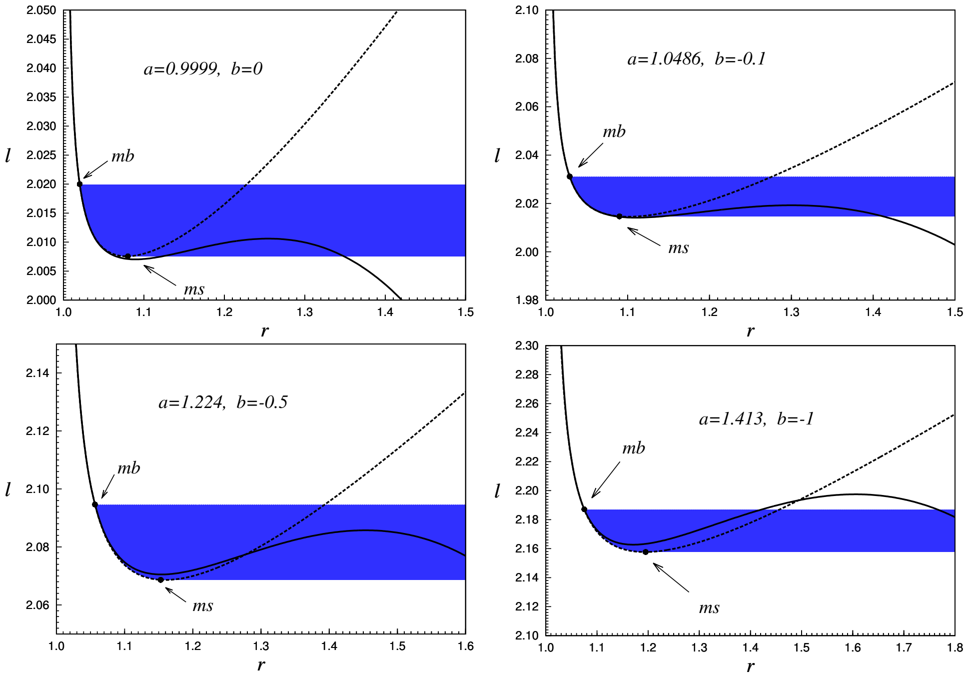

Figure 6. Classifications of the Kerr black-hole spacetimes according to the properties of the function $l_{\mathrm{ex}}(r; a, b)$ (solid curve) and $l_{\mathrm{K}}(r; a, b)$ (dashed curves) for some values of black hole spin parameter a and brany tidal charge parameter b. The constant specific angular momentum tori can exist in the *blued region* only along $l = \text{const}$ lines.

whereas negative values have positive influence on the region where the Aschenbach effect can exist. It is very similar effect like case for Keplerian orbits.

In the Fig. 5 there is demonstrated the influence of the tidal charge b on the mb-marginally bound and ms-marginally stable orbits for one chosen specific angular momentum $a = 0.996$.

4 CONCLUSIONS

We have shown that the Aschenbach effect is a typical feature of the circular geodetical motion in the field of both standard and braneworld Kerr naked singularities with a relatively large interval of spins above the extreme black-hole limit. For naked-singularity spin sufficiently close to the extreme black-hole state, the Aschenbach effect is manifested by the retrograde plus-family circular orbits. For black hole spacetimes, such retrograde orbits can appear under the inner horizon, being thus irrelevant from the astrophysical point of view. In the field of near-extreme rotating black holes, the Aschenbach effect located above the outer black hole horizon can be thus considered as a small remnant of typical naked singularity phenomenon.

ACKNOWLEDGEMENTS

The presented work was supported by EU grant Synergy CZ.1.07./2.3.00/20.0071, the internal student grant SGS/23/2013 of the Silesian University, and the Albert Einstein Centre for gravitation and astrophysics supported by the Czech Science Foundation Grant No. 14-37086G.

REFERENCES

Aliev, A. N. and Gümrükçüoğlu, A. E. (2005), Charged rotating black holes on a 3-brane, *Phys. Rev. D*, **71**(10), p. 104027, arXiv: `hep-th/0502223`.

Aschenbach, B. (2004), Measuring mass and angular momentum of black holes with high-frequency quasi-periodic oscillations, *Astronomy and Astrophysics*, **425**, pp. 1075–1082, arXiv: `astro-ph/0406545`.

Aschenbach, B. (2008), Measurement of Mass and Spin of Black Holes with QPOs, *Chinese Journal of Astronomy and Astrophysics Supplement.*, **8**, pp. 291–296.

Bardeen, J. M., Press, W. H. and Teukolsky, S. A. (1972), Rotating black holes: locally nonrotating frames, energy extraction, and scalar synchrotron radiation, *Astrophys. J.*, **178**, pp. 347–369.

Carter, B. (1973), Black hole equilibrium states, in C. D. Witt and B. S. D. Witt, editors, *Black Holes*, pp. 57–214, Gordon and Breach, New York–London–Paris.

de Felice, F. (1974), Repulsive Phenomena and Energy Emission in the Field of a Naked Singularity, *Astronomy and Astrophysics*, **34**, p. 15.

de Felice, F. (1978), Classical instability of a naked singularity, *Nature*, **273**, pp. 429–431.

Gimon, E. G. and Hořava, P. (2009), Astrophysical violations of the Kerr bound as a possible signature of string theory, *Phys. Lett. B*, **672**, pp. 299–302, arXiv: `0706.2873`.

McClintock, J. E., Shafee, R., Narayan, R., Remillard, R. A., Davis, S. W. and Li, L.-X. (2006), The Spin of the Near-Extreme Kerr Black Hole GRS 1915+105, *Astrophys. J.*, **652**, pp. 518–539, arXiv: `astro-ph/0606076`.

Meyer, L., Eckart, A., Schödel, R., Duschl, W. J., Mužić, K., Dovčiak, M. and Karas, V. (2006), Near-infrared polarimetry setting constraints on the orbiting spot model for Sgr A* flares, *Astronomy and Astrophysics*, **460**, p. 15.

Misner, C. W., Thorne, K. S. and Wheeler, J. A. (1973), *Gravitation*, W. H. Freeman and Co, New York, San Francisco.

Miyakawa, T., Ebisawa, K., Terashima, Y., Tsuchihashi, F., Inoue, H. and Zycki, P. (2009), Spectral Variation of the Seyfert 1 Galaxy MCG 6-30-15 Observed with Suzaku, *Publications of the Astronomical Society of Japan*, **61**, p. 1355, arXiv: `0910.0773`.

Reynolds, C. S., Fabian, A. C., Brenneman, L. W., Miniutti, G., Uttley, P. and Gallo, L. C. (2009), Constraints on the absorption-dominated model for the X-ray spectrum of MCG-6-30-15, *Monthly Notices Roy. Astronom. Soc.*, **397**, pp. L21–L25, arXiv: `0904.3099`.

Shapiro, S. (2005), Spin, Accretion, and the Cosmological Growth of Supermassive Black Holes, *Astrophys. J.*, **620**, pp. 59–68, arXiv: `arXiv:astro-ph/0411156`.

Steiner, J. F., McClintock, J. F., Orosz, J. A., R.Narayan, Torres, M. A. and Remillard, R. A. (2008), Estimating The Spin Of The Stellar-Mass Black Hole XTE J1550-564, in *AAS/High Energy Astrophysics Division*, volume 10.

Stuchlík, Z. (1980), Equatorial circular orbits and the motion of the shell of dust in the field of a rotating naked singularity, *Bull. Astronom. Inst. Czechoslovakia*, **31**(3), pp. 129–144.

Stuchlík, Z. (1981), Evolution of Kerr naked singularities, *Bull. Astronom. Inst. Czechoslovakia*, **32**(2), pp. 68–72.

Stuchlík, Z., Hledík, S. and Truparová, K. (2011), Evolution of Kerr superspinars due to accretion counterrotating thin discs, *Classical Quantum Gravity*, to be published.

Stuchlík, Z. and Kotrlová, A. (2009), Orbital resonances in discs around braneworld Kerr black holes, *General Relativity and Gravitation*, **41**, pp. 1305–1343, arXiv: `0812.5066`.

Stuchlík, Z. and Schee, J. (2010), Appearance of Keplerian discs orbiting Kerr superspinars, *Classical and Quantum Gravity*, **27**(21), p. 215017.

Stuchlík, Z., Slaný, P. and Török, G. (2007), LNRF-velocity hump-induced oscillations of a Keplerian disc orbiting near-extreme Kerr black hole: A possible explanation of high-frequency QPOs in GRS 1915+105, *Astronomy and Astrophysics*, **470**(2), pp. 401–404, arXiv: `0704.1252v2`.

Stuchlík, Z., Slaný, P., Török, G. and Abramowicz, M. A. (2005), Aschenbach effect: Unexpected topology changes in the motion of particles and fluids orbiting rapidly rotating Kerr black holes, *Phys. Rev. D (3)*, **71**, p. 024037, arXiv: `arXiv:gr-qc/0411091`.

Tanaka, Y., Nandra, K., Fabian, A. C., Inoue, H., Otani, C., Dotani, T., Hayashida, K., Iwasawa, K., Kii, T., Kunieda, H., Makino, F. and Matsuoka, M. (1995), Gravitationally Redshifted Emission Implying an Accretion Disk and Massive Black-Hole in the Active Galaxy MCG-6-30-15, *Nature*, **375**, p. 659.

Török, G. (2005), QPOs in microquasars and Sgr A*: measuring the black hole spin, *Astronom. Nachr.*, **326**(9), pp. 856–860, arXiv: `astro-ph/0510669`.

Török, G., Abramowicz, M. A., Kluźniak, W. and Stuchlík, Z. (2005), The orbital resonance model for twin peak kHz quasi periodic oscillations in microquasars, *Astronomy and Astrophysics*, **436**, pp. 1–8.

Volonteri, M., Madau, P., Quataert, E. and Rees, M. (2005), The Distribution and Cosmic Evolution of Massive Black Hole Spins, *Astrophys. J.*, **620**, pp. 69–77, arXiv: `arXiv:astro-ph/0410342`.

Proceedings of *RAGtime 10–13, 15–17/20–22/15–17/14–16 September, 2008/2009/2010/2011, Opava, Czech Republic*
Z. Stuchlík, G. Török and T. Pecháček, editors, Silesian University in Opava, 2014, pp. 185–193

Ejection of string loop from region near black hole horizon

Zdeněk Stuchlík[a] and Martin Kološ[b]

Institute of Physics, Faculty of Philosophy & Science, Silesian University in Opava,
Bezručovo nám. 13, CZ-746 01 Opava, Czech Republic
[a]Zdenek.Stuchlik@fpf.slu.cz
[b]Martin.Kolos@fpf.slu.cz

ABSTRACT
We study ejection speed of current-carrying string-loops governed by the presence of an outer tension barrier and an inner angular momentum barrier in the field of the Schwarzschild black holes. We restrict attention to the axisymmetric motion of string loops with energy high enough, when the string loop can overcome the gravitational attraction and escape to infinity. Due to the chaotic character of the string loop motion, the strings can be scattered and the energy of the string oscillations can be efficiently converted to the energy of the linear motion that can represent a jet motion. We give the condition limiting energy available for conversion onto jet-like motion.

Keywords: string loops – black holes – Schwarzschild – spacetime – accelerating jets

1 INTRODUCTION

Relativistic current carrying strings moving axisymmetrically along the axis of a Kerr black hole (Jacobson and Sotiriou, 2009) or a Schwarzschild-de Sitter black hole (Kološ and Stuchlík, 2010) could in a simplified way represent plasma that exhibits associated string-like behaviour via dynamics of the magnetic field lines in the plasma (Christensson and Hindmarsh, 1999; Semenov et al., 2004) or due to thin isolated flux tubes of plasma that could be described by an one-dimensional string (Spruit, 1981). Tension of such a loop string prevents its expansion beyond some radius, while its worldsheet current introduces an angular momentum barrier preventing the loop from collapsing into the black hole. Such a configuration was also studied in (Larsen, 1994; Frolov and Larsen, 1999). It has been proposed in (Jacobson and Sotiriou, 2009) that this current configuration can be used as a model for jet formation. Here we shall test the possibility to converse motion of a string loop originally oscillating around a black hole in one direction to the perpendicular direction, modelling thus an accelerating jet. It is well known that due to the chaotic character of the motion of string loops, such a transformation of the energy from the oscillatory to the linear mode is possible (Jacobson and Sotiriou, 2009; Kološ and Stuchlík, 2010). Here we make the estimate of efficiency of such a transformation in the Schwarzschild gravitation field.

978-80-7510-125-9

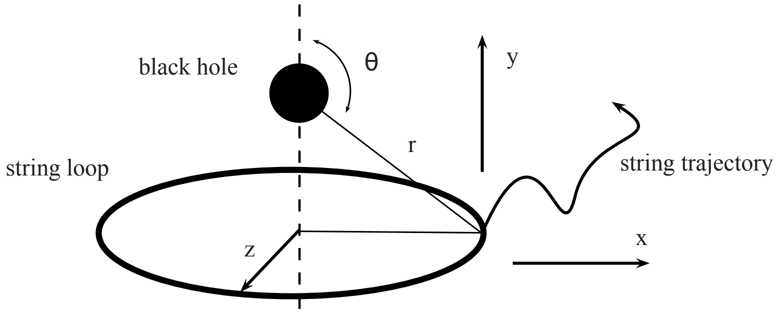

Figure 1. Schematic picture of a string loop moving around a black hole. Assumed axial symmetry of the string loop allows to investigate only one point on the loop; one point path can represent whole string movement. Trajectory of the loop is then represented by the black curve on the picture, given in 2D x-y plot.

2 CURRENT-CARRYING STRING LOOPS

We study a string loop motion in the field of a black hole described by the Schwarzschild metric

$$\mathrm{d}s^2 = -A(r)\,\mathrm{d}t^2 + A^{-1}(r)\,\mathrm{d}r^2 + r^2\big(\mathrm{d}\theta^2 + \sin^2\theta\,\mathrm{d}\phi^2\big)\,, \quad A(r) = 1 - \frac{2M}{r}\,. \tag{1}$$

We use the geometric units with $c = G = 1$ and the Schwarzschild coordinates. In order to properly describe the string loop motion, it is useful to use the Cartesian coordinates

$$x = r\sin(\theta)\,, \quad y = r\cos(\theta)\,. \tag{2}$$

The string loop is threaded on to an axis of the black hole chosen to be the y-axis – see Fig. 1. The string loop can oscillate, changing its radius in x-z plane, while propagating in y direction. The string loop tension and worldsheet current form barriers governing its dynamics. These barriers are modified by the gravitational attraction of the black hole characterized by the mass M.

2.1 Equations of motion

The string worldsheet is described by the spacetime coordinates $X^\alpha(\sigma^a)$ (with $\alpha = 0, 1, 2, 3$) given as functions of two worldsheet coordinates σ^a (with $a = 0, 1$) that imply induced metric on the worldsheet in the form

$$h_{ab} = g_{\alpha\beta} X^\alpha{}_{,a} X^\beta{}_{,b}\,. \tag{3}$$

Any two-dimensional metric is conformally flat metric, i.e. in our case when we use the standard Schwarzschild coordinates (1), there is

$$-h_{\tau\tau} = h_{\sigma\sigma} = g_{\phi\phi}\,, \quad h_{\tau\sigma} = h_{\sigma\tau} = 0\,, \tag{4}$$

where we adopt coordinates $a = (\tau, \sigma)$.

Dynamics of the string is described by the action related to a scalar field φ and tension μ (worldsheet with minimal area), expressed in the form (Jacobson and Sotiriou, 2009)

$$S = \int \mathrm{d}^2\sigma \sqrt{-h}(\mu + h^{ab}\varphi_{,a}\varphi_{,b}) \,, \tag{5}$$

where $\varphi_{,a} = j_a$ determines current of the string and $\mu > 0$ reflects the string tension. For $j_a = 0$, we have Nambu–Goto string (Zwiebach, 2004), for $j_a = 0, \mu = 0$ we have null string.

Varying the action with respect to φ yields the $1+1$ dimensional wave equation

$$\left(\sqrt{-h}h^{ab}\varphi_{,a}\right)_{,b} = 0 \,. \tag{6}$$

Using the scalar field equation of motion (6) and the assumption of axisymmetry we can conclude that the scalar field can be expressed in linear form with constants j_σ and j_τ

$$\varphi = j_\sigma \sigma + j_\tau \tau \,. \tag{7}$$

Varying the action with respect to the induced metric h_{ab} yields the worldsheet stress-energy tensor density $\tilde{\Sigma}^{ab}$ with the components that can be expressed in the form (Jacobson and Sotiriou, 2009)

$$\tilde{\Sigma}^{\tau\tau} = \frac{J^2}{g_{\phi\phi}} + \mu \,, \quad \tilde{\Sigma}^{\sigma\sigma} = \frac{J^2}{g_{\phi\phi}} - \mu \,, \quad \tilde{\Sigma}^{\sigma\tau} = \frac{-2j_\tau j_\sigma}{g_{\phi\phi}} \,, \qquad J^2 \equiv j_\sigma^2 + j_\tau^2 \,. \tag{8}$$

Varying the action with respect to X^α, we arrive to equations of motion

$$\left(\tilde{\Sigma}^{ab} g_{\alpha\gamma} X^\alpha_{,a}\right)_{,b} - \frac{1}{2}\tilde{\Sigma}^{ab} g_{\alpha\beta,\gamma} X^\alpha{}_{,a} X^\beta{}_{,b} = 0 \,. \tag{9}$$

In spherically symmetric spacetimes, the axisymmetric string loops can be characterized by coordinates

$$X^\alpha(\tau,\sigma) = \Big(t(\tau), r(\tau), \theta(\tau), \sigma\Big) \,. \tag{10}$$

Equation of motion (9) for coordinates $\gamma = t$ and $\gamma = \phi$ imply two conserved quantities

$$\left(\tilde{\Sigma}^{\tau\tau} g_{tt} \dot{t}\right)_{,\tau} = 0 \,, \quad \left(\tilde{\Sigma}^{\sigma\tau} g_{\phi\phi}\right)_{,\tau} = 0 \,, \tag{11}$$

while for coordinates $\gamma = r$ and $\gamma = \theta$ we obtain two second order ordinary differential equations describing the string motion (Kološ and Stuchlík, 2010).

2.2 Hamiltonian formulation in spherically symmetric spacetimes

The string motion can be also formulated using Hamiltonian formalism (Larsen, 1993). We can consider Hamiltonian

$$\tilde{H} = \frac{1}{2} g^{\alpha\beta} P_\alpha P_\beta + \frac{1}{2}\mu^2 r^2 \sin^2\theta + \mu J^2 + \frac{1}{2}\frac{\left(j_\tau^2 - j_\sigma^2\right)^2}{r^2 \sin^2\theta} \,, \tag{12}$$

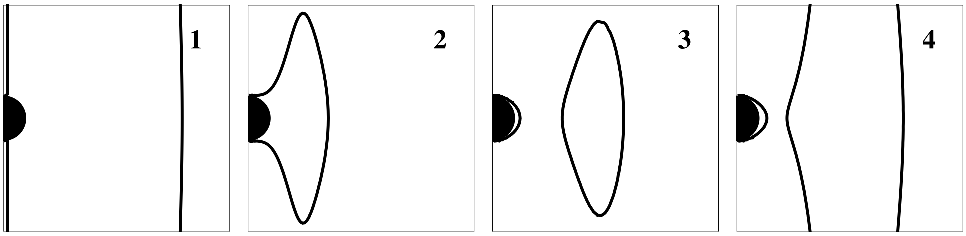

Figure 2. In the Schwarzschild spacetimes, we can distinguish four different types of the behavior of the boundary energy function E_b.

where α, β correspond to coordinates t, r, θ, ϕ. The spacetimes symmetries imply existence of two constants of motion

$$P_t = -E\,, \qquad P_\phi = L = -2 j_\tau j_\sigma\,. \tag{13}$$

Then in spherically symmetric spacetimes the Hamiltonian can be expressed in the form

$$H = \frac{1}{2}A(r)P_r^2 + \frac{1}{2}\frac{1}{r^2}P_\theta^2 - \frac{1}{2}\frac{E^2}{A(r)} + \frac{V_{\rm eff}(r,\theta)}{A(r)}, \tag{14}$$

where an effective potential for the string motion has been introduced by the relation

$$V_{\rm eff}(r,\theta) = \frac{1}{2}A(r)\left(\mu r\sin\theta + \frac{J^2}{r\sin\theta}\right)^2. \tag{15}$$

The Hamilton equations

$$\frac{\mathrm{d}X^\mu}{\mathrm{d}\lambda} = \frac{\partial H}{\partial P_\mu}, \quad \frac{\mathrm{d}P_\mu}{\mathrm{d}\lambda} = -\frac{\partial H}{\partial X^\mu} \tag{16}$$

applied to the Hamiltonian (14) imply equation of motion in the form

$$r' = A P_r\,, \quad (P_r)' = \frac{1}{A}\frac{P_\theta^2}{r^4}\left(Ar - \frac{1}{2}\frac{\mathrm{d}A}{\mathrm{d}r}r^2\right) - \frac{\mathrm{d}A}{\mathrm{d}r}P_r^2 - \frac{1}{A}\frac{\mathrm{d}V_{\rm eff}}{\mathrm{d}r}\,, \tag{17}$$

$$\theta' = \frac{P_\theta}{r^2}\,, \quad (P_\theta)' = -\frac{1}{A}\frac{\mathrm{d}V_{\rm eff}}{\mathrm{d}\theta}\,. \tag{18}$$

where prime is derivative with respect to the lambda: $f' = \mathrm{d}f/\mathrm{d}\lambda$.

Systems of equations for the string motion in the form (9) and (17–18) are related by transformation

$$\mathrm{d}\tau = \Sigma^{\tau\tau}\,\mathrm{d}\lambda\,. \tag{19}$$

3 STRING LOOP IN SCHWARZSCHILD SPACETIME

The Schwarzschild metric (1) introduces a characteristic length scale corresponding to the radius of the black hole horizon (that is given by the condition $A(r) = 0$, $r_{\rm h} = 2M$). It is convenient to use the dimensionless coordinates $\tilde{r} = r/M$ ($\tilde{x} = x/M, \tilde{y} = y/M$), the dimensionless string (angular momentum) parameter $\tilde{J} = J/M$ and energy $\tilde{E} = E/M$. Then the condition $H = 0$ can be written in the form

$$\tilde{E}^2 = \left((r')^2 + Ar^2(\theta')^2\right) + 2\tilde{V}_{\rm eff}\,, \tag{20}$$

The conditions $r' = 0$, $\theta' = 0$ determine boundary for the string motion. The boundary energy reads

$$\tilde{E}_{\rm b}^2 = 2\tilde{V}_{\rm eff}\,. \tag{21}$$

In Cartesian coordinates it takes the form

$$E_{\rm b}(x, y) = \sqrt{A(r)}\left(J^2/x + x\mu\right) = \sqrt{A(r)}\,f(x)\,, \tag{22}$$

where $r = r(x, y) = \sqrt{x^2 + y^2}$. The function $A(r)$ reflects the spacetime properties, while $f(x)$ those of the string loop. The behaviour of the boundary energy function is given by interplay of the functions $A(r)$ and $f(x)$. The local extrema of the boundary energy function $E_{\rm b}$, given by

$$(E_{\rm b})'_x = 0 \Leftrightarrow xA'_r f = -2rAf'_x \qquad (E_{\rm b})'_y = 0 \Leftrightarrow A'_r y = 0\,, \tag{23}$$

are of crucial importance since they determine the regions of different character of the string loop motion.

In the Schwarzschild geometry the extrema equations (23) can be expressed in the form

$$\tilde{J}^2 = \tilde{J}_{\rm E}^2 \equiv \frac{\tilde{x}^2(\tilde{x}-1)}{\tilde{x}-3}\,, \quad \tilde{y} = 0\,. \tag{24}$$

The boundary energy function $E_{\rm b}$ has two extrema, maximum and minimum, located above the black-hole horizon (at $\tilde{x} > 2$), when

$$\tilde{J} > \tilde{J}_{\rm E(min)} \doteq 7\,. \tag{25}$$

The detailed discussion of the properties of the effective potential and the string loop motion can be found in (Kološ and Stuchlík, 2010). Here we summarize some relevant results.

We can distinguish four different types of the behaviour of the boundary energy function $E_{\rm b}$ in the Schwarzschild spacetimes; in Fig. 2 we denote them by numbers 1 to 4. The first case corresponds to no inner and outer boundary and the string can be captured by the black hole or escape to infinity. In the second case, there is an outer boundary, the string loop cannot escape to infinity and it must be captured by the black hole. The third case corresponds to the situation when both inner and outer boundary exist and the string is trapped in some region forming a potential “lake” around the black hole. In the fourth case string cannot fall into the black hole but it can escape to infinity (or be trapped).

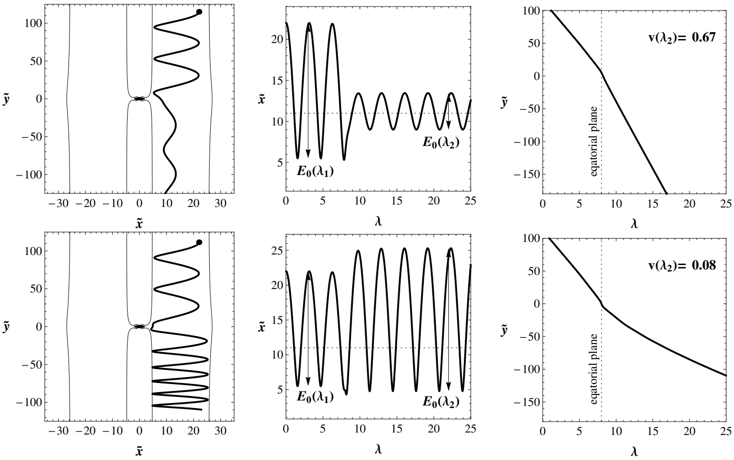

Figure 3. Conversion of energy between $E_{\rm x}$ and $E_{\rm y}$ modes – string transmutation effect in the Schwarzschild spacetime. Thick lines represents string trajectory, while thin lines on the first column form boundary for the string motion $E_{\rm b}$. The string with current $\tilde{J} = 11$ is starting from region away from black hole horizon $\tilde{x} = 22$ and $\tilde{y} = 115$ (first row), $\tilde{y} = 111.5$ (second row). Near the starting point the spacetime is almost flat, so string oscillates in the x-direction, while moving with initial speed in y direction $v(\lambda_1) \doteq 0.41\,c$ towards the black hole. Around conformal factor $\lambda \sim 8$ the string approaches region near the black hole horizon, where transmutation regime begins, and crosses the equatorial plane. Near the black hole horizon, the modes of energy in the x and y direction are interchanging, and the string is chaotically scattered. First row of pictures represents acceleration of the string in y direction $v(\lambda_2) \doteq 0.67\,c$, while the second one represents its deceleration $v(\lambda_2) \doteq 0.08\,c$.

4 STRING TRANSMUTATION

4.1 Flat spacetime energies

The Schwarzschild metric is flat at infinity. Therefore, we first discuss the motion of the string loop in the flat spacetime. The energy of the string loop (20) in Cartesian coordinates is given by

$$E^2 = (y')^2 + (x')^2 + \left(J^2/x + x\right)^2 = E_{\rm y}^2 + E_{\rm x}^2\,, \tag{26}$$

where prime is derivative with respect to the affine parameter λ. We introduce energy in x and y directions by the relations

$$E_{\rm y}^2 = (y')^2\,, \quad E_{\rm x}^2 = (x')^2 + \left(J^2/x + x\right)^2 = (x_{\rm i} + x_{\rm o})^2 = E_0^2\,. \tag{27}$$

The energy in x direction E_0 (for flat spacetime we introduce new marking $E_{\rm x} = E_0$) can be determined by the inner $x_{\rm i}$ and outer $x_{\rm o}$ radii limiting motion of the string loop

$$x_{\rm o,i} = \frac{1}{2}\left(E \pm \sqrt{E^2 - 4J^2}\right). \tag{28}$$

The energy E_0 is minimal if the inner and the outer radii coincide – then $x_\mathrm{i} = x_\mathrm{o} = J$; there is

$$E_{0(\mathrm{min})} = 2J \, . \tag{29}$$

Clearly, E_x and E_y are constants of the string loop motion in the flat spacetime and no transmutation is possible.

4.2 Schwarzschild spacetime energies

If the spacetime in not flat, $A(r) \neq 1$, we can write the string loop energy (20) in Cartesian coordinates in the form

$$E^2 = A(r)\Big[g_{xx}\big(x'\big)^2 + 2g_{xy}\big(x'\big)\big(y'\big) + g_{yy}\big(x'\big)^2\Big] + A(r)\big(\tilde{\Sigma}^{\tau\tau}\big)^2 x^2 \, , \tag{30}$$

where metric coefficients for the Schwarzschild spacetime in x and y coordinates are given by

$$g_{xx} = \frac{x^2 + Ay^2}{A\big(x^2 + y^2\big)} \, , \quad g_{xx} = \frac{y^2 + Ax^2}{A\big(x^2 + y^2\big)} \, , \quad g_{xy} = xy\frac{1 + A}{A\big(x^2 + y^2\big)} \, . \tag{31}$$

The term $g_{xy}(x')(y')$ is responsible for interchange of energy between E_x and E_y modes – string transmutation effect. The coefficient g_{xy} is significant only in the neighbourhood of the black hole, so the effect of string transmutation can occur only in this region.

All energy from the E_y mode can be transmitted to the E_x mode – oscillations of the string loop in the x direction will grown up, while the string will stop moving in the y direction. On the other hand, all energy from E_x mode can not be transmitted to the E_y mode – there remains always inconvertible energy $E_{0(\mathrm{min})} = 2J$ in E_x mode, see (29).

The string motion transmutation will change rate of the string propagation in the y direction; an example of acceleration (deceleration) in the y direction can be found on Fig. 3.

4.3 String ejection speed

We consider the toy model of jets represented as string loops starting from region near equatorial plane. We are interested in the maximum speed in y direction that strings can achieve through the transmutation effect, if starting from the rest.

The relativistic gamma factor reads (Jacobson and Sotiriou, 2009)

$$\gamma^2 = \frac{1}{1 - v^2} = \frac{E^2}{E_0^2} \, , \tag{32}$$

where E is the energy, E_0 is energy of the string in the x-direction taken at infinity, and v is string velocity in y direction ($v \in [0, 1\,c)$).

Maximal gamma factor (32) (maximal speed) can be obtained if the string loop energy E is large and the final energy in x direction (its value at infinity) is minimal, i.e. $E_{0(\mathrm{min})} = 2J$.

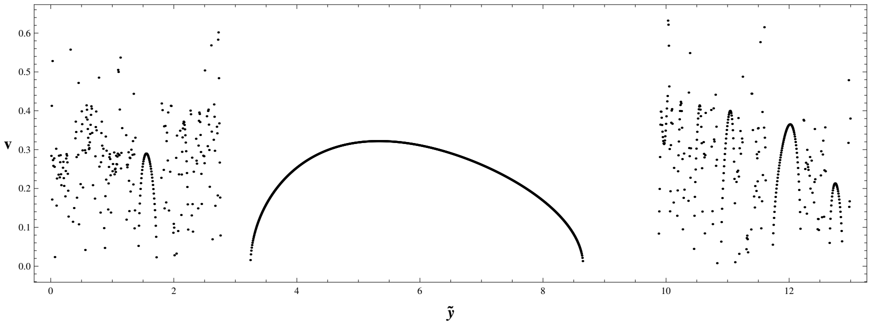

Figure 4. Speed of the string starting from the rest with fixed current $J = 11$ and starting point $\tilde{x} = 20$ while $\tilde{y}$ position (and total energy $\tilde{E}$) is changing. There are velocities up to the $v = 0.65\,c$.

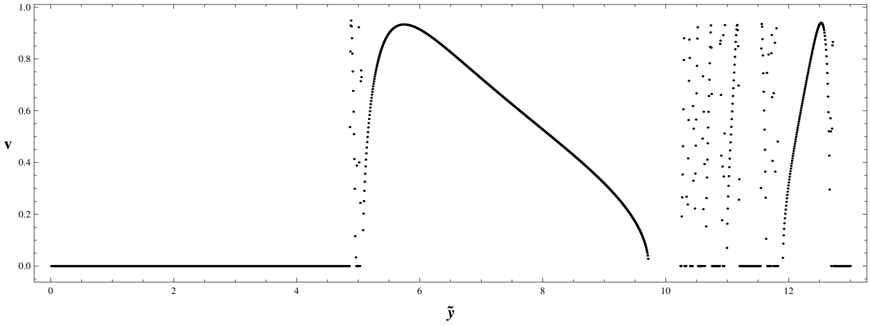

Figure 5. Speed of the string starting from the rest with fixed current $J = 2$ and starting point $\tilde{x} = 20$ while $\tilde{y}$ position (and total energy $\tilde{E}$) is changing. There are velocities up to the $v = c$.

In order to reach acceleration of the string loop in the y-direction the string must past region near the black hole horizon, where string transmutation effect $E_{\mathrm{x}} \leftrightarrow E_{\mathrm{y}}$ occurs.

Astrophysically most interesting situation corresponds to the string loop initially oscillating in (or near) the equatorial plane when the oscillatory energy is transmitted to the perpendicular direction; such transmutation represents jet ejection. The largest velocities for the string ejection reported in (Jacobson and Sotiriou, 2009) is $v = 0.39\,c$. On the other hand, in our study of strings with $\tilde{J} > \tilde{J}_{\mathrm{E(min)}}$ we have found substantially higher values of speed with $v = 0.65\,c$. The results are represented in Fig. 4 clearly demonstrating the chaotic nature of the string transmutation effect. Notice that the regular part of the results of the simulations (in the region $3 < \tilde{y} < 9$) gives maximal $v \sim 0.3\,c$, or $v \sim 0.4\,c$ for $\tilde{y} \sim 11$, in accord with results of (Jacobson and Sotiriou, 2009), while the chaotic region allows $v \sim 0.65\,c$.

There is an important question, whether ultrarelativistic speed of the jet model can be achieved, and under which conditions. The ultra relativistic speeds can be achieved only for small string currents $\tilde{J} < \tilde{J}_{\mathrm{E(min)}}$ starting from region out of the equatorial plane. We have type 1 of the motion boundary is such case of $\tilde{J} < \tilde{J}_{\mathrm{E(min)}}$ and any string starting close to the equatorial plane will collapse to the black hole. This implies necessity to start the string motion in sufficient distance from the equatorial plane. The results of modelling chaotic string loop motion finishing at infinity for $\tilde{J} < \tilde{J}_{\mathrm{E(min)}}$ is demonstrated in Fig. 5. Notice that now even in the regular part ultrarelativistic speeds $v \sim c$ occur.

5 CONCLUSIONS

We can summarize the possibility of substantial acceleration of string loops that can model jet ejection in the field of Schwarzschild black hole by the statements

- string transmutation effect $E_{\mathrm{x}} \leftrightarrow E_{\mathrm{y}}$ occurs only near the black hole horizon,
- string can be accelerated for $\tilde{J} > \tilde{J}_{\mathrm{min}}$ up to $v \sim 0.65\,c$ and up to $v \sim c$ only for small J and for type 1 of energy boundary.

ACKNOWLEDGEMENTS

The present work was supported by the Czech Grant MSM 4781305903.

REFERENCES

Christensson, M. and Hindmarsh, M. (1999), Magnetic fields in the early universe in the string approach to MHD, *Phys. Rev. D*, **60**, p. 063001, arXiv: `astro-ph/9904358`.

Frolov, A. V. and Larsen, A. L. (1999), Chaotic scattering and capture of strings by a black hole, *Classical Quantum Gravity*, **16**, p. 3717, arXiv: `gr-qc/9908039`.

Jacobson, T. and Sotiriou, T. P. (2009), String dynamics and ejection along the axis of a spinning black hole, *Phys. Rev. D*, **79**, p. 065029, arXiv: `gr-gc/0812.3996`.

Kološ, M. and Stuchlík, Z. (2010), Current-carrying string loops in black-hole spacetimes with a repulsive cosmological constant, *Phys. Rev. D*, **82**, p. 125012, arXiv: `gr-qc/1103.40056`.

Larsen, A. L. (1993), Dynamics of cosmic strings and springs; a covariant formulation, *Classical Quantum Gravity*, **10**, p. 1541, arXiv: `hep-th/9304086`.

Larsen, A. L. (1994), Chaotic string capture by black hole, *Classical Quantum Gravity*, **11**, p. 1201, arXiv: `hep-th/9309086`.

Semenov, V., Dyadechkin, S. and Punsly, B. (2004), Simulations of jets driven by black hole rotation, *Science*, **305**, p. 978, arXiv: `astro-ph/0408371`.

Spruit, H. C. (1981), Equations for thin flux tubes in ideal MHD, *Astronomy and Astrophysics*, **102**, p. 129.

Zwiebach, B. (2004), *A First Course in String Theory*, Cambridge University Press, Cambridge.

Proceedings of *RAGtime 10–13, 15–17/20–22/15–17/14–16 September, 2008/2009/2010/2011, Opava, Czech Republic*
Z. Stuchlík, G. Török and T. Pecháček, editors, Silesian University in Opava, 2014, pp. 195–207

String loop oscillation model applied to the twin HF QPOs in the atoll source 4U 1636-53

Zdeněk Stuchlík[a] and Martin Kološ[b]

Institute of Physics, Faculty of Philosophy & Science, Silesian University in Opava,
Bezručovo nám. 13, CZ-746 01 Opava, Czech Republic
[a]Zdenek.Stuchlik@fpf.slu.cz
[b]Martin.Kolos@fpf.slu.cz

ABSTRACT
The current-carrying string loops oscillating around a stable equilibrium position in the Kerr background are considered to explain the twin high-frequency quasiperiodic oscillations (HF QPOs) observed in the low-mass X-ray binary 4U 1636-53 containing a neutron star. The frequencies of the radial and vertical string loop oscillations are governed by the mass and spin parameters of the neutron star, and by the string parameter describing combined effects of its tension and angular momentum. The frequencies of the radial and vertical modes of the string loop oscillations can cover the large scatter of the twin HF QPO data observed in the 4U 1636-53 source, but the estimates of the mass M and spin a of the neutron star are rather high, $M \sim 2.65\, M_{\odot}$ and $a \sim 0.45$, while related to the theory of the neutron star structure. Therefore, the string loop oscillation model in the case of the 4U 1636-53 source requires a correction based on an electrically charged string loop interacting with the magnetic field of the neutron star.

Keywords: string loop oscillations – X-ray variability – HF QPO observations

1 INTRODUCTION

Current-carrying string loops can represent combined systems of magnetic field and plasma, exhibiting a string-like behaviour due to dynamics of the magnetic field lines (Semenov et al., 2004; Christensson and Hindmarsh, 1999), or due to the thin flux tubes of magnetized plasma simply described as 1D strings (Semenov and Bernikov, 1991; Cremaschini and Stuchlík, 2013; Cremaschini et al., 2013; Kovář, 2013). The string loops are governed by their tension and angular momentum. (Recall that first the cosmic strings were introduced as remnants of the phase transitions in the very early universe (Vilenkin and Shellard, 1995), and strings represented as superconducting vortices were introduced by (Witten, 1985)). Dynamics of axially symmetric string loops in axially symmetric backgrounds is relatively very simple and can be fully governed by an appropriately defined effective potential, in analogy with test particle motion (Jacobson and Sotiriou, 2009; Kološ and Stuchlík, 2010; Stuchlík and Kološ, 2012a; Kološ and Stuchlík, 2013). The current-carrying string loops

978-80-7510-125-9

moving axisymmetrically along the symmetry axis of the Kerr or Schwarzschild–de Sitter black holes can be relevant in astrophysical processes (Jacobson and Sotiriou, 2009; Kološ and Stuchlík, 2010; Stuchlík and Kološ, 2012a; Kološ and Stuchlík, 2013). Electrically charged current-carrying string loops oscillating in combined external gravitational and electromagnetic fields can be also fully described by an effective potential, if the string loop and the background have common axial symmetry (Tursunov et al., 2013).

Recently, the axisymmetric current-carrying string loops were considered as a model of ultrarelativistic jet formation due to transmutation effect governing transmission of the internal energy of the oscillatory motion to the energy of translational motion (Stuchlík and Kološ, 2012a,b; Kološ and Stuchlík, 2013). On the other hand, it has been shown that small oscillations of the current-carrying string loops can explain frequency of the HF QPOs observed with frequency ratio 3:2 in the three Galactic microquasars, GRS 1915+105, XTE 1550-564, GRO 1655-40, i.e. Low-Mass X-ray Binary (LMXB) systems containing a black hole (Stuchlík and Kološ, 2014b), and the special set of HF QPOs observed in the peculiar neutron star low-mass X-ray binary XTE 1701-407 (Stuchlík and Kološ, 2014a). The string loop oscillation model in both the cases assumes relevance of some resonant phenomena and predicts reasonable restrictions on the values of the mass and spin of the black holes in the microquasars, and the neutron star in the XTE J1701-407 source.

Here we test the string loop oscillation model in the case of the well studied atoll source 4U 1636-53, where a large scatter of the twin HF QPOs is observed (Barret et al., 2005, 2006; Belloni et al., 2007a; Wang et al., 2013, 2014). Then a different approach has to be applied in order to match the observed twin HF QPOs where resonant phenomena are not taken into consideration. On the other hand, we keep the assumption that mass of the neutron star is large enough so that the external field of the neutron star can be well approximated by the Kerr geometry (Urbanec et al., 2013).

2 STRING LOOP OSCILLATION MODEL

2.1 Motion of axisymmetric string loops

Dynamics of an axisymmetric current-carrying string loop in a given axially symmetric and stationary, Kerr, spacetime with metric $g_{\alpha\beta}$ was treated in (Jacobson and Sotiriou, 2009; Kološ and Stuchlík, 2013). Oscillations of such string loops have been studied in (Stuchlík and Kološ, 2014b). The oscillations of the string loop can be characterized by two parameters, J and ω, reflecting the effect of the magnitude and components of the angular momentum and the string tension (Stuchlík and Kološ, 2014b).

As demonstrated in (Larsen, 1993; Stuchlík and Kološ, 2014b), the string loop motion can be described by the Hamilton equations and an appropriately defined Hamiltonian H with a dynamic, $H_{\rm D}$, and a potential, $H_{\rm P}$, parts. The potential part is related to the constants of motion associated to the background symmetries, namely, the energy E and the angular momentum parameters J and ω. The boundary of the string loop motion is given by vanishing of the potential parts of the Hamiltonian that implies the so called energy boundary function $E_{\rm b}(r, \theta; a, J, \omega)$, (Kološ and Stuchlík, 2013; Stuchlík and Kološ, 2014b), serving as an effective potential of the string loop motion. The turning points of the string loop motion are determined by the condition $E = E_{\rm b}(r, \theta; a, J, \omega)$.

In the Kerr metric and the standard Boyer–Lindquist r, θ coordinates, (Carter, 1973), the energy boundary function takes the form (Stuchlík and Kološ, 2014b),

$$E_{\mathrm{b}}(r,\theta;a,J,\omega) = \frac{4a\omega J^2 r}{\left(\omega^2+1\right)G} + \sqrt{\Delta}\left(\frac{J^2R^2}{G\sin(\theta)} + \sin(\theta)\right), \tag{1}$$

where

$$G(r,\theta;a) = \left(a^2+r^2\right)R^2 + 2a^2 r\sin^2(\theta), \tag{2}$$

and

$$R^2 = r^2 + a^2\cos^2\theta, \quad \Delta = r^2 - 2Mr + a^2, \tag{3}$$

a denotes spin and M mass parameters of the Kerr spacetimes. Here we consider only the Kerr black hole spacetimes ($a < M$), at the external region located above the outer event horizon given by

$$r_+ = M + \left(M^2 - a^2\right)^{1/2}. \tag{4}$$

Of course, for the exterior of neutron stars we have to consider only the part of the Kerr spacetime limited by the condition $r \geq R_{\mathrm{surface}} > r_+$.

In the following, we shall use for simplicity the dimensionless radial coordinate $r \to r/M$, dimensionless time coordinate $t \to t/M$ and dimensionless spin $a \to a/M$; this is equivalent to using of $M = 1$ in the metric tensor. We will return to the dimensional quantities in the Section 3.

Detailed discussion of the properties of the energy boundary function $E_b(r,\theta)$ is presented in (Kološ and Stuchlík, 2013) for both the Kerr black hole and naked singularity spacetimes. Here we focus on the properties in the black hole spacetimes that can be relevant for rotating neutron stars as demonstrated in (Urbanec et al., 2013; Török et al., 2008) – in this case the local extrema of the energy boundary function can be located in the equatorial plane only.

The local extrema of the energy boundary function $E_{\mathrm{b}}(r;a,J,\omega)$, governing the equilibrium positions of the string loops in the equatorial plane ($\theta = \pi/2$), are determined by the relation (Kološ and Stuchlík, 2013; Stuchlík and Kološ, 2014b),

$$J^2 = J^2_{\mathrm{E}}(r;a,\omega) \equiv \frac{(r-1)\left(\omega^2+1\right)H^2}{4a\omega\sqrt{\Delta}\left(a^2+3r^2\right) + \left(\omega^2+1\right)F}, \tag{5}$$

where

$$H(r;a) = r^3 + a^2(2+r), \quad F(r;a) = (r-3)r^4 - 2a^4 + a^2 r\big(r^2 - 3r + 6\big). \tag{6}$$

The oscillations of the string loops around a stable equilibrium position in the Kerr background has been discussed in (Kološ and Stuchlík, 2013; Stuchlík and Kološ, 2014b). In the basic approximation, for the first term in the perturbation expansion of the Hamiltonian around the stable equilibrium positions, the oscillations can be separated to two modes of

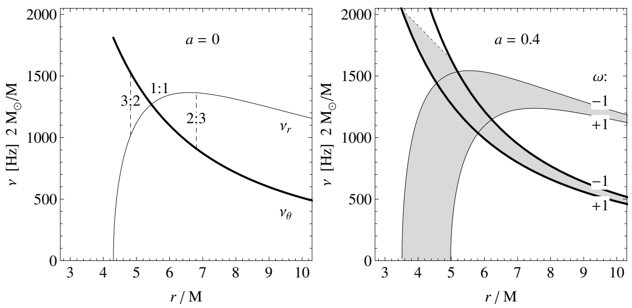

Figure 1. String-loop oscillatory frequencies ν_r (thin curves) and ν_θ (thick curves), calculated for the Kerr metrics with $M = 2\,M_\odot$. Their radial profiles are illustrated for values of dimensionless spin $a = 0, 0.4$ that are characteristic of our study of neutron star system. We demonstrate extension of the frequency radial profiles for the complete range of the string loop parameter $\omega \in \langle -1, 1\rangle$. The vertical frequency curves are restricted to the region of existence (zero point) of the corresponding radial frequency curves – the relevant region is greyed.

independent linear-harmonic oscillations in the radial and vertical direction. The higher order terms of the expansion govern subsequent transition to the quasiharmonic oscillations and finally to the fully chaotic oscillatory motion; it is very important that frequency of the quasiharmonic oscillations of the string loops agrees with frequency of their harmonic oscillations, (Stuchlík and Kološ, 2014b).

The rotating neutron stars are conveniently described by the Hartle–Thorne geometry that is characterized in the exterior part by three parameters: mass M, dimensionless spin a, and dimensionless quadrupole moment q, as shown in (Hartle, 1967; Hartle and Thorne, 1968; Chandrasekhar and Miller, 1974). The Hartle–Thorne model can be used for rotating neutron stars with rotation frequency significantly smaller that the mass-shedding frequency, $f_{m-sh} \sim 1100$ Hz, and spin $a < 0.5$ (Urbanec et al., 2013). The rotation frequency of neutron stars described well by the Hartle–Thorne model can be as high as $f_\mathrm{rot} \sim 600$ Hz.

For $q/a^2 = 1$, the Hartle–Thorne geometry coincides with Kerr geometry, and for $1 < q/a^2 < 2$ these two geometries are very close each other giving very close predictions for astrophysical phenomena (Török et al., 2008; Török et al., 2010; Bejger et al., 2010; Bini et al., 2013). It has been demonstrated recently that for a wide variety of equations of state, the Hartle–Thorne models predict $q/a^2 < 2$, if the neutron star mass is close to the maximum allowed by a given equation of state, implying thus applicability of the Kerr geometry (Urbanec et al., 2013).

2.2 Frequency of the radial and vertical harmonic oscillatory modes

For the string loop harmonic oscillations around a stable equilibrium position at a given r_0 and $\theta_0 = \pi/2$ the locally measured angular frequencies of the radial and vertical oscillatory motion reads (Stuchlík and Kološ, 2014b)

$$\omega_\mathrm{r}^2 = \frac{1}{g_{rr}} \frac{\partial^2 H_\mathrm{P}}{\partial r^2}\,, \quad \omega_\theta^2 = \frac{1}{g_{\theta\theta}} \frac{\partial^2 H_\mathrm{P}}{\partial \theta^2}\,. \tag{7}$$

The partial derivatives of the potential part of the Hamiltonian are calculated at the local minimum of the energy boundary function at r_0 and $\theta_0 = \pi/2$. The location of the stable equilibrium point is determined by the angular momentum parameters J and ω of the string loop – see (Stuchlík and Kološ, 2014b).

The locally measured angular frequencies are connected to the angular frequencies related to distant observers, $\Omega_{(\mathrm{r},\theta)}$, by the gravitational redshift transformation (Stuchlík and Kološ, 2014b),

$$\Omega_{(\mathrm{r},\theta)} = \frac{\omega_{(\mathrm{r},\theta)}}{P^t} \,. \tag{8}$$

If the angular frequencies $\Omega_{(\mathrm{r},\theta)}$, or frequencies $\nu_{(\mathrm{r},\theta)}$, are expressed in the physical units, their dimensionless form has to be extended by the factor c^3/GM. Then the frequencies of the string loop oscillations measured by the distant observers are given by

$$\nu_{(\mathrm{r},\theta)} = \frac{1}{2\pi} \frac{c^3}{GM} \Omega_{(r,\theta)} \,. \tag{9}$$

The same factor occurs in the case of the orbital and epicyclic frequencies of the geodesic motion in the Kerr spacetime (Aliev and Galtsov, 1981; Török and Stuchlík, 2005; Stuchlík and Schee, 2012). The mass-scaling of the frequencies of the radial and vertical oscillations is the same for both the current-carrying string loops and test particles and we are approved to expect that the string loop oscillations could serve as an explanation of the HF QPOs observed in the strong gravity regions of black holes and neutron stars. In the Kerr geometry, the angular frequencies of the string loop oscillations related to distant observers take the dimensionless form (Stuchlík and Kološ, 2014b),

$$\Omega_{\mathrm{r}}^2(r;a,\omega) = \frac{J_{\mathrm{E(ex)}}\Big(2a\omega\sqrt{\Delta}\big(a^2+3r^2\big)+\big(\omega^2+1\big)F_1\Big)}{2r\big(a^2(r+2)+r^3\big)^2F_3^2} \,, \tag{10}$$

$$\Omega_{\theta}^2(r;a,\omega) = \frac{\sqrt{\Delta}\Big(2a\omega\sqrt{\Delta}\big(2a^2-3a^2r-3r^3\big)+\big(\omega^2+1\big)F_2\Big)}{r^2\big(a^2(r+2)+r^3\big)F_3} \,, \tag{11}$$

where

$$\begin{aligned}
F_1(r,a) &= a^2r^3 - a^2\Delta + r^5 - 2r^4 \,, && (12)\\
F_2(r;a) &= a^4(3r-2) + 2a^2(2r-3)r^2 + r^5 \,, && (13)\\
F_3(r;a,\omega) &= 2a\omega\big(a^2+3r^2\big) + \sqrt{\Delta}\big(\omega^2+1\big)\big(r^3-a^2\big) \,, && (14)\\
J_{\mathrm{E(ex)}}(r;a,\omega) &\equiv \big(\omega^2+1\big)H(r-1)\big(6a^2r-3a^2r^2-6a^2-5r^4+12r^3\big) \\
&\quad + 4a\omega H\Delta^{-1/2}\Big[\big(a^2+3r^2\big)\Big(\Delta-\big(r-1\big)^2\Big)-6\Delta r(r-1)\Big] \\
&\quad - \big(\omega^2+1\big)\Big[FH+2F\big(a^2+3r^2\big)(r-1)\Big] \\
&\quad + 8a\omega\sqrt{\Delta}\big(a^2+3r^2\big)^2(r-1) \,. && (15)
\end{aligned}$$

The function $J_{\mathrm{E(ex)}}(r;a,\omega)$ determines the local extrema of the function $J_{\mathrm{E}}(r;a,\omega)$ and character of the local extrema of the energy boundary function. Its zero points correspond to the marginally stable equilibrium positions of the string loops – the frequency of the radial oscillatory modes of the string loops vanishes there. The conditions

$$J_{\mathrm{E(ex)}} = 0 \quad \text{and} \quad J_{\mathrm{E}}^2 \geq 0\,, \tag{16}$$

satisfied simultaneously, put the limit on validity of the formulae giving the angular frequencies of the radial and vertical oscillations (Stuchlík and Kološ, 2014b).

In the case of spherically symmetric spacetimes, $a = 0$, the parameter ω is irrelevant for the string loop oscillatory motion. The vertical oscillations are then fully governed by the gravity effect of the black hole (or neutron star) and the string tension and angular momentum play no role (Kološ and Stuchlík, 2013). The frequency of the vertical oscillations of the string loops equals those of the test particle epicyclic motion. In the rotating Kerr spacetimes, even for string loops with $\omega = 0$, the vertical harmonic oscillations are different for the string loops and test particles, implying relevance of the string tension and angular momentum even in the simplest state of $\omega = 0$ (Stuchlík and Kološ, 2014b).

Behaviour of the radial profiles of the radial and vertical frequencies of the string loop harmonic oscillations is illustrated in Figure 1 for two characteristic values of the Kerr spin parameter $a = 0, 0.4$. In the Schwarzschild spacetime ($a = 0$), a degeneration occurs, and both the frequencies are independent of the parameter ω. In the Kerr spacetimes, the range of the radial and vertical frequencies depends on the string-loop parameter ω, and the spin parameter a of the spacetime. Extension of the range of allowed frequencies increases with increasing spin a, if we consider the full range of the angular momentum parameter ω. For all values of the spin, and at each radius where the two oscillatory modes can occur, the vertical frequency has its maximum (minimum) for string loops with $\omega = -1$ ($\omega = +1$), while the radial frequency has its maximum (minimum) for string loops with $\omega = +1$ ($\omega = -1$) – see Fig. 1.

3 TWIN HF QPOS IN ATOLL AND Z SOURCES

The low mass X-ray binary (LMXB) systems containing neutron stars are separated into two categories – the so called atoll and Z sources. This categorisation reflects distinct spectral properties of the sources and its details can be found in (Hasinger and van der Klis, 1989). Distinctions of these two classes of the neutron star LMXB systems are discussed, e.g. in (van der Klis, 2006); remarkably, the Z sources are persistent, brighter and harder than the atoll sources. Both atoll and Z sources demonstrate twin HF QPOs. Details of observed HF QPO are presented in original papers related to individual sources, a review detailed study comparing properties of HF QPOs in a large variety of observed atoll and Z sources is prepared in (Török et al., 2014), other details are presented in (Barret et al., 2005; Belloni et al., 2007b; Wang et al., 2013).

In the LMXB systems the frequencies of observed quasiperiodic oscillations range from $\sim 10^{-2}$ Hz up to $\sim 10^{3}$ Hz. We restrict attention to the kHz (high-frequency) QPOs, with frequencies in the range 200–1300 Hz that are comparable to the frequencies of the orbital motion in strong gravity near neutron stars and stellar-mass black holes (van der Klis, 2006). In the neutron-star sources, HF QPOs usually occur as two simultaneously observed peaks in the X-ray flux, with frequencies that substantially change over time – see,

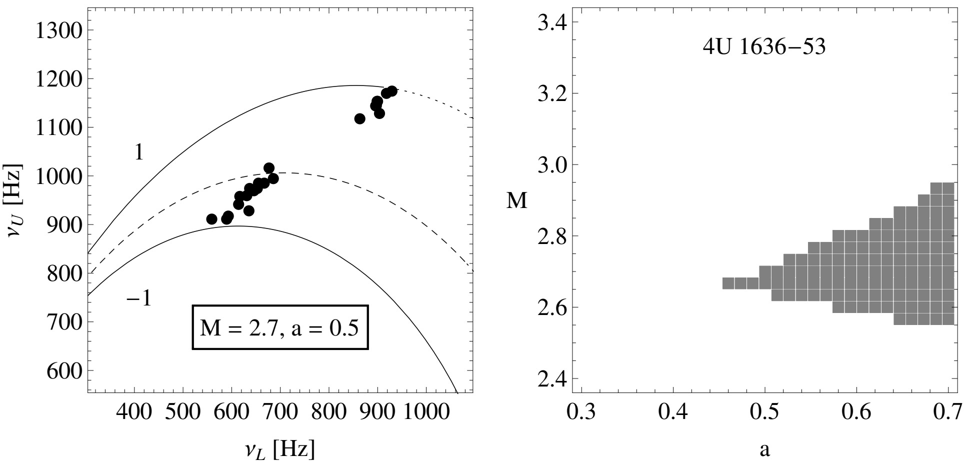

Figure 2. Restrictions on the mass M and spin a parameters of the neutron star in the 4U 1636-53 source implied by the string loop oscillation model applied to the whole variety of observational events of HF QPOs at the source. The limiting $\nu_r - \nu_\theta$ (corresponding to $\nu_\mathrm{U} - \nu_\mathrm{L}$) dependences are given for the limiting values of $\omega = \pm 1$ (*left figure*) in the case of properly chosen spacetime parameters M, a. We then give the allowed range in the space of the spacetime parameters $M - a$ where covering of all the observational twin HF QPO data in the source 4U 1636-53 is possible (*right figure*).

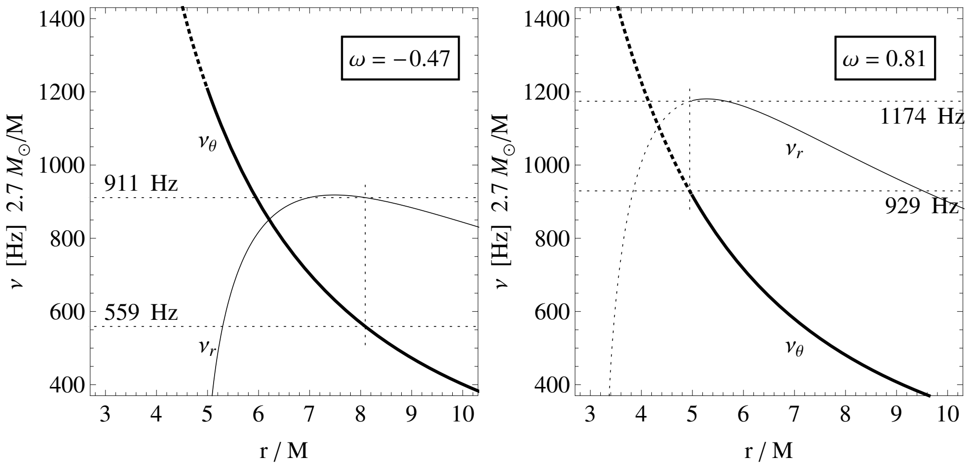

Figure 3. Examples of the radial profiles of the string-loop oscillatory frequencies ν_r (*thin curves*) and ν_θ (*thick curves*) as related to the two observational events, with maximal and minimal frequency ν_U. The parameters of the Kerr metric are mass $M = 2.7\,M_\odot$ and spin $a = 0.5$. The curved are dashed for $r < 5$, which is consider to be the inner parts of central object. The related values of the parameter ω are depicted in both subfigures, relevant frequencies are also given.

e.g. (Barret et al., 2005; Méndez, 2006).[1] According to the standard convention, we call the two peaks corresponding to a twin HF QPOs the lower and upper QPO denoting their frequencies $\nu_{\rm L} < \nu_{\rm U}$. The observed twin HF QPOs span in the atoll or Z sources a large frequency range following an approximately linear $\nu_{\rm L} - \nu_{\rm U}$ relation (Belloni et al., 2005). The frequency ratio in twin HF QPOs changes in the range of 3:2 to 5:4 in the atoll sources and in some of the Z sources, but for a variety of the Z sources the frequency ratio starts at 3:1 and finishes at 3:2. Recall that we know also a peculiar neutron star source XTE J1701-407 where the observed HF QPOs resemble those observed in the microquasars, displaying two twin HF QPOs with frequency ratio 3:2 and a single HF QPO (Pawar et al., 2013). A similar behaviour occurs in the case of the peculiar source XTE J1701-462 (Homan et al., 2007).

The string loop oscillation model has been successfully applied to explain the frequencies of the HF QPOs with ratio 3:2 observed in the three Galactic microquasars GRS 1915+105, XTE 1550-564, GRO 1655-40 (Stuchlík and Kološ, 2014b), and the frequencies of HF QPOs observed in the peculiar source XTE 1701-407 where one observed frequency is mixed with two twin frequencies with ratio very close to the 3:2 ratio, typically observed in the black hole systems (microquasars), (Stuchlík and Kološ, 2014a). In both the cases, relevance of resonant phenomena in the string loop oscillation model has been assumed, and the limits of the string loop model implied for the black hole (neutron star) mass and spin are in agreement with independent measurements of these spacetime parameters. The resonance phenomena can be relevant for the behaviour of the oscillating string loops as indicated by the Kolmogorov–Arnold–Moser (KAM) theory (Möser, 1962; Stuchlík and Kološ, 2014b), or some resonance phenomena could be relevant even for creation of the string loops, selecting thus some special radii related to the resonant phenomena.

4 FITTING THE FREQUENCIES OF THE TWIN KHZ QPOS IN THE ATOLL SOURCE 4U 1636-53

Here we concentrate our attention on the frequency distribution of the observed twin HF QPOs in the widely studied atoll source 4U 1636-53. In this case the resonant phenomena cannot be relevant in explaining the observed twin HF QPOs because of the large scatter of the 4U 1636-53 observational data spanning the whole interval of the frequency ratio 3:2–5:4 (Barret et al., 2005; Török, 2009). The data reflecting all the observed twin HF QPOs in 4U 1636-53 are illustrated in Fig. 2.

For a given twin HF QPOs observed in a given source, we have to consider fixed values of the string parameter ω and the spacetime parameters M and a. For a variety of twin HF QPOs being observed in the source, the spin and mass parameters have to be fixed, but the string loop parameter ω can be varied. Various twin frequency observations could be generated by different string loops being created and decayed successively with different values of the parameter ω reflecting locally different conditions in the source. The

[1] In the black hole systems (microquasars), the HF QPOs are detected at constant frequencies that are characteristic of a given source (Remillard and McClintock, 2006). When two or more frequencies are detected, they occur with a fixed small-number ratio; for twin observations the ratio 3:2 typically occurs (Török et al., 2005).

string-loop oscillation model thus naturally introduces a possibility of significant scatter in distribution of frequencies of the twin HF QPOs. A large scatter in the distribution of twin HF QPOs in the $\nu_L - \nu_U$ diagram can occur, if string loops with differing parameter ω arise at a fixed radius of the disc under evolving conditions, or if they arise at different radii of the disc under differing local conditions. Naturally, we can expect mix of these two possibilities. On the other hand, a regular distribution of the twin HF QPOs along a line in the $\nu_L - \nu_U$ diagram is possible only if string loops with a fixed parameter ω occur on different radii of the Kerr spacetime describing the exterior of the neutron star; however, this is not the case of the 4U 1636-53 source.

For the largely scattered twin HF QPOs in the atoll sources 4U 1636-53, the resonance phenomena are evidently irrelevant in the framework of the string loop oscillation model and will not be considered here. Each point representing a twin HF QPO in the $\nu_L - \nu_U$ diagram determines both the upper and lower frequencies, and their ratio. The frequencies given by an observed twin HF QPOs can be related to the frequencies of the radial and vertical oscillatory modes of the string loop. The upper frequency can be identified to the vertical (radial) frequency, if the oscillating string loop is located under (above) the radius of coincidence of the radial and vertical frequencies of a given string loop governed by its parameter ω.

The procedure of fitting the string loop oscillation frequencies to the observed frequencies in an observational event of a twin HF QPO has been determined in (Stuchlík and Kološ, 2014b). The fitting procedure gives for each of the observed events an allowed region of the parameter space of the spacetime parameters M, a, determined by the limiting values of the string loop parameter $\omega \in \langle -1, 1 \rangle$. The resulting restriction of the spacetime and string parameters M, a, ω is then given by the conjunction of the restrictions given for individual twin-frequency data points. While this procedure works quite efficiently for the simple situations of the observed HF QPOs in the microquasars and the XTE J1701-407 neutron star source, for the complex data sets related to the atoll source 4U 1636-53 it is complex and inconvenient.

Therefore, we use a different method, giving directly the dependence of the frequency of the radial and vertical oscillatory modes in the $\nu_L - \nu_U$ diagram of the observed data points, assuming that the whole interval of the string loop parameter $\omega \in \langle -1, 1 \rangle$ is relevant. For given mass parameter M, the fitting predicts only one line of the radial and vertical frequencies for the spin $a = 0$, due to the degeneracy of the radial profiles of the string loop oscillation frequencies in the Schwarzschild spacetimes ($a = 0$), i.e. their independence of the stringy parameter ω. Extension of the frequency region covered by the lines of the radial and vertical frequencies being related to the whole interval of the string loop parameter $\omega \in \langle -1, 1 \rangle$ (i.e. the interval of allowed values of frequencies) increases with increasing spin a. We have to look for the values of the neutron star parameters M, a when the region of the allowed radial and vertical frequencies of the string loops cover all the observed twin HF QPO data. The situation is illustrated in Fig. 2 (left), where the example of the $\nu_r - \nu_\theta$ dependence is given for properly chosen values of the spacetime parameters M, a. The limiting lines correspond to the limiting values of $\omega \in \langle -1, 1 \rangle$. The spin parameter has been taken at the value of $a = 0.5$ corresponding to the limit of applicability of the Hartle–Thorne theory (Urbanec et al., 2013).

Finally, the restrictions on the spacetime parameters M, a of the neutron stars in the atoll sources 4U 1636-53, predicted by the string loop oscillation model, are presented in Fig. 2 (right). The allowed region of the neutron star spacetime parameters is determined by a numeric procedure searching for the values of M, a parameters allowing to cover all the twin HF QPO data of the given source with the whole range of the string loop parameter ω. For completeness, we have considered whole the range of the neutron star spin, $a < 0.7$, as predicted by the fully general relativistic models of neutron stars (Lo and Lin, 2011). In the presented approach, restrictions on the string loop parameter ω are not discussed, as the whole range of $\omega \in (-1, +1)$ is allowed. In Figure 3, the radial profiles of the frequency of the radial and vertical harmonic oscillatory modes are presented in a typical situation enabling fitting of observational data, while limiting role of the neutron star surface is depicted.

We can see that the string loop oscillation model allows for the neutron star atoll source 4U 1636-53 its spin in the range $0.45 < a < 0.7$ and its mass in the range $2.5M_{\odot} < M < 2.9M_{\odot}$. These ranges seem to be in marginal agreement with the Hartle–Thorne theory of the neutron stars, and the limits implied on neutron star mass by realistic equations of state (Urbanec et al., 2013). In fact, the limiting value of $a = 0.45$ implies the mass of $M \sim 2.65\, M_{\odot}$ that can be explained by the very hard, mean-field equation of state.

5 CONCLUSIONS

We have demonstrated that the twin HF QPOs observed in the atoll 4U 1636-53 source can be explained by the string loop oscillation model introduced in (Stuchlík and Kološ, 2014b). This model, reflecting oscillations of string loops governed by interplay of the tension and angular momentum that can approximate magneto-plasma toroidal structures, has been for the atoll source applied in a way different to those related to simple systems of HF QPOs observed in microquasars or the peculiar neutron star XTE J1701-407 system, where resonant phenomena can be assumed. In the atoll source 4U 1636-53, the string loop oscillation model gives restrictions on the spacetime parameters M, a assuming no restrictions on the string loop parameter ω. We summarize that

- we cannot fit the observed data in the 4U 1636-53 source assuming only one string loop having a fixed value of the parameter ω, but we have to consider string loop with ω varied in the whole interval of allowed values $\omega \in (-1, +1)$.
- the neutron star has to be fast rotating, as the spin has to be in the range $0.45 < a < 0.7$,
- the neutron star has to be very massive, with mass parameter limited to the interval $2.5\,\mathrm{M}_{\odot} < M < 2.8\,\mathrm{M}_{\odot}$.

Since the neutron star has to be very massive, we can conclude that the application of the Kerr geometry in the fitting procedure is justified, as for the near-maximum-mass neutron stars the exterior Hartle–Thorne geometry has to be close to the exterior Kerr geometry, giving close predictions of the physical phenomena occurring in their vicinity. However, the predicted spin, $a \geq 0.45$, is too high for the Hartle–Thorne theory to be applicable. The applicability can be only marginal. Therefore, we could expect that some proper modifications of the spacetime parameters of the external field of the neutron star are possible due to an additional electromagnetic interaction of electrically charge string loops with the magnetic field of the neutron star (Tursunov et al., 2013, 2014).

Therefore, it is clearly worth to investigate the string loop oscillation model in more detailed way, concentrating on the conditions for creation of "magnetic" string loops due to the kinetic dynamo effect along the lines proposed in (Cremaschini and Stuchlík, 2013; Cremaschini et al., 2013).

ACKNOWLEDGEMENTS

The authors would like to thank the EU grant Synergy CZ.1.07/2.3.00/20.0071, the internal student grant SGS/23/2013 of the Silesian University, and the Albert Einstein Centre for gravitation and astrophysics supported by the Czech Science Foundation Grant No. 14-37086G.

REFERENCES

Aliev, A. N. and Galtsov, D. V. (1981), Radiation from relativistic particles in nongeodesic motion in a strong gravitational field, *General Relativity and Gravitation*, **13**, pp. 899–912.

Barret, D., Olive, J.-F. and Miller, M. C. (2005), An abrupt drop in the coherence of the lower kHz quasi-periodic oscillations in 4U 1636-536, *Monthly Notices of the Royal Astronomical Society* , **361**, pp. 855–860, arXiv: `astro-ph/0505402`.

Barret, D., Olive, J.-F. and Miller, M. C. (2006), The coherence of kilohertz quasi-periodic oscillations in the X-rays from accreting neutron stars, *Monthly Notices of the Royal Astronomical Society* , **370**, pp. 1140–1146, arXiv: `astro-ph/0605486`.

Bejger, M., Zdunik, J. L. and Haensel, P. (2010), Approximate analytic expressions for circular orbits around rapidly rotating compact stars, *Astronomy and Astrophysics* , **520**, A16, arXiv: `1008.0384`.

Belloni, T., Homan, J., Motta, S., Ratti, E. and Méndez, M. (2007a), Rossi XTE monitoring of 4U1636-53 - I. Long-term evolution and kHz quasi-periodic oscillations, *Monthly Notices of the Royal Astronomical Society* , **379**, pp. 247–252, arXiv: `0705.0793`.

Belloni, T., Méndez, M. and Homan, J. (2005), The distribution of kHz QPO frequencies in bright low mass X-ray binaries, *Astronomy and Astrophysics* , **437**, pp. 209–216, arXiv: `astro-ph/0501186`.

Belloni, T., Méndez, M. and Homan, J. (2007b), On the kHz QPO frequency correlations in bright neutron star X-ray binaries, *Monthly Notices of the Royal Astronomical Society* , **376**, pp. 1133–1138, arXiv: `astro-ph/0702157`.

Bini, D., Boshkayev, K., Ruffini, R. and Siutsou, I. (2013), Equatorial Circular Geodesics in the Hartle-Thorne Spacetime, *ArXiv e-prints*, arXiv: `1306.4792`.

Carter, B. (1973), Black hole equilibrium states., in C. Dewitt and B. S. Dewitt, editors, *Black Holes (Les Astres Occlus)*, pp. 57–214.

Chandrasekhar, S. and Miller, J. C. (1974), On slowly rotating homogeneous masses in general relativity, *Monthly Notices of the Royal Astronomical Society* , **167**, pp. 63–80.

Christensson, M. and Hindmarsh, M. (1999), Magnetic fields in the early universe in the string approach to MHD, *Phys. Rev. D* , **60**(6), 063001, arXiv: `astro-ph/9904358`.

Cremaschini, C. and Stuchlík, Z. (2013), Magnetic loop generation by collisionless gravitationally bound plasmas in axisymmetric tori, *Phys. Rev. E* , **87**(4), 043113.

Cremaschini, C., Stuchlík, Z. and Tessarotto, M. (2013), Kinetic theory of quasi-stationary collisionless axisymmetric plasmas in the presence of strong rotation phenomena, *Physics of Plasmas*, **20**(5), p. 052905.

Hartle, J. B. (1967), Slowly Rotating Relativistic Stars. I. Equations of Structure, *The Astrophysical Journal* , **150**, p. 1005.

Hartle, J. B. and Thorne, K. S. (1968), Slowly Rotating Relativistic Stars. II. Models for Neutron Stars and Supermassive Stars, *The Astrophysical Journal* , **153**, p. 807.

Hasinger, G. and van der Klis, M. (1989), Two patterns of correlated X-ray timing and spectral behaviour in low-mass X-ray binaries, *Astronomy and Astrophysics* , **225**, pp. 79–96.

Homan, J., van der Klis, M., Wijnands, R., Belloni, T., Fender, R., Klein-Wolt, M., Casella, P., Méndez, M., Gallo, E., Lewin, W. H. G. and Gehrels, N. (2007), Rossi X-Ray Timing Explorer Observations of the First Transient Z Source XTE J1701-462: Shedding New Light on Mass Accretion in Luminous Neutron Star X-Ray Binaries, *The Astrophysical Journal* , **656**, pp. 420–430, arXiv: `astro-ph/0610803`.

Jacobson, T. and Sotiriou, T. P. (2009), String dynamics and ejection along the axis of a spinning black hole, *Phys. Rev. D* , **79**(6), 065029, arXiv: `0812.3996`.

Kološ, M. and Stuchlík, Z. (2010), Current-carrying string loops in black-hole spacetimes with a repulsive cosmological constant, *Phys. Rev. D* , **82**(12), 125012, arXiv: `1103.4005`.

Kološ, M. and Stuchlík, Z. (2013), Dynamics of current-carrying string loops in the Kerr naked-singularity and black-hole spacetimes, *Phys. Rev. D* , **88**(6), 065004, arXiv: `1309.7357`.

Kovář, J. (2013), Spiral motion formation in astrophysics, *European Physical Journal Plus*, **128**, p. 142.

Larsen, A. L. (1993), Dynamics of cosmic strings and springs; a covariant formulation, *Classical and Quantum Gravity*, **10**, pp. 1541–1548, arXiv: `hep-th/9304086`.

Lo, K.-W. and Lin, L.-M. (2011), The Spin Parameter of Uniformly Rotating Compact Stars, *The Astrophysical Journal* , **728**, 12, arXiv: `1011.3563`.

Méndez, M. (2006), On the maximum amplitude and coherence of the kilohertz quasi-periodic oscillations in low-mass X-ray binaries, *Monthly Notices of the Royal Astronomical Society* , **371**, pp. 1925–1938, arXiv: `astro-ph/0607433`.

Möser, J. K. (1962), On invariant curves of area-preserving mappings of an annulus, *Nachr. Akad. Wiss. Göttingen*, pp. 1–20.

Pawar, D. D., Kalamkar, M., Altamirano, D., Linares, M., Shanthi, K., Strohmayer, T., Bhattacharya, D. and van der Klis, M. (2013), Discovery of twin kHz quasi-periodic oscillations in the low-mass X-ray binary XTE J1701-407, *Monthly Notices of the Royal Astronomical Society* , **433**, pp. 2436–2444, arXiv: `1306.0168`.

Remillard, R. A. and McClintock, J. E. (2006), Active X-ray States of Black Hole Binaries: Current Overview, in *American Astronomical Society Meeting Abstracts*, volume 38 of *Bulletin of the American Astronomical Society*, p. 903.

Semenov, V., Dyadechkin, S. and Punsly, B. (2004), Simulations of Jets Driven by Black Hole Rotation, *Science*, **305**, pp. 978–980, arXiv: `astro-ph/0408371`.

Semenov, V. S. and Bernikov, L. V. (1991), Magnetic flux tubes - Nonlinear strings in relativistic magnetohydrodynamics, *Astrophysics and Space Science* , **184**, pp. 157–166.

Stuchlík, Z. and Kološ, M. (2012a), Acceleration of string loops in the Schwarzschild-de Sitter geometry, *Phys. Rev. D* , **85**(6), 065022, arXiv: `1206.5658`.

Stuchlík, Z. and Kološ, M. (2012b), String loops in the field of braneworld spherically symmetric black holes and naked singularities, *Journal of Cosmology and Astroparticle Physics* , **10**, 008, arXiv: `1309.6879`.

Stuchlík, Z. and Kološ, M. (2014a), String loop oscillation model fitting frequency of kHz quasiperiodic oscillations in the low-mass X-ray binary XTE J1701-407, *submitted to CLAQG*.

Stuchlík, Z. and Kološ, M. (2014b), String loops oscillating in the field of Kerr black holes as a possible explanation of twin high-frequency quasiperiodic oscillations observed in microquasars, *Phys. Rev. D* , **89**(6), 065007, arXiv: `1403.2748`.

Stuchlík, Z. and Schee, J. (2012), Observational phenomena related to primordial Kerr superspinars, *Classical and Quantum Gravity*, **29**(6), 065002.

Török, G. (2009), Reversal of the amplitude difference of kHz QPOs in six atoll sources, *Astronomy and Astrophysics* , **497**, pp. 661–665.

Török, G., Abramowicz, M. A., Kluźniak, W. and Stuchlík, Z. (2005), The orbital resonance model for twin peak kHz quasi periodic oscillations in microquasars, *Astronomy and Astrophysics* , **436**, pp. 1–8.

Török, G., Bakala, P., Horák, J., Bursa, M., Stuchlík, Z., Šrámková, E. and Čech, P. (2014), On high frequency QPOs in attoll and Z sources, *in preparation*.

Török, G., Bakala, P., Stuchlík, Z. and Čech, P. (2008), Modeling the Twin Peak QPO Distribution in the Atoll Source 4U 1636-53, *Acta Astronomica* , **58**, pp. 1–14.

Török, G., Bakala, P., Šrámková, E., Stuchlík, Z. and Urbanec, M. (2010), On Mass Constraints Implied by the Relativistic Precession Model of Twin-peak Quasi-periodic Oscillations in Circinus X-1, *The Astrophysical Journal* , **714**, pp. 748–757, arXiv: `1008.0088`.

Török, G. and Stuchlík, Z. (2005), Radial and vertical epicyclic frequencies of Keplerian motion in the field of Kerr naked singularities. Comparison with the black hole case and possible instability of naked-singularity accretion discs, *Astronomy and Astrophysics* , **437**, pp. 775–788, arXiv: `astro-ph/0502127`.

Tursunov, A., Kološ, M., Ahmedov, B. and Stuchlík, Z. (2013), Dynamics of an electric current-carrying string loop near a Schwarzschild black hole embedded in an external magnetic field, *Phys. Rev. D* , **87**(12), 125003.

Tursunov, A., Kološ, M., Stuchlík, Z. and Ahmedov, B. (2014), Acceleration of electric current-carrying string loop near a Schwarzschild black hole immersed in an asymptotically uniform magnetic field, *Phys. Rev. D* , **90**(8), 085009, arXiv: `1409.4536`.

Urbanec, M., Miller, J. C. and Stuchlík, Z. (2013), Quadrupole moments of rotating neutron stars and strange stars, *Monthly Notices of the Royal Astronomical Society* , **433**, pp. 1903–1909, arXiv: `1301.5925`.

van der Klis, M. (2006), *Rapid X-ray Variability*, pp. 39–112.

Vilenkin, A. and Shellard, E. P. S. (1995), *Cosmic Strings and Other Topological Defects*.

Wang, D. H., Chen, L., Zhang, C. M., Lei, Y. J. and Qu, J. L. (2013), Constraints on kilohertz quasi-periodic oscillation models and stellar equations of state from SAX J1808.4-3658, Cyg X-2 and 4U 1820-30, *Monthly Notices of the Royal Astronomical Society* , **435**, pp. 3494–3499, arXiv: `1310.4037`.

Wang, D. H., Chen, L., Zhang, C. M., Lei, Y. J. and Qu, J. L. (2014), Statistical properties of twin kHz QPO in neutron star LMXBs, *Astronomische Nachrichten*, **335**, pp. 168–177, arXiv: `1301.5478`.

Witten, E. (1985), Superconducting strings, *Nuclear Physics B*, **249**, pp. 557–592.

Proceedings of *RAGtime 10–13, 15–17/20–22/15–17/14–16 September, 2008/2009/2010/2011, Opava, Czech Republic* 209
Z. Stuchlík, G. Török and T. Pecháček, editors, Silesian University in Opava, 2014, pp. 209–229

Modelling steep radial emissivity in relativistic iron lines from black-hole accretion discs

Jiří Svoboda,[1,2,a] Michal Dovčiak,[1] Vladimír Karas[1] and René Goosmann[3]

[1]Astronomical Institute, Academy of Sciences, Boční II. 1401, CZ-141 31 Prague, Czech Republic
[2]European Space Astronomy Centre of ESA, Spain
[3]Strasbourg Observatory, France
[a]jiri.svoboda@asu.cas.cz

ABSTRACT
X-ray spectroscopy of active galaxies and black hole binaries provides an opportunity to explore the innermost regions of black hole accretion discs. Some of the recent measurements have revealed a very steep radial decrease of the disc reflection emissivity, especially in the central region, suggesting the disc-irradiating corona to be compact and very centrally localised. We discuss whether the special conditions on the corona properties are indeed required, and / or whether the steep radial emissivity could be an artefact of model assumptions. The inter-dependencies and possible degeneracies between the radial emissivity index and other parameters of the relativistic reflection model are studied. A set of simulations using a preliminary response matrix for a planned Athena mission is performed for this purpose. We show that the measurements of the radial emissivity are indeed degenerate with some model assumptions and parameters, even for more sensitive spectra than for those available from current X-ray missions. We also realise that the radial dependence of the disc ionisation might be another factor which can account for the steep radial emissivities.

Keywords: black holes – accretion discs – relativistic iron lines

1 INTRODUCTION

Relativistic iron lines in X-ray spectra of active galactic nuclei and black hole binaries represent one of the most suitable opportunities to measure the angular momentum of accreting black holes, see e.g. Reynolds and Nowak (2003) for a review. Spin measurements are influenced by the geometry of the disc-illuminating corona and local properties of the disc that affect the re-processing and re-emission of the incident photon. Usually, the current iron line models (Laor, 1991; Dovčiak et al., 2004; Beckwith and Done, 2004; Brenneman and Reynolds, 2006) employ a simplified approach where the complex relationship between the disc illumination and consequent emission is approximated by a simple or broken power-law dependence on radial coordinate, and local angular emissivity profile is assumed to be either isotropic or limb-darkened.

In our recent paper (Svoboda et al., 2009), we investigated the effect of different emission angular directionality on the spin measurements. Here, we extend our analysis by study of a possible degeneracy between the assumption of the angular distribution and model parameters describing the radial profile of the emissivity. More generally, we investigate further effects which might account for the radial emissivity profile, namely the localisation of the corona and the radial structure of the disc ionisation.

The intrinsic disc emissivity is naturally expected to decrease with the growing distance. The temperature of the disc decreases as r^{-3} (Shakura and Sunyaev, 1973; Novikov and Thorne, 1973). Therefore, one of the naive assumptions is to assume the same dependence for the reflection, i.e. the reflection emissivity $\epsilon \propto r^{-q}$, where $q = 3$. The simplest physical picture is that of a corona uniformly sandwiching the disc. The more energetic photons are injected in the innermost regions, and so, more intense irradiation of the disc occurs there.

However, non-thermal coronal emission does not necessarily need to behave in the same way as the thermal dissipation of the disc. The interaction between the disc and the corona is more complicated, including the radiation and magnetic processes (see e.g. Haardt and Maraschi, 1991; Czerny and Goosmann, 2004; Goosmann et al., 2006; Różańska et al., 2011). Especially when the magnetic field is considered, the resulting profile might be as steep as e.g. r^{-5} (Kawanaka et al., 2005).

Steep radial emissivities were indeed reported in several sources, in active galaxies like MCG -6-30-15 (Fabian et al., 2002; Vaughan and Fabian, 2004; Miniutti et al., 2007), 1H0707-495 (Fabian et al., 2009; Zoghbi et al., 2010; Dauser et al., 2012), IRAS 13224-3809 (Ponti et al., 2010) as well as in black hole binaries, e.g. XTE J1650-500, GX 339-4 (Miller, 2007). In order to provide a physical picture of the steep radial emissivity in MCG -6-30-15, Wilms et al. (2001) invoke strong magnetic stresses that should act in the innermost region of the system. This should correspond to the enhanced dissipation of a considerable amount of energy in the accretion disc at small radii. If the magnetic field lines thread the black hole horizon, the dissipation could be triggered by magnetic extraction of the black hole rotational energy, perhaps via Blandford–Znajek effect (Blandford and Znajek, 1977), but it could be also supplemented by a rather efficient slowing of the rotation, as also seen in recent GRMHD simulations (e.g. Penna et al., 2010). The efficiency of the competing processes still needs to be assessed.

Martocchia et al. (2000) examined whether the required steep emissivity law as well as the predicted equivalent width of the cold reflection line of iron and the Compton reflection component can be reproduced in a phenomenological (lamp-post) model where the X-ray illuminating source is located on the common symmetry axis of the black hole and the equatorial accretion disc. These works suggested that the radial emissivity function of the reflection component steepens when the height parameter of the primary irradiation source decreases. The enhanced anisotropy of the primary X-rays was identified as a likely agent acting in this process. The emissivity in the XMM-Newton spectrum of MCG -6-30-15 was successfully reproduced with the lamp-post geometry (Martocchia et al., 2002; Miniutti et al., 2003).

In some cases, like in the spectrum of 1H0707-495, the measured radial emissivity in the innermost region $q \approx 7$ (Fabian et al., 2009; Wilkins and Fabian, 2011) is, however, steeper than any current theoretical model predicts. In this paper, we will discuss some possible explanations of detecting such steep radial emissivities. To this end, we explore several simple test models and analyse them with the simulated data.

2 DATA SIMULATION

We used a preliminary response matrix[1] for the planned X-ray mission Athena (Nandra, 2011) in our various simulations. There are several reasons for this choice. First of all, this mission has been proposed only recently and ongoing scientific discussions on feasible applications are timely. We would like to show by this analysis that in the case of approval the Athena mission will be suitable for studying reflection features from the innermost accretion discs around black holes. The main aim of these simulations is to constrain possible degeneracies among different parameters of the relativistic reflection model. For this purpose, Athena allows for a more sensitive analysis than is possible with the spectra from current X-ray missions. Using a sensitive response planned for the future mission allows us to find degeneracies which are not only adherent to the current data, but which also will not be resolved with the on-coming X-ray detectors.

We performed the spectral analysis between 2–10 keV energy range where one of the most prominent reflection feature, the iron Kα line, occurs. We re-binned the response matrix by a factor of 10 between channels 2700 and 8800 (2–10 keV), the other channels were not used. We used Xspec (Arnaud, 1996), version 12.6.0ab for the spectral fitting. We used the most recent version of KY code (Dovčiak et al., 2004) which includes the lamp-post geometry (Dovčiak et al., in prep.). The flux of the model was chosen to be similar to that of bright Seyfert galaxies, i.e. $\approx 3 \times 10^{-11}\,\mathrm{ergs{\cdot}cm^{-2}\,s^{-1}}$ (Nandra et al., 2007). The simulated observation time was always 100 ks, which is a typical value for average exposure time of AGN observed with the current X-ray satellites.

3 LAMP-POST SCHEME

First, we investigate how the radial emissivity depends on the geometry of the corona. If the corona is localised the illumination of the disc decreases with the growing distance from the source in a particular way determined by the position of the corona and by the gravitational pull of the central black hole. The configuration when the corona is very compact and located just above the black hole, known also as the lamp-post scheme, has been studied as a simple disc-corona scenario by Matt et al. (1991); George and Fabian (1991). In a physical picture, the source above the black hole can be imagined, e.g. as a base of a jet.

In this scenario the irradiation far from the source radially decreases as r^{-3}. In the central region, the relativistic effects – energy shift, aberration and light-bending – influence the disc illumination, and thus shape the reflection spectra of black hole accretion discs (Miniutti and Fabian, 2004). As a result, the different parts of the disc are irradiated with different

[1] up-to-date to 9/5/2011, ftp://ftp.rssd.esa.int/pub/athena/09052011_Responses

Table 1. The inner radial emissivity index $q_{\rm in}$, and the break radius $r_{\rm b}$ inferred for different heights and directionalities in the lamp-post model.

$a = 0.94$

	numerical		limb brightening		isotropic		limb darkening	
$h[r_g]$	$q_{\rm in}$	$r_{\rm b}$	$q_{\rm in}$	$r_{\rm b}$	$q_{\rm in}$	$r_{\rm b}$	$q_{\rm in}$	$r_{\rm b}$
1.5	$4.8^{+0.2}_{-0.1}$	$6.1^{+0.2}_{-0.2}$	$4.5^{+0.1}_{-0.1}$	$6.4^{+0.2}_{-0.2}$	$5.0^{+0.4}_{-0.1}$	$6.0^{+0.3}_{-0.2}$	$5.3^{+0.1}_{-0.1}$	$5.7^{+0.2}_{-0.1}$
3.0	$3.3^{+0.1}_{-0.1}$	$6.3^{+1.9}_{-1.1}$	$3.2^{+0.3}_{-0.2}$	$8.0^{+3.4}_{-2.6}$	$3.2^{+0.1}_{-0.1}$	15^{+10}_{-3}	$3.3^{+0.1}_{-0.1}$	20^{+70}_{-5}
10	$1.3^{+0.1}_{-0.2}$	16^{+1}_{-1}	$2.3^{+0.1}_{-0.1}$	55^{+9}_{-10}	$2.3^{+0.2}_{-0.1}$	48^{+5}_{-7}	$2.5^{+0.1}_{-0.1}$	60^{+15}_{-15}

intensity, making the emissivity profile in reflection models distinct from the standard value of $q = 3$. If the height of the source is sufficiently close to the black hole event horizon the light bending implies higher irradiation of the innermost region compared to the outer parts of the disc. In the most extreme scenario, when the source is moving towards the black hole, the Doppler boosting might increase this effect. However, there is no observational evidence for such an inflow of the matter perpendicular to the disc plane, while outflows in the form of a jet are observed in many sources (e.g. Merloni et al., 2003).

Further, we consider the stationary lamp-post source and investigate the radial emissivity profile of the disc reflection radiation for different heights of the source. The fully relativistic code including the azimuthal dependence of the reflected emission coming from a neutral disc was employed. The radial emissivity profiles are shown in Dovčiak et al. (in prep.). Here, we study whether it is possible to approximate the radial emissivity in the lamp-post model by a simplified profile in the form of a broken power-law, as this is usually used in current modelling of the data.

Figures 1 and 2 show contour plots for the radial emissivity index and the spin, and the break radius, respectively. The fiducial value of the spin was set to $a = 0.94$ (indicated by the dashed line). The other parameters of the seed model were the photon index of the primary power-law radiation $\Gamma = 1.9$, the inclination of the disc $i = 30$ deg, the inner radius $r_{\rm in} = r_{\rm ms}$, and the outer radius $r_{\rm out} = 400\,r_{\rm g}$. The data were modelled by the power-law component with the fixed value of the photon index and the KYRLINE model for the iron line with the adopted broken power-law for the radial emissivity. Different angular directionality was used (see the next section for further details). The best-fit parameters are summarised in Table 1. In the contour calculations, only the two interesting parameters were allowed to vary. Others were fixed to their default or best-fit (in the case of break radius) values.

Figures 6–8 show the same but for different parameters. The steep radial emissivity is reached only if the primary source is at a very low height above the black hole where the strong gravity considerably bends the light rays of the primary radiation. Very steep radial emissivities detected in the spectra would imply that the black hole must be rapidly rotating, and moreover, the source would have to be very bright because the radiation would lose its intensity on its way out of the deep gravitational well.

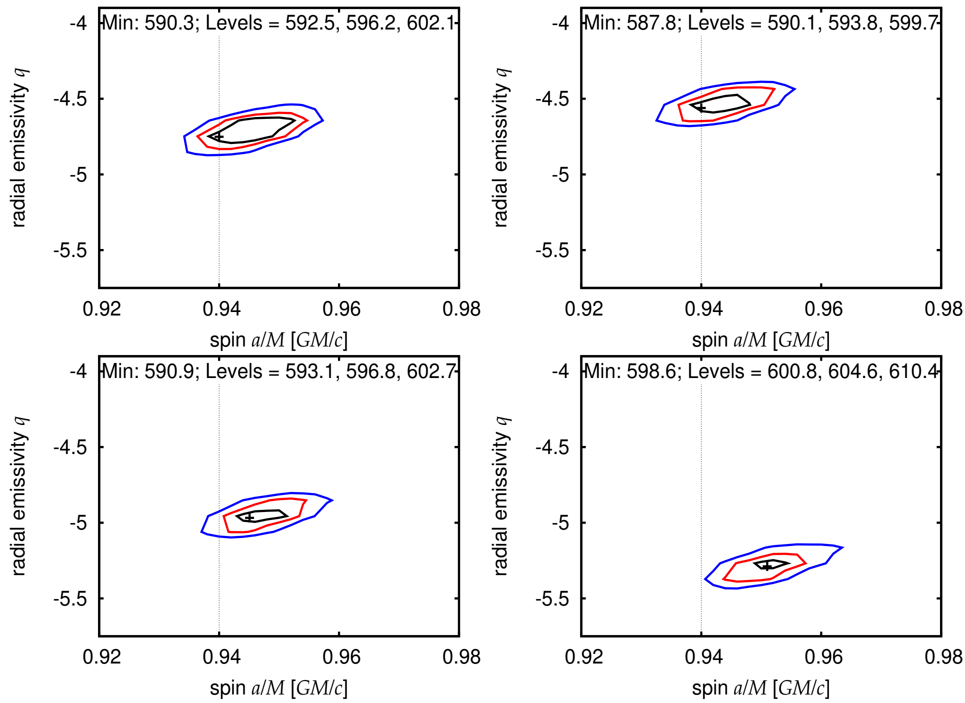

Figure 1. Contour plots of the spin a and the radial emissivity parameter q. The data were generated with the lamp-post model with the height $h = 1.5\,r_g$. The default value of the spin was $a = 0.94$, which is indicated by a dashed line in the graph. Different prescriptions for the angular emissivity were used: *Top left:* angular emissivity from numerical calculations. *Top right:* limb brightening. *Bottom left:* isotropic. *Bottom right:* limb darkening. The χ^2 values corresponding to the best fit (minimum) and to the 1σ, 2σ, 3σ levels are indicated in the text legend.

4 INTERPLAY BETWEEN THE RADIAL AND ANGULAR EMISSIVITY PROFILE

When fitting the data, the local intensity of the re-processed radiation emitted from the disc is often assumed to be divided into two separate parts – the radial and angular dependence. The latter one characterises the emission directionality. However, due to large rotational velocity of the disc and the strong gravity near the black hole, the photons that reach the observer are emitted under different angles at different locations. Therefore, the angular part of the emissivity depends on radius as well, and the above separation is not valid. The relativistic effects, aberration and light bending, cause that the emission angle in the innermost region is always very high (almost 90 degrees with respect to the disc normal) – see Appendix C in Dovciak (2004), or Fig. 3 in Svoboda et al. (2009). Although it is not an axi-symmetric problem, the almost radial decrease of the emission angle is apparent, which invokes the link between the radial and angular emissivity (Beckwith and Done, 2004; Svoboda et al., 2009).

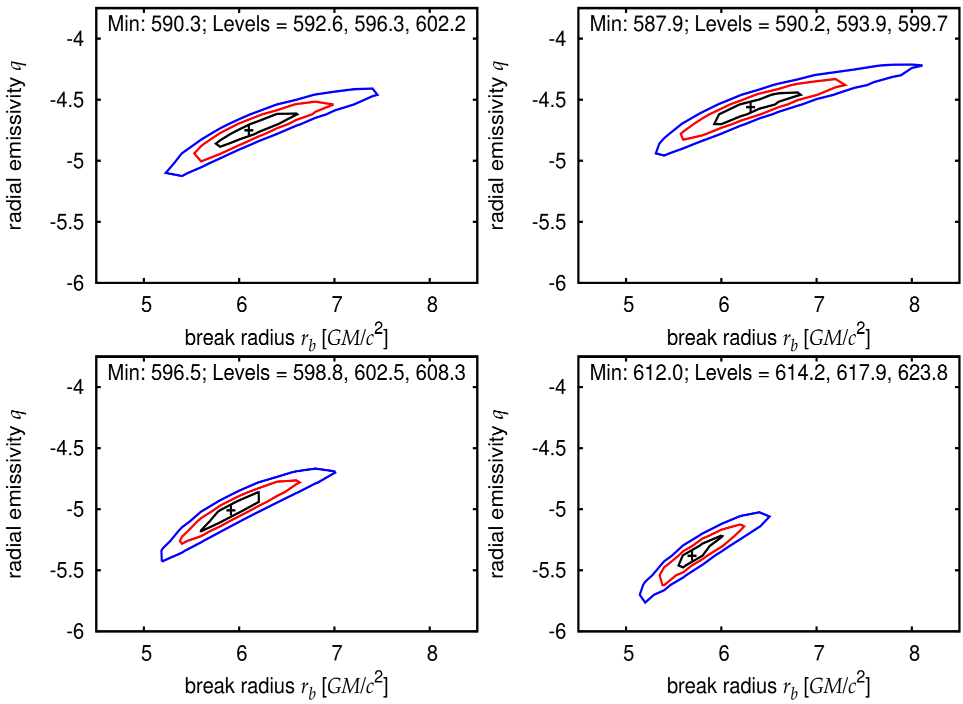

Figure 2. Contour plots of the radial emissivity and the break radius for the height $h = 1.5\,r_g$. The legend is the same as in Fig. 1. The spin and the inclination were frozen to their default values.

Hence, we used different assumptions about the directionality:

(1) our numerical computations[2] (Svoboda et al., 2009),
(2) limb brightening $I(\mu_e) \approx \ln(1 + \mu_e^{-1})$ (Haardt, 1993),
(3) isotropic,
(4) limb darkening $I(\mu_e) \approx 1 + 2.06\mu_e$ (Laor, 1991),

where μ_e is the cosine of the emission angle. The simulated data were created with our numerical model of the directionality calculated with the NOAR code (Dumont et al., 2000). Free-free absorption, the recombination continua of hydrogen- and helium- like ions, the direct and inverse Compton scattering were taken into account (see Svoboda et al., 2009, for more details).

The fact that we get different results confirms that constraining the radial emissivity is influenced by the prescription for the angular emissivity. Steeper radial emissivities are required in the best fits with limb darkening. This emissivity law is widely used in the reflection models, however, it is somewhat in contradiction with several models of X-ray illuminated disc atmospheres (Ghisellini et al., 1994; Zycki and Czerny, 1994; Goosmann

[2] integrated over incident angles

et al., 2006; Różańska et al., 2011). Its application causes an appreciable underestimation of the innermost flux. The radial emissivity parameter must then be set to an artificially steeper value in order to compensate this loss of the counts from the central region where the emission angle is grazing.

5 RADIALLY STRUCTURED IONISATION OF THE DISC

The interplay between the radial and angular emissivity shows that the steep radial emissivity in the observational data might be caused by an invalid model assumption. Yet, there is another frequently used assumption in the reflection scenario that can contribute to this effect as well – the constant ionisation over the whole surface of the disc. The intensity of the disc irradiation, whether it is approximated by a (broken) power-law decrease or by a lamp-post illumination in curved space-time, decreases with the radius. Therefore the ionisation of the disc surface may respond accordingly, as suggested before by Matt et al. (1993).

Ballantyne et al. (2001) investigated the importance of the photo-ionisation of the disc surface in active galactic nuclei. The presence of ionised reflection features in their X-ray spectra was reported in several sources (see Ballantyne et al., 2011, and references therein). The photo-ionisation was also suggested as a possible explanation for non-detection of the spectral imprints of the relativistically smeared reflection (Reynolds et al., 2004; Svoboda et al., 2010; Bhayani and Nandra, 2011; Brenneman et al., 2012). The radially dependent ionisation was discussed recently with the existing data by Zhou et al. (2011).

More generally, the ionisation of the disc surface depends on several other physical quantities like density, vertical structure, thermal heating etc. (see e.g. Nayakshin and Kallman, 2001; Różańska et al., 2002; Goosmann et al., 2007 and references therein). A detailed description of the disc ionisation is beyond the scope of this paper. Here, we simply suppose that the radial dependence of the ionisation may be relevant, as a natural consequence of the radial dependence of the disc illumination by the primary radiation. Thus, we suppose that the accretion disc around a black hole might be more ionised in the central region and colder in the outer regions.

5.1 Test case: two ionisation zones

Currently, no model can consistently describe the radial structure of the disc ionisation. Hence, as a test case, we used two REFLIONX models (Ross and Fabian, 2005) with a different ionisation state convolved with KY model (Dovčiak et al., 2004), corresponding to different emission regions on the disc. The inner disc ionisation was set to $\xi = 50, 80, 100, 130, 150, 200\,\mathrm{ergs{\cdot}cm\,s^{-1}}$, respectively, and the outer disc ionisation was $\xi = 30\,\mathrm{ergs{\cdot}cm\,s^{-1}}$. The boundary radius was set to $r_{\mathrm{boundary}} = 4\,r_{\mathrm{g}}$. The innermost radius coincides with the marginally stable orbit, and the outer radius was set to $400\,r_{\mathrm{g}}$. The spin value was chosen to be $a = 0.94$, i.e. $r_{\mathrm{ms}} \approx 2\,r_{\mathrm{g}}$. The inclination angle was chosen to 30 deg which is a typical value for the inclination of Seyfert 1 galaxies. The primary power-law radiation photon index and normalisation were set to $\Gamma = 1.9$ and $K_{\Gamma} = 10^{-3}$. We assumed isotropic irradiation, i.e. disc-sandwiching corona scenario. The standard value,

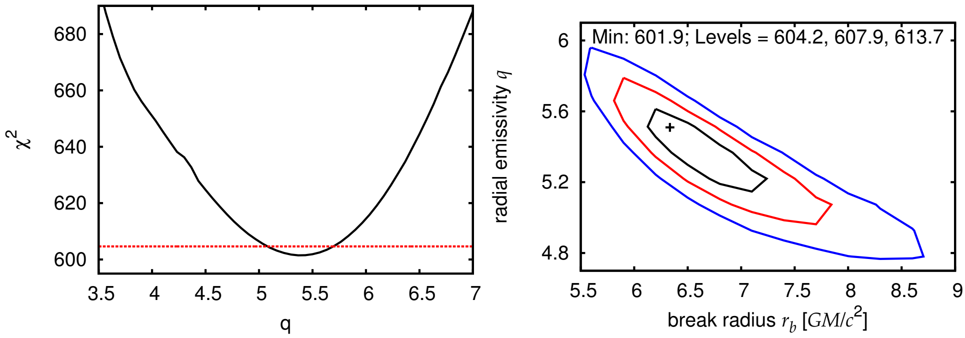

Figure 3. Left: Dependence of the fit-goodness on the radial emissivity parameter of the single reflection model. **Right:** The contour graph between the radial emissivity and the break radius. The default data were created by the two-reflection model with the inclination $i = 30$ deg, the break radius $r_{\mathrm{b,def}} = 4\,r_{\mathrm{g}}$, and the ionizations $\xi_{\mathrm{in}} = 130$ and $\xi_{\mathrm{out}} = 30$.

Table 2. Resulting parameter values of the single reflection model applied to the data simulated by a "two-reflection" model.

ξ_{in} / ξ_{out} (def.)	q	r_{b}	ξ	χ^2/ν
50 / 30	$4.04^{+0.76}_{-0.48}$	$6.1^{+1.7}_{-1.2}$	28^{+11}_{-6}	544/604
80 / 30	$4.70^{+0.73}_{-0.87}$	$6.6^{+0.8}_{-0.9}$	25^{+8}_{-3}	542/604
100 / 30	$4.88^{+0.36}_{-0.69}$	$6.1^{+1.2}_{-0.6}$	23^{+3}_{-2}	548/604
130 / 30	$4.93^{+0.20}_{-0.26}$	$7.1^{+0.7}_{-0.6}$	24^{+3}_{-2}	569/604
150 / 30	$5.51^{+0.19}_{-0.43}$	$6.3^{+0.8}_{-0.4}$	21^{+1}_{-1}	602/604
200 / 30	$4.95^{+0.45}_{-0.15}$	$8.3^{+0.8}_{-1.0}$	21^{+1}_{-5}	652/604

Table 3. Resulting parameter values of the single reflection model applied to the data simulated by a "complex" reflection model.

parameter	default value	fit value	error
photon index	1.9	2.10	0.05
power-law norm.	10^{-3}	2.55×10^{-3}	0.15×10^{-3}
spin	0.94	0.94	f
inclination [deg]	30	30	f
inner rad. emissivity	3	4.2	0.1
break radius [r_{g}]	–	35	20
ionisation [ergs·cm s^{-1}]	different	40	10
refl. norm.	10^{-5}	2×10^{-4}	0.5×10^{-4}
fit goodness	$\chi^2/\nu \approx 0.96$	$\chi^2/\nu \approx 1.13$	–

Note: the sign 'f' in the error column means that the values were frozen during the fitting procedure.

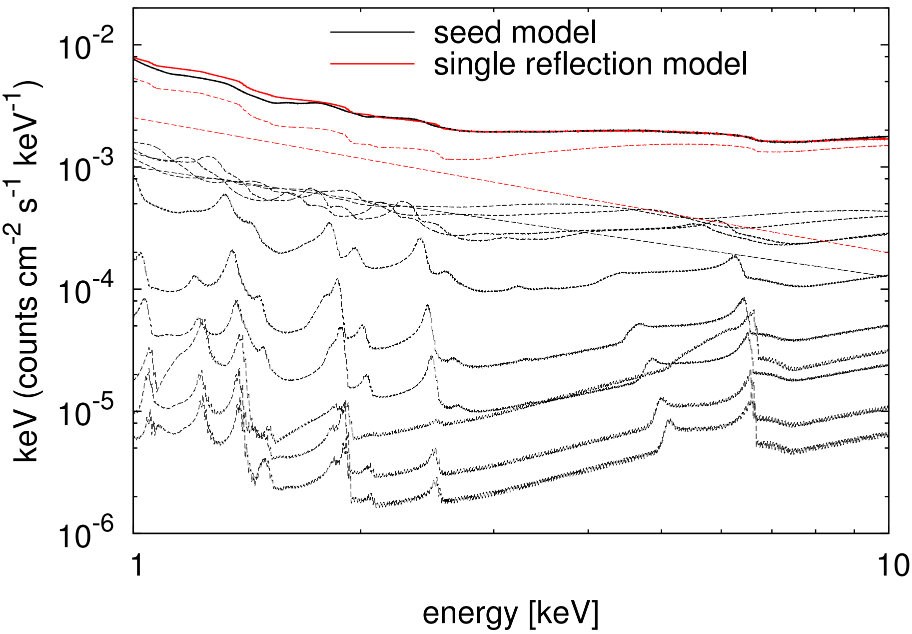

Figure 4. Comparison of the 'complex' and the 'single' ionisation reflection model. The solid lines show the total model fluxes while the dashed ones are their components. The straight dashed lines correspond to the power-law continua irradiating the disc. Black: the seed 'complex' reflection model and its components. The iron line around 6 keV may be used as a diagnostic of the individual components. The more smeared and red-shifted iron lines belong to the more ionised innermost parts of the disc. The cold reflection from the outer disc (17– 400 r_g) is the one with the most blue-shifted peak, the fourth weakest component at 10 keV. Red: the best-fit single-ionisation reflection model. See the main text for more details.

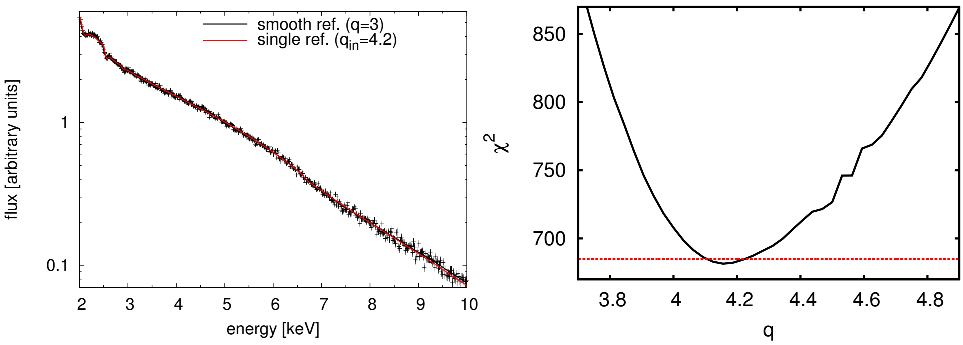

Figure 5. *Left:* The degeneracy between the radially-structured ionisation and the radial emissivity for the reflected radiation. Black: data generated with the radially decreasing ionisation, red: the best fit with a single ionisation but steeper radial emissivity. *Right:* Dependence of the fit goodness on the radial emissivity index for the single-ionisation reflection model.

$q = 3$, was adopted for the radial emissivity index. For the reflection components, we used solar iron abundances and normalisation $K_R = 10^{-5}$, fixed to the same value for each component.

We generated the data by this model in the same way as described in Section 2. Then we fit the data in the 2–10 keV energy range with a model consisting of only a power-law continuum and a single reflection component with a broken power-law radial emissivity. The photon index, the inner radial emissivity index, the break radius, the ionisation and the normalisations were the only parameters which were allowed to vary during the fitting procedure. The best-fit values and the errors are summarised in Table 2. A significant steepening of the radial emissivity occurs already for a relatively small ionisation gradient. The highest value of the radial emissivity index, $q \approx 5.5$, was found for $\xi_{\rm in} = 150$ ergs·cm s^{-1}. The dependence of the fit goodness and the contours between the radial emissivity and the break radius are shown in Fig. 3 for this case, and in the Appendix (Figs. 9–14) for the other parameters.

For larger values than $\xi_{\rm in} \approx 200$, the ionisation component becomes much more significant than the cold reflection, dominates in the total spectrum, and the interplay between the ionised and the cold component vanishes. This is due to the fact that the efficiency of the reflection from the ionised surface is much higher (Ross and Fabian, 2005). Table 2 also shows the goodness of the best fit. The resulting χ^2-values increase with the larger ionisation gradient in the simulated data. This suggests that the radially structured ionisation cannot be simply modelled in the 2–10 keV energy range by a single-ionisation component with the broken power-law radial emissivity and with the assumption of the existence of the outer disc ($r_{\rm out} = 400\,r_{\rm g}$) where the radial emissivity decreases as r^{-3}.

Rather surprising result is that the best-fit value of the single ionisation parameter has always a lower value than the default one for the outer-disc ionisation. Also, the value of the break radius of the radial emissivity is in all the fits higher than the value of the boundary radius used in the simulations.

5.2 Smooth decrease of ionisation

The previous analysis showed that ionisation gradient plays an important role in the total shape of the reflection spectra. Further, we considered a rather smooth radial decrease of the disc ionisation. We used 10 regions with decreasing ionisation: 200, 170, 140, 110, 80, 50, 30, 20, 15, 10 ergs·cm s^{-1}, with the boundaries at the radii: 3, 4, 5, 7, 9, 11, 13, 15, 17 $r_{\rm g}$, respectively. The other parameters were the same as before. We call this model as a "complex" reflection model, and it is plotted in the 1–10 keV energy range in Fig. 4.

The data were generated by this model in the same way as described in Section 2, and then fitted in the 2–10 keV energy range with a model consisting of only a power-law continuum and a single reflection component with a broken power-law radial emissivity. The photon index, the inner radial emissivity index, the break radius, the ionisation and the normalisations were the only parameters which were allowed to vary during the fitting procedure. The best-fit model is compared to the seed model in Fig. 4.

Figure 5 (left panel) shows how well the single-reflection model suits to the data in the 2–10 keV energy range. This clearly reveals the degeneracy between the radially-structured ionisation and the radial emissivity of the re-processed radiation smeared by the relativistic effects. The radial emissivity index is required to be significantly steeper in the single-reflection model, $q \geq 4$, whereas with the standard value, $q = 3$, the fit gives high $\chi^2/\nu \approx 3.1$. See also the right panel of Fig. 5. The best-fit parameters are summarised in Table 3. In addition to the steepening of the radial emissivity, the photon index of the primary power-law was found to be significantly larger. It changed from the value $\Gamma = 1.9$ to $\Gamma = 2.1$. This softening of the primary power-law is due to the different slope of the ionised reflection continuum.

6 DISCUSSION

We addressed steep radial emissivities recently detected in the reflection components of the X-ray spectra of active galaxies and black-hole binaries. We investigated some possible explanations. To this end, we performed several simulations to reveal the degeneracies of the radial emissivity with other parameters and intrinsic assumptions of the relativistic reflection model.

6.1 Lamp-post scenario

The steep radial emissivity may be related to the properties of the disc-illuminating corona as suggested before by Wilms et al. (2001). The geometry of the emitting region certainly plays a significant role. A very centrally localised source at a low height above the black hole horizon would irradiate the disc mainly in its central region. The illumination in this area is greatly enhanced due to the gravitational light-bending effect (Miniutti and Fabian, 2004; Wilkins and Fabian, 2011, Dovčiak et al., in prep.).

To achieve steep radial emissivity, which is assumed to be proportional to the illumination, the source must be sufficiently close to the black hole. However, in this case the primary emission has to be extremely bright because only a small fraction would overcome the strong gravitational pull of the black hole and reach the observer (see Fig. 2 in Dovčiak et al., 2011). The importance of these effects drops quickly with the height. Already at heights $h \gtrsim 3\, r_{\mathrm{g}}$ the radial emissivity profile is similar to the simple power-law with the standard value ($q = 3$). For even larger heights, the irradiation profile is more complicated (see Fig. 3 and 4 in Dovčiak et al., 2011). It decreases steeply only very close to the black-hole horizon, then becomes rather flat ($q < 3$) still in the inner parts of the disc and finally reaches the standard value far from the centre.

Although this effect may steepen the radial emissivity significantly, a very large value, $q \approx 7$, as observed by Fabian et al. (2009); Wilkins and Fabian (2011) has not been reached in our calculations (Dovčiak et al., in prep.) even when the height was set very close to the black hole. We therefore proposed additional explanation.

6.2 Angular directionality

For the angular emissivity, the limb darkening law is frequently used. Several simulations, however, suggest that the directionality is opposite to limb darkening (see e.g. Różańska et al., 2011 and references therein). The emission angle in the innermost region of the disc is always very high due to the strong aberration. The flux contribution from this region is therefore underestimated by models with limb darkening if the angular emissivity is indeed different. This effect could lead to an approximately 20 % overestimation of the spin or the inner radial emissivity parameter. Svoboda et al. (2009) re-analysed the

XMM-Newton observation of MCG -6-30-15 and showed that the radial emissivity might be a more sensitive parameter to the angular directionality than the spin. This is especially true when the spin value itself is very high (close to one).

6.3 Radially structured ionisation

We also discussed the impact of the probable radial dependence of the disc surface ionisation. The disc illumination by corona is commonly assumed to be stronger in the innermost regions. Therefore, we simply assumed that the ionisation is higher at the innermost region as well, and decreases with the radius. We have not considered other aspects which affect the ionisation structure of the disc such as the density profile, vertical structure, and thermal processes (the last one especially relevant for the stellar-mass black hole binaries). With our simple assumption, we performed several tests with the simulated data using different initial values of the model parameters.

The broad iron-line profile is formed by two competing effects – the ionisation that shifts the rest energy of the line to higher values and the gravitational redshift with the opposite impact. The latter effect prevails sufficiently close to the black hole, and so the line is still shifted downwards from the rest neutral iron line energy in the more ionised central regions. The contribution to the reflection spectral component is higher from the more ionised part of the disc, which is located closer to the centre. Thus, ionisation contributes to the red wing of the broad relativistic line, as limb brightening and steep radial emissivity do. Consequently, when a simplified model with a single ionisation is used for fitting the data it may lead to an underestimation of the flux from the innermost regions.

In the presented analysis, we used an assumption of the fixed normalisations between the individual REFLIONX components. The ionisation parameter is defined there as $\xi = 4\pi F_{\mathrm{inc}}/n_{\mathrm{H}}$, where F_{inc} is the incident flux, and n_{H} is the hydrogen number density. This means that the higher ionisation parameter implies larger incident flux and consequently, also the more intense reflected flux. The mutual dependence between the irradiating flux and the ionisation parameter can be intuitively expected. However, a simple proportionality will have to be eventually replaced by a more complicated relation taking into account the actual solution of the radiation reprocessing of the incident flux in the disc medium as well as the effects of general relativity.

The contribution from the ionised reflection is thus larger for a given value of the normalisation. The higher radial emissivity parameter, q, found in the fitting by the single-reflection model is partly due to higher ionising incident flux and partly due to a different shape of the ionised reflection component. As a next step, we intend to fix the normalisation factors in a self-consistent way with the assumed incident flux that decreases smoothly with the radius. We also plan to take the radial dependence of the density into account in the forthcoming analysis.

7 CONCLUSIONS

The very steep radial emissivity of the disc reflection, which has been recently detected in the X-ray spectra of active galactic nuclei and black hole binaries, may be explained by geometrical properties of the disc-illuminating corona, by radially structured ionisation and/or by use of an improper model assumption about the angular directionality. The first puts rather extreme requirements on the corona. It needs to be very bright and occur at a very low height above the black hole. We realised that the radial decrease of the disc ionisation may account for the radial-emissivity steepness equally well as the assumption of the centrally localised corona. If the ionisation decreases with growing distance from the black hole, the contribution from the innermost region is enhanced due to the larger reflection efficiency. The reported very high values for the radial emissivity in several sources, like $q \approx 7$, suggest that all of the discussed effects may take part together. Due to degeneracy it is difficult to distinguish among these effects from the spectral analysis of real data, and therefore, more theoretical attempts to constrain the disc-corona interactions are desirable. Development of a model with the self-consistent calculations of the disc surface ionisation that would depend on the irradiation intensity should be the next step in this research.

ACKNOWLEDGEMENTS

The present work was supported by the Czech Grant GAČR 14-20970P and the EU 7th Framework Programme No. 312789 “StrongGravity”. JS thanks Prashin Jethwa for useful comments and also some language corrections.

REFERENCES

Arnaud, K. A. (1996), XSPEC: The First Ten Years, in G. H. Jacoby and J. Barnes, editors, *Astronomical Data Analysis Software and Systems V*, volume 101 of *Astronomical Society of the Pacific Conference Series*, p. 17.

Ballantyne, D. R., McDuffie, J. R. and Rusin, J. S. (2011), A Correlation between the Ionization State of the Inner Accretion Disk and the Eddington Ratio of Active Galactic Nuclei, *Astrophys. J.*, **734**, 112.

Ballantyne, D. R., Ross, R. R. and Fabian, A. C. (2001), X-ray reflection by photoionized accretion discs, *Monthly Notices Roy. Astronom. Soc.*, **327**, pp. 10–22, arXiv: `astro-ph/0102040`.

Beckwith, K. and Done, C. (2004), Iron line profiles in strong gravity, *Monthly Notices Roy. Astronom. Soc.*, **352**, pp. 353–362, arXiv: `astro-ph/0402199`.

Bhayani, S. and Nandra, K. (2011), On the apparent absence of broad iron lines in Seyfert galaxies, *Monthly Notices Roy. Astronom. Soc.*, **416**, pp. 629–636.

Blandford, R. D. and Znajek, R. L. (1977), Electromagnetic extraction of energy from Kerr black holes, *Monthly Notices Roy. Astronom. Soc.*, **179**, pp. 433–456.

Brenneman, L. W., Elvis, M., Krongold, Y., Liu, Y. and Mathur, S. (2012), NGC 5548: Lack of a Broad Fe Kα Line and Constraints on the Location of the Hard X-Ray Source, *Astrophys. J.*, **744**, 13, arXiv: `1109.4651`.

Brenneman, L. W. and Reynolds, C. S. (2006), Constraining Black Hole Spin via X-Ray Spectroscopy, *Astrophys. J.*, **652**, pp. 1028–1043, arXiv: `astro-ph/0608502`.

Czerny, B. and Goosmann, R. (2004), Flare-induced fountains and buried flares in AGN, *Astronomy and Astrophysics*, **428**, pp. 353–363, arXiv: `astro-ph/0408472`.

Dauser, T., Svoboda, J., Schartel, N., Wilms, J., Dovčiak, M., Ehle, M., Karas, V., Santos-Lleó, M. and Marshall, H. L. (2012), Spectral analysis of 1h 0707-495 with xmm-newton, *Monthly Notices Roy. Astronom. Soc.*, **422**(3), pp. 1914–1921.

Dovciak, M. (2004), *Radiation of Accretion Discs in Strong Gravity*, Ph.D. thesis, PhD Thesis, 2004, arXiv: `arXiv:astro-ph/0411605`.

Dovčiak, M., Karas, V. and Yaqoob, T. (2004), An Extended Scheme for Fitting X-Ray Data with Accretion Disk Spectra in the Strong Gravity Regime, *Astrophys. J. Suppl.*, **153**, pp. 205–221, arXiv: `astro-ph/0403541`.

Dovčiak, M., Muleri, F., Goosmann, R. W., Karas, V. and Matt, G. (2011), Light-bending Scenario for Accreting Black Holes in X-ray Polarimetry, *Astrophys. J.*, **731**, 75, arXiv: `1102.4247`.

Dumont, A.-M., Abrassart, A. and Collin, S. (2000), A code for optically thick and hot photoionized media, *Astronomy and Astrophysics*, **357**, pp. 823–838, arXiv: `astro-ph/0003220`.

Fabian, A. C., Vaughan, S., Nandra, K., Iwasawa, K., Ballantyne, D. R., Lee, J. C., De Rosa, A., Turner, A. and Young, A. J. (2002), A long hard look at MCG-6-30-15 with XMM-Newton, *Monthly Notices Roy. Astronom. Soc.*, **335**, pp. L1–L5, arXiv: `astro-ph/0206095`.

Fabian, A. C., Zoghbi, A., Ross, R. R., Uttley, P., Gallo, L. C., Brandt, W. N., Blustin, A. J., Boller, T., Caballero-Garcia, M. D., Larsson, J., Miller, J. M., Miniutti, G., Ponti, G., Reis, R. C., Reynolds, C. S., Tanaka, Y. and Young, A. J. (2009), Broad line emission from iron K- and L-shell transitions in the active galaxy 1H0707-495, *Nature*, **459**, pp. 540–542.

George, I. M. and Fabian, A. C. (1991), X-ray reflection from cold matter in active galactic nuclei and X-ray binaries, *Monthly Notices Roy. Astronom. Soc.*, **249**, pp. 352–367.

Ghisellini, G., Haardt, F. and Matt, G. (1994), The Contribution of the Obscuring Torus to the X-Ray Spectrum of Seyfert Galaxies – a Test for the Unification Model, *Monthly Notices Roy. Astronom. Soc.*, **267**, p. 743, arXiv: `astro-ph/9401044`.

Goosmann, R. W., Czerny, B., Mouchet, M., Karas, V., Dovčiak, M., Ponti, G. and Różańska, A. (2006), Magnetic flares in Active Galactic Nuclei: modeling the iron Kα line, *Astronomische Nachrichten*, **327**, pp. 977–980, arXiv: `astro-ph/0611020`.

Goosmann, R. W., Mouchet, M., Czerny, B., Dovčiak, M., Karas, V., Różańska, A. and Dumont, A.-M. (2007), Iron lines from transient and persisting hot spots on AGN accretion disks, *Astronomy and Astrophysics*, **475**, pp. 155–168, arXiv: `0709.1356`.

Haardt, F. (1993), Anisotropic Comptonization in thermal plasmas – Spectral distribution in plane-parallel geometry, *Astrophys. J.*, **413**, pp. 680–693.

Haardt, F. and Maraschi, L. (1991), A two-phase model for the X-ray emission from Seyfert galaxies, *Astronomy and Astrophysics Lett.*, **380**, pp. L51–L54.

Kawanaka, N., Mineshige, S. and Iwasawa, K. (2005), Iron Fluorescent Line Emission from Black Hole Accretion Disks with Magnetic Reconnection-heated Corona, *Astrophys. J.*, **635**, pp. 167–172, arXiv: `astro-ph/0508507`.

Laor, A. (1991), Line profiles from a disk around a rotating black hole, *Astrophys. J.*, **376**, pp. 90–94.

Martocchia, A., Karas, V. and Matt, G. (2000), Effects of Kerr space-time on spectral features from X-ray illuminated accretion discs, *Monthly Notices Roy. Astronom. Soc.*, **312**, pp. 817–826, arXiv: `astro-ph/9910562`.

Martocchia, A., Matt, G. and Karas, V. (2002), On the origin of the broad, relativistic iron line of MCG-6-30-15 observed by XMM-Newton, *Astronomy and Astrophysics*, **383**, pp. L23–L26.

Matt, G., Fabian, A. C. and Ross, R. R. (1993), Iron K-alpha lines from X-ray photoionized accretion discs, *Monthly Notices Roy. Astronom. Soc.*, **262**, pp. 179–186.

Matt, G., Perola, G. C. and Piro, L. (1991), The iron line and high energy bump as X-ray signatures of cold matter in Seyfert 1 galaxies, *Astronomy and Astrophysics*, **247**, pp. 25–34.

Merloni, A., Heinz, S. and di Matteo, T. (2003), A Fundamental Plane of black hole activity, *Monthly Notices Roy. Astronom. Soc.*, **345**, pp. 1057–1076, arXiv: `astro-ph/0305261`.

Miller, J. M. (2007), Relativistic X-Ray Lines from the Inner Accretion Disks Around Black Holes, *Annual Review of Astronomy & Astrophysics*, **45**, pp. 441–479, arXiv: 0705.0540.

Miniutti, G. and Fabian, A. C. (2004), A light bending model for the X-ray temporal and spectral properties of accreting black holes, *Monthly Notices Roy. Astronom. Soc.*, **349**, pp. 1435–1448, arXiv: astro-ph/0309064.

Miniutti, G., Fabian, A. C., Anabuki, N., Crummy, J., Fukazawa, Y., Gallo, L., Haba, Y., Hayashida, K., Holt, S., Kunieda, H., Larsson, J., Markowitz, A., Matsumoto, C., Ohno, M., Reeves, J. N., Takahashi, T., Tanaka, Y., Terashima, Y., Torii, K., Ueda, Y., Ushio, M., Watanabe, S., Yamauchi, M. and Yaqoob, T. (2007), Suzaku Observations of the Hard X-Ray Variability of MCG -6-30-15: the Effects of Strong Gravity around a Kerr Black Hole, *Publications of the Astronomical Society of Japan*, **59**, pp. 315–325, arXiv: astro-ph/0609521.

Miniutti, G., Fabian, A. C., Goyder, R. and Lasenby, A. N. (2003), The lack of variability of the iron line in MCG-6-30-15: general relativistic effects, *Monthly Notices Roy. Astronom. Soc.*, **344**, pp. L22–L26, arXiv: astro-ph/0307163.

Nandra, K. (2011), ATHENA: The Advanced Telescope for High Energy Astrophysics, in J.-U. Ness and M. Ehle, editors, *The X-ray Universe 2011*, p. 22.

Nandra, K., O'Neill, P. M., George, I. M. and Reeves, J. N. (2007), An XMM-Newton survey of broad iron lines in Seyfert galaxies, *Monthly Notices Roy. Astronom. Soc.*, **382**, pp. 194–228, arXiv: 0708.1305.

Nayakshin, S. and Kallman, T. R. (2001), Accretion Disk Models and Their X-Ray Reflection Signatures. I. Local Spectra, *Astrophys. J.*, **546**, pp. 406–418, arXiv: astro-ph/0005597.

Novikov, I. D. and Thorne, K. S. (1973), Astrophysics of black holes., in C. Dewitt and B. S. Dewitt, editors, *Black Holes (Les Astres Occlus)*, pp. 343–450.

Penna, R. F., McKinney, J. C., Narayan, R., Tchekhovskoy, A., Shafee, R. and McClintock, J. E. (2010), Simulations of magnetized discs around black holes: effects of black hole spin, disc thickness and magnetic field geometry, *Monthly Notices Roy. Astronom. Soc.*, **408**, pp. 752–782, arXiv: 1003.0966.

Ponti, G., Gallo, L. C., Fabian, A. C., Miniutti, G., Zoghbi, A., Uttley, P., Ross, R. R., Vasudevan, R. V., Tanaka, Y. and Brandt, W. N. (2010), Relativistic disc reflection in the extreme NLS1 IRAS13224-3809, *Monthly Notices Roy. Astronom. Soc.*, **406**, pp. 2591–2604, arXiv: 0911.1003.

Reynolds, C. S., Brenneman, L. W., Wilms, J. and Kaiser, M. E. (2004), Iron line spectroscopy of NGC 4593 with XMM-Newton: where is the black hole accretion disc?, *Monthly Notices Roy. Astronom. Soc.*, **352**, pp. 205–210, arXiv: astro-ph/0404187.

Reynolds, C. S. and Nowak, M. A. (2003), Fluorescent iron lines as a probe of astrophysical black hole systems, *Physics Reports*, **377**, pp. 389–466, arXiv: astro-ph/0212065.

Ross, R. R. and Fabian, A. C. (2005), A comprehensive range of X-ray ionized-reflection models, *Monthly Notices Roy. Astronom. Soc.*, **358**, pp. 211–216, arXiv: astro-ph/0501116.

Różańska, A., Dumont, A.-M., Czerny, B. and Collin, S. (2002), The structure and radiation spectra of illuminated accretion discs in active galactic nuclei - I. Moderate illumination, *Monthly Notices Roy. Astronom. Soc.*, **332**, pp. 799–813, arXiv: astro-ph/0202069.

Różańska, A., Madej, J., Konorski, P. and SaĐowski, A. (2011), Iron lines in model disk spectra of Galactic black hole binaries, *Astronomy and Astrophysics*, **527**, A47, arXiv: 1011.2061.

Shakura, N. I. and Sunyaev, R. A. (1973), Black holes in binary systems. Observational appearance., *Astronomy and Astrophysics*, **24**, pp. 337–355.

Svoboda, J., Dovčiak, M., Goosmann, R. and Karas, V. (2009), Role of emission angular directionality in spin determination of accreting black holes with a broad iron line, *Astronomy and Astrophysics*, **507**, pp. 1–17, arXiv: 0908.2387.

Svoboda, J., Guainazzi, M. and Karas, V. (2010), Warm absorber and truncated accretion disc in IRAS 05078+1626, *Astronomy and Astrophysics*, **512**, A62, arXiv: `0912.5165`.

Vaughan, S. and Fabian, A. C. (2004), A long hard look at MCG-6-30-15 with XMM-Newton- II. Detailed EPIC analysis and modelling, *Monthly Notices Roy. Astronom. Soc.*, **348**, pp. 1415–1438, arXiv: `astro-ph/0311473`.

Wilkins, D. R. and Fabian, A. C. (2011), Determination of the X-ray reflection emissivity profile of 1H 0707-495, *Monthly Notices Roy. Astronom. Soc.*, **414**, pp. 1269–1277, arXiv: `1102.0433`.

Wilms, J., Reynolds, C. S., Begelman, M. C., Reeves, J., Molendi, S., Staubert, R. and Kendziorra, E. (2001), XMM-EPIC observation of MCG-6-30-15: direct evidence for the extraction of energy from a spinning black hole?, *Monthly Notices Roy. Astronom. Soc.*, **328**, pp. L27–L31, arXiv: `astro-ph/0110520`.

Zhou, X. L., Zhao, Y. H. and Soria, R. (2011), Ionization structure and Fe Kα energy for irradiated accretion discs, *Monthly Notices Roy. Astronom. Soc.*, **413**, pp. L61–L65, arXiv: `1102.3327`.

Zoghbi, A., Fabian, A. C., Uttley, P., Miniutti, G., Gallo, L. C., Reynolds, C. S., Miller, J. M. and Ponti, G. (2010), Broad iron L line and X-ray reverberation in 1H0707-495, *Monthly Notices Roy. Astronom. Soc.*, **401**, pp. 2419–2432, arXiv: `0910.0367`.

Zycki, P. T. and Czerny, B. (1994), The Iron K-Alpha Line from a Partially Ionized Reflecting Medium in an Active Galactic Nucleus, *Monthly Notices Roy. Astronom. Soc.*, **266**, p. 653.

APPENDIX

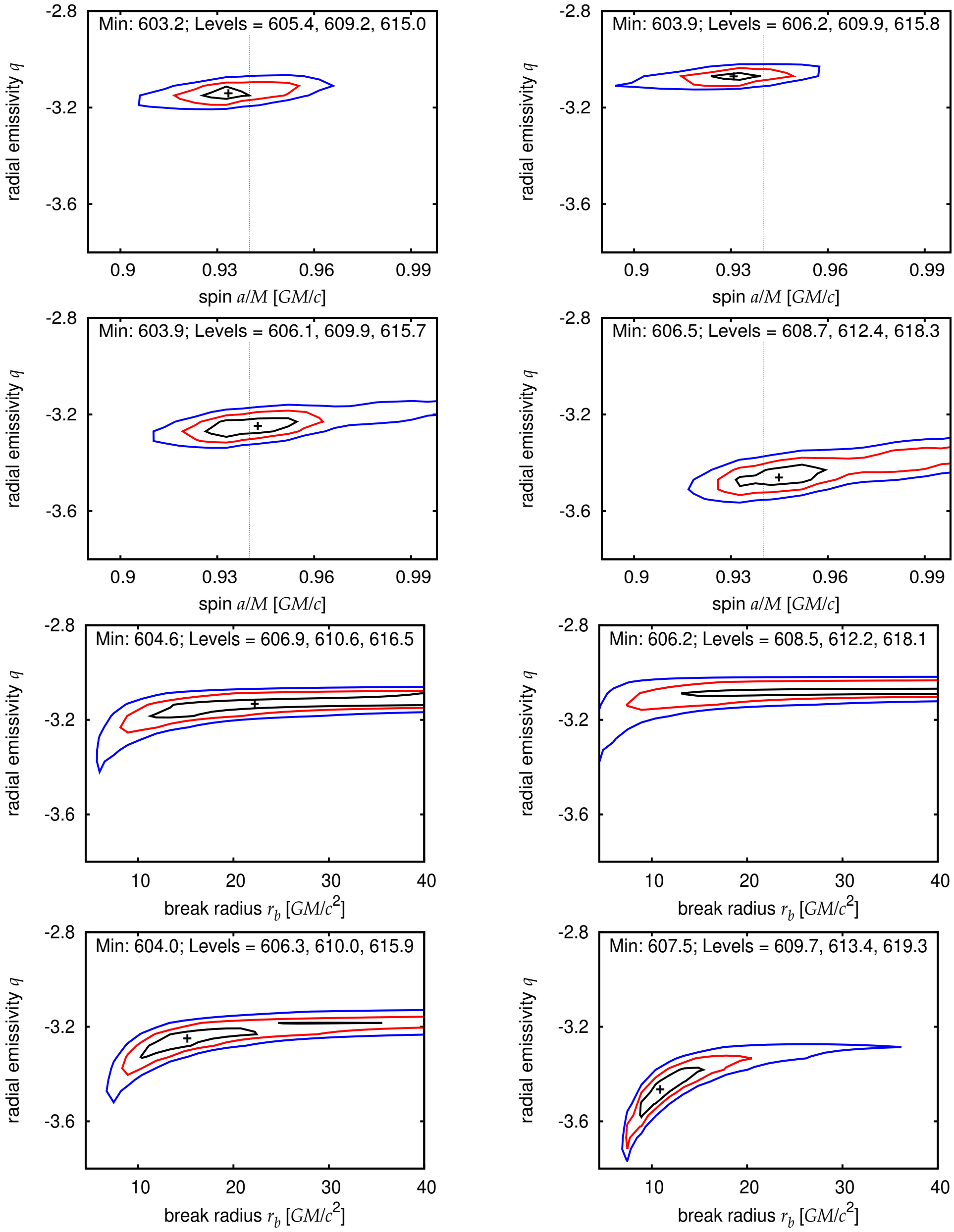

Figure 6. The same as in Fig. 1 and 2 but for the height $h = 3\,r_g$.

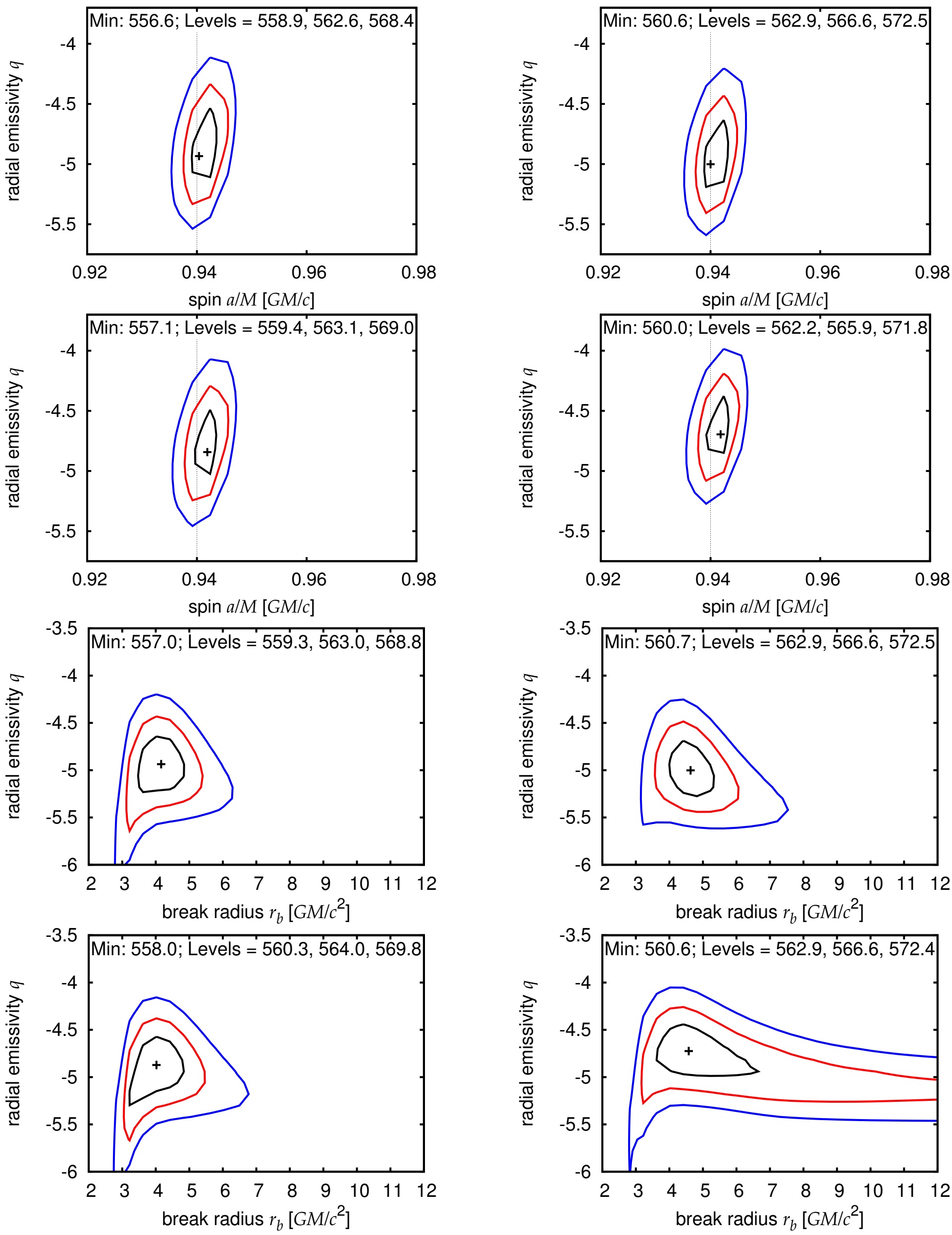

Figure 7. The same as in Fig. 1 and 2 ($h = 1.5\, r_g$) but for inclination 70 deg.

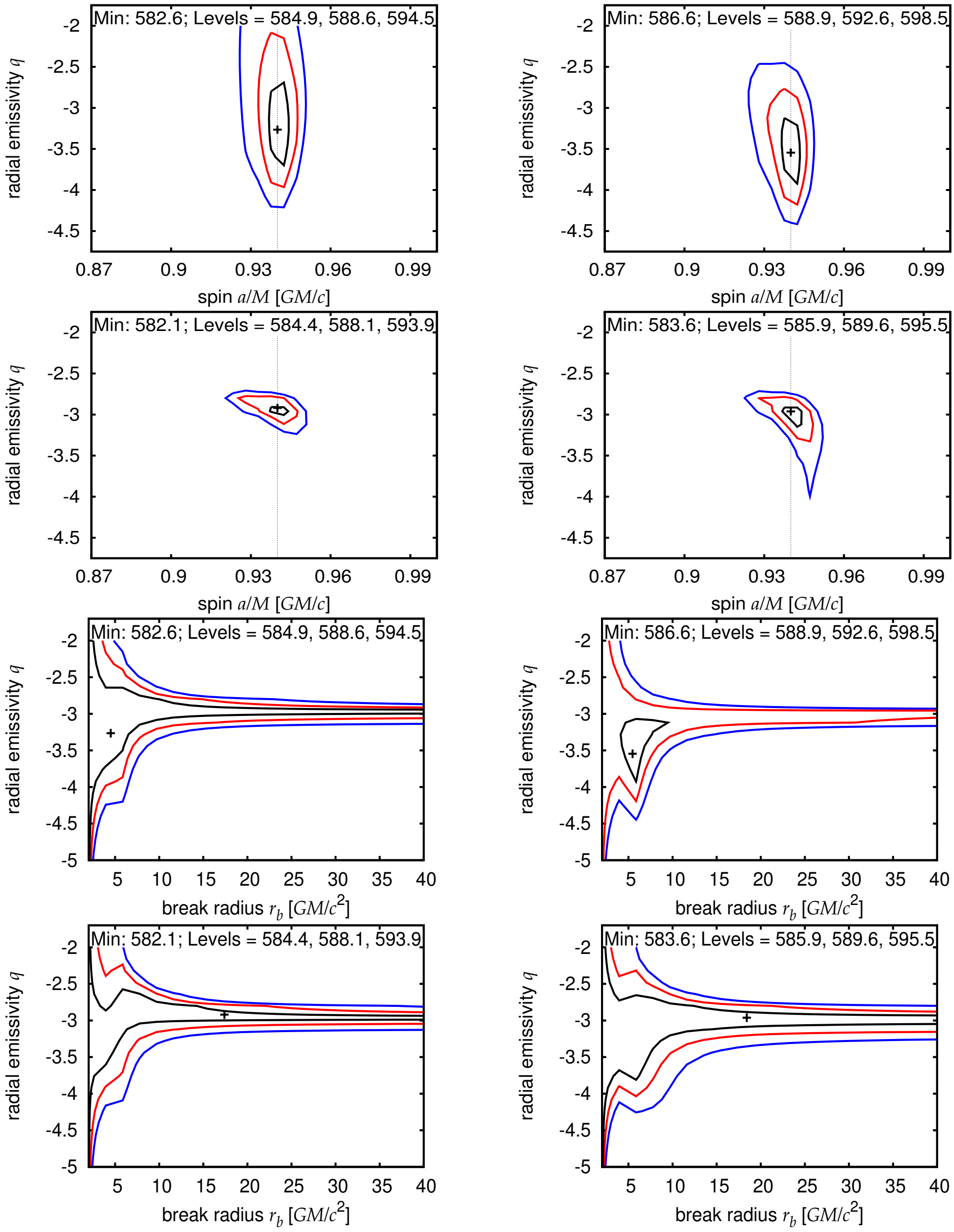

Figure 8. The same as in Fig. 6 ($h = 3\,r_g$) but for inclination 70 deg.

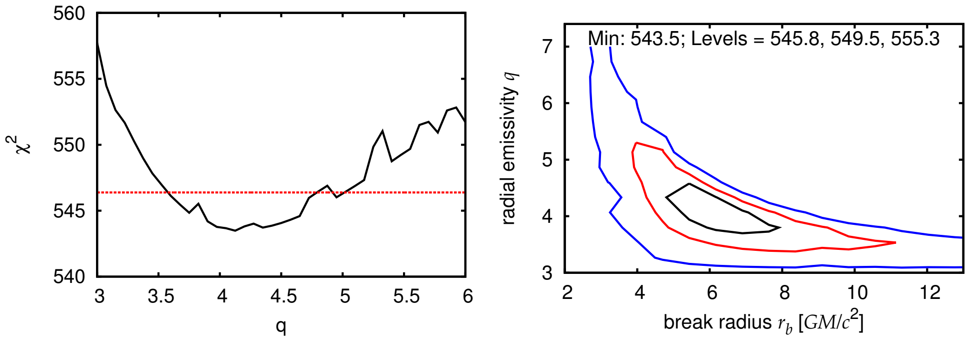

Figure 9. The same as in Fig. 3 but for $\xi_{\text{in}} = 50$ and $\xi_{\text{out}} = 30$.

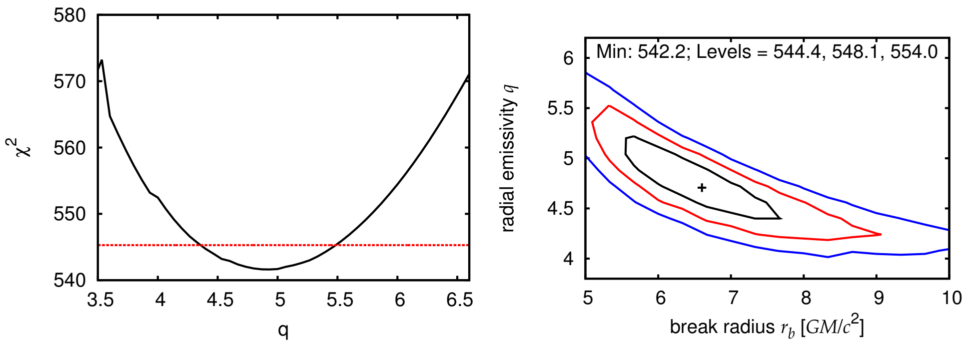

Figure 10. The same as in Fig. 3 but for $\xi_{\text{in}} = 80$ and $\xi_{\text{out}} = 30$.

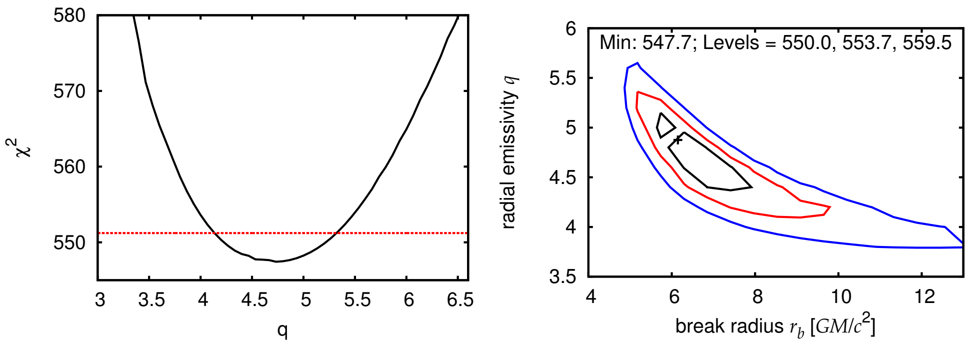

Figure 11. The same as in Fig. 3 but for $\xi_{\text{in}} = 100$ and $\xi_{\text{out}} = 30$.

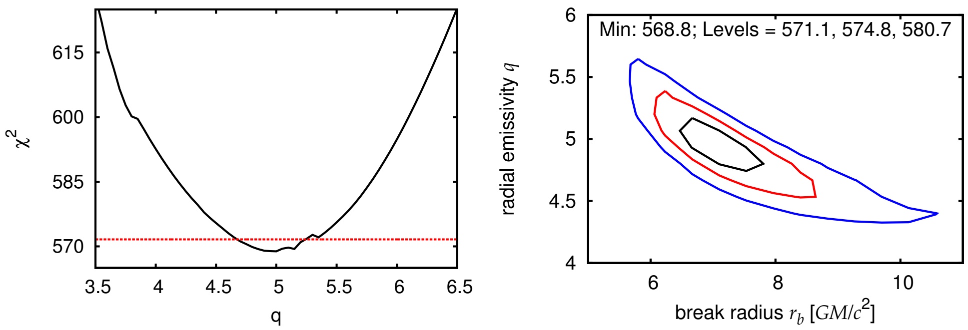

Figure 12. The same as in Fig. 3 but for $\xi_{\rm in} = 130$ and $\xi_{\rm out} = 30$.

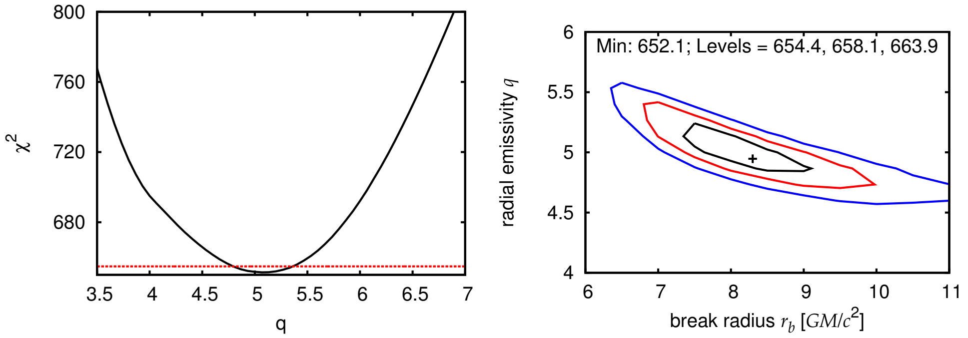

Figure 13. The same as in Fig. 3 but for $\xi_{\rm in} = 200$ and $\xi_{\rm out} = 30$.

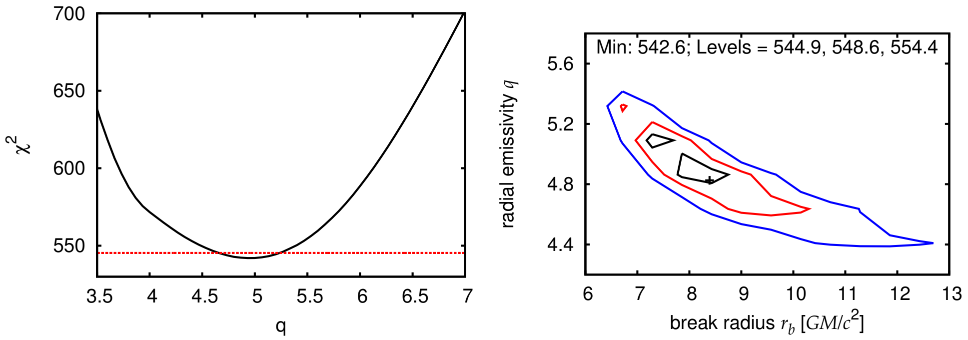

Figure 14. The same as in Fig. 13 but for spin $a = 0.99$.

Title: **Proceedings of RAGtime 10–13: Workshops on black holes and neutron stars, 15–17/20–22/15–17/14–16 September 2008/2009/2010/2011, Opava, Czech Republic**

Published by: Silesian University in Opava
Faculty of Philosophy and Science
Institute of Physics
Bezručovo nám. 13
CZ-746 01 Opava
Czech Republic

Editors: Z. Stuchlík, G. Török and T. Pecháček

Cover design: Otakar Karlas

1st edition

Printed by: Z + M Partner, s.r.o.
Valchařska 3261/17
CZ-702 00 Ostrava-Moravská Ostrava
Czech Republic

Published in December 2014

european social fund in the czech republic
EUROPEAN UNION
MINISTRY OF EDUCATION, YOUTH AND SPORTS
OP Education for Competitiveness
Silesian University in Opava
INVESTMENTS IN EDUCATION DEVELOPMENT

The publication was prepared as the study material in the framework of the project "Supporting Integration with the International Theoretical and Observational Research Network in Relativistic Astrophysics of Compact Objects", CZ.1.07/2.3.00/20.0071. The project is co-financed by European Social fund and state budget of the Czech Republic.

ISBN 978-80-7510-125-9
ISSN 2336-5668 (Print)
ISSN 2336-5676 (Online)

Typeset in LaTeX

Název: **Proceedings of RAGtime 10–13: Workshops on black holes and neutron stars, 15–17/20–22/15–17/14–16 September 2008/2009/2010/2011, Opava, Czech Republic**

Nakladatel: Slezská univerzita v Opavě
Filozoficko-přírodovědecká fakulta
Ústav fyziky
Bezručovo nám. 13
CZ-746 01 Opava
Česká republika

Editoři: Z. Stuchlík, G. Török and T. Pecháček

Obálka: Otakar Karlas

První vydání

Tisk: Z + M Partner, s.r.o.
Valchařska 3261/17
CZ-702 00 Ostrava-Moravská Ostrava
Czech Republic

Vydáno v prosinci 2014

european social fund in the czech republic
EUROPEAN UNION
MINISTRY OF EDUCATION, YOUTH AND SPORTS
OP Education for Competitiveness
Silesian University in Opava
INVESTMENTS IN EDUCATION DEVELOPMENT

The publication was prepared as the study material in the framework of the project "Supporting Integration with the International Theoretical and Observational Research Network in Relativistic Astrophysics of Compact Objects", CZ.1.07/2.3.00/20.0071. The project is co-financed by European Social fund and state budget of the Czech Republic.

ISBN 978-80-7510-125-9
ISSN 2336-5668 (Print)
ISSN 2336-5676 (Online)

Vysázeno systémem LaTeX

european
social fund in the
czech republic

EUROPEAN UNION

MINISTRY OF EDUCATION,
YOUTH AND SPORTS

OP Education
for Competitiveness

INVESTMENTS IN EDUCATION DEVELOPMENT

ISBN 978-80-7510-125-9
ISSN 2336-5676